

Abstract

LOEBL, ANDREW JAMES. Surface Chemistry and Precursor Material Effects on the Performance of Pyrolyzed Nanofibers as Anodes for Lithium-ion Batteries. (Under the direction of Dr. Peter S. Fedkiw).

Next-generation lithium-ion batteries to meet consumer demands and new applications require the development of new electrode materials. Electrospinning of polymers is a simple and effective method to create one-dimensional, self-supporting materials, with no inactive components after pyrolysis. Composites of these nanofibers and high-capacity lithium materials have been demonstrated to possess superior reversible capacity than state-of-the-art commercial anodes.

Despite impressive reversible discharge capacities polyacrylonitrile-based composites are not ready for adoption in commercial applications. These materials suffer from irreversible losses of Li to formation on the electrode of the solid electrolyte interphase during the first charge of the cell. This thesis work has taken two approaches to engineer high-performing nanofiber-based electrodes.

First, the chemistry at the interface of the electrode and the electrolyte has been changed by depositing new surfaces. Attempts to create a graphitic fiber surface via plasma enhanced chemical vapor deposition did not result in an improvement of the irreversible losses. However, the experiments did demonstrate the growth of large surface area carbon nanowalls on the pyrolyzed electrospun fibers, creating a material which could serve as a substrate in catalysis or as an electrode for composite ultra-capacitors. Additionally, passivation surfaces were deposited by atomic layer deposition and molecular layer deposition. These new surfaces were employed to reduce the irreversible consumption of

lithium by moving the charge transfer reaction to the interface of the carbon and the new material. The removal the lithium from the solvent prior to charge transfer limits the irreversible reduction of solvent by metallic lithium.

Alumina films grown by atomic layer deposition reduced lithium losses to the solid electrolyte interphase by up to 42% for twenty deposition cycles. This large improvement in irreversible capacity resulted in a nearly 50% reduction in reversible lithium storage. Thinner coatings of alumina had a less dramatic effect on both the irreversible capacity losses and the reversible discharge capacity. A coating of ten cycles of alumina at a temperature of 150 °C resulted in a 17% reduction in irreversible capacity with negligible impact on the reversible capacity.

Hybrid aluminum-organic films grown by molecular layer deposition also reduced irreversible lithium losses. The largest reduction was 23% for electrodes coated with 40 cycles of the alucone material. For all thicknesses studied these hybrid films delivered less improvement than the alumina grown by atomic layer deposition, with poor reversible lithium storage capacity available at high charging and discharging currents.

Second, polyacrylonitrile has served as the precursor for electrospun composite electrodes because of its ease of processing and well-known carbonization process. Polyimides represent a family of polymers for which the material properties can be tailored by careful monomer selection. These polymers were used as the non-woven matrix to create materials capable of delivering a larger percentage of their maximum reversible capacities at high currents when compared to polyacrylonitrile-based electrodes. These materials had a more graphitic structure based on Raman spectroscopy, and resulted in lower irreversible

capacity losses than polyacrylonitrile-based fibers for fibers based on pyromellitic dianhydride and *p*-phenylene diamine.

Surface Chemistry and Precursor Material Effects on the Performance of Pyrolyzed
Nanofibers as Anodes for Lithium-ion Batteries

by
Andrew James Loebel

A dissertation submitted to the Graduate Faculty of
North Carolina State University
in partial fulfillment of the
requirements for the degree of
Doctor of Philosophy

Chemical Engineering

Raleigh, North Carolina

2012

APPROVED BY:

Peter S. Fedkiw
Committee Chair

Saad A. Khan

Xiangwu Zhang

Jerome J. Cuomo

Dedication

I dedicate this work to my grandparents: Arthur and Dorothy Cieslik and Herman and June Loebel. Each of them fostered and indulged my curiosity as a child. Their efforts helped shape my passion for learning about the world around me and I am grateful for every moment we have shared.

Biography

Andrew James Loebel was born on the south side of Milwaukee, WI in 1979. Prior to high school he lived in Portage, WI; Rockford, IL; and Billings, MT. His family returned to Rockford and he graduated from Boylan Central Catholic High School. In high school Andrew was most influenced by his math and chemistry teachers. He enrolled at Northwestern University in the fall of 1997 with a major in chemical engineering and graduated in 2001. He also studied archeology and anthropology. While at Northwestern he met Nora Schuette and they married 6 years later in the spring of 2005.

Andrew's first job after college was as a metrology engineer at Intel Corporation's Fab 11X in Rio Rancho, NM. As part of this work, he completed a six month temporary business assignment at the process research and development site in Hillsboro, OR. Andrew returned to New Mexico and contributed to two process startups at his home site, where he was primarily responsible for the metrology control of the gate oxides and back-end dielectrics. In 2004 Andrew moved to New York to join IBM and became the lead measurement engineer responsible for implementation of an inline wavelength dispersive X-ray spectroscopy system for measuring hafnium and nitrogen content in the gate dielectrics on production material. At IBM, Andrew again worked very closely with the research and development team. His experience with the talented Ph.D. level scientists and engineers at Intel and IBM led him to apply to graduate school in 2006. He joined the Fedkiw group at North Carolina State University because of an interest in energy systems and a desire to broaden his technical expertise.

Acknowledgements

I would first like to acknowledge the patience, insight, and counsel of my advisor, Dr. Peter S. Fedkiw. His efforts have sharpened my thoughts and dramatically improved my writing. Second, I want to acknowledge my committee, Dr. Saad A. Khan, Dr. Xiangwu Zhang, and Dr. Jerome Cuomo. Their expertise, advice, and resources were invaluable in navigating the challenges that lead to this document.

I offer sincere thanks to Dr. Chris Bonino, a classmate, whose fellowship, inside and outside the lab, I greatly value. Within the Fedkiw group, I appreciated all the give-and-take discussions with my fellow graduate students and post-docs. Special thanks is given to Joshua McClure for his assistance in performing plasma enhanced chemical vapor deposition of carbon and for his time spent collecting Raman spectra.

I wish to credit Dr. Gregory Parsons and his research group for their assistance in performing the atomic and molecular layer deposition. In particular, I wish to thank Dr. Christopher Oldham, Dr. Bo Gong, Christina Devine, and Sarah Atanasov. Additional consideration is given to Dr. Jackson Thornton, a student under the direction of Dr. Cuomo. He was the first collaborator I partnered with beyond the initial scope of the project.

I thank Chuck Mooney at the NC State Analytical Instrumentation facility for training (and retraining) me in the art of scanning electron microscopy. I would also like to thank Kim Hutchison for her efforts to assay the aluminum and tin content of the nanofibers in this research by inductively coupled plasma mass spectrometry.

I thank the employees of Caribou Coffee store #306 for supplying me a perfect environment in which to work or to relax, and for providing me with a steady supply of Earl Grey.

I thank all my friends and extended family around the world for the times we have shared. You are all very special to me.

I must acknowledge my loyal and energetic dog, Chloe. I know of no better exercise partner, nor of any better example of living for and enjoying the moment (or cheese).

To my parents, John and Pat Loebel, I offer my most sincere gratitude for their love and support. Their choices, time, and energy created the foundation for what I have achieved in life. My younger brother, Joe Loebel, as good a man as I know, has always been there when I need him.

Most importantly I thank my dear wife, Nora Schuette. This endeavor would not have been possible without her unwavering love, support, and encouragement. She is everything I could ever ask for in a partner in the adventure that is life.

Table of Contents

List of Tables	ix
List of Figures	xi
Chapter 1. Introduction	1
Chapter 2. Literature Review	5
2.1. Lithium-ion Battery Technology	6
2.2. Graphitic Anodes	8
2.3. Non-Graphitic Carbon Anodes	9
2.4. Non-Carbon Anodes	11
2.5. Electrolytes and the Solid Electrolyte Interphase	19
2.6. Electrospinning	27
2.7. Polyacrylonitrile	31
2.8. Polyimide	34
2.9. Chemical Vapor Deposition	40
2.10. Raman Spectroscopy	45
2.11. Atomic Layer Deposition	48
2.12. Molecular Layer Deposition	49
Chapter 3. Plasma Enhanced Chemical Vapor Deposition of Graphitic Carbon on Pyrolyzed Nanofiber Li-ion Anodes	53
3.1. Introduction	54
3.2. Materials and Methods	58
3.3. Results and Discussion	63

3.3.1. CVD Experiments #1 and #2	63
3.3.2. CVD Experiment #3	68
3.3.3. CVD Experiment #4	75
3.3.4. Micro Raman Spectroscopy	82
3.4. Conclusions	85
Chapter 4. Atomic Layer Deposition of Alumina onto Lithium-ion Carbon Nanofiber Electrodes	87
4.1. Introduction	88
4.2. Materials and Methods	90
4.3. Results and Discussion	93
4.3.1. Fiber Morphology and Composition	93
4.3.2. Electrochemical Performance	97
4.4. Conclusion	106
Chapter 5. Molecular Layer Deposition of Alucone onto Lithium-ion Carbon Nanofiber Electrodes	108
5.1. Introduction	109
5.2. Materials and Methods	112
5.3. Results and Discussion	115
5.3.1. Fiber Morphology	115
5.3.2. Electrochemical Performance	118
5.4. Conclusion	122
Chapter 6. Pyrolyzed Polyimide/Tin Composite Nanofibers as Anodes in Lithium-ion Batteries	124

6.1.	Introduction	125
6.2.	Materials and Methods	129
6.3.	Results and Discussion	133
6.3.1.	Impact of Polymerization Methods on Solution Properties and Electrospinning	133
6.3.2.	Impact of Tin Complexes on Solution Properties and Electrospinning	147
6.3.3.	Results of Size Exclusion Chromatography	155
6.3.4.	Electrochemical Performance	169
6.4.	Conclusion	181
Chapter 7.	Summary and Conclusions	184
Chapter 8.	Proposed Future Research	190
8.1.	ALD/MLD of Lithium-Organic Films as an Artificial SEI Layer on Electrospun Carbon Nanofiber Anodes	191
8.2.	Vapor Phase MLD of PMDA-PPD Polyimide on PAN-based Nanofibers	193
8.3.	Anodes Made by Chemical Vapor Deposition of Silicon onto Electrospun Carbonized Nanofibers	195
8.4.	Ultra-capacitors made from Electrospun Fibers Coated with Carbon Nanowalls by PECVD and the Potential Role of ALD in Further Performance Increases	197
8.5.	Electrospun ALD/MLD Coated Electrodes with an Embedded Mesh Current Collector	200
8.6.	Thermochemical Reduction of SnO ₂ Nanoparticles in Pyrolyzed Nanofibers via a Hydrogen Containing Atmosphere	203
References	205

List of Tables

Table 2.1.	Examples of recent structures and composites utilizing silicon and the resulting performance as Li-ion anodes	15
Table 2.2.	Examples of recent structures and composites utilizing silicon and the resulting performance as Li-ion anodes	17
Table 2.3.	Mass of cathode material required to compensate for C_{irr} . The capacity of $LiCoO_2$ and $LiFePO_4$ are assumed to be 140 mAh/g and 170 mAh/g, respectively	23
Table 2.4.	Hypothetical surface area of a smooth fiber of density 1 g/cm ³ for various diameters	28
Table 3.1.	Processing conditions during PECVD	62
Table 3.2.	Change in mass of samples treated in CVD Experiment #2	65
Table 3.3.	Change in mass of samples treated in CVD Experiment #3	69
Table 3.4.	Change in mass of the reference samples for CVD Experiment #3 during pyrolysis at the indicated temperature	72
Table 3.5.	Change in mass of samples treated in CVD Experiment #4	76
Table 3.6.	Fiber diameters of the samples of CVD Experiment #4 measured by SEM for the surface facing the plasma coils	77
Table 3.7.	Raman parameters for the G and D peaks for Experiments #3 and #4, the estimated basal plane crystallite size and estimated sp^3 carbon content based on reference 331	84
Table 4.1.	Relative elemental composition by EDX of samples to nearest 0.5%, absolute aluminum mass content as measured by ICP-MS, and thickness of alumina film on silicon measured by ellipsometry	95
Table 4.2.	Relative layer-by-layer elemental composition measured by EDX of pyrolyzed fibers coated for 10 alumina ALD cycles at 90 °C from top (1) to bottom (4) as seen in Figure 4.2	96
Table 5.1.	Mass gain during MLD on pyrolyzed PAN nanofibers, estimated thickness of the film, and the film thickness on Si when available	116

Table 5.2.	Summary of average irreversible capacity improvements produced by MLD of alucone onto pyrolyzed PAN electrodes	122
Table 6.1.	Range of morphologies produced from PMDA-ODA solutions during electrospinning	133
Table 6.2.	Summary of attempts to utilize dimethyldiodecanoate tin with low concentrations of PMDA-PPD derived poly(amic acid). Unless otherwise noted, the flow rate for electrospinning was set at 1 mL/h, tip to collector distance was 15 cm, and the needle was 22-gauge	154
Table 6.3.	Reported number average molecular weight (M_n), weight-average molecular weight (M_w), and polydispersity index (PDI) of the PEO standards used to calibrate the differential RI detector on the size exclusion chromatography column	156
Table 6.4.	Equivalent number and weight average molecular weight of PMDA-ODA samples as measured by SEC over three days beginning on the day of polymerization	159
Table 6.5.	Equivalent number and weight average molecular weight of PMDA-PPD samples as measured by SEC over three days beginning on the day of polymerization	161
Table 6.6.	Equivalent number and weight average molecular weight of 15 wt% PMDA-PPD samples, polymerized with the indicated amount of tin compounds relative to polymer mass, as measured by SEC	169
Table 6.7.	Comparison of the capacity retention at the indicated increasing applied currents for the various precursor polymers used in this work	170

List of Figures

Figure 2.1.	Diagram depicting the typical experimental setup for electrospinning polymer solutions	29
Figure 2.2.	Chemical structure of a) the acrylonitrile monomer and b) polyacrylonitrile .	32
Figure 2.3.	The reactions to form poly(amic acid) and subsequent thermal imidization by dehydration between a) pyromellitic dianhydride and 4,4'-oxydianiline and b) pyromellitic dianhydride and <i>p</i> -phenylene diamine	35
Figure 3.1.	First-cycle irreversible capacity for electrodes made from PAN fibers pyrolyzed at the indicated temperatures throughout the work leading to this dissertation. The electrolyte was 1 M LiPF ₆ in EC:EMC (1:1)	57
Figure 3.2.	Shear viscosity of 150,000 g/mol weight average molecular weight (M _w) PAN dissolved in DMF between 0.125 and 20 wt% polymer	59
Figure 3.3.	Schematic of the PECVD chamber used to deposit carbon	61
Figure 3.4.	Scanning electron micrographs of (a) fibers after coating during CVD Experiment #1 and (b) uncoated reference fibers	64
Figure 3.5.	Scanning electron micrograph at 50,000x magnification of a single large fiber showing small platelet growth perpendicular to the fiber surface	64
Figure 3.6.	Scanning electron micrographs of fibers from CVD Experiment #2 (a) Sample 2, (b) Sample 3, and (c) untreated reference	66
Figure 3.7.	First-cycle irreversible capacity of a) untreated reference samples, b) PECVD Sample 2, and c) PECVD Sample 3	67
Figure 3.8.	Reversible discharge capacity of a) untreated reference samples, b) cells from PECVD sample 2, and c) cells from PECVD sample 3 at cycled at a specific current of 25 mA/g	68
Figure 3.9.	Scanning electron micrograph of untreated nanofibers used as a reference in CVD Experiment #3 magnified (a) 2,000x and (b) 10,000x	69
Figure 3.10.	Scanning electron micrograph of fibers from Sample 5 on the surface facing towards the plasma coil and away from the heater magnified (a) 2,000x and (b) 10,000x	10

Figure 3.11.	Scanning electron micrograph at one location on fibers from Sample 5 for the surface facing towards the heater and away from the plasma coil, displaying ribbons of carbon nanowalls in place of fibers magnified (a) 2,000x and (b) 10,000x	71
Figure 3.12.	Scanning electron micrograph at a different location on the surface of fibers from Sample 5, facing towards the heater and away from the plasma coil displaying carbon nanowalls on the fiber surface and possible single rolls of graphene which may have formed around the fibers magnified (a) 2,000x and (b) 10,000x	71
Figure 3.13.	Reversible discharge capacity of cells from CVD Experiment #3 at the indicated charge/discharge currents	73
Figure 3.14.	Reversible discharge capacity of reference anodes made of fibers pyrolyzed at various temperatures and cycled at the indicated charge/discharge currents ..	74
Figure 3.15.	Comparison of experimental cells with the reference cells made from fibers pyrolyzed at 1100 °C at the indicated charge/discharge currents	74
Figure 3.16.	Comparison of the first-cycle irreversible capacity losses of the cells made for CVD Experiment #3	75
Figure 3.17.	Scanning electron micrograph of untreated nanofibers used as a reference in CVD Experiment #4 magnified (a) 2,000x and (b) 10,000x	77
Figure 3.18.	Scanning electron micrograph of Sample 6 from CVD Experiment #4 on the surface facing towards the plasma coil and away from the heater magnified (a) 2,000x and (b) 10,000x	78
Figure 3.19.	Scanning electron micrograph of Sample 7 from CVD Experiment #4 on the surface facing towards the plasma coil and away from the heater magnified (a) 2,000x and (b) 10,000x	78
Figure 3.20.	Scanning electron micrograph of Sample 8 from CVD Experiment #4 on the surface facing towards the plasma coil and away from the heater magnified (a) 2,000x and (b) 10,000x	79
Figure 3.21.	Scanning electron micrograph of Sample 8, where the surface facing towards the heater, displaying fibers with carbon nanowalls taking the place of the fibers, magnified (a) 2,000x and (b) 10,000x	80

Figure 3.22.	Reversible discharge capacity of cells from CVD Experiment #4 cycled at 25 mA/g	81
Figure 3.23.	Comparison of the first-cycle irreversible capacity losses of the cells made for CVD Experiment #4	82
Figure 3.24.	Raman spectra collected from a PAN nanofibers pyrolyzed at 700 °C containing the dominant features of nano-crystalline carbon: a broad D peak located at 1320 cm ⁻¹ and a broad G peak located at 1582 cm ⁻¹	83
Figure 4.1.	Scanning electron micrographs of nanofibers used for atomic layer deposition as electrospun, (b) and after pyrolysis at 700 °C	94
Figure 4.2.	Illustration of the layer-by-layer sectioning of the nanofiber mat used to assess the uniformity of the deposition alumina throughout the non-woven mat	96
Figure 4.3.	First-cycle irreversible capacity loss of cells using carbon fibers coated with alumina at 90 °C compared to uncoated reference samples	97
Figure 4.4.	First-cycle irreversible capacity loss of cells using carbon fibers coated with alumina by ALD at 45 °C, both with and without the 60 second soak, and at 150 °C, compared to untreated reference samples.....	99
Figure 4.5.	Typical results for cell voltage as a function of capacity at 25 mA/g C/D current for (a) 0 ALD cycles, (b) 10 ALD cycles, (c) 20 ALD cycles	100
Figure 4.6.	Typical charge and discharge capacities for electrodes coated by ALD at 90 °C over 60 cell cycles with symmetric charge and discharge currents as indicated on the figure	101
Figure 4.7.	Typical charge and discharge capacities for electrodes coated by ALD- at 45 °C with a soak step during the ALD process. The charge and discharge currents indicated on the figure were symmetric. The reference cell was deliberately stopped after cycle 24 to free up test equipment for other experiments	102
Figure 4.8.	Typical charge and discharge capacities for electrodes coated by ALD at 45 °C without a soak step during the ALD process. The charge and discharge currents indicated on the figure were symmetric	103
Figure 4.9.	Typical charge and discharge capacities for electrodes coated by ALD at 150 °C. The charge and discharge currents indicated on the figure were symmetric	104

Figure 4.10.	Typical coulombic efficiency over 60 cycles for electrodes coated by ALD at 90 °C with symmetric charge and discharge currents indicated on the figure	105
Figure 4.11.	Typical charge and discharge capacities for electrodes coated by ALD at 90 °C over 60 cycles with asymmetric current. The charge was conducted at 25 mA/g with discharge current indicated on the figure	106
Figure 5.1.	Percentage of mass gain of the pyrolyzed fiber mat as a function of the number of MLD cycles. The trend line is fit to the data for 20 or more cycles	115
Figure 5.2.	Scanning electron micrograph of untreated fibers, pyrolyzed at 700 °C, used as reference material for comparison to fibers coated with alucone by molecular layer deposition at a) 2,000x and b) 10,000x	117
Figure 5.3.	Scanning electron micrograph of fibers coated for 40-cycles with alucone by molecular layer deposition at a) 2,000 x and b) 10,000x	118
Figure 5.4.	Reversible discharge capacity of materials coated with 40 and 20 alucone MLD cycles, and untreated reference materials, at the indicated symmetric charge and discharge currents	119
Figure 5.5.	Average reduction in irreversible capacity of 23% for 40 cycles of alucone and 20% for 20 cycles of alucone on electrodes made of pyrolyzed PAN fibers	120
Figure 5.6.	Reversible discharge capacity of materials coated with 10 and 6 alucone cycles, and untreated reference materials, at the indicated symmetric charge and discharge currents.....	121
Figure 5.7.	Average reduction in irreversible capacity of 9.4% for 10 cycles of alucone and 12.5% for 6 cycles of alucone on electrodes made of pyrolyzed PAN fibers	122
Figure 6.1.	The reactions to form poly(amic acid) and subsequent thermal imidization by dehydration between a) pyromellitic dianhydride and 4,4'-oxydianiline and b) pyromellitic dianhydride and <i>p</i> -phenylene diamine	127
Figure 6.2.	Scanning electron micrograph illustrating the range of morphologies produced from PMDA-ODA solutions during electrospinning, a) 22, b) 24, c) 26, d)28, and e) 30.2 wt% total polymer in DMF	135

Figure 6.3.	Change in shear viscosity for solutions of PMDA-PPD with 7.5, 10 and 12.5 wt% total polymer measured every 12 hours for up to 48 hours after polymerization	136
Figure 6.4.	Scanning electron micrograph containing a mixture of fibers and beads produced from a PMDA-PPD solution of 15 wt% total polymer in the first hour after polymerization	137
Figure 6.5.	Observed change in shear viscosity for co-polymer of PMDA-PPD/ODA with an 85:15 PPD:ODA ratio for a 15 wt% total polymer solution	139
Figure 6.6.	The addition of 1% phthalic anhydride to shorten chain length did not eliminate the gelling and shear thinning for a PMDA-PPD solution with 15 wt% total polymer	140
Figure 6.7.	The use of phthalic anhydride with PMDA-ODA solution of 25 wt% total polymer resulted in lower shear viscosity	140
Figure 6.8.	Proposed double reaction mechanism, creating irreversible chemically cross-linked chains in PMDA-PPD solutions	141
Figure 6.9.	The addition of 2 Mg/mol PEO to PMDA-PPD solutions containing 15 wt% total polymer increased sheer viscosity slightly	142
Figure 6.10.	Scanning electron micrographs of fibers electrospun from 15 wt% PMDA-PPD polymer containing an additional 0.25% PEO (a,c,e), 0.5% PEO (d,e,f). The electric field strength was (a,b) 1 kV/cm, (c,d) 1.33 kV/cm, and (e,f) 1.67 kV/cm	143
Figure 6.11.	Comparison of the shear viscosity of PMDA-ODA solutions with 24 wt% or 25 wt% total polymer polymerized by homogeneous and heterogeneous methods. Heterogeneous methods began with complete dissolution of one monomer then followed by addition of the second solid monomer to the resulting solution	144
Figure 6.12.	Comparison of the shear viscosity of 15 wt% total polymer PMDA-PPD solutions polymerized by homogeneous and heterogeneous methods. Heterogeneous methods began with complete dissolution of one monomer then followed by addition of the second solid monomer to the resulting solution	146

Figure 6.13.	Inclusion of 2 Mg/mol PEO resulted in a lower viscosity solution for the heterogeneous polymerization technique applied to PMDA-PPD solutions of 15 wt% total polymer	147
Figure 6.14.	Addition of 2 wt% Pd(II) acac increased viscosity for a PMDA-ODA solution with 24 wt% total polymer	149
Figure 6.15.	The chemical structure of Sn(II) acetylacetonate	150
Figure 6.16.	Addition of 15 wt% Sn(II) acac relative to the polymer mass resulted in increased viscosity for PMDA-ODA solutions of 28 wt% total polymer	151
Figure 6.17.	The chemical structure of dimethyldineodecanoate tin	152
Figure 6.18.	Increased shear viscosity resulting from the addition of DMDND-tin prior to polymerization of PMDA-PPD with 15 wt% total polymer	153
Figure 6.19.	Elution of PEO standards measured by differential refractive index (RI) and used to calibrate the column used for size exclusion chromatography. The high molecular weight standards elute at earlier times than the low molecular weight standards	157
Figure 6.20.	Calibration curve constructed using PEO standards for measuring the equivalent molecular weight of poly(amic acids) based on the differential refractive index response.	158
Figure 6.21.	MW distribution of a PMDA-ODA solution of 20 wt% total polymer measured once a day for three days, beginning on the day of polymerization	159
Figure 6.22.	MW distribution of a PMDA-ODA solution of 25 wt% total polymer measured once a day for three days, beginning on the day of polymerization	160
Figure 6.23.	MW distribution of a PMDA-ODA solution of 25 wt% total polymer with and without 4% PA	160
Figure 6.24.	MW distribution of a PMDA-PPD solution 15 wt% total polymer measured once a day for three days, beginning on the day of polymerization (NOTE: the highest MW standard available was ~400 kg/mol)	162

Figure 6.25.	MW distribution of a PMDA-PPD solution of 20 wt% total polymer measured once a day for three days, beginning on the day of polymerization (NOTE: the highest MW standard available was ~400 kg/mol)	162
Figure 6.26.	Raw light scattering data shows a strong response to very large molecules, which elute at shorter times, forming in a PMDA-PPD solution of 15 wt% total polymer measured once a day for three days beginning on the day of polymerization	163
Figure 6.27.	Reduction of average MW for a PMDA-ODA solution of 20 wt% total polymer, measured once each a day for three days by re-injecting the sample diluted in the buffered DMF mobile phase on the day of polymerization	164
Figure 6.28.	Reduction of average MW for a PMDA-PPD solution of 15 wt% total polymer, measured by re-injecting the sample diluted in the buffered DMF mobile phase on the day of polymerization the next day. (NOTE: the highest MW standard available was ~400 kg/mol)	165
Figure 6.29.	Comparison of raw light scattering response of a sample measured on the second day to a re-injection of the first day sample for a PMDA-PPD solution of 15 wt% total polymer	166
Figure 6.30.	Change in MW distribution for PMDA-ODA solutions of 25 wt% total polymer with the inclusion of Sn(II) acac and DMDND-tin. (NOTE: the highest MW standard available was ~400 kg/mol)	167
Figure 6.31.	Change in in MW distribution for PMDA-PPD solutions of 15 wt% total polymer polymerized with the inclusion of Sn(II) acac and DMDND-tin. (NOTE: the highest MW standard available was ~400 kg/mol)	168
Figure 6.32.	Reversible discharge capacity of polyimide-based nanofiber electrodes. Fibers were pyrolyzed at two different temperatures and then cycled over a range of symmetric currents for charge and discharge	171
Figure 6.33.	First-cycle irreversible capacity losses of polyimide-based nanofiber electrodes	172
Figure 6.34.	Scanning electron micrograph of PMDA-ODA fibers pyrolyzed at 700 °C, with visible tin oxide particles. Samples were electrospun from a 26 wt% solution (a,c) and a 28wt% solution (b,d) containing 15 wt% Sn(II) acac relative to the polymer mass. Imaged at 2,000x (a,b) and 10,000x (c,d)	174

Figure 6.35.	Voltage profiles during charge and discharge for a typical electrode made of fibers spun from a PMDA-ODA solution of 26 wt% polymer, containing 15 wt% Sn(II) acac with respect to polymer mass, pyrolyzed at 700 °C and containing tin oxide. No feature corresponding to reversible Li alloying with Sn is observed near 0.4 V	175
Figure 6.36.	Voltage profiles during charge and discharge for a typical electrode made of fibers spun from a PMDA-ODA solution of 28 wt% polymer, containing 15 wt% Sn(II) acac with respect to polymer mass, pyrolyzed at 700 °C and containing tin oxide. No feature corresponding to reversible Li alloying with Sn is observed near 0.4 V	175
Figure 6.37.	Scanning electron micrograph of PMDA-ODA fibers produced from a 22 wt% polymer solution containing 23.25% DMDND-tin pyrolyzed at 700 °C	176
Figure 6.38.	Scanning electron micrograph of PMDA-ODA fibers produced from a 22 wt% polymer solution containing 23.25% DMDND-tin pyrolyzed at 900 °C. A significant number of micron-sized tin oxide particles are visible decorating the surface of the fibers	177
Figure 6.39.	Energy dispersive X-ray spectra obtained for a particle similar to the one seen in Figure 6.38b. The elemental ratio of Sn to O (1.28:3.01) confirms the particles are made of SnO ₂	178
Figure 6.40.	First-cycle irreversible capacity losses of PMDA-ODA derived nanofiber electrodes with and without tin oxide	179
Figure 6.41.	Reversible discharge capacity of PMDA-ODA derived nanofiber electrodes containing tin oxide. Fibers were pyrolyzed at two different temperatures and cycled over a range of indicated symmetric currents for charge and discharge	180
Figure 6.42.	Voltage profiles during charge and discharge for a typical PMDA-ODA electrode, pyrolyzed at 700 °C and containing tin oxide. No feature corresponding to reversible Li alloying with Sn is observed near 0.4 V	181

Chapter 1
Introduction

Since their development in 1991, lithium-ion (Li-ion) secondary batteries have become the dominant power supply for high-value portable communication and computing devices¹. Forecasts predict continued market growth as Li-ion batteries find use in power tools, hybrid-electric cars, and fully electric vehicles^{2, 3}. These new devices and applications require higher power batteries than are currently available. In mobile computing and communication applications, consumer preference requires batteries that last longer. Engineering these more valuable lithium-ion batteries depends on creating new and better materials.

Engineering composite materials of carbon and lithium alloying metals is a way to boost energy density⁴. Composites have been made using pyrolyzed carbon coatings⁴⁻⁷, ball milling⁸, sol-gel chemistry^{9, 10}, carbon nanotubes¹¹⁻¹³, and graphene¹⁴⁻¹⁹ with materials such as silicon, tin and titanium dioxide. Recently, electrospinning has been used to create pyrolyzed polyacrylonitrile nanofibers containing metallic nanoparticles²⁰. When used as anodes in Li-ion batteries, these fibers have reversible capacities more than twice that of commercial Li-ion materials^{21,22-24}.

The irreversible capacity loss of pyrolyzed nanofibers, significantly larger than state-of-art materials, is a barrier to commercialization²⁵. Every mAh lost at the anode during the first charge of the battery creates dead weight in the cathode where the lithium originated, lowering the energy and power density of the cell. To date there have been no attempts to reduce these losses in electrospun composites. Coating the surface of pyrolyzed hard carbons such as sugar and viscose with furnace deposited soft carbon has reduced the capacity losses in micron-sized materials^{26,27}. Atomic layer deposition, a process widely used in the semi-

conductor industry, has been employed to create conformal coatings on electrospun nanofibers^{28, 29} and to stabilize traditional micron-scale electrode materials³⁰⁻³². Molecular layer deposition builds on the principles of atomic layer deposition to deposit well-controlled thicknesses of polymers and metal-organic hybrid molecules³³⁻³⁷. Using these techniques to modify pyrolyzed nanofiber materials and characterizing benefits of changes in surface chemistry can improve the commercial value of pyrolyzed nanofibers as Li-ion anodes.

Polyacrylonitrile is not the only polymer that can be both pyrolyzed and electrospun³⁸.³⁹ Polyimides are a family of aromatic polymers whose material properties can be specifically tailored to an application based on the monomers chosen⁴⁰⁻⁴². When pyrolyzed the electronic conductivity of the material can vary based on the monomer composition⁴³⁻⁴⁵. One polyimide, commercially known as Kapton, has been electrospun⁴⁶ from solution as a poly(amic acid). No reports have yet documented the use of pyrolyzed polyimides as battery materials. Moreover, the solvents used to create polyimide (PI) nanofibers are the same solvents used to create composite polyacrylonitrile fibers containing tin²⁴, manganese²², and cobalt²¹. This is an opportunity to investigate the impact on the precursor material choice on the performance of pyrolyzed nanofiber anodes.

This dissertation opens by presenting a review of the peer reviewed literature relevant to the use and modification of pyrolyzed nanofibers as composite anodes. The topics covered include lithium-ion battery electrode materials and electrolytes, the solid electrolyte interphase layer, the polymers employed throughout the course of research, surface deposition techniques, and material characterization methods. Four chapters presenting results follow. Three of these contain material describing attempts to use chemical vapor

deposition, atomic layer deposition, and molecular layer deposition to change the electrode surface chemistry and improve electrode performance. The following chapter reports the processing required to create polyimide derived pyrolyzed nanofibers and the resulting electrochemical performance. The next chapter summarizes the results and presents important conclusions. The document closes with a series of recommendations for future work that builds upon the results of this dissertation.

Chapter 2
Literature Review

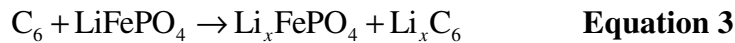
2.1 Lithium-ion Battery Technology

Lithium-ion (Li-ion) secondary (rechargeable) batteries currently power the majority of personal portable electronic devices. Their advantages over previous technologies include the low mass of Li, high and flat discharge voltage, lack of a memory effect, and low rate of self discharge¹. Only batteries that use metallic Li as anodes have a higher volumetric and gravimetric capacity although Li cells are not widely used due to safety concerns⁴⁷.

Lithium-ion cells, first commercialized by Sony in 1991¹, rely on the intercalation of Li atoms into insertion compounds for both the anode and cathode. The most commonly used material for the anode is graphite. Lithium-ion secondary cells are significantly safer and more durable than lithium secondary cells because the insertion compounds replace the lithium electrode. Lithium ions undergo the charge transfer reaction at the electrode surface and then intercalate into the insertion material avoiding the deposition of metallic Li onto the anode surface. Without proper voltage control during charging it is possible to drive the potential of the anode sufficiently negative and plate lithium onto the surface to create an unsafe condition.

The active cathode materials for both Li and Li-ion cells are typically lithiated transition metal oxides such as LiCoO_2 ⁴⁸, spinels as in LiMn_2O_4 ⁴⁹, or the recently commercialized LiFePO_4 ⁵⁰. The high mass of the metal and oxygen means commercial cathodes have theoretical gravimetric capacities less than 200 mAh/g. Some cathode materials cannot be fully de-lithiated or they will be irreversibly damaged⁵¹, a further limitation of their capacity.

Current state-of-art anodes are based on graphitic or mesosphere carbons, naturally occurring⁵², but often synthetic⁵³. The lithium inserts between the layers of graphite up to a maximum stoichiometry of LiC_6 , which correlates to a theoretical capacity of 372 mAh/g. Shown below are examples of the half-cell reactions occurring during cell charging, as well as the overall reaction.



Both the anode and cathode have some common design features. The materials are typically prepared as slurries of micron-sized particles of active material in solution with polymeric and conductive additives, cast onto an appropriate current collector⁵³. The conductive additives both ensure continuous electrical contact between active particles and the current collector and raise electrical conductivity^{52, 54, 55}. The polymeric binder, often polyvinylidene fluoride, holds the mixture together and to the collector⁵⁶.

The final components of a Li-ion cell are electrolyte to conduct Li^+ ions and a thin porous polymer separator to prevent shorts⁵⁷. Lithium hexafluorophosphate (LiPF_6) is the most commonly used salt today, although it represents a compromise between performance, safety, and the environment⁵⁷. The most common solvent is ethylene carbonate (EC) because of its high dielectric constant^{58, 59}. Ethylene carbonate is solid at room temperature, and is commonly dissolved in dimethyl carbonate, ethylmethyl carbonate or diethyl carbonate^{60, 61}.

A subset of Li-ion batteries is polymer Li-ion batteries using an ionically conductive polymer layer as both the electrolyte and spacer⁶², which simplifies processing and improves safety.

2.2 Graphitic Anodes

The development of graphite-based anodes was the key to the commercialization of Li-ion batteries¹. Developments since have focused on the properties of different types of graphite. Studies have covered both natural and synthetic graphite – manufactured by heating a carbon source above 2800 °C⁶³. Different morphologies produced include fibers⁶⁴, flakes, and beads⁶⁵. The maximum theoretical reversible capacity of graphite is 372 mAh/g corresponding to a value of 1 for x in **Equation 1**, but manufactured anodes have less capacity^{63, 64}.

Graphitic carbon, such as mesosphere pitch⁶⁶, shows clear voltage plateaus during charging and discharging. The charge plateaus correspond to the formation of different phases of LiC_x with x taking the value of 36, 12, and 6 as the battery charges. The different compounds can also be clearly seen as anodic and cathodic peaks in a cyclic voltamogram⁶⁴. Another benefit of graphite is its small hysteresis or polarization, *i.e.*, Li insertion and removal occur at similar voltages for low currents. Limiting polarization is important to improving the energy efficiency of a cell⁶⁷.

Electrical conductivity of graphite anodes is also important. For example, by segregating graphitized coke particles into three categories, Sato *et al.* investigated how the ratio between particle size and the relative fraction of particles affected anode capacity⁶⁸. When the difference between particle sizes (25.8 vs. 4.2 μm) was largest the capacity of the cell was largest, usually peaking around a large particle weight fraction of 0.7. More

important is the demonstration that the electrical resistance of the electrode was minimized when the ratio of large particles was at that same 0.7 wt%, indicating the importance of conductive paths to maximize capacity. Taking the concept a bit further, Ahn, *et al.* added 30 μm stainless steel needles to an anode based on mesocarbon microbeads (MCMB)⁶⁹. The resulting anodes showed higher capacities at all currents, but significantly (1.5x) higher capacity at charging rates of 1 or 2C. A rate of 1C represents a current of sufficient magnitude to exhaust the theoretical capacity in one hour and higher values of C represent a higher multiple of current.

2.3 Non-Graphitic Carbon Anodes

Exceeding 372 mAh/g requires higher capacity materials than graphite. One option is the use of non-graphitic carbons. These are materials created by methods similar to synthetic graphite – pyrolysis under inert gas – but at temperatures well below the graphitization point⁷⁰. Typically, these materials are small crystallites of graphite arranged in a highly disordered way⁷¹. Some disordered carbons are capable of graphitization with further heating these are classified as soft carbons. Those carbons which cannot be graphitized at any temperature are known as hard carbons⁷⁰. The source of carbon can vary widely and examples include simple table sugar⁷², condensed aromatic molecules⁷³, biomass⁷⁴, and petroleum pitch⁷⁵. Some reversible capacities exceed 600 mAh/g²⁵.

The use of materials like common sugar as a carbon source has the additional advantage of low material costs. Its carbonization has been well documented and a wide range of processing conditions is available by changing process gas and/or process temperature^{25, 70, 72}. The reversible capacity of a pyrolyzed sugar decreases with increasing

temperature. Unfortunately, the high capacity at lower temperatures comes with two penalties. First, there is a large increase in the irreversible capacity. Additionally the hysteresis of the materials is larger for lower temperature carbonization. Processing with high argon flow rate and slow heating rates reduced the amount of CO₂ liberated during carbonization and reduced irreversible capacity losses and hysteresis. Condensed aromatics pyrolyzed under nitrogen showed lower reversible capacities than the sugars discussed above at similar carbonization temperatures^{73,75-77}. The materials also showed a reduction in capacity as the carbonization temperature increased.

Waste biomass represents another inexpensive source of carbon for use in Li-ion batteries. In one study banana fibers pyrolyzed at 800 °C under nitrogen were made into anodes⁷⁴. Some of the samples were treated with ZnCl₂ and KOH, known porogens, to enhance the surface area. The samples treated with either porogen had higher reversible capacities (~500 mAh/g) than the untreated fibers, but this again came at the cost of much greater irreversible capacity – nearly 2500 mAh/g.

The reasons for the higher reversible and irreversible capacities, as well as the hysteresis observed with pyrolyzed carbon, are related to the structure of the material. The size of graphitic crystallites has been investigated in pyrolyzed pitch⁷⁷. A linear correlation existed between the reversible discharge capacity and the surface area of the crystallites. This result indicates that the additional capacity beyond the theoretical capacity of graphite is due to the insertion of Li in excess of LiC₆ at the surfaces or interfaces between crystallites. The use of ⁷Li-NMR (nuclear magnetic resonance) on pyrolyzed pitch has also shown that there exists some Li with a different binding state than typically associated with graphite⁷⁵.

2.4 Non-Carbon Anodes

Many materials exist that possess capacities equal to or greater than disordered carbons¹. These materials can be divided into three classifications: lithium alloying materials⁷⁸⁻⁸⁰, lithium insertion materials⁸¹, and lithium converting materials⁸². Historically lithium alloying materials have received the most research attention. Most of these materials are in Group 14 of the periodic table, the carbon group, and these include silicon⁸³, germanium, tin, and even lead⁸⁰. Outside of Group 14, intermetallics of some transition metals can deliver large reversible capacities by reversible alloying of Li^{84, 85}. The most commonly studied non-carbon insertion material for Li-ion batteries are the various morphologies of titanium dioxide and lithium titanate⁸⁶. There are many non-carbon anode materials that undergo a conversion reaction during charging. Most of these are based on transition metal phosphides⁸⁷⁻⁸⁹ or oxides⁹⁰⁻⁹² which form a Li₃P or Li₂O phase in combination with nanocrystals of the pure metal during charging. The possibility of using hydrides has been demonstrated recently⁶⁷. During discharge the Li is removed and the original phosphide or oxide is recovered. Thus far only the insertion compound Li₄Ti₅O₁₂ has found any commercial use, and all of these non-carbon materials, including TiO₂, have significant deficits when compared to graphite which will require creative engineering solutions to effectively implement. Deficits include low material conductivity, low operating voltages, and poor mechanical durability.

The material with the largest theoretical capacity to store Li is silicon, which can alloy with lithium up to a stoichiometry of Li₂₂Si₅⁸³ corresponding to a capacity in excess of 4200 mAh/g. Making use of this high capacity material has proven very difficult. The

volume of a Si particle changes by 300% when alloying and de-alloying with Li^{79, 93} to the maximum stoichiometry. The mechanical stress on the particle leads to pulverization and portions of the active material become electrically isolated and no longer participate in the electrochemistry^{79, 93}. Attempts to overcome these and other problems usually rely on at least one of the following four concepts: conductive additives and coatings^{5, 12, 94}, mechanical buffers^{95, 96}, voltage limits, and nanoscale materials^{8, 97-99}, though it is very common to see several of these approaches used simultaneously. Voltage limits prevent full lithiation of the silicon, limiting the volume expansion, but also limiting the energy density of the resulting battery. Conductive materials like carbon additives or coatings are used to maintain electrical contact between active materials. Mechanical buffers are used to restrain the movement of active materials and maintain electrical contact even after pulverization. Finally nanoscale materials are typically more resilient to mechanical stress.

Pyrolyzed carbons are a common theme in Si coating¹⁰⁰. Simple mixing of nanosized Si particles with carbon black was shown to improve cyclability when compared to micron sized silicon particles with a capacity > 1500 mAh/g after 20 cycles, although capacity was continuously decreasing¹⁰¹. By limiting either the capacity or the anode voltage, good cyclability has been seen^{102, 103}. A very common method of combining Si and carbon is through high-energy mechanical milling^{4, 8, 104-106}. Composites made in this manner routinely exhibit initial capacities near or exceeding 1000 mAh/g, but rarely maintain a level above 500 mAh/g for more than 20 cycles⁴. One notable exception was with the inclusion of multi-walled carbon nanotube (MWCN) in the ball mill. At a ratio of 1:1 Si:MWCN (w:w) the capacity was still > 1200 mAh/g after 50 cycles¹³. Some groups have grown carbon

nanotubes on the surface of silicon particles to maintain conductivity between active particles or between the particles and surrounding conductive matrix^{11, 12}.

Carbon nanotubes on the surface of silicon are also good examples of a mechanical buffer. Another technique used is to surround small silicon particles with inactive matrix via sol-gel chemistry^{10, 107, 108}, which produces composite structures with capacities in excess of 1000 mAh/g after 50 cycles. Mechanical milling is another way to create buffers¹⁰⁹⁻¹¹¹. This technique creates very fine active particles uniformly dispersed in a non-active material, though these results have yielded lower capacities than the sol-gel techniques. With the recent development of cost efficient graphene production this carbon nanomaterial has also found use as a mechanical buffer and conductive additive in combination with silicon and other materials.

Shrinking the active material to nanoscale dimensions is a third technique used to engineer silicon anodes. Some of the examples already cited have created nanosized materials or nanocrystalline structures^{96, 111}. Several studies have adapted techniques from the microelectronics industry to control the structure of silicon on a collector making pillars⁹⁵, thin films¹¹², and nanowires⁹⁹. The example of Si clearly illustrates the value that can be added by using nanomaterials: The wires are an efficient 1D electrical path, have a high surface area for contact with the electrolyte, and have room to expand when lithiated⁹⁹. The reversible capacity of the first cells assembled from this kind of material is ~3000 mAh/g at C/20 and remained ~2000 mAh/g for a 1C charging rate. The chemical vapor deposition (CVD) of polycrystalline silicon onto commercially available carbon fibers was able to create materials with nearly 2000 mAh/g at low currents¹¹³. Similarly CVD deposition of Si has

been used on high surface area annealed carbon black particles, with subsequent CVD of carbon to bind individual particles into larger spherical particles suitable for standard slurry casting anode production methods¹¹⁴. These hierarchical structures again delivered reversible performance in the neighborhood of 1500 mAh/g.

Silicon nanowires made via novel solution chemistry were evaluated by researchers recognizing the importance of the cost of processing conditions on the commercial utility of a material¹¹⁵. These materials mixed with multiwall carbon nanotubes were still able to deliver reversible capacities of approximately 1500 mAh/g. Similar high surface to volume silicon nanotubes were created via solution templating upon alumina or silica⁹⁷. This was followed by substrate removal and subsequent carbon coating to improve interfacial properties and the resulting material delivered over 3000 mAh/g after 80 cycles at 1C and nearly 2500 mAh/g at a discharge current of 5C. A significant challenge remaining in all of these high-surface area alloying materials is poor first cycle coulombic efficiency from well-known interfacial side reactions at insertion anode materials.

Table 2.1 – Examples of recent structures and composites utilizing silicon and the resulting performance as Li-ion anodes.

Silicon Structure	Other Materials	Reversible Capacity (mAh/g)	C-rate	Year Published
Nanoparticles	In pyrolyzed PAN nanofibers	700	3C	2012 ⁹⁴
Coated on nanotubes	Porous TiO ₂	1600	0.5C	2010 ¹¹⁶
Silicon nanowires	Carbon nanotubes	1500	Variable current	2010 ¹¹⁵
CVD silicon	Deposited on carbon black	1400	1C	2010 ¹¹⁴
Nanoparticles	Mixed with graphene	1200	C/12	2010 ¹⁸
CVD silicon	On commercial nanofibers	800	1C	2009 ¹¹³
Nanoparticles	In pyrolyzed PAN nanofibers	800	C/8	2009 ¹¹⁷
Nanotubes	Carbon coating	3000	5C	2009 ⁹⁷
Nanowires	N/A	200	1C	2008 ⁹⁹
Porous particles	Carbon coating	2800	1C	2008 ¹¹⁸

While silicon is capable of storing large quantities of Li, other Group 14 metals such as germanium and tin are also viable alloying materials, though they have lower theoretical maximum capacities than silicon⁸⁰. When considering tin, it is common for the tin to be oxidized as SnO or SnO₂ during electrode processing¹¹⁹⁻¹²¹. Subsequent reduction of the SnO₂ to pure Sn is accomplished chemically¹²², electrochemically^{6, 17} or thermally^{24, 123} before lithium can actively alloy with the material. When fully alloyed as Li_{4.4}Sn the specific capacity of the material approaches 1000 mAh/g⁸⁰. As with silicon, tin undergoes significant volume expansion upon alloying with lithium. While the expansion is less than with Si the materials still experience capacity fade without properly engineered structures⁷⁹. Thus similar techniques and structures to silicon based anodes are seen in studies of tin-based

anodes with a recent focus on nanoscale composites¹²⁴. Examples of the structures explored to improve cycle life and power density for tin oxide based anodes include carbon coated nanoparticles^{6, 123}, tin decorated carbon nanotubes¹²⁵ or graphene^{16, 17}, tin oxide nanosheets¹²⁶, tin oxide nanorods^{121, 127}, and carbon/tin oxide composite nanofibers^{24, 128}, and calcined tin oxide nanofibers. Each of the nanoscale morphologies have delivered reduced capacity fade when compared to micron scale tin materials and, when reported, capacity retention of up to 50% for charging rates as high as 10C²⁴. The first-cycle efficiency of these materials is quite low, as a significant quantity of Li is consumed in the reduction of SnO₂ to Sn prior to alloying, as seen in **Equations 4** and **5**.

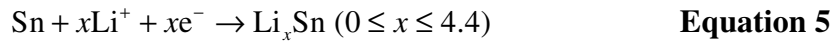
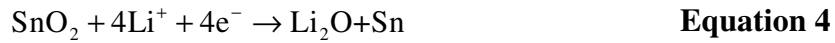


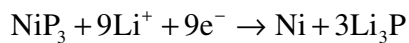
Table 2.2 – Examples of recent structures and composites utilizing tin and the resulting performance as Li-ion anodes.

Tin Structure	Other Materials	Reversible Capacity (mAh/g)	C-rate	Year Published
SnO ₂ nanocrystals	On pyrrole derived fibers	600	~C/8	2011 ¹²⁹
Sn nanoparticles	In PAN derived fibers	750	C/10	2011 ¹³⁰
SnO ₂ nanoparticles	Supported on graphene	900	C/15	2011 ¹⁶
SnO ₂ nanoparticles	Supported on reduced graphene oxide	600	C/20	2011 ¹⁷
Porous SnO ₂ nanotubes	N/A	700	C/	2010 ¹³¹
SnO ₂ nanosheets	Carbon black, PVDF binder	<400	C/10	2010 ¹²⁶
SnO ₂ nanoparticles	Carbon coated	800	C/2	2009 ⁶
Sn nanoparticles	In PAN derived fibers	600/400	2C/10C	2009 ²⁴

Safety concerns associated with the development of large Li-ion battery systems for transportation applications, not energy density, are the major factor behind interest in anodes based upon lithium titanates and polymorphs of titanium dioxide (TiO₂)⁸⁶. These materials operate at a voltage between 1.5 and 2.0 V vs. Li/Li⁺, sufficiently positive to prevent electrodeposition of lithium onto the electrode surface, and thus avoid the safety hazards associated with this condition. The different structures of TiO₂, and the related, already commercialized lithium titanate (Li₄Ti₅O₁₂) each store slightly different amounts of Li¹³²⁻¹³⁵, but all are less than the theoretical capacity of graphite. The insertion of Li does very little to change the volume or structure of the material, leading to low capacity fade and long cell life even at high currents. The anatase phase of TiO₂ has been the most widely studied, but the

polymorph known as bronze (TiO₂-B) possesses the highest theoretical capacity (355 mAh/g). The implementation of the TiO₂ polymorphs in commercial cells requires improvements in electronic conductivity and lithium diffusion, and as with previously discussed materials nanotechnology has found a role^{86, 136-138}. Some of the most promising methods used solution chemistry to create self-assembled TiO₂ nanoparticles (<10nm diameter) on graphene sheets¹³⁹. The anatase version of this material delivered an initial reversible capacity of 200 mAh/g at low current rates (C/5), ~160 mAh/g at 1C, and more than 100 mAh/g at 30C. But these materials also have superior capacity retention at high currents when compared to carbonaceous or alloying materials, with a report of 50% capacity retention at charging rates as high as 60C for a mesoporous form of TiO₂-B¹⁴⁰. The high potential of Li intercalation/deintercalation paired with cathodes that operate around 4 V results in cells with lower power density for a given current, and is the primary limitation to the widespread commercial adoption of these materials.

The final category of non-carbon anode materials is those which undergo a reversible conversion reaction when storing Li. A wide range of materials have been studied, including various sulfides¹⁴¹, oxides^{90, 142-144}, and phosphides^{87, 145, 146} of iron, cobalt, nickel, and copper. These materials can show very high specific capacities as they convert to a nanocrystalline metal phase embedded in a lithium rich amorphous matrix. For example, nine lithium ions are required in the conversion reaction:



Equation 6

and this material could theoretically store 1475 mAh per g of NiP_3 ¹⁴⁷. Similar very large capacities are possible for other members of this class of material. The large theoretical capacities are insufficient to result in commercialization though, as these conversion electrodes commonly suffer from the following barriers: low operating voltages^{91, 142}, poor capacity retention due to pulverization and incomplete re-conversion^{147, 148}, large polarization resulting in low energy efficiency⁶⁷, and unstable interfaces with the electrolyte¹⁴¹. Similar strategies of carbon coating^{7, 149}, graphene^{15, 150-152} or carbon nanotube composites^{15, 142, 150, 151, 153}, and nanoscale material production^{90, 149, 154-156}, are being used to address the issues with pulverization, re-conversion efficiency, and interfacial stability. Possible resolution of the large polarization may be possible by using metal hydrides as the conversion material, as these have shown the lowest polarization differential between charge and discharge⁶⁷.

2.5 Electrolytes and the Solid Electrolyte Interphase

Electrochemistry is an interfacial science, which is to say charge transfer reactions occur at the interface between two distinct phases. In the case of Li-ion batteries the interfaces are where the solid phase electrodes come into contact with the liquid electrolyte phase. In the early days of Li-ion battery development it was recognized the developments for Li cells, themselves impractical due to safety issues, were very applicable to electrolytes in Li-ion cells^{58, 59}. This has led to the widespread use of salts such as LiPF_6 and LiBF_4 in Li-ion research and commercialization¹⁵⁷, as well as the less safe or environmentally friendly LiClO_4 and LiAsF_6 ⁶¹.

The majority of cells sold today use the mixtures of linear and cyclic carbonates as the solvent. The most common solvent component is ethylene carbonate (EC) for it has a high dielectric constant and a potential window wider than that of the functioning cell. Unfortunately, EC cannot be used alone as the solvent because it is a solid at room temperature with a melting point of 36.4°C, and thus unsuitable for any application where the cell will be used or stored below this temperature¹⁵⁸. To compensate EC is mixed in approximately equal parts with one or more linear carbonates such as dimethylcarbonate (DMC), diethylcarbonate (DEC), and most commonly ethylmethylcarbonate (EMC)^{59-61, 64}. While these components have dielectric constants and order of magnitude lower than EC, they are low viscosity liquids over the full range of operating temperatures under which Li-ion batteries are expected to function and result in an ionic conductivity approaching 10 mS/cm. Propylene carbonate (PC) would be the most desirable solvent; it is a liquid between -48.8 and 242 °C and possesses a dielectric constant only slightly below EC, and as such less solvent mixing would be required¹⁵⁸. Though the use of PC in commercial cells is problematic as during charging PC will intercalate between the graphite layers in most anodes, decompose, and exfoliate the layers. In some extreme cases the cell never completes the initial charge before the active anode material is completely destroyed¹⁵⁹. Even in cases where the cell does complete the first cycle, capacity retention is poor over the life of the battery, but there is a constant stream of research aimed at making PC based electrolytes a reality and thus improving the low temperature performance of Li-ion batteries.

This behavior of PC electrolytes primarily indicates they do not form a proper solid electrolyte interphase (SEI). The formation of the SEI is an important part of the first charge

of a Li-ion cell, and this is another benefit of using solvent mixtures of EC, DMC, DEC, and EMC¹⁶⁰. When stable, the SEI layer “coats” the anode and prevents the interaction of metallic Li with the components of the electrolyte in subsequent cycles. It is important that the SEI permits diffusion of Li to the active electrode surface where the charge transfer occurs. The SEI film has been studied by spectroscopic techniques such as Fourier transform infrared spectroscopy (FTIR) and X-ray photoelectron spectroscopy (XPS)¹⁶⁰⁻¹⁶². Those results show the SEI is composed of decomposition products of Li⁰, the organic solvents, and the electrolyte salt. This consumption of Li atoms which have already participated in the charge transfer process at the anode results in an irreversible loss of capacity during the first charge. The specific salt used in the electrolyte is also a factor, with the most commonly used electrolyte LiPF₆ being more reactive to the solvents than other potentials salts, and forming a somewhat thicker and more resistive SEI. Additionally the formation of HF from LiPF₆ and solvent decomposition or water contaminants plays a role in reducing cell life by promoting dissolution of the cathode.

Researchers have demonstrated that the formation of the SEI occurs in two phases on graphite¹⁶³. The first at high voltages, before the intercalation of Li, is more inorganic in nature, and more resistive. The second phase occurs simultaneous to Li intercalation and tends to be composed of more organic products, and is a better ionic conductor. After the first full cycle of the cell a good SEI is predominantly composed of the later products, and it will have a negligible resistive impact on future cycles, though the specific resistance of the SEI changes throughout the charging and discharging processes as the anode swells and shrinks with intercalation and deintercalation of Li¹⁶⁴.

The relationship between the SEI layer and first cycle irreversible capacity (C_{irr}) has been studied on many forms of carbon^{162, 165-168}. The general trend is that carbons with a greater disorder, such as hard carbons resulting from the pyrolysis of natural or synthetic organic species, show larger capacity losses than natural and synthetic graphite. The capacity loss due to SEI is a surface effect and studies often compare it to the surface area of the active material as determined by methods such as BET and results have shown linear correlations between C_{irr} and BET surface area on graphite¹⁶⁶. When considering graphite and its layered structure, there are two surfaces to consider, the basal surface of the graphene sheets and the edge faces corresponding to the c-axis of the unit cell. In the case of graphite or nearly graphitic carbons, the SEI formation is most critical on the edge surfaces where possible solvent intercalation and exfoliation occurs. Reactions to protect the basal surfaces are less critical, but this surface still irreversibly consumes lithium. The contribution of each to C_{irr} was tested by Chung *et al.* by mixing propylene carbonate (PC) into EC-based electrolyte. The PC made it possible to separate the capacity losses from both edge and basal surfaces and showed the edge sites have a C_{irr} that is seven times larger than the basal surfaces¹⁶⁵. When non-graphitic carbons are studied, the C_{irr} for the material is typically a factor of 2 to 5 larger than graphite (~400 mAh/g) and is attributed to the greater disorder of exposed surface^{21, 167}.

Since the formation of the SEI is so critical but the irreversible losses of Li are undesirable, many researchers have worked to maximize good SEI formation while minimizing the C_{irr} losses and improve the overall energy density of the cell. For example, reduction of the first-cycle C_{irr} from 500 to 350 mAh in an 18650-type cell with a 2.2 Ah

capacity would save approximately 1 g of LiCoO₂ cathode material. One gram saves 6% of the cathode from becoming dead weight after the first cycle. **Table 2.3** presents the mass of additional cathode needed for the recently commercialized LiFePO₄ in addition to the more common LiCoO₂.

Table 2.3 – Mass of cathode material required to compensate for C_{irr}. The capacity of LiCoO₂ and LiFePO₄ are assumed to be 140 mAh/g⁵⁰ and 170 mAh/g¹⁶⁹, respectively.

First Cycle C_{irr} (mAh)	Additional LiCoO₂ Required (g)	Additional LiFePO₄ Required (g)
100	0.714	0.588
200	1.429	1.176
300	2.143	1.765
400	2.857	2.353
500	3.571	2.941
600	4.286	3.529

One method used to improve SEI formation and reduce Li consumption has been the direct modification of the anode surface. Examples include a mild oxidation of the edge sites of graphite, which was proposed to produce an improved chemical adhesion of the SEI at these locations¹⁷⁰. The resulting cells demonstrated an improved degree of lithiation and an up to 20% reduction in C_{irr} with a complex mixed solvent of EC, DEC, DMC, and dioxolane. Other researchers have transferred polymers in solution to graphite, similar to the binder in conventional electrodes, and created encapsulated graphite. Polydimethylsiloxane improved the first cycle coulombic efficiency – the ratio of discharged amps to charged amps – of natural graphite cells by 40% in an 1 M LiPF₆ EC:DMC electrolyte¹⁷¹. The resulting cells showed equivalent reversible capacities in the first few cycles, and improved capacity retention over the limited number of cycles studied. Similarly when

poly{[oligo(oxyethylene) methacrylate]-co-(methacrylic acid lithium)} was polymerized in a suspension of natural graphite in methanol the encapsulated graphite suffered over 50% less C_{irr} and again showed improved reversible capacity and capacity retention in a EC:DEC:PC mixed solvent⁵². The polymer coatings are acting as an artificial SEI that separates the active material from the electrolyte while permitting Li diffusion. This work did show that there was an ideal of approximately 1% polymer mass to graphite mass that resulted in the best performance.

Alternatively, the surface of a non-graphitic carbon can be pre-coated with a layer of soft graphitic carbon to reduce C_{irr} ^{172, 173}. Pyrolysis of ethylene onto carbonized sucrose decreased the irreversible capacity from 149 mAh/g to 60 mAh/g²⁷. The irreversible capacity of carbonized viscose felt was reduced from 264 mAh/g to 97 mAh/g with a carbon coating formed by vapor decomposition of propylene¹⁷⁴ without negatively impacting the reversible capacity. In the same paper Beguin, *et al.* showed a linear correlation between the active surface area (ASA) and the irreversible capacity in milled graphite. The ASA of carbon was measured by di-oxygen adsorption and is a function of surface impurities, basal surface defects, crystallite size and crystallite orientation¹⁷⁵. Finally sputter deposited LiPON – a known solid electrolyte – reduced irreversible capacity on mesosphere artificial graphitic carbon from 120 mAh/g to 90 mAh/g¹⁷⁶.

A second technique to improve SEI formation and reduce Li consumption is selective use of additives in the electrolyte phase which will help to form a stable SEI¹⁷⁷. The additives commonly fall into two camps: organic molecules which will undergo a selective polymerization on the electrode surface and inorganic compounds which promote or enhance

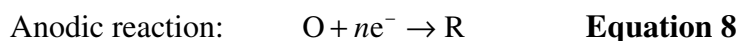
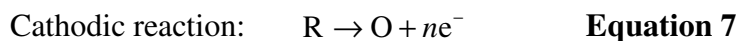
the natural process. Some examples of the organic molecules studied are vinylene carbonate^{178, 179}, vinyl acetate¹⁵⁹, divinyl adipate¹⁵⁹, allyl alkyl carbonates¹⁸⁰, and acrylic acid nitrile¹⁸¹. Results with vinylene carbonate are mixed, with some studies showing C_{irr} reduction, while others have shown a negative effect, but in both of those cases the presence of the VC additive improved capacity retention of the graphitic material under study. In a study of several additives with PC based electrolytes used to test their ability to protect the graphite surface, 1% of vinyl acetate was the best at stabilizing the performance of one natural and two synthetic forms of graphite for which the first cycle failed to complete without the additive¹⁵⁹. In a similar situation 1% of acrylic acid nitrile also permitted the successful use of PC based electrolytes with synthetic graphite active materials¹⁸¹. And finally another small unsaturated molecule, allyl ethyl carbonate, as 2% of a PC:DEC based electrolyte allowed for the successful formation of an SEI layer and subsequent cycling of the cell, when none was possible without the additive¹⁸⁰.

The organic molecules acted by inducing a cathodic radical polymerization upon the surface of the electrodes, inorganic additives tend to simply promote or improve the formation of the natural SEI film. The incorporation of small molecules such as CO_2 , N_2O , CO and some small polysulfides in a $LiClO_4$ and PC electrolyte did improve the initial cyclability and reduce total irreversible of pitch-based carbon fibers, but still resulted in significant capacity decay and subsequent irreversible solvent decomposition with less than 50% of the reversible capacity remaining after 60 cycles¹⁸². Lithium carbonate (Li_2CO_3) and derivative compounds have been shown to be the basis of many naturally formed SEI films, and as such the addition of Li_2CO_3 in various electrolytes has been widely studied. This

additive has been shown to significantly reduce the amount of volatile flammable gasses formed during the cycling of full Li-ion cells with EC based electrolyte mixtures, which improves battery safety¹⁸³. Lithium carbonate added to an electrolyte based on a mixture of EC and DEC also reduced C_{irr} on mesosphere pitch carbon fibers from 80 mAh/g to 50 mAh/g¹⁸⁴. Similar studies have introduced limited quantities of other alkali salts into the electrolyte. Small quantities of sodium perchlorate ($NaClO_4$) in electrolytes based on $LiClO_4$, EC, and DEC created a 60% reduction in C_{irr} and showed significant capacity improvement and retention at low (C/20) and high (1C) charge rates for natural graphite¹⁸⁵. And three different potassium based salts also demonstrated C_{irr} reductions of 50 to 75% while delivering larger reversible capacities¹⁸⁶. Additionally, the US Army Research Lab has demonstrated that salts such as lithium bis(oxalate) borate (LiBOB) and the related lithium oxalyldifluoroborate (LiODFB) promote SEI formation and allow for the use of PC in electrolytes with common commercial electrode materials^{187, 188}.

Other reasons for introducing additives into Li-ion electrolytes are performance improvement and overcharge safety. Anion receptors have been added to electrolytes to improve the dissolution of the Li salts, the ionic conductivity of the electrolyte, and the Li transference number – a measure of the amount of ionic transport due to Li in the electrolyte. For example, small amounts of boron based fluorophenyl additives have boosted the power a Li-ion cell delivered without interfering with the chemistry of a carbon anode, delivered 33% better capacity, and excellent capacity retention in a full cell using a mixed Ni/Co based cathode¹⁸⁸, and improved the high temperature performance of $LiMn_2O_4$ based cathodes⁴⁹.

Finally a significant means of improving the safety of Li-ion batteries is the inclusion of redox shuttles into the electrolyte¹⁸⁹. In an overcharge state the cell can exist at potentials capable of oxidizing the solvents, creating dangerous pressure increases in the cell. At high temperatures these overcharged cells can catastrophically fail and burn. At potentials reached during the overcharge, but before a dangerous condition exists, small molecules used as redox couples undergo an oxidation at the cathode, with subsequent reduction of the new species to back to the original molecule at the anode:



The continual diffusion of these redox couples between the electrodes prevents other electrochemical processes from altering the steady-state condition of the active materials in the Li-ion cell. A wide range of aromatic compounds have been studied as potential redox shuttles in standard Li-ion electrolyte systems^{190, 191}. And in one particularly interesting case lithium fluorododecaborates ($\text{Li}_2\text{B}_{12}\text{F}_x\text{H}_{12-x}$) were used as both the electrolyte salt and the redox couple, and demonstrated the ability to serve as a stable redox shuttle at up to 4.5 V for over 100 hours and some overcharge protection at up to $2C$ ¹⁹².

2.6 Electrospinning

The first patents for electrospinning date back to 1902¹⁹³. Recently, the technique has been revived because it is a simple and inexpensive method to create one-dimensional (1D) nanoscale materials. A wide variety of polymers have been electrospun from polymer solutions or polymer melts¹⁹⁴⁻¹⁹⁶. A complex interplay of experimental factors, such as

polymer molecular weight (MW), solvent, solution viscosity, flow rate, electric field strength, and collector geometry, determines the precise morphology and arrangement of the fibers¹⁹⁷⁻²⁰².

Table 2.4 – Hypothetical surface area of a smooth fiber of density 1 g/cm³ for various diameters

Fiber Diameter (nm)	Surface Area (m²/g)
100,000	0.04
10,000	0.4
1,000	4
100	40
10	400

Because surface area is inversely related to the diameter of a fiber, electrospun nanofibers have very high surface-to-volume (or -mass) ratios (**Table 2.4**). The nonwoven mats also have void fractions of 65 to 75%, resulting in an easily accessed large interfacial area. Groups have been electrospinning fibers for application to tissue engineering^{203, 204}, drug delivery^{205, 206}, membrane creation^{207, 208}, and energy storage^{21, 209}.

A typical set-up for creating electrospun fibers is shown in **Figure 2.1**. A viscous polymer solution is pumped through a small conductive needle that is fixed several centimeters from a grounded conductive collector. The needle is connected to a high-voltage power supply and an electric field exists between the needle and collector.

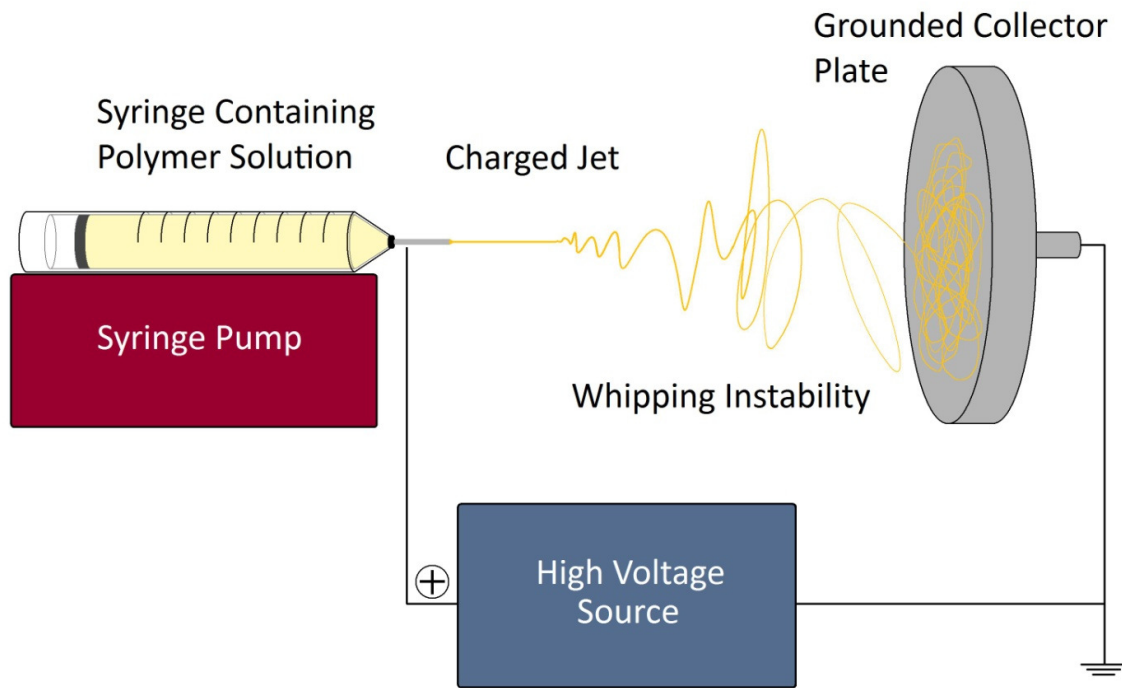


Figure 2.1 – Diagram depicting the typical experimental setup for electrospinning polymer solutions.

Electrospinning occurs because of the physics of electrostatic repulsion and surface tension in a droplet formed at the end of the needle¹⁹³. Charge builds in the droplet driving an increase in the surface area. Under the extensional force of the electric field, a conical distortion forms of the surface of the droplet known as a Taylor cone²¹⁰. When the charge density on the surface exceeds a maximum for the given solution, known as the Rayleigh limit, a spray of very small droplets or a jet of solution is released at the tip of the Taylor cone. The charged droplets or jet travel towards the grounded collector because of the electric field. The transition from electrospaying²¹¹ to electrospinning in polymer systems occurs when the amount of polymer in solution is in the dilute entanglement regime. At this

point the concentration of polymer molecules is sufficient that individual molecules begin to interact (entangle) with each other, rather than exist as distinct elements in solution. The entanglements prevent the droplet from exploding into a spray of smaller droplets when in excess of the Rayleigh limit. In the case of electrospinning small deviations in the jet are unstable. The electrostatic force acting upon these instabilities begins to stretch the fiber. This is commonly referred to as the whipping instability, because when viewed by the eye it appears the fiber is whipping back and forth. When viewed by a high speed camera it can be seen that all the points along the fiber are being continually stretched away from each other, and this stretching thins the fiber²¹⁰. Depending on the experimental conditions the fiber diameter can range from tens of nanometers to microns³⁹. Reduction of fiber diameter can typically be accomplished by using less concentrated solutions, lower MW polymer, increased electric field strength, decreased flow rate, and a smaller needle diameter. The intermediate case between electrospinning and electrospraying of beads strung along fibers is also possible²⁰².

Changing the geometry of the current collector is a simple modification of the electrospinning process. In efforts to create anisotropic fiber mats, groups have used rotating drums²¹² and separated magnetic bars²⁰¹ to produce fibers aligned in one direction. Additionally composite materials of nanoparticles in nanofibers have been made using electrospinning. Two methods exist to accomplish this, *ex situ* and *in situ*. The *ex situ* process relies on solution mixing of pre-made particles^{117, 213}. If the particles are stable in solution, they should be in the fiber after electrospinning²¹⁴ though sometimes the particles form aggregates²¹⁵. The *in situ* technique relies on creating the nanoparticles from metallic

salts or organometallic complexes added to the solution that later coalesce into nanoparticles in a different processing step^{216, 217,24, 218-220}.

One area where electrospun fibers have been studied for a direct application in Li-ion batteries is the formation of a polymer electrolyte to act as both the transport medium of the Li ions and as the separator. The most commonly published polymers for this use are polyvinylidene fluoride (PVDF)²²¹⁻²²⁴ and polyacrylonitrile (PAN)^{225, 226}. The electrospun materials are more attractive than cast polymer films because of the micro porous nature inherent to the non-woven structure. The pore volume, when wetted by an electrolyte can provide a diffusion pathway for Li ions, resulting in an ionic conductivity significantly higher than possible for Li diffusion through a solid polymer. Additional Li conducting solid particles can be included in the polymer matrix to boost ion transport²²⁵.

2.7 Polyacrylonitrile

Polyacrylonitrile is the preferred polymer when producing high-strength carbon fiber¹³⁰. The production of carbon fiber is a two-step process. First the PAN is drawn or spun into a fiber. This is followed by the carbonization process itself composed of two steps: stabilization and carbonization (**Figure 2.2**)²²⁷. During stabilization the polymer fibers are heated to temperatures between 250 and 300 °C in air for a few hours. This step partially oxidizes the fibers and then initiates cyclization with outgassing of hydrogen and nitrogen compounds²²⁸. The second half occurs under inert or reducing atmosphere (N₂, Ar, or forming gas) with typical heating to between 700 and 1000 °C. During this step the remaining hydrogen and nitrogen are driven off and large aromatic structures remain.

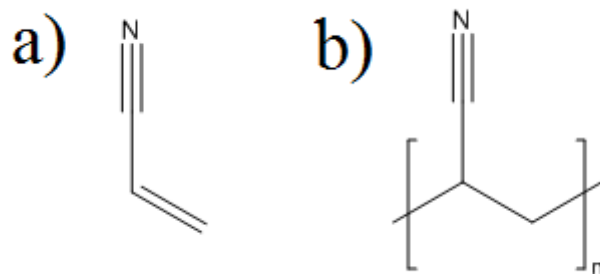


Figure 2.2 – Chemical structure of a) the acrylonitrile monomer and b) polyacrylonitrile.

There are many studies of electrospun PAN^{209, 229-231}. A particularly comprehensive look at the electrospinning of 100,000 MW poly(acrylonitrile-co-methyl acrylate) (4% PMMA) was published in 2005²⁰². Wang and Kumar explored the impact of electric field (1.3 to 2.7 kV/cm), flow rate from the syringe pump (0.5 to 6 mL/h), solution concentration (5.1 to 20.3 wt%) and MW on the resulting PAN nanofibers. Fibers ranging from 50 nm to 2 μ m were spun, although when fiber diameter was below 300 nm the solution formed mixes of beads and fibers. A 2007 paper by Borhani *et al.* reinforces the sensitivity of the electrospinning process to experimental setup²³². Using the same molecular weight, but pure PAN at a much lower flow rate (0.17 mL/h), different needle diameter (0.7 vs. 0.84 mm) and a lower electric field (0.667 kV/cm), they found fiber diameters of ~400 nm for a 14 wt%, compared to <200 nm for all cases of a 13.8 wt% solution in the previous paper.

PAN fiber surface area has been increased by electrospinning a solution containing both PAN and polyethylene oxide (PEO). Washing away the PEO left irregular PAN fibers with an enhanced surface area²³³. Hollow PAN nanofibers were created by vapor

polymerization onto a polystyrene electrospun scaffold. Removal of the polystyrene after carbonization created tubes with 100 nm outer diameters and a 14 nm wall thickness²³⁴.

The *in situ* nanoparticle technique has successfully produced Ag nanoparticles in small diameter (50 nm) PAN fibers²¹⁶. Yang *et al.* used 80,000 MW PAN and silver nitrate as the salt and the nanoparticles were visible under TEM. An *ex situ* technique has been demonstrated for electrospinning carbon nanotubes into PAN nanofibers^{209, 220, 235, 236}. The carbon nanotubes were functionalized with either carboxylic groups^{209, 220, 235, 236} or Triton X-100⁵⁵ so they would be stable in DMF. The nanotubes are predominantly aligned in the axial direction of the resulting fibers.

There are already several examples of carbonized PAN nanofibers used in electrochemical energy storage. *In situ* addition of cobalt acetate created metallic Co⁰ nanoparticles²¹. Nanoparticles were not imaged, but X-ray diffraction (XRD) indicated the presence of Co⁰ in the nanofibers. The cycle performance of the composite fibers was impressive, maintaining 800 mAh/g (71%) of initial capacity after 50 cycles at 100 mA/g and retaining 600 mAh/g of capacity at 1C charging rate. Reduced cobalt is not an active anode material so the authors theorize this improvement is directly attributable to the conductivity improvement of the fibers, though effective conductivity was not directly measured. Ji *et al.* investigated the effect of enhanced nanofiber surface area on anode performance¹⁹⁵. Relatively large pores were created by the *ex situ* spinning of aggregated SiO₂ nanoparticles later removed by hydrofluoric acid. Much smaller pores were created by electrospinning PAN with in solution ZnCl₂ followed by a thermal activation step. The ZnCl₂ technique created a higher portion of pores smaller than 2 nm and showed better high-rate capacity

retention and slightly smaller irreversible capacity losses than standard PAN fibers. Kim and Yang have also investigated the utility of activated carbon nanofibers as supercapacitor electrodes²³¹. Ji et al have also used *in situ* techniques to create MnO_x particles, a conversion material, from manganese acetate²¹⁸. The resulting fibers showed capacities of ~600 mAh/g upon conversion to Mn, larger than PAN alone, and excellent capacity retention at high rates. The most impressive result used a single nozzle electrospinning setup to create fibers with a PAN core and a PMMA/tin octoate core from an emulsion in DMF. During the stabilization step in air tin oxide nanoparticles were formed. Then pyrolysis was conducted in a Ar/H₂ atmosphere to produce carbon fibers and reduce the tin oxide nanoparticles to metallic tin. The resulting electrodes produced a stable reversible capacity of around 700 mAh/g over 140 cycles at 0.5C, and capacity retention of nearly 400 mAh/g at 10C²⁴. There are significant first-cycle irreversible capacity losses for of all these electrospun carbonized fibers owing to the formation of the SEI layer over such a significant surface area.

2.8 Polyimide (PI)

Polyimides are class of chemically and thermally resistant, flexible, strong, low dielectric polymers^{42, 238-240}. These polymers find uses in adhesives, thermal resistant coatings, composites, moldings, membranes, and films^{41, 241, 242}. They are commonly formed from the reaction of an aromatic dianhydride with an aromatic diamine to produce poly(amic acid) (PAA)^{243, 244}, with each reaction resulting in a carboxylic acid group, making PAA a polyelectrolyte^{245, 246} (**Figure 2.3**).

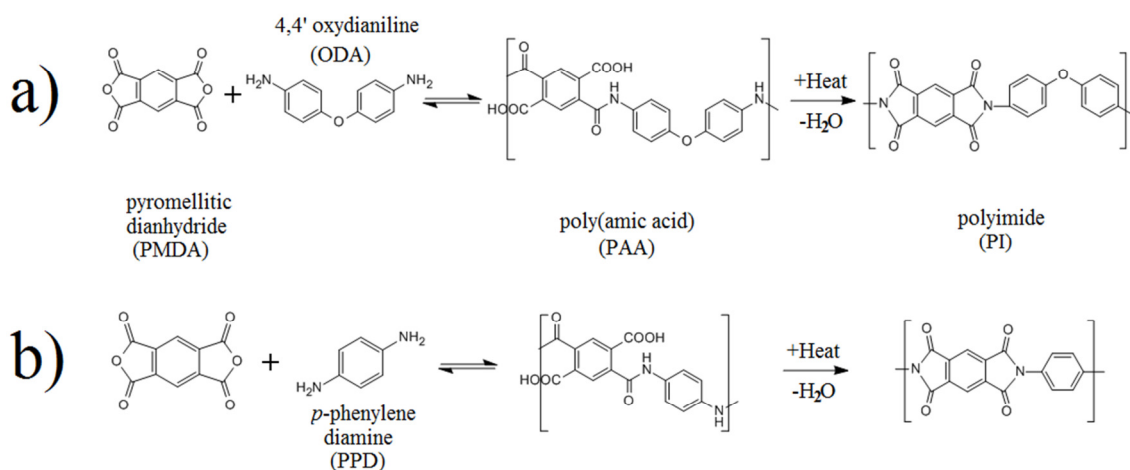


Figure 2.3 – The reactions to form poly(amic acid) and subsequent thermal imidization by dehydration between a) pyromellitic dianhydride and 4,4'-oxydianiline and b) pyromellitic dianhydride and *p*-phenylene diamine.

This is a reversible reaction, and some equilibrium quantity of unreacted amine and dianhydride groups will always exist in solution^{247, 248}. The step-growth polymerization is commonly carried out in aprotic solvents such as DMF²⁴⁶, DMAc²⁴³, NMP⁴⁵, and THF:MeOH solutions²⁴⁹ and in a controlled inert atmosphere to prevent reactions with water²⁴⁴. The molecular weight of the polymer obtained varies widely based on the order of addition of the components, with higher molecular weight products resulting from the addition of the dianhydride to diamine already dissolved in solution²⁵⁰. That process would be considered a heterogeneous polymerization. One monomer is already dissolved into the liquid phase, and when added the other exists as a solid. The polymerization proceeds at the interface between these two phases. The impact of polymerization condition on the resulting product is best understood by two mechanisms. First there is a competition between the

desired aminolysis reaction resulting in poly(amic acid), and an undesired hydrolysis reaction opening the anhydride ring and producing two carboxylic groups. The aminolysis reaction is kinetically favored by a factor of 5 over the hydrolysis, and excess diamine will drive the process down that pathway²⁵¹. Second, in the case of a heterogeneous reaction particles of dianhydride added to the solution will undergo reactions at their surface faster than dissolution occurs²⁵¹. Thus the polymerization is occurring at a solid liquid interface where the local concentration of reactive sites is significantly greater than would be present in bulk solution, resulting in weight average molecular weights (M_w) in excess of predictions based on the stoichiometric equilibrium. Differing reactivity's of diamine monomers can also have an impact on the molecular weight distribution and the resin viscosity²⁴⁴.

The stability of various PAA resins also varies based on the constituent monomers, and the equilibrium of poly(amic acid) forming reaction. The viscosity of a resin produced from the combination of pyromellitic dianhydride (PMDA) and oxydianiline (4,4'-aminophenyl ether, ODA) will often decrease over a period of days or weeks in a degradation process that is highly temperature and environment dependent²⁵². This process results from equilibration of the length of the polymer chains away from the very high M_w formed under heterogeneous polymerization, as well as some irreversible hydrolysis of anhydride groups. Alternatively the combinations of PMDA and *p*-phenylene diamine (PPD) or *m*-phenylene diamine are known to gel over time²⁴⁶. When two resins formed from different monomer combinations are mixed, the equilibrium of the amic acid bond will lead to the formation of random co-polymers, which can be observed by a gradual change in the miscibility of the

respective resins, or from the elimination of phase-separation in solid films of the condensed poly(amic acids)^{247, 253}.

Much of the work in understanding the solution behavior and properties of the poly(amic acid) resins comes from size exclusion chromatography (SEC), also referred to as gel permeation chromatography (GPC)^{254, 255}. The technique became a powerful analytical tool with the development of highly stable and well controlled pumps and in-line detectors for light scattering and refractive index measurements^{245, 252, 256, 257}. Size exclusion chromatography separates the constituent molecules of a solution based on their residence time within a highly porous media, known as the stationary phase^{258, 259}. It is important that the residence time of the components be based on purely steric factors rather than any chemical affinity between the stationary phase and the analyte. Polystyrene is the most commonly used material for the stationary phase. A very dilute solution of the sample is injected into the system and is then carried by a very precisely controlled flow of the mobile phase through a series of columns containing packed beads of the stationary phase with a well-known porosity and pore size distribution²⁶⁰. Any components in the solution larger than the largest pores will be unable to access the pore volume, and thus will be carried elute from the system first. As the size of components decreases, a greater fraction of the pore volume will be accessible, and the analyte will take longer to elute from the column. Upon elution the solution passes through the in-line analytical tools and results in a change in the refractive index or light scattering behavior when compared to a reference sample of the mobile phase alone, and this difference is recorded as a function of the residence time of the solution. Calibration of a given column with the residence time of known standards of

narrow molecular weight is necessary to then convert the data into a molecular weight distribution²⁶¹.

The use of SEC on poly(amic acids) is more complicated than for simple polymers like polyethylene oxide or polystyrene because the PAA is a polyelectrolyte²⁴⁵. As a result in dilute solution the equilibrium dissociation of the carboxylic acid groups will cause the polymer to interact with itself and with the stationary phase. Most studies of the molecular weight of PAA by SEC then use additives to the mobile phase to suppress these interactions. A typical mobile phase thus will consist of less than 0.1 M each of LiBr and H₃PO₄ in a good solvent for PAA such as DMF, DMAc, THF, or NMP^{259, 260, 262}.

The high chemical resistance of PI means resins are often cast as PAA then and then imidized^{241, 263, 263}, though there is a continual stream of publications based upon the formation of polyimides that can be processed in the imidized state. In either case the imidization is accomplished by chemical or thermal cyclodehydration to form PI²³⁸.

Similar to PAN, polyimides are carbonized at temperatures between 600 and 1100 °C under inert atmosphere²⁶⁴⁻²⁶⁶. TGA, TVA, ¹³C NMR, and XPS have been used to examine the process and the products released during carbonization for rigid, semi-flexible, and flexible PI from various monomers. Benzimide decomposition between 500 and 550 °C releases CO, CO₂, H₂O, HCN, and H₂²⁶⁷. The main loss of mass is typically completed by 650 °C, with final carbonization between 800 and 900 °C. The yield of the process at 800 °C was dependent on sample morphology with films yielding 75 to 80% and fibers yielding 60 to 65%. Conductivity of a carbonized polyimide film increases with increasing temperature and varies over an order of magnitude for different combinations of monomers⁴⁵. For the

purposes of pyrolysis polyimides are considered soft carbons, and will go through a mesosphere and graphitize when heated above 2500 °C. This approach has been used to convert polyimide coatings into high quality graphite films^{43, 44, 268}. Finally changes in inert carbonization atmosphere were studied for Kapton, a commercially available PI formed by polymerization of pyromellitic dianhydride (PMDA) and 4,4'-oxydianiline (ODA). The use of He resulted in the highest porosity under BET analysis²⁶⁶, compared to N₂ and Ar.

Electrospinning of PI is also done from the PAA precursor followed by imidization treatment^{39, 46, 269}. Published fiber diameters of pure PI have been as small as 120 nm²⁷⁰. Those fibers were subsequently carbonized and the conductivity was shown to increase with decreasing diameter as measured by four-point probe when carbonization was carried out under high mechanical pressure (22 kPa). Additionally PAA has been blended with PAN and then electrospun and turned into carbon fibers²¹⁸. The subsequent imidization of PI and stabilization of PAN occur at the same time. Kim et al. showed a similar relationship between decreasing diameter and increasing conductivity measured via four-point probe.

The smallest PI fibers reported in the literature are 60 nm and contain ~15 nm silver nanoparticles prepared via the *in situ* method²⁷¹. These were produced from pyromellitic dianhydride (PMDA) and 4,4'-oxydianiline (ODA) polymerized in DMF with silver acetate as the salt and cured to 300 °C. The inclusion of silver salt in the solution raised the conductivity during the electrospinning process produces finer fibers which are stretched more in the electric field. These fibers were not subjected to pyrolysis. Carbon fibers of 2 to 3 μm have been produced from electrospinning of 12% PAA in THF:MeOH (80:20)³⁹.

Despite the large fiber diameters, the paper is interesting because it showed PAA can be directly carbonized without imidization, though a lower yield of carbon results.

2.9 Chemical Vapor Deposition

The continuous growth of solid materials onto solid substrates through the reaction of precursor gasses is known as chemical vapor deposition (CVD)^{272, 273}. The technique is most widely used in the semiconductor industry where it is valued because of the capability of producing conformal, high purity films meeting the stringent performance requirements of ultra large scale integrated devices of the 21st century^{272, 274-276}. During the CVD process one or more precursor gasses are continually flowed into a reaction chamber where they react with each other and the surface to leave behind a solid material. One means of driving the reaction is to heat the substrate to temperatures many hundred degrees above ambient²⁷⁵. In the process gaseous by-products are often produced and these are purged out of the reaction chamber by the continuous flow of feed and waste gas. The most common examples of CVD products in microelectronics are silicon dioxide²⁷⁷⁻²⁷⁹, doped silicon dioxide²⁷⁵, and silicon nitride²⁸⁰; but the CVD process has been demonstrated for a wide range of products^{272, 281-283}. Many different reaction schemes exist for the most common films and the specific precursors chosen depend on the thermal constraints of the substrate and the desired purity and properties of the resulting material.

There are many classifications of CVD processes, most made distinct by the reaction conditions within the process chamber. Variation in the pressure within the chamber during deposition results in either atmospheric pressure chemical vapor deposition (APCVD)^{273, 282}, low-pressure chemical vapor deposition (LPCVD)^{276, 284}, or ultrahigh vacuum chemical vapor

deposition (UHVCVD)^{283, 285}. Variation of the pressure is one means of controlling the reaction rate, since lower pressure chambers will have fewer collisions between precursor gases at the surface²⁸⁶. Additional benefits of lower operating pressures inside the chamber include improved control of material properties, uniformity, and conformity of the film^{275, 276}.

An additional variation of the typical CVD process is the introduction of a radio frequency coiled power supply to produce plasma. The plasma will enhance the rate of reactions when there are kinetic limits and allow for processing at lower temperatures^{275, 279, 280}, thus protecting the substrate from exceeding a thermal budget and preventing mechanical or device failure or chemical decomposition. In some applications the presence of the plasma also helps to ensure a more uniform conformal coating is applied to high aspect ratio structures by performing a simultaneous reactive-ion etch.

When considering the growth of carbon materials via CVD, a wide range of processes have produced a wide range of products²⁸⁷⁻²⁹⁰. The variation in carbon materials grown by CVD methods can be explained by factors such as the precursor species, reactor pressure, process temperature, substrate material, and the presence of catalysts. While the most common precursor used when producing carbon materials is methane²⁹¹, many different hydrocarbons have been employed successfully^{288, 292-295}. Experimental results indicate the formation of acetylene and benzene in the vapor phase are important steps in the reaction pathway leading to carbon deposition^{296, 297}, and for methane to deposit it must first undergo a homogeneous gas phase reaction to yield unsaturated hydrocarbons with two or more carbon atoms²⁹¹.

Pyrolytic carbon is carbon formed by the thermal decomposition of hydrocarbons in atmospheric or low pressure CVD. Pyrocarbon is nearly graphitic in nature but with some disorder and covalent bonding between graphite layers, and has been created from a wide range of precursor materials typically at temperatures exceeding 1000 °C^{297, 298}. Some researchers have used evaporation or sublimation of a typically solid-phase organic molecule in one region of a tubular furnace. The sublimated material is then transported by a carrier gas to the desired substrate in a different region of the furnace. It is common for the sublimation region and deposition region to exist at different temperatures²⁹⁹. In other systems, large, but still volatile molecules are introduced into the CVD chamber or tube along with carrier gases, typical of standard CVD processing, where they decompose on the heated substrate²⁹⁵.

A variant of CVD known as chemical vapor infiltration (CVI) is associated with the production of macro-scale composites, with carbon/carbon composites being one common variation³⁰⁰⁻³⁰². This is a process in which the precursors flow through a porous substrate and then react on the surfaces throughout the volume of the substrate with the goal of completely filling the pores with graphitic pyrocarbon to produce a composite block reinforced by the substrate material^{303, 304}. Graphitic and/or pyrolytic carbons are very commonly produced during CVI. These depositions typically occur at standard pressure or at pressures on the order of 10 kPa to ensure full densification of the composite^{305, 306}. The competition between homogeneous gas phase reactions and the heterogeneous surface depositions dictates that operating at too low of a pressure will result in pore blocking and incomplete densification. Additionally the presence of small quantities of hydrogen in the feed gas results in greater

inhibition of rapid deposition pyrocarbon at the interface between the substrate and the bulk processing gas than within pore volumes³⁰⁷.

The controlled production of thin layers of carbons with greater order, and thus more graphitic, commonly requires the use of smaller hydrocarbon molecules and the introduction of plasma processing³⁰⁸ or other modifications such as laser-assisted CVD³⁰⁹. Introduction of various catalyst materials upon the substrate is another means of producing highly ordered graphitic carbons, such as vapor-grown carbon fibers around a small diameter iron wire core³¹⁰.

Silicon is typically used as a model substrate when growing various carbon films, but depositions are possible on various forms of carbon and many other solid surfaces. When highly ordered forms of carbon are desired, a catalyst metal is commonly introduced upon the substrate, and nickel is often chosen as this catalyst. And the production of the diamond phase of carbon is often performed in a modified CVD process, most commonly the hot-filament^{287, 311} method but PECVD and microwave assisted CVD have also been demonstrated to produce highly ordered sp³ carbon³¹². Diamond formation is commonly carried out at low pressures with low methane to hydrogen ratio. The ideal operating range for the production of diamond is a substrate temperature near 900 °C, but not exceeding 1100 °C where graphitic carbon formation is preferred.

Carbon nanotubes, highly regarded because of their mechanical strength³¹³ and potential electronic properties³¹⁴ can be produced by a variety of methods: chemical vapor deposition³¹³, arc discharge³¹⁵, and laser ablation³¹⁶, but catalyzed CVD growth shows the most promise for the production of nanotubes in commercial scale³¹³. In this method the

nanotubes grow at catalyst sites, such as nanoparticles of Ni³¹⁷ or Fe³¹⁸, located on a substrate, typically silicon. Root-growth nanotubes are formed when the catalyst remains on the substrate surface. Tip-growth nanotubes form when the catalyst is pushed away from the surface by the nanotubes growing in-between. Additionally, nanotubes produced via CVD can be purified in one step with removal of the metal catalyst and other defects via high temperature graphitization³¹⁹. Carbon nanotubes have featured prominently in research on Li-ion battery electrodes.

The most recent variant of carbon to be produced via chemical vapor deposition is graphene: a two-dimensional material of a single layer of carbon atoms bonded in a sp² structure³²⁰. The theoretical room temperature electronic resistivity of this material is the lowest known, leading to widespread interest in using it in electronic and electrochemical applications. One means of producing graphene has been made chemical exfoliation of graphite but there is little control of the process and a low percentage of the material is true single layer graphene³²¹. Low pressure plasma enhanced chemical vapor deposition has been shown to produce 1 to 2 μm wide sheets of graphite of only a few layers thick using a mixture of methane and hydrogen upon a Ni substrate³²². The use of copper as a substrate in LPCVD, without the need for plasma processing, has led to an impressive result of predominantly single layer graphene on substrates up to 30 inches in the diagonal rolled up within an 8-inch diameter tube furnace²⁸⁹. The resulting films had superior conductivity to the indium-tin-oxide films currently used as transparent electrodes in solar cells and touch screens, and were easily transferred unto new substrates and used in functional touch screens.

2.10 Raman Spectroscopy

Raman spectroscopy is a useful tool for studying the myriad forms of carbon³²³⁻³²⁷. The process is quick, non-destructive, and can be carried out at ambient conditions³²⁸. It can be used to determine the degree of disorder in a near graphite material³²⁹, the chirality of carbon nanotubes³³⁰, and the number of layers in “graphene”³³¹. A Raman measurement relies on the shift in frequency of single wavelength light that undergoes inelastic scattering (energy of the photon is changed) upon interacting with matter. The incident wavelength is selected so the photons possess only enough energy to transition to atoms of the sample to a virtual energy state. Most photons undergo elastic (Rayleigh) scattering and their energy is unchanged. The less than 1 in 10^5 photons that are inelastically scattered lose an amount of energy equal to an allowed transition between energy levels below the virtual state. The Raman shift reported is the difference between energy of the incident light and the scattered photons, and like many forms of spectroscopy are most commonly plotted as wavenumber with units of cm^{-1} .

When investigating a solid crystalline material the lattice structure has certain allowed vibrational modes, referred to as phonons, and these vibrational states restrict the possible transitions which are allowed under Raman selection rules³²⁸. For example, perfect crystalline graphite has a 4 atom unit cell, and a degree of freedom analysis provides for six possible vibrational modes. Of these, two are Raman active^{332, 333}, one at 42 cm^{-1} and another at 1582 cm^{-1} . In the idealized case of a perfect sample of graphite, the Raman spectra will be a very simple plot with two main peaks and subsequent overtones. The peak at 1582 cm^{-1}

was assigned a designation of G, for graphite³³⁴ during the initial characterization of graphitic carbon.

In non-idealized, real samples of graphitic carbon, there exist defects, impurities, and edges, and these deviations from the 4-atom sp^2 bonded structure allow for additional phonons and scattering events, producing a more complex spectra. The most common second peak used when characterizing carbons is known as the D peak, for disorder³³⁴. The location of this peak is variable, with its position dictated by the wavelength of light used to probe the sample^{332, 333, 335}. It has been recently demonstrated that the variation in the location of the D peak occurs because the relaxation process is doubly resonant^{336, 337}.

Simple characterization of the degree of disorder in a carbon sample is possible with the information from just these two peaks. The spectra are fit by two Gaussian-Lorentzian curves, at which point the peak location can be identified, and the curves can be integrated to get the intensity of both the G and D peak, respectively denoted I_G and I_D . The degree of amorphization, or sp^2 versus sp^3 bonding, can be determined using the location of the G peak and the intensity ratio I_D/I_G ³³⁸. Additional information about the sp^3 content can be seen in a peak at 1100 cm^{-1} when carbon is probed with a ultra-violet (UV) source^{326, 339}. A study of the Raman spectra of 29 different forms of carbon, including highly ordered natural and synthetic graphite, carbonized fibers, carbon blacks, cokes, activated carbons, and coal, found good correlation between the ratio $I_D/(I_G + I_D)$ and many parameters including the width and location of the D and G peaks⁷¹. The results of Cuesta *et al.* demonstrated that the family of carbons could be grouped into populations based on these parameters, where the slope of regression lines would change at key transitions of peak locations and the intensity

ratios of the D and G peaks. The ratio (I_G/I_D) can be correlated to the average in-plane crystallite size of the graphitic regions of various carbons using the following equation, valid for any wavelength of light used to probe the sample³⁴⁰:

$$L_a = \frac{560}{E_{laser}^4} \left(\frac{I_G}{I_D} \right) = (2.4 \times 10^{-10}) \lambda_{laser}^4 \left(\frac{I_G}{I_D} \right) \quad \text{Equation 9}$$

where L_a is the crystallite size in the basal plane (in nm), I_D and I_G are the measured intensities of the D and G peaks, and E_{laser} is the energy or λ_{laser} is the wavelength of the incident photons.

Additional signals are present in carbons that are more disordered, and these are often studied to determine the bonding structure of the carbons under probe. Near the G peak there are often found D' and D'' peaks. The D' is only able to be distinctly observed in highly ordered graphite and is located around 1620 cm^{-1} . The D'' peak located around 1500 cm^{-1} is important in fitting carbons of greater disorder, such as pyrolyzed solids, where the region between the G and D peaks has a greater signal than can be fit by only two peaks^{71, 324}.

Finally some additional information is available by moving to the second-order spectra between 2200 and 4000 cm^{-1} . A peak originally labeled as G' around 2700 cm^{-1} because it was found in highly ordered graphite is actually the first overtone of the D peak, and is now better labeled as D* or 2D. This peak occurs because of phonon-phonon scattering, not defect scattering, and therefore it is most pronounced in highly ordered graphites³³³. In the most ordered graphite this peak will actually split based on the distinction

between stokes and anti-stokes scattering, and like the D peak, this peak is doubly resonant and will shift with the intensity of the laser wavelength.

2.11 Atomic Layer Deposition

Atomic layer deposition (ALD) is a material deposition technique which provides greater control of thickness and chemistry than chemical vapor deposition^{341, 342}. A typical ALD process consists of alternating, self-limiting reactions of vapor-phase precursors (commonly referred to as chemicals A and B) with functional groups on the surface of a substrate. Precursor A reacts with a particular functionality on the surface of the substrate. The result is the deposition of one monolayer of material upon the surface (reaction A), and a new surface functionality. The reaction self-limits because chemical A cannot react with the new functionality created during its reaction with the previous surface chemistry. After the reaction has completed, precursor A, and any by-products of the reaction, must be purged from the system prior to the introduction of precursor B. The subsequent step (reaction B) uses precursor B, which will readily react with the current surface functionality, deposit another monolayer of material, and leave behind the surface functionality favored in reaction A. This step is again followed by a purge to remove precursor B from the system. Through repetition of the A-B reaction sequence these alternating and self-limiting steps can be used to precisely control the number of layers of a given material deposited onto the surface. And while binary reactions are the most commonly published examples of ALD, it is possible to employ more elaborate ternary³⁴³ (A-B-C).

Atomic layer deposition is capable of producing highly conformal coatings of a well-controlled thickness. This unique combination has led to widespread use in the semi-

conductor industry as part of the fabrication of microelectronics^{344, 345}. Careful selection of the precursor chemicals and the reaction conditions has resulted in the creation of ALD schemes to deposit insulators³⁴⁶, doped semi-conductors³⁴⁷, and metals³⁴⁴. Depositing a film composed of a single element commonly requires that the second self-limiting reaction be one which removes certain functional groups, such as the use of hydrogen plasma to remove chlorine atoms in the deposition of tantalum from tantalum pentachloride³⁴⁴. The ALD process has also been demonstrated on polymeric, fiber substrates^{28, 348} to affect surface properties such as wettability³⁴⁹.

There are some recent examples of the application of ALD to electrode materials for Li-ion batteries. For example aluminum oxide grown from trimethylaluminum (TMA) and water (H₂O) has been used to stabilize the interface between conventional electrolyte solvents and both natural graphite^{31, 32} and metal oxide cathodes³⁰, resulting in improved cyclability. Those depositions were performed after the slurry of active material had been cast onto the current collector to avoid placing an insulating barrier between the active material and the current collector. A group based in Finland initially demonstrated the ability to create lithium-containing films via atomic layer deposition³⁵⁰. The George group has built on this with the goal of creating lithium carbonate films, in an effort to mimic the natural SEI formed on Li-ion anodes³⁴³. Thus far only results for the deposition of the carbonate film are available, while the electrochemical properties remain under study.

2.12 Molecular Layer Deposition

The concept of molecular layer deposition (MLD) is an extension of atomic layer deposition³⁵¹. While ALD builds a film through the net addition of single atoms, MLD

replaces one, or both, precursors with a larger molecule in which the functional groups are separated by several atoms^{33, 352}. These atoms located between the functional groups are thus added to the surface during one of the self-limiting steps, resulting in the addition of a small molecule to the surface of the film.

The technique was initially used to grow thin conformal polymer layers using traditional organic monomers from step growth polymerization^{353, 354}. Polymers grown via MLD include polyamides³⁷, polyimides³⁵⁵, and polyurea³⁵. The versatility of MLD has enabled successful polymer film growth on a variety of substrates³⁵⁶.

More recently the MLD technique has been used to produce a class of metal-organic hybrid coatings commonly referred to as “metal-cones”, named as such because of their structural similarity to various silicones^{34, 357}. Aluminum metal-organic hybrid molecules, referred to as alucone polymers at the time, were first reported in the late 1950s. In 1999 a version of alucone was synthesized utilizing a sol-gel technique in which ethylene glycol and tert-butyl aluminum ($\text{Al}(\text{t-Bu}_3)$) were reacted in hexane³⁵⁷. The first report of alucone formed by MLD occurs almost a decade later when the water commonly used as the oxidant in alumina ALD was replaced with ethylene glycol³³. The substitution of ethylene glycol for water in another well-known ALD chemistry has produced films of zincone³⁴.

In many cases the observed growth rates for these films are lower than what is observed for the pure ALD deposition. Using ethylene glycol and TMA as an example, the length of the glycol molecule ($> 5 \text{ \AA}$) is sufficient that both alcohols could react with functional groups, leading to a reduction in the number of available functionalities in subsequent steps³³. The use of ternary reaction schemes with hetero-bifunctional precursors

can eliminate the possibility of the double reaction³⁵². Secondly, it is possible that the size of the MLD precursors produce steric hindrance, preventing access to the reactive sites by available precursors³⁵¹.

Another significant difference between similar ALD and MLD films is the thermodynamic stability of the hybrid film. When considering the reaction of ethylene glycol and diethyl zinc, the resulting films are unstable in ambient (i.e., humid) air, or under an annealing treatment. In either case, the film, studied by infra-red spectroscopy, tended to revert towards the composition of the comparable ALD process of diethyl zinc and water³⁴. But when the films were maintained in cool, dry air the deposited films were unchanged after 3 days. Alucone polymers produced with ethylene glycol are also known to be moisture sensitive as probed by FTIR, though these films are more stable than the zincone films, and do not revert to a simple alumina structure³³. The use of an ABC reaction scheme with TMA, ethanolamine, and maleic anhydride, produced a film in which unquenched aluminum methyl functionalities reacted with ambient moisture within ten minutes of exposure, but did not suffer any longer term degradation when left at ambient conditions³⁵². A film created from TMA and glycidol showed similar stability at ambient conditions³⁵⁸.

There are few reports of applications of these metal-organic hybrid films. Some preliminary studies of alucone polymers have demonstrated that the hybrid films possess mechanical and thermal properties more typical of polymer films rather than ceramic ones³⁵⁹,³⁶⁰. One demonstrated application took advantage of the susceptibility of an alucone film to hydrochloric acid etch to create a sacrificial layer in a nano-electrical mechanical system (NEMS). The removal of the alucone layer produced an air gap beneath a tungsten bridge

spanning two electrodes³⁶¹. Alucone via MLD has also been proposed as a means to both passivate the photocatalytic properties of titanium dioxide to prevent the pigment from degrading the polymer in which it is suspended, and also to prevent agglomeration/improve dispersion of the particles in the polymer matrix^{362, 363}. Finally a unique arrangement of copper oxide nanoparticles on the exterior of an alumina fiber support was formed by creating core-shell fibers of copper surrounded by alucone. The subsequent annealing of the alucone resulted in an alumina film with angstrom sized pores, which allowed the out-diffusion of copper atoms, but not the in-diffusion of oxygen³⁶⁴.

Chapter 3

Plasma Enhanced Chemical Vapor Deposition of Graphitic Carbon on Pyrolyzed Nanofiber Li-ion Anodes

3.1 Introduction

Lithium-ion batteries are the dominant power supply in 21st century portable communications and computing devices. Li-ion secondary cells have high energy densities and high operating voltages resulting in higher power densities when compared to other mature rechargeable battery technologies¹. Additionally Li-ion cells have low rates of self-discharge and do not suffer from the memory effect present in nickel-cadmium cells. While the adoption of Li-ion technology is widespread, further improvements in battery capacity, life, and safety are required to meet the increasing demands in mobile technologies and to deliver affordable performance in transportation applications³⁶⁵⁻³⁶⁷.

The majority of commercial cells are based on micron sized particles of a metal oxide cathode, such as LiCO_2 ⁴⁸, and a graphitic anode¹⁶³. Both electrodes are typically made of at least 85% active material, with the remainder made up of polymer binder and electronically conductive additives. Graphite is used as the active material in the anode because of its low, flat potential when compared to Li/Li^+ and its long term capacity retention⁶⁶. The theoretical maximum Li intercalation into graphite is one Li ion for every six carbon atoms, yielding a potential specific capacity of 372 mAh/g. Many materials are known to possess larger potential reversible capacities^{24, 72, 99}.

For example, there are extensive literature reports concerning the electrochemical properties of hard-carbon materials^{70, 75, 77}, defined as organic material which cannot form graphite under any pyrolysis conditions²²⁷. These materials are known to suffer from significantly larger irreversible capacity losses during the first cycle of the cell⁷²⁻⁷⁴. These losses are predominantly caused by the formation of the solid electrolyte interphase (SEI)

upon the electrode surface^{160, 368}. The SEI formation occurs during the reduction of electrolyte salts and solvents in the presence of lithium at the electrode/electrolyte interface. Each Li atom consumed in this process has undergone an electrochemically irreversible process and is lost to further cycling. The irreversible losses of graphitic carbons is known to be lower than hard carbons, and as a result there have been attempts to create a graphitic surface upon hard carbons via chemical vapor deposition^{27, 172, 173}. While these techniques have been successful in lowering the irreversible losses, some of the other properties of hard carbons, such as cycle hysteresis, have prevented their adoption as commercial electrode materials.

Some additional potential replacements for graphite anodes include titanium dioxide⁸⁶, Li-alloying metals such as Sn and Si⁸⁰; and conversion materials based on transition metal oxides^{87, 92} or phosphides. Each of these potential replacements for the negative electrode material has properties which make them unsuitable to supplant graphitic carbon as the anode of choice in commercial cells. In many cases insertion of Li is a reversible process, but repeated transformation of materials between lithiated and de-lithiated states produces enough mechanical stress to cause particles to fracture. As a result a large amount of research and development activities have focused on creating composite materials of carbon and non-carbon lithium storing compounds, which when used together will outperform graphite^{4, 6, 16, 101, 114, 123, 152, 153}.

One possible avenue towards this goal is the use of electrospinning to create novel nanoscale one dimensional composites²⁰. The electrospinning process creates a continuous polymer fiber with a non-woven structure¹⁹⁶. The process has been used to create composites

of nanoparticles embedded within the matrix of the polymer fibers. If the polymer used as the matrix can be pyrolyzed, such as polyacrylonitrile (PAN)^{39, 218}, and the nanoparticles are capable of storing Li, a free-standing electrode can be produced with long term reversible capacities well in excess of graphite^{23, 24, 128}. The high aspect-ratio fibers produced also yield excellent capacity retention at high currents, owing to the large surface area for charge transfer²⁴.

The polymer most commonly chosen as the precursor to the carbon fiber matrix is PAN. It is pyrolyzed at temperatures below graphitization, and when combined with the very large surface area produced in the electrospinning process, the irreversible losses incurred during SEI formation can be in excess of 500 mAh/g as seen in **Figure 3.1**. Irreversible losses of this magnitude are larger than the reversible capacities of all common cathode materials, making the commercialization of the 1D nanomaterials unrealistic.

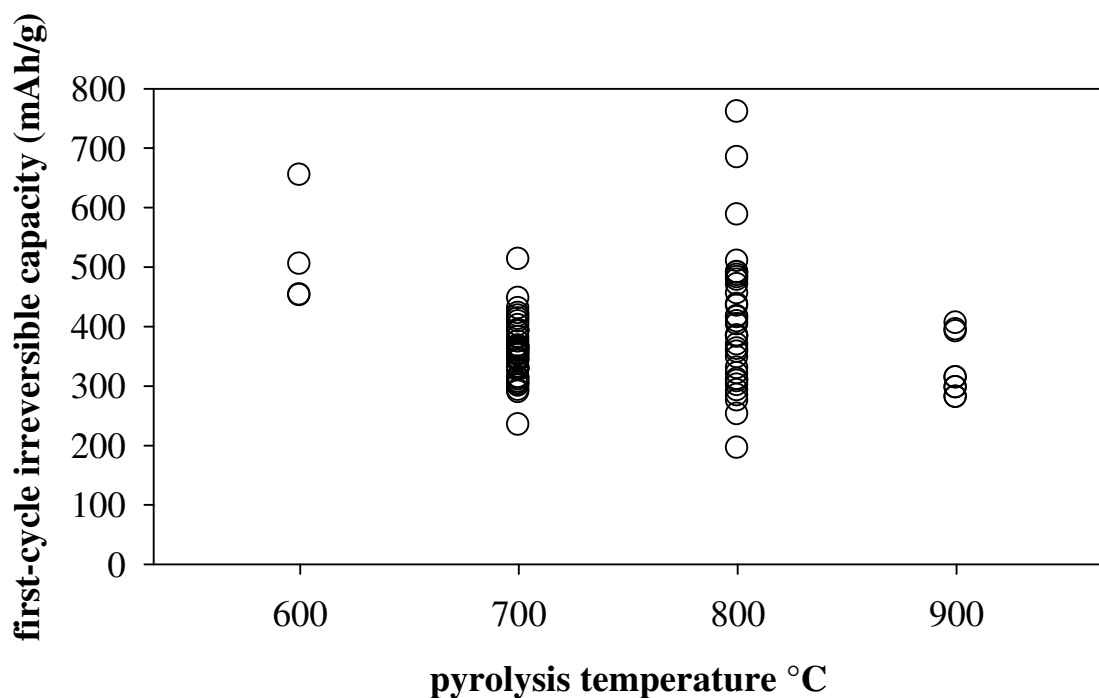


Figure 3.1 - First-cycle irreversible capacity for electrodes made from PAN fibers pyrolyzed at the indicated temperatures throughout the work leading to this dissertation. The electrolyte was 1 M LiPF₆ in EC:EMC (1:1).

The significant void fraction present in non-woven, electrospun materials presents a means to overcome this undesirable level of irreversible Li losses. Vapor phase reactions have been used to deposit new material on the surface of electrospun fibers²³⁴. Previous attempts to use CVD carbon to change the surface layer have operated at either atmospheric pressure or under moderate vacuum. In these cases the particles were on the order of tens of microns or more. Tight control of the deposition process was not necessary, with a micron or more of graphitic carbon grown quickly being the desired outcome^{27, 173}. Given the desirable aspect ratio of non-woven electrospun mats, a significantly thinner film is required to maintain the sub-micron critical dimension, and care must be taken not to obstruct the voids.

To achieve this goal low pressure plasma enhanced chemical vapor deposition is proposed to produce a highly graphitic carbon coating upon the surface of these carbon nanofibers mats and potentially reduce the irreversible losses of lithium.

3.2 Materials and Methods

The precursor polymer chosen for the nanofibers was polyacrylonitrile (PAN) (Sigma Aldrich MW 150,000). The polymer was dissolved in anhydrous dimethylformamide (Sigma Aldrich), heated to 40 °C and stirred for 24 hours to dissolve the polymer. The vials containing the final 11% PAN solution were then sealed and stored at room temperature. The viscosity for this weight fraction of 150,000 MW PAN in DMF is located near the upper end of the dilute entanglement regime (**Figure 3.2**), ideal for continuous electrospinning of nanofibers¹⁹³.

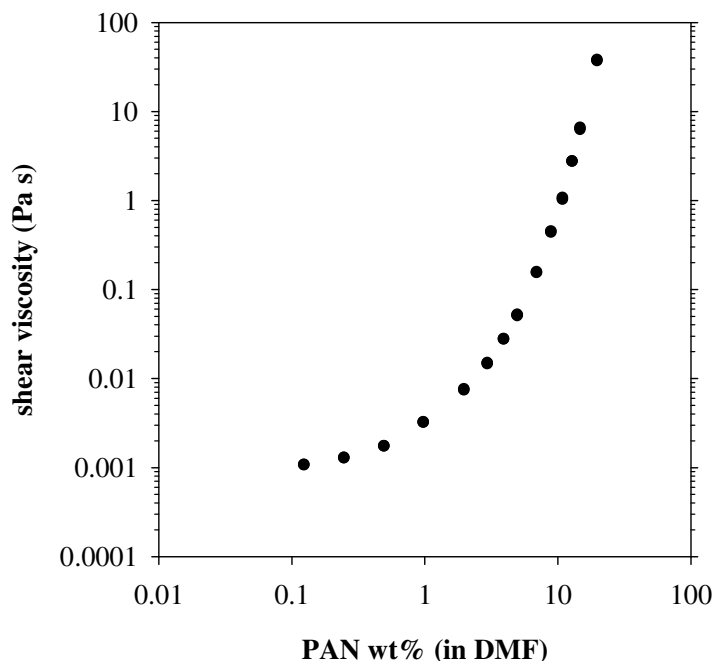


Figure 3.2 - Shear viscosity of 150,000 g/mol weight average molecular weight (M_w) PAN dissolved in DMF between 0.125 and 20 wt% polymer.

The electrospinning setup was arranged horizontally with a 30-cm, flat, metallic, circular disk serving as the collector. The PAN solution was pumped through a 22-gauge stainless-steel needle at a rate of 1 mL/h. The distance from the tip of the needle to the collector plate was 15 cm. To maintain a stable Taylor cone the electric field was varied between 0.75 and 1 kV/cm, as needed. Three to four hours of electrospinning produced a non-woven mat of about 15-cm diameter and a total mass of between 0.3 and 0.4 g. The central, thickest portion of the mat was cut out, and divided into swatches measuring approximately 3-cm wide by 12-cm length. These samples were removed from the aluminum foil prior to thermal treatment.

Pyrolysis of the fibers was conducted within a 45-mm inner diameter quartz tube mounted in a single zone Lindberg Blue tube furnace (model 55322-3). The swatches were loaded onto boats consisting of flat quartz shelves so the processing gasses flowed over the samples and down the length of the tube. The pyrolysis process of PAN proceeds in two steps²²⁷, stabilization and carbonization. The stabilization step was conducted at 250 °C with a 5 °C/min ramp rate from room temperature and a soak of 2 hours at 250 °C followed by uncontrolled cooling to ambient conditions. For stabilization a flow of dry air (National Welders) was maintained through the tube furnace. The carbonization step was done under a flow of high-purity nitrogen (National Welders) at 700, 900, or 1100 °C with a 5 °C/min ramp rate from room temperature and a soak of 2 hours followed by uncontrolled cooling to ambient conditions. Care was taken to ensure the samples remained flat and smooth during the thermal processing to attempt to ensure more uniform processing during the CVD process.

The subsequent deposition of carbon was performed using a radio frequency inductively coupled PECVD process. Pyrocarbon deposition of graphite is typically performed at temperature over 1000 °C, which would exceed the desired thermal budget for these materials, so the plasma processing is used to provide the necessary reactivity. A three-turn planar coil inductively couples 13.56 MHz power through a quartz window into a vacuum chamber. The sample stage consists of a temperature controlled resistive heater located 10 cm below the quartz window (**Figure 3.3**).

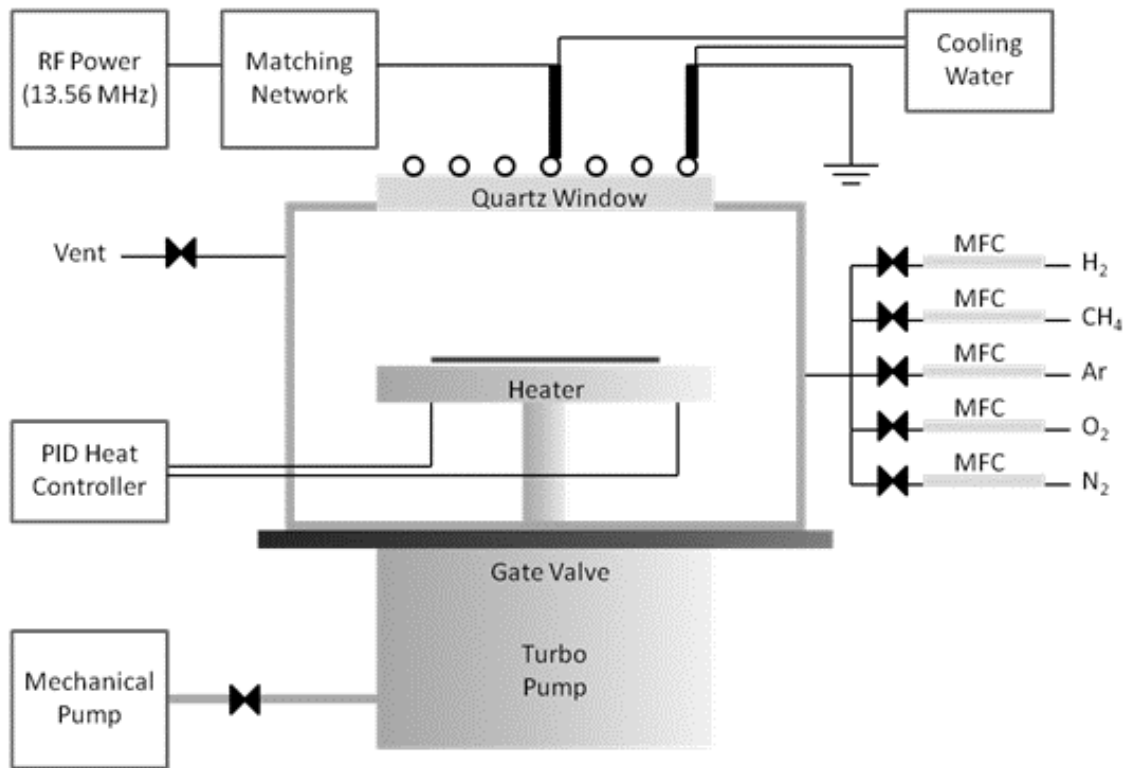


Figure 3.3 - Schematic of the PECVD chamber used to deposit carbon³⁶⁹.

The non-woven swatch of material was clipped to the heating element. Despite the care taken to ensure the swatches remained flat after pyrolysis, only a small portion of each sample was in direct contact with heater. The carbon source was methane diluted in hydrogen and/or argon. The pressure in the discharge chamber varied between 50 and 350 mTorr and the plasma power was set between 600 and 1200 kW for the various treatments. Before igniting the plasma, the temperature of the substrate was allowed to equilibrate in H₂ gas. The deposition temperatures were 860, 730, or 650 °C. The reaction conditions for the various experiments are summarized in **Table 3.1**. The change in mass of the non-woven was measured on a balance accurate to ±0.1 mg for Experiments 2, 3, and 4. For each

experiment one untreated swatch from the same electrospinning and carbonization batch was reserved as a reference. Imaging of the samples was performed by scanning electron microscopy at 5 kV using a secondary electron detector (JEOL 6400).

Table 3.1 - Processing conditions during PECVD.

Experiment	Sample	Temperature (°C)	Gas Ratio CH₄:H₂:Ar (mTorr)	Plasma Power (W)	Processing Time (min)	Mass change measured
1	1	650	50:0:300	600	1	No
2	2	650	10:35:5	600	10	Yes
2	3	730	10:35:5	600	10	Yes
3	4	860	50:100:0	1200	10	Yes
3	5	860	50:100:0	1200	10	Yes
4	6	730	50:100:0	1200	10	Yes
4	7	730	50:100:0	800	10	Yes
4	8	730	50:50:0	1200	10	Yes
4	9	730	50:50:0	800	10	Yes

In later work small pieces of samples from Experiments #3 and #4 were subjected to Raman spectroscopy. The instrument was a Horiba-Jobin Yvon LabRAM HS VIS high-resolution confocal Raman microscope using a 632.8 nm laser as the excitation source. The laser was focused normal to the substrate through a 50X objective lens resulting in an approximately 1 μm spot size. The instrument was calibrated using the 520.7 cm^{-1} line of a silicon wafer. LabSpec software (Horiba Scientific, Ltd.) was used to process all spectra.

After the deposition was completed, 1.3 cm diameter disks were die-cut from the non-woven samples to use as electrodes in 2032 size coin cells. The electrodes were dried overnight in a vacuum oven at 80 °C prior to introduction to a high-purity argon filled glove box (Labconco Protector) for coin-cell assembly. Each anode had a mass between 1 and 4

mg. A similarly sized copper disc was used at the current collector with contact maintained by the mechanical force of a disc spring. The counter electrode was lithium metal (Sigma Aldrich) and the separator was polypropylene (Celgard). The electrolyte was 1M LiPF₆ in a 1:1 (w:w) solvent mixture of ethylene carbonate (EC) and ethylmethylcarbonate (EMC). All electrochemical data was collected in galvanostatic mode with an Arbin Instruments (BT-2000) battery tester. The currents were set on a gravimetric basis between 25 and 200 mA/g. The cutoff voltages used were 0.025 V on charge and 2.0 V on discharge.

3.3 Results and Discussion

3.3.1 CVD Experiments #1 and #2 - The goal of this work was to produce highly graphitic, conformal carbon that enveloped the PAN fibers to create a surface which would suffer less irreversible loss of Li during the first charging cycle. The material used for Experiment #1 was carbonized at 700 °C prior to deposition in the PECVD reactor. Under SEM the material resulting from this deposition experiment was not conformal to the fibers, but instead had nucleated and grown a fluffy, amorphous carbon distributed randomly throughout the non-woven structure (**Figure 3.4**). Magnification to 50,000x on one particularly large fiber does show the growth of small ridges of material perpendicular to the fiber surface (**Figure 3.5**).

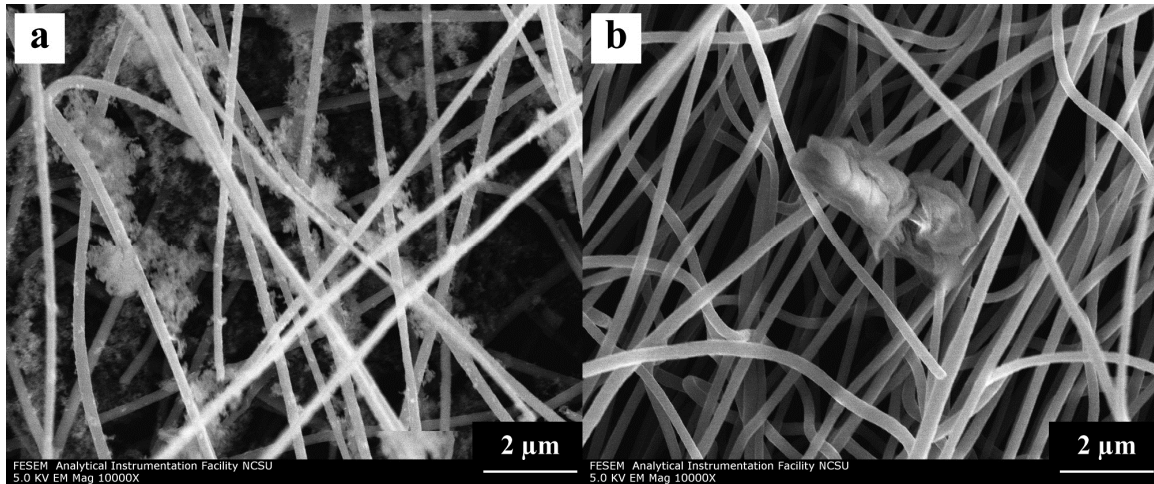


Figure 3.4 – Scanning electron micrographs of (a) fibers after coating during CVD Experiment #1 and (b) uncoated reference fibers.

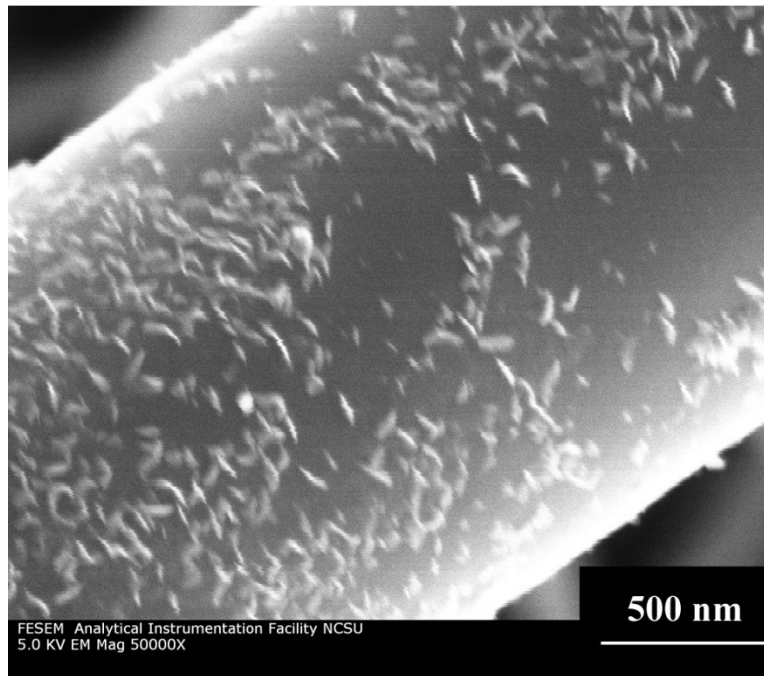


Figure 3.5 – Scanning electron micrograph at 50,000x magnification of a single large fiber showing small platelet growth perpendicular to the fiber surface

For Experiment #2 the gas mixture was modified. The methane content was substantially reduced to lower the growth rate. Operating at a lower overall pressure would also lower the growth rate of the material. Hydrogen gas was added to potentially scavenge sp^3 bonded carbon. The deposition time was extended to 10 minutes to compensate for these changes. Imaging of the samples (**Figure 3.6**) indicated no noticeable change in the treated fibers compared to the reference sample, and the new process conditions have eliminated the fluffy, amorphous carbon seen in CVD Experiment #1. Given the inherent conductivity of the fibers, and the desire for a thin, conformal, and conductive coating; if this goal were accomplished it would be unlikely to be visible under these conditions. The observed mass of the samples did not change in any significant amount as shown in **Table 3.2**.

Table 3.2 - Change in mass of samples treated in CVD Experiment #2.

Sample	Mass Before (mg)	Mass After (mg)
2	17.8	17.9
3	14.7	14.9
untreated reference	21.1	21.0

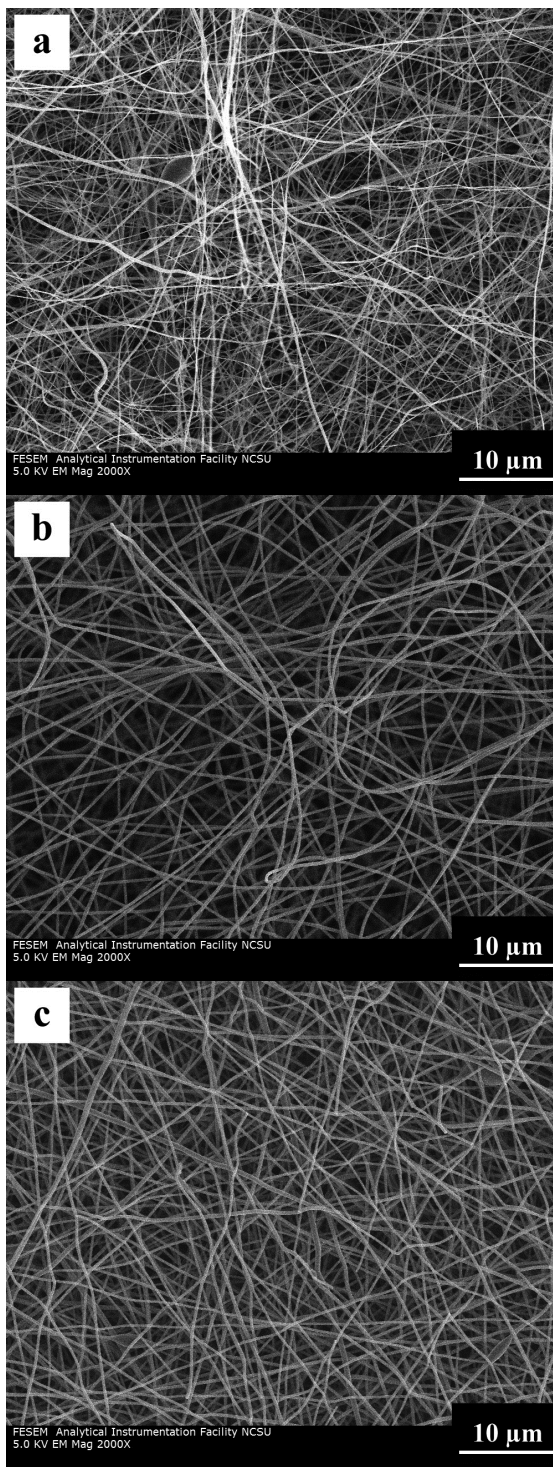


Figure 3.6 - Scanning electron micrographs of fibers from CVD Experiment #2 (a) Sample 2, (b) Sample 3, and (c) untreated reference.

All of these materials were cycled at a low charge and discharge rate of 25 mA/g. **Figure 3.7** shows that the irreversible capacity losses of the PECVD electrodes were still very large and not distinguishable from the reference samples. Over the course of ten charge/discharge cycles the plasma treatment did not have a noticeable impact the reversible discharge capacity shown in **Figure 3.8**.

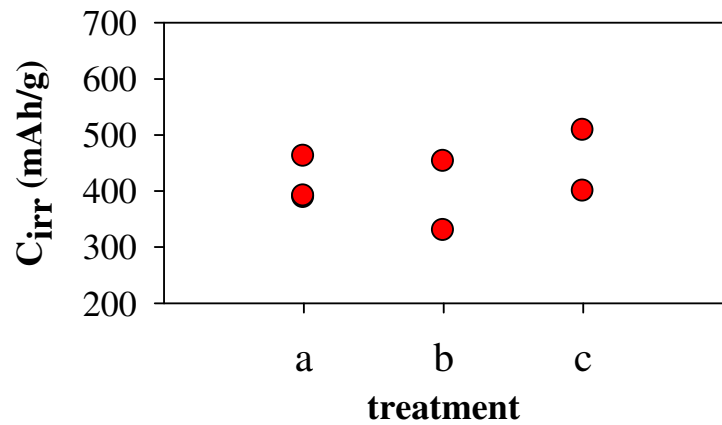


Figure 3.7 – First-cycle irreversible capacity of a) untreated reference samples, b) PECVD sample 2, and c) PECVD sample 3.

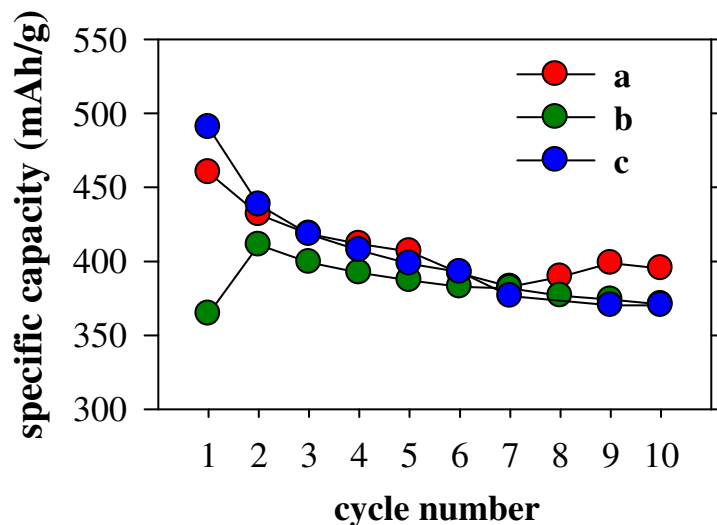


Figure 3.8 – Reversible discharge capacity of a) untreated reference samples, b) cells from PECVD sample 2, and c) cells from PECVD sample 3 cycled at a specific current of 25 mA/g.

3.3.2 *CVD Experiment #3* - The results of Experiment #2 suggest that no appreciable deposition took place at the conditions under study. The deposition conditions chosen for the third phase of this work have shown growth rates approaching 150 nm per minute of highly graphitic carbon nanowalls on glassy carbon electrodes, even accounting for a significant low growth nucleation period³⁷⁰. At such high growth rates the amount of material was expected to be significant. Surprisingly the mass of the samples after CVD processing decreased (**Table 3.3**). The untreated sample is included to demonstrate day-to-day variability in these measurements likely due to changes in the ambient humidity. The magnitude of the mass loss suggests that at these conditions the 1200 W plasma is etching away the fibers.

Table 3.3 - Change in mass of samples treated in CVD Experiment #3.

Sample	Mass Before (mg)	Mass After (mg)	Percent Remaining
4	20.0	10.9	54.5%
5	29.3	11.7	39.9%
untreated reference	34.5	33.8	97.9%

When viewed under SEM there was significant variation in the appearance of the fibers within a single sample. The first pair of images (**Figure 3.9**) are from the front (a) and back (b) of the untreated reference fibers. The fiber diameters range between 225 and 400 nm as observed in several regions and show a reasonably smooth texture.

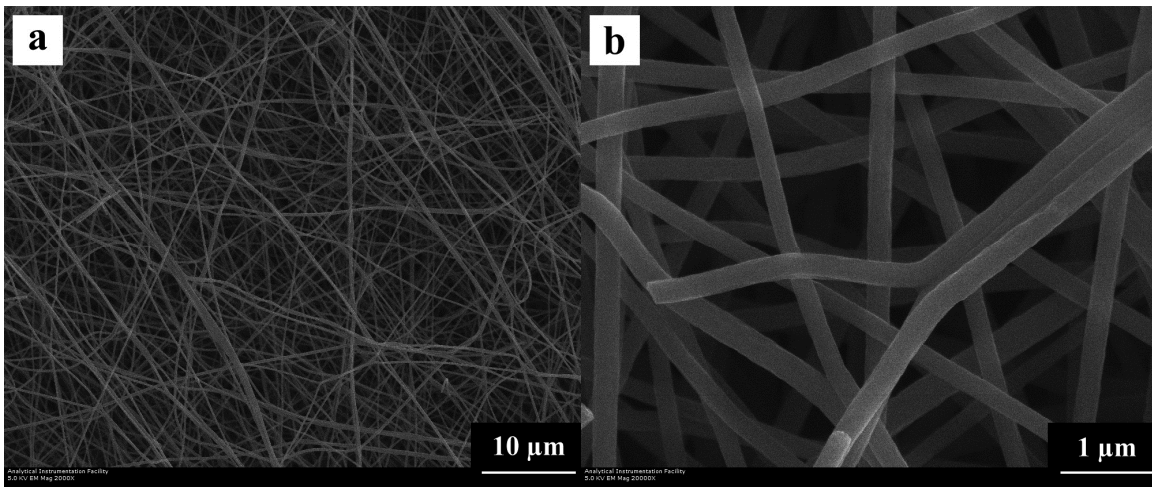


Figure 3.9 - Scanning electron micrograph of untreated nanofibers used as a reference in CVD Experiment #3 magnified (a) 2,000x and (b) 10,000x

The fibers shown in **Figure 3.10** are from the side of the sample that was facing away from the heater and towards the plasma coils in the PECVD reactor. These fibers have a measureable decrease in diameter, ranging between 150 and 315 nm and have greater visible surface texture. This surface texture might arise from more crystalline (sp^2) regions of the

fiber showing greater resistance to the etching process. Alternatively, it could be a small region of deposited carbon.

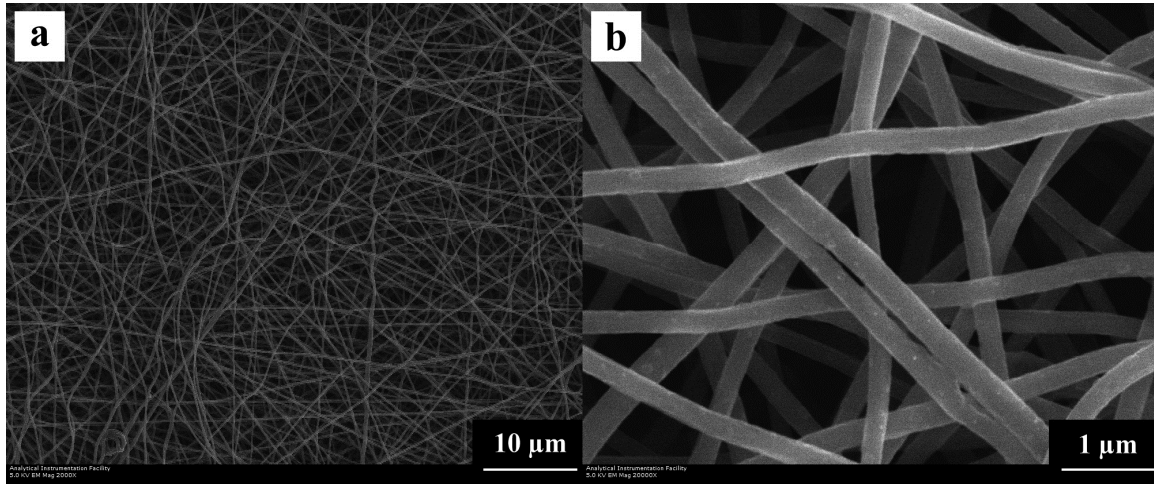


Figure 3.10 -- Scanning electron micrograph of fibers from Sample 5 on the surface facing towards the plasma coil and away from the heater magnified (a) 2,000x and (b) 10,000x.

Finally, the images in **Figure 3.11** and **Figure 3.12** are from the side of the sample which was in contact with the heater. The fibers closest to the surface have been almost completely replaced by thin ribbons of what is likely a highly graphitic material. Looking at fibers deeper into the mat the formation of the aforementioned carbon nanowalls on the surface of the fibers is clear. At a different location on the same sample (**Figure 3.12**) there exist structures which appear to be rolled up sheets of just a few layers of graphite that may have once covered the surface of the fiber. Taken as a whole, these images suggest the fastest growth of carbon nanowalls occurs on the hottest surface of the fibers – that which is facing or in contact with the heater. This deposition exists in competition with the etching process that is acting on the mat as a whole. So there is deposition advancing into the fiber

mat while the surface of the mat is receding in the same direction. Simultaneously the fibers on the top surface facing the plasma are also being etched away.

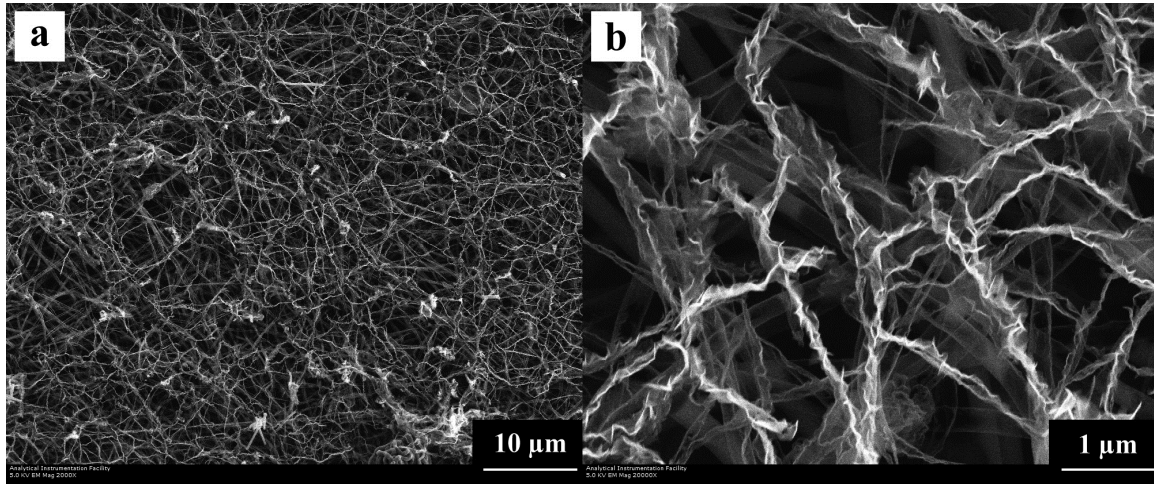


Figure 3.11 - Scanning electron micrograph at one location on fibers Sample 5 for the surface facing towards the heater and away from the plasma coil, displaying ribbons of carbon nanowalls in place of fibers magnified (a) 2,000x and (b) 10,000x

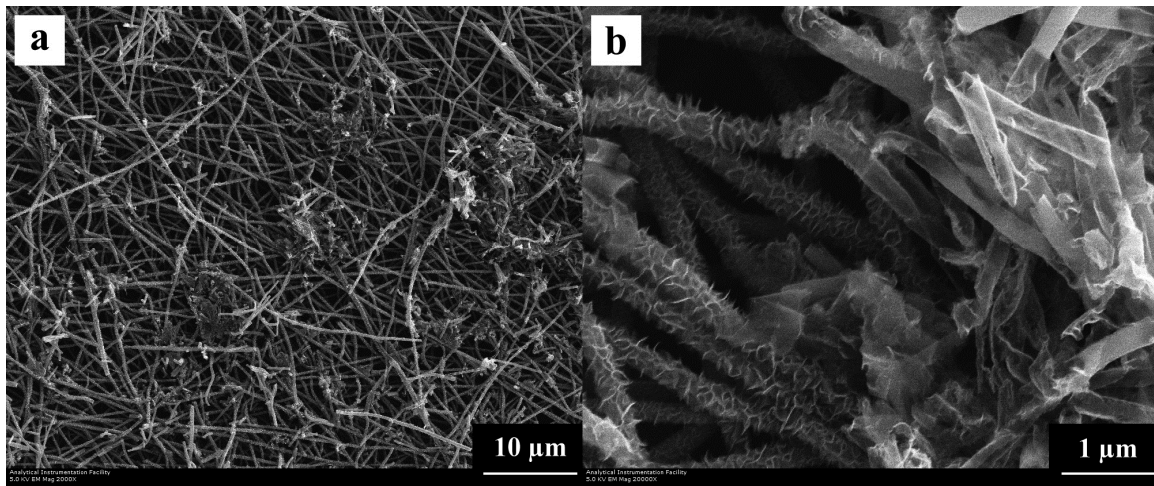


Figure 3.12 - Scanning electron micrograph at a different location on the surface of fibers from Sample 5, facing towards the heater and away from the plasma coil displaying carbon nanowalls on the fiber surface and possible single rolls of graphene which may have formed around the fibers magnified (a) 2,000x and (b) 10,000x

The significant mass and morphology change of the fibers was evident in the electrochemical behavior when electrodes were die-cut from the samples and assembled into coin cells. Given the significant mass loss during the PECVD processing, it was theorized that the fibers may have become similar to carbons pyrolyzed at higher temperatures. As a test some additional reference material was carbonized at 700 and 1100 °C to allow comparison over a wide range of pyrolysis conditions. **Table 3.4** presents the mass of the all the reference samples used in this experiment both before and after pyrolysis. As would be expected, increasing pyrolysis temperature increases the mass loss as the non-carbon species are lost and the material becomes more graphitic.

Table 3.4 - Change in mass of the reference samples for CVD Experiment #3 during pyrolysis at the indicated temperature.

Pyrolysis Temp (°C)	Mass Before (mg)	Mass After (mg)	Percent Remaining
700	29.3	17.0	58.0%
900	66.3	34.5	52.0%
1100	43.5	18.6	42.8%

There were two functional cells from each experimental condition, and their discharge capacity as a function of cycle number is shown in **Figure 3.13**. At each step shown on the plot the current was doubled, until the final step where it returned to the initial 25 mA/g. The two different samples have slightly different reversible capacity, with the sample that lost more mass having a higher discharge capacity. The most interesting part of this graph is that all four cells showed very little capacity fade in the first five cycles.

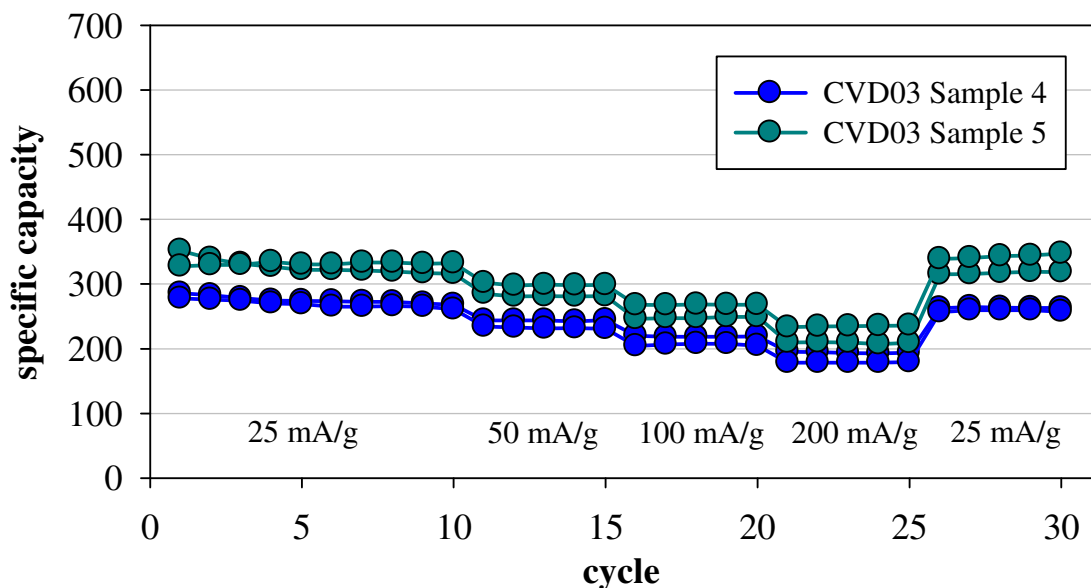


Figure 3.13 - Reversible discharge capacity of cells from CVD Experiment #3 at the indicated charge/discharge currents.

For comparison the reference cells pyrolyzed at 700, 900 and 1100 °C are presented in **Figure 3.14**, and significant capacity fade occurs during the initial cycles for the lower carbonization temperatures. This contrasts with the cells assembled from material pyrolyzed at 1100 °C which show almost no early-cycle capacity fade. For ease of comparison the PECVD samples are presented with the 1100 °C cells in **Figure 3.15** and all of these materials appear to be part of the same population despite the pyrolysis temperature of 900 °C for the cells subjected to the plasma deposition. Given the mass loss of the PECVD samples during plasma processing, and the thermal energy available during processing it is likely the samples became more ordered, as the 1100 °C pyrolysis sample is more ordered than the 900 and 700 °C samples.

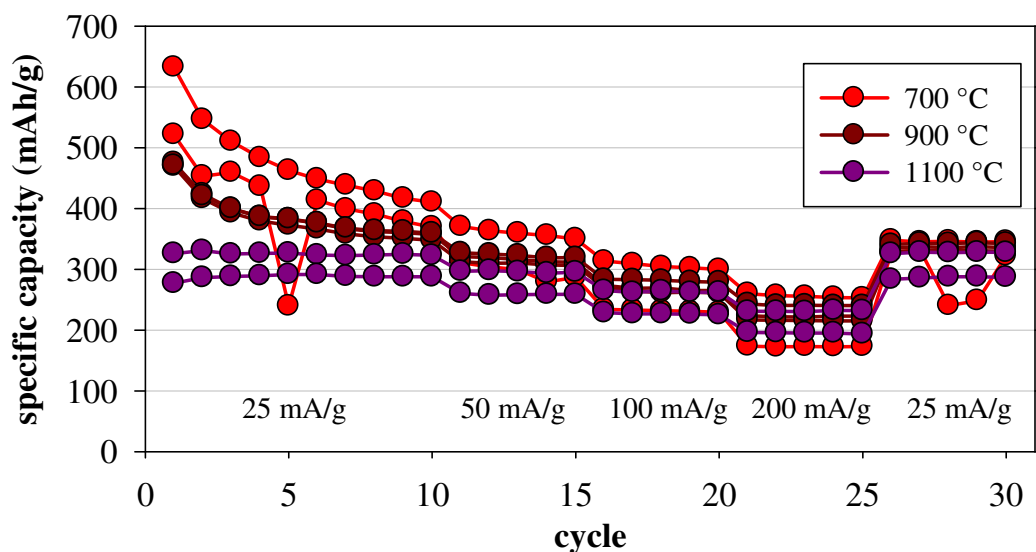


Figure 3.14 - Reversible discharge capacity of reference anodes made of fibers pyrolyzed at various temperatures and cycled at the indicated charge/discharge currents.

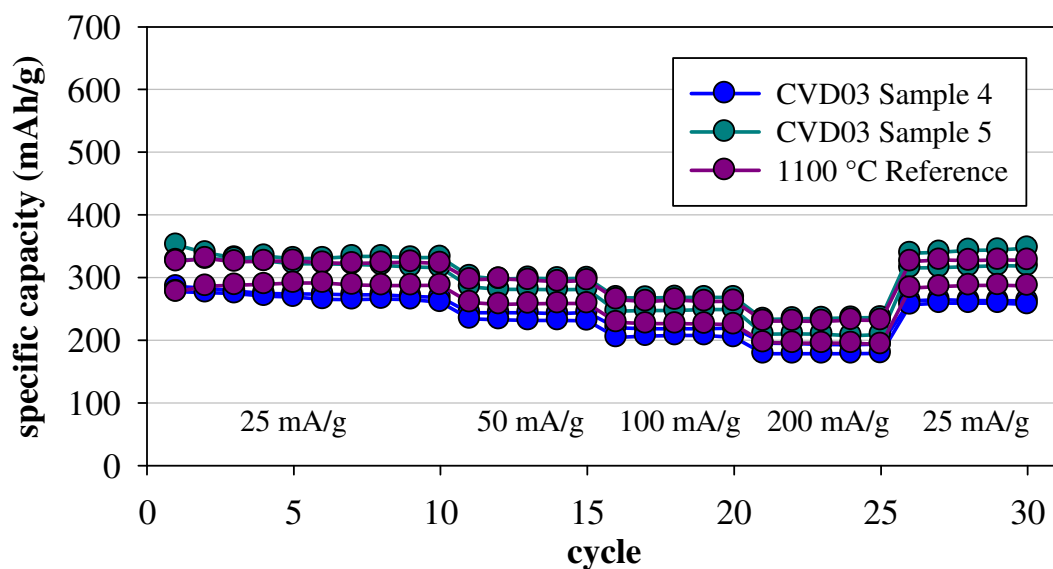


Figure 3.15 - Comparison of experimental cells with the reference cells made from fibers pyrolyzed at 1100 °C at the indicated charge/discharge currents.

If the reduction of disorder in the sample is changing the surface morphology, the first-cycle irreversible capacity losses should be reduced, similar to the reductions seen for many non-graphitic carbons. The PECVD samples showed only marginal average improvement over the 900 °C reference (**Figure 3.16**), while the 1100 °C reference is noticeably lower than all the other data points. Thus any potential order created within the fiber structure has not dramatically improved the surface reactivity with respect to the irreversible loss of Li.

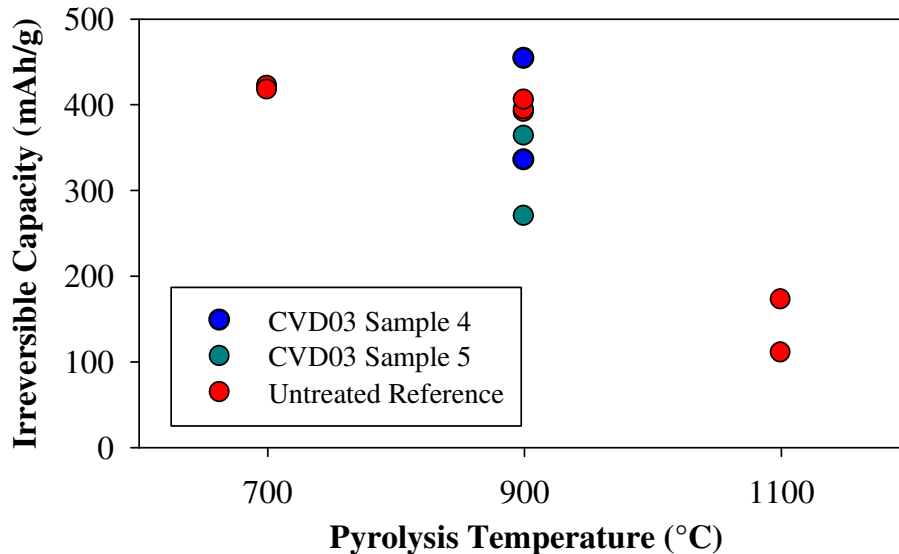


Figure 3.16 - Comparison of the first-cycle irreversible capacity losses of the cells made for CVD Experiment #3.

3.3.3 CVD Experiment #4 – Given the dramatic mass loss seen during the last set of experiments an attempt was made to reverse with reduced substrate heating (730 °C), reduced plasma power (800 W vs. 1200 W), and a feed gas with lower hydrogen content (1:1 vs. 1:2). Compared with the up to 60% mass loss in the hot, hydrogen rich plasma much

more mass remained, shown in **Table 3.5**, especially samples processed at only 800 W (7 and 9). The impact of the hydrogen reduction (samples 8 and 9) was a greater reduction in mass. It may have been better to increase the CH₄ pressure to equalize the ratio, rather than reducing the chamber pressure by cutting the H₂ pressure in half. Time and resource constraints prevented further experimentation with the feed gas ratios.

Table 3.5 – Change in mass of samples treated in CVD Experiment #4.

Sample	Plasma Power (W)	H₂:CH₄ ratio	Mass Before (mg)	Mass After (mg)	Percent Remaining
6	1200	2:1	45.0	28.8	64.0%
7	800	2:1	37.2	29.0	78.0%
8	1200	1:1	31.2	19.3	61.9%
9	800	1:1	25.4	18.6	73.2%

The loss of mass is evident when comparing the fibers near the surface of the PECVD processed non-woven mats to the unprocessed reference samples. The diameter of the fibers again decreases and the overall roughness of these samples increases. The reference fiber diameters for this work had a larger overall diameter than the fibers from CVD Experiment #3, with diameters ranging between 350 and 625 nm. **Table 3.6** contains the breakdown by processing conditions for fibers on the surface facing the plasma. Additionally some typical SEM results are provided in **Figures 3.17 to 3.20** for the reference material and samples 6, 7, and 8.

Table 3.6 – Fiber diameters of the samples of CVD Experiment #4 measured by SEM for the surface facing the plasma coils

Sample	Average Fiber Diameter (nm)	Fiber Diameter Range (nm)
untreated reference	444	349 to 630
6	170	97 to 312
7	187	89 to 330
8	216	120 to 328
9	232	86 to 385

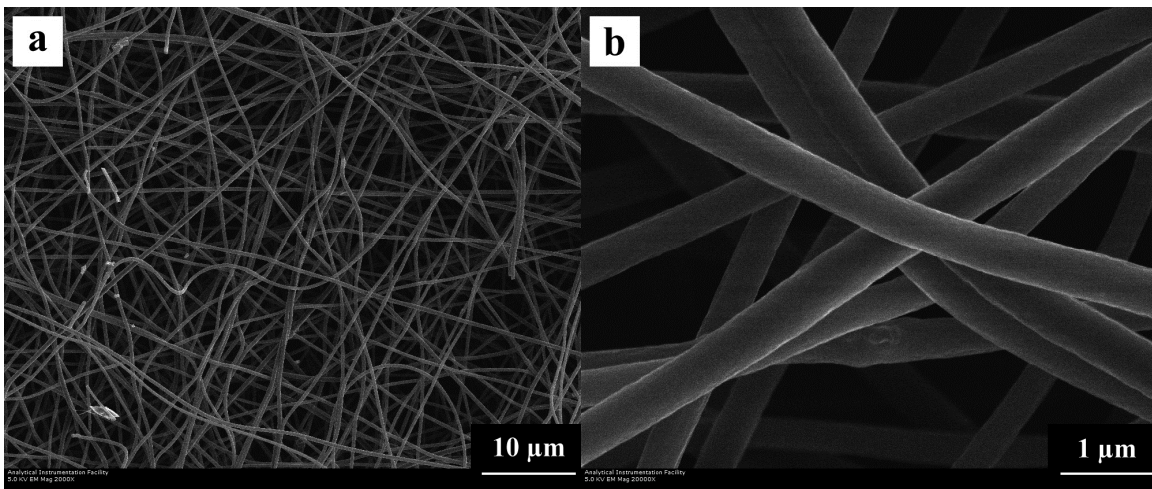


Figure 3.17 – Scanning electron micrograph of untreated nanofibers used as a reference in CVD Experiment #4 magnified (a) 2,000x and (b) 10,000x.

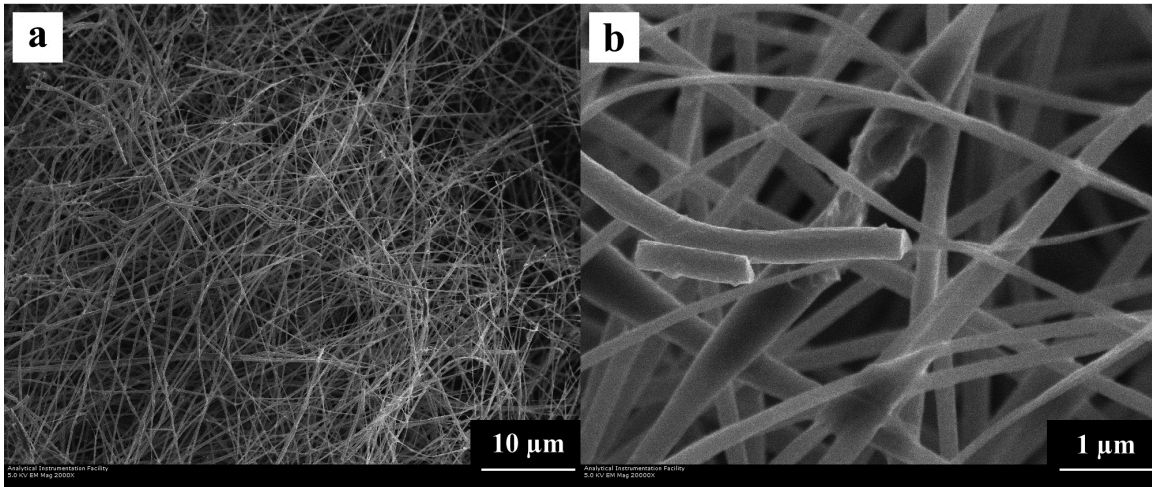


Figure 3.18 – Scanning electron micrograph of Sample 6 from CVD Experiment #4 on the surface facing towards the plasma coil and away from the heater magnified (a) 2,000x and (b) 10,000x.

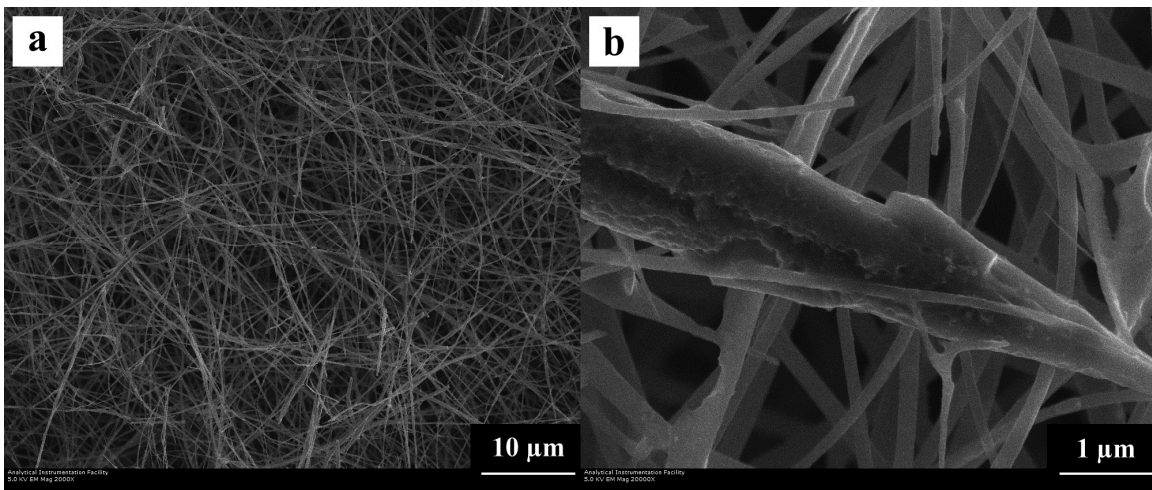


Figure 3.19 – Scanning electron micrograph of Sample 7 from CVD Experiment #4 on the surface facing towards the plasma coil and away from the heater magnified (a) 2,000x and (b) 10,000x.

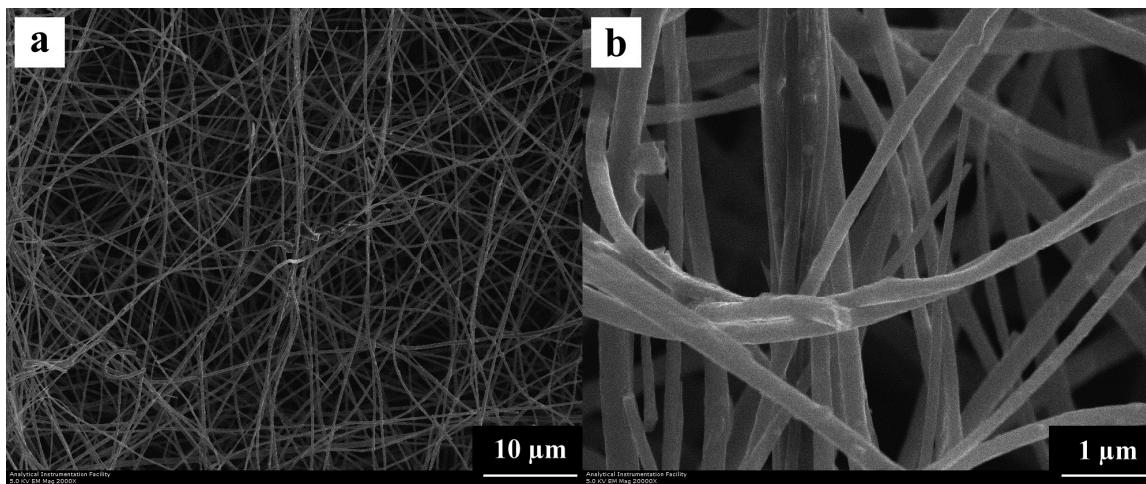


Figure 3.20 – Scanning electron micrograph of Sample 8 from CVD Experiment #4 on the surface facing towards the plasma coil and away from the heater magnified (a) 2,000x and (b) 10,000x.

Just as the previous experiment, the most interesting images came from a part of the sample that was in closest proximity to the heating element. During processing a region of Sample 3 may have been slightly bent under the rest of the sample and in direct contact with the heater. The structures observed in this area (**Figure 3.21**) are similar to the “graphene ribbons” seen in the previous experiment, but most resemble to the carbon nanowalls grown on glassy carbon and studied for fuel cell applications³⁷⁰.

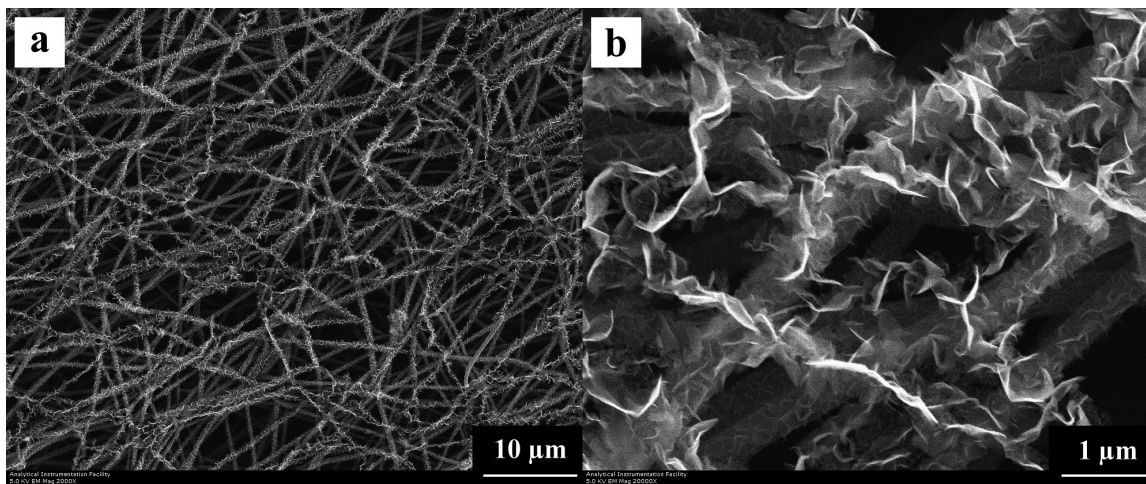


Figure 3.21 - Scanning electron micrograph of Sample 8, where the surface facing towards the heater, displaying fibers with carbon nanowalls taking the place of the fibers, magnified (a) 2,000x and (b) 10,000x.

In this area material was clearly added to the fiber structure, as seen in fibers deeper in the mat, again with concurrent consumption of the fiber resulting in potentially freestanding carbon nanowalls fully replacing the fibers nearest the surface. This region of the mat was thin enough to be seen through, rather than opaque like the rest of the samples. So in this region the rate of material consumption was very high, and eventually would consume the deposited material, but it also seems to be the only area with confirmed carbon deposition.

Electrochemically these samples were similar to the work of Experiment #3. The cells created from Sample 2 malfunctioned and are not included in the data below. Generally, typical anodes showed equivalent or slightly worse reversible discharge capacity than the reference electrodes over 15 cycles shown in **Figure 3.22**. The first-cycle irreversible capacity was also not noticeably improved by these plasma treatments and is

presented in **Figure 3.23**. Half of the plasma treated electrodes had lower irreversible losses than the reference mean, but no two electrodes from the same sample were better than the reference mean.

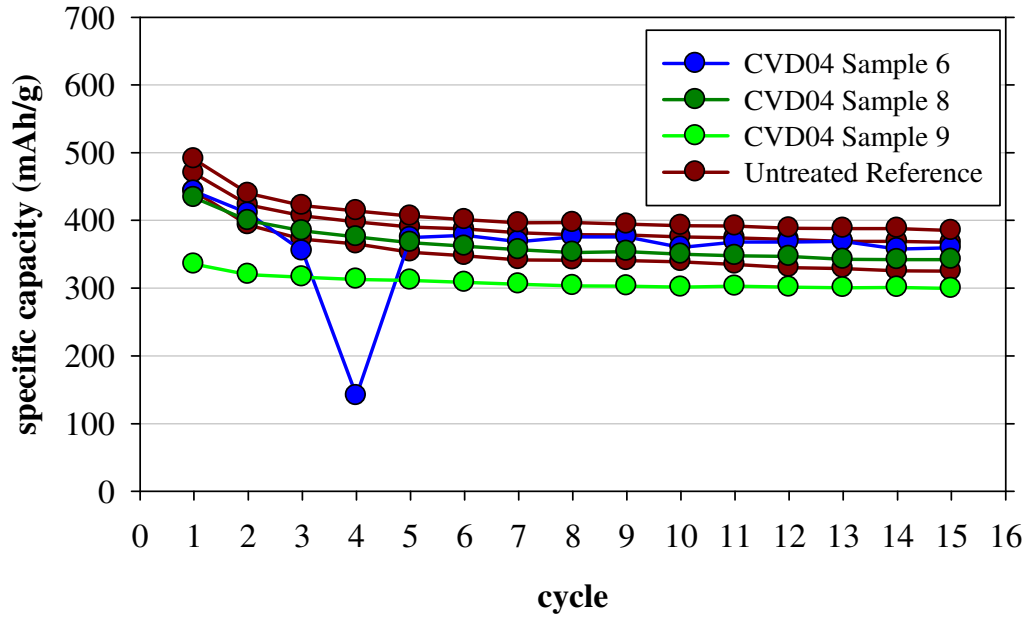


Figure 3.22 – Reversible discharge capacity of cells from CVD Experiment #4 cycled at 25 mA/g.

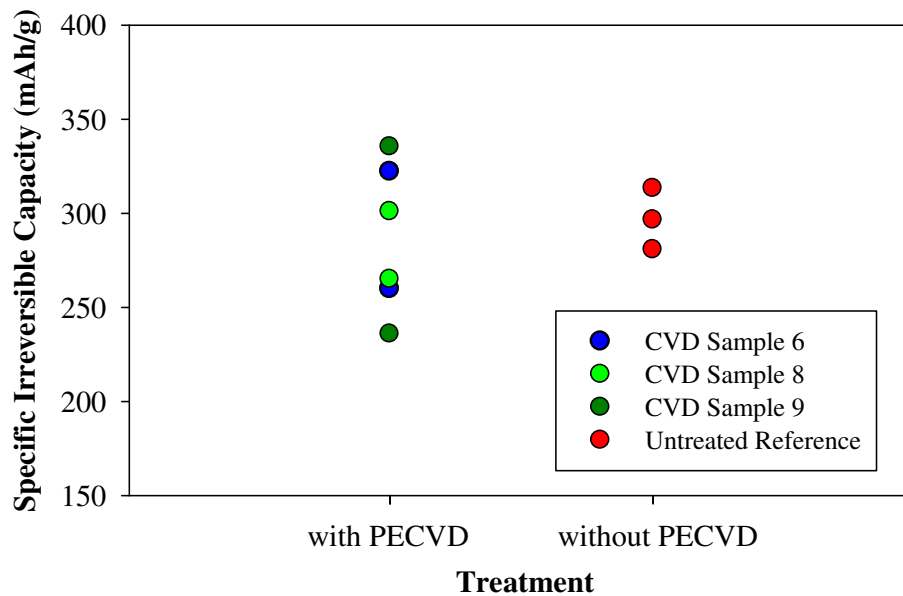


Figure 3.23 – Comparison of the first-cycle irreversible capacity losses of the cells made for CVD Experiment #4.

3.3.4 *Micro Raman Spectroscopy*

Raman spectroscopy was used to investigate if any structural changes could be identified as a result of the plasma processing in Experiments #3 and #4. The features utilized are the locations and intensity ratio of the graphitic (G) and disordered (D) peaks (Figure 3.24).

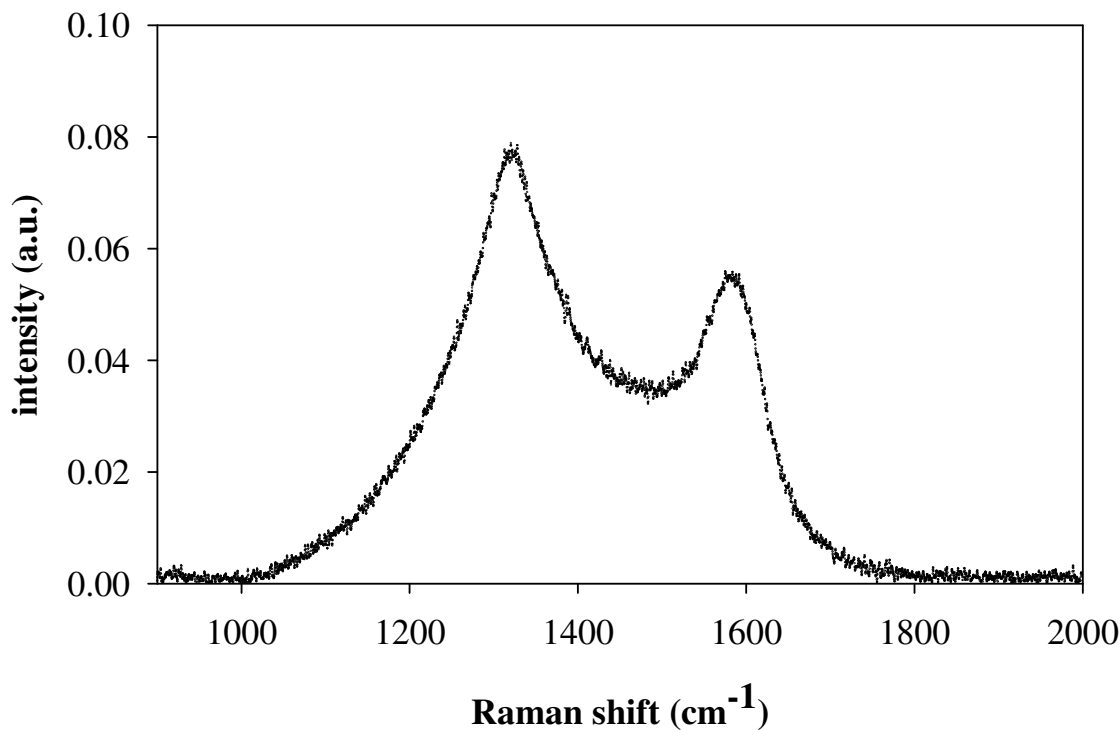


Figure 3.24 – Raman spectra collected from a PAN nanofibers pyrolyzed at 700 °C containing the dominant features of nano-crystalline carbon: a broad D peak located at 1320 cm^{-1} and a broad G peak located at 1582 cm^{-1} .

The intensity ratio of the peaks is used to estimate the graphite crystallite sizes within the fibers with **Equation 9** provided earlier. The location of the G peak and the intensity ratio can be used to estimate degree of amorphization of the samples³³⁶. **Table 3.7** presents the relevant parameters for all samples from Experiments #3 and #4.

Table 3.7 – Raman parameters for the G and D peaks for Experiments #3 and #4, the estimated basal plane crystallite size and estimated sp³ carbon content based on reference 331.

Sample	D Peak Location (cm ⁻¹)	G Peak Location (cm ⁻¹)	(I _D /I _G)	L _a (nm)	Estimated sp ³ content ³³⁶
700 °C Ref	1318.5	1582.0	1.424	27.0	<5%
900 °C Ref	1324.5	1583.2	1.344	28.6	<5%
1100 °C Ref	1325.6	1582.6	1.234	31.2	~0%
4	1317.6	1583.5	1.266	30.4	<2.5%
5	1316.2	1584.0	1.564	24.6	<5%
900 °C Ref	1340.3	1579.4	1.259	30.6	~5%
6	1323.4	1579.9	1.361	28.3	~5%
7	1327.5	1578.0	1.296	29.7	~5%
8	1328.4	1579.5	1.400	27.5	~5%
9	1335.6	1575.9	1.406	27.4	~5%

As would be expected, the reference samples for Experiment 3 show increasing internal order as the pyrolysis temperature is increased with both the estimated crystallite size increasing (decreasing I_D/I_G ratio) and the elimination of the sp³ carbon content. Based on the above data, samples 4 and 5 could be considered to have approximately the same disorder as the 900 °C reference. The cells using samples 4 and 5 had very similar discharge capacity to the 1100 °C reference but irreversible capacity similar to the 900 °C reference. This might be explained by the potential sp³ bonding, representing similar disorder to the 900 °C reference even after plasma treatment based on the movement of the G peak further from the perfectly graphitic location of 1582 cm⁻¹.

The samples from Experiment 4, and the reference, all indicate more sp³ bonding than the previous samples because of the low I_D/I_G ratios (below 1.5) and the graphitic peak shifting to values below the nominal 1582 cm⁻¹. The plasma treatment has reduced the

estimated crystallite size for all 4 samples, and those processed with a lower H₂:CH₄ ratio have changed more, which could correlate to the increased mass loss for these samples relative to the H₂ rich plasma samples.

3.4 Conclusions

The types of carbon deposited by the PECVD conditions utilized were not the kind of graphitic coating that was the objective. This is primarily attributed to the difficulty of creating graphitic carbon at temperatures below the optimal conditions for graphitic pyrocarbon formation. The inclusion of plasma processing to increase the reactivity of the precursor gasses with the substrate both produced the growth of highly graphitic nanowalls, but also resulted in the net loss of material due to etching. Without hydrogen in the gas mixture, a fluffy and amorphous carbon material was found throughout the samples. When hydrogen was added and processing proceeded at low temperature, pressure, and plasma power, no morphology changes in the material were evident. Attempts to generate significant deposition rates by increased temperature, plasma power, and source gas pressure resulted in a net loss of material, with clear reductions in the fiber diameter for the surface of the samples facing the plasma. The use of micro Raman spectroscopy suggests that the net effect of the plasma processing was to slightly increase the overall disorder of the carbon substrate. In select areas on the side of the sample facing away from the plasma and in intimate contact with the heating element, the processing conditions produced carbon deposition of graphene-like ribbons or nanowalls. This deposition existed in competition with the plasma etch that was consuming the fibers serving as the substrate. This

competition leads to an advancing deposition front with destruction of the deposited material once the fiber substrate was eliminated.

None of the experiments reported here had a noticeable impact on the first-cycle irreversible capacity losses attributed to SEI formation during the first charge of the non-woven nanofiber electrodes. Generally, the plasma treated samples had subtly reduced reversible discharge capacities when compared to the reference samples subjected to the same pyrolysis conditions. The most aggressive plasma treatment resulted in fibers with a reduced capacity fade during the initial cycling, similar to references from a higher pyrolysis temperature, but without any of the benefit to irreversible capacity losses seen with increase heat treatment of hard carbons.

Chapter 4

Atomic Layer Deposition of Alumina onto Lithium-ion Carbon Nanofiber Electrodes

4.1 Introduction

Lithium-ion batteries are the power supply of choice for mobile computing and communications¹. Most commercial Li-ion cells are comprised of a graphitic anode and a lithiated metal oxide cathode, and have been since the initial commercialization by Sony³⁶⁵. But developments in mobile communications and computing technology and the needs of modern consumers are driving the need for safer batteries with larger energy densities and higher power ratings⁵⁰.

To meet these needs some research efforts have focused on creating nanoscale materials, with the intention of increasing the reactive surface for electron transfer, decreasing the diffusion paths for Li-ions, and limiting the scope of mechanical deformation^{99, 109}. An alternative to nano-particulate based composite electrodes are composites made of continuous one-dimensional structures²⁴. A facile method to create one-dimensional non-woven nanofiber webs is electrospinning^{193, 199, 203}. In a laboratory setup the process only requires a stable flow of polymer solution through a needle, a high voltage supply, and a grounded collector to capture the resulting fibers.

When the fibers are made of pyrolyzable polymers it is possible to treat the electrospun materials thermally and make non-graphitic carbon anodes that require no binder materials or conductive additives³⁷¹⁻³⁷³. Further, composites of nanoparticles and nanofibers can be made using electrospinning. Techniques exist to create nanoparticles embedded in the fibers via *ex situ*²¹⁴ and *in situ*^{216, 219} methods. Some researchers have taken this path to create composite anodes of nanoparticles of lithium-storing metals or metal oxides embedded in a continuous one-dimensional nanofiber web^{22, 24}. Some of these materials show stable

specific reversible capacities over 600 mAh/g, well above the known limits of graphitic based anodes²⁴.

There are, however, some impediments to using the electrospun nano-composites in a commercial Li-ion cell. One of particular concern is the irreversible losses of lithium due to the formation of the solid electrolyte interphase (SEI) layer at the anode/electrolyte interface during the first charge of the battery^{160, 162}. The SEI is composed of the decomposition products from the reduction of the electrolyte and solvents by lithium present after charge transfer at the anode surface¹⁶⁰. The Li participating in those reactions is irreversibly lost and is an important consideration in the material balance for commercial cells³⁶⁸. When accounting for SEI formation, the large surface area of electrospun nanofibers, which facilitates rapid Li transfer, will irreversibly consume more Li per unit electrode mass than traditional micron-scale materials^{166, 174}. Nevertheless, the creation of a stable SEI which permits the diffusion of Li⁺ is necessary to a functional Li-ion cell¹⁵⁹.

The literature describes efforts to alter the SEI or stabilize electrodes by changing the electrode surface or using additives in the electrolyte^{159, 176, 184}. One recent vein of research has been the use of atomic layer deposition (ALD) to place aluminum oxide on the active surface prior to battery assembly³⁷⁴. The use of ALD is favored because the method uses self-limiting reactions to create a highly conformal surface coating of well-controlled thickness at processing temperatures low enough to avoid altering the substrate³⁴¹. These aluminum oxide films have produced improved stability in both graphitic anodes³² and metal oxide cathodes³⁰. Furthermore, fibers have been coated using atomic layer deposition for a variety of applications^{28, 349, 375}.

For this work we hypothesized atomic layer deposition would be the best method to create a thin uniform layer of alumina on the high-surface area of carbonized nanofibers and reduce the amount of lithium lost to the formation of the SEI layer. A combination of electron microscopy, X-ray spectroscopy, and mass spectrometry was used to characterize the physical and chemical structure of the resulting fibers. The impact of processing temperature was considered since temperature can affect the porosity and stoichiometry of the resulting alumina films. The alumina coating is electronically insulating and a potential barrier to Li^+ diffusion, therefore, the performance of the anode materials was studied at various currents to assess the impact of the ALD coating on rate capability.

4.2 Materials and Methods

The precursor polymer nanofibers were made of polyacrylonitrile (PAN) (Sigma Aldrich MW 150,000). The PAN was weighed and dissolved in anhydrous dimethylformamide (Sigma Aldrich) to make a solution of 11 weight%. The mixture was heated to 40 °C and stirred for 24 hours to dissolve the polymer, and the final solution was sealed and stored at room temperature.

For electrospinning the PAN solution was pumped from a syringe pump at 1 mL/h through a 22-gauge stainless-steel needle. The electrospinning setup was arranged horizontally. The collector was a flat metallic circular disk of 30-cm diameter covered in aluminum foil. The distance from the tip of the needle to the collector plate was 15 cm. The electric field was varied between 0.75 and 1 kV/cm, as needed, to maintain a stable Taylor cone. Electrospinning for approximately 3 hours produced a non-woven mat of about 15-cm diameter and a total mass of around 0.3 g. Swatches were cut from the central portion of

the mat and measured approximately 3-cm wide by 12-cm length. These samples were removed from the aluminum foil prior to thermal treatment.

The carbonization process of PAN proceeds in two steps²²⁷. The stabilization step was conducted under a flow of dry air (National Welders) at 250 °C with a 5 °C/min ramp rate from room temperature and a soak of 2 hours at 250 °C followed by uncontrolled cooling to ambient conditions. The carbonization step was done under a flow of high-purity nitrogen (National Welders) at 700 °C with a 5 °C/min ramp rate from room temperature and a soak of 2 hours at 700 °C followed by uncontrolled cooling to ambient conditions. The carbonization was conducted in a single zone Lindberg Blue tube furnace (model 55322-3) within a 45-mm inner diameter quartz tube. Swatches were loaded onto flat quartz shelves and the processing gasses flowed over them rather than through the mat.

All alumina atomic layer deposition was conducted in a reactor previously described with samples arranged so the processing gases flowed over the samples³⁷⁵. The aluminum precursor was trimethylaluminum (TMA, $\text{Al}(\text{CH}_3)_3$, Strem) and the oxidant was deionized water (H_2O). The ALD process is a repetition of binary self-limiting A/B reaction cycles. The TMA adsorbs and reacts with surface hydroxyl groups (reaction A) to create aluminum-methyl species bound to the oxygen, with methane as a byproduct that is carried away. After the reactor is purged of residual TMA and methane, the water oxidant is introduced. Water reacts with the Al-methyl groups producing a monolayer of Al_2O_3 (reaction B) terminated by hydroxyl groups. Again the byproduct of the reaction is methane, and it and residual water are purged from the reactor to complete one cycle. High-purity argon served as both the purge gas and the carrier for the ALD precursors. The samples were subjected to either six,

ten, or twenty full A/B cycles at processing temperatures of 45, 90, and 150 °C, with an untreated sample serving as reference. Each purge cycle was 60 seconds. Precursors were pulsed for 5 seconds followed by a 60 second soak time to ensure complete penetration throughout the non-woven mat. All processing was conducted at a pressure of 2 torr maintained by a rotary mechanical pump and monitored by a Baratron pressure gauge (MKS Instruments Inc.). For reference a square silicon wafer piece (1 cm by 1 cm) was placed in the reactor during processing and the thickness of alumina deposited upon it was measured using an Alpha-SE spectroscopic ellipsometer (J.A. Woollam) at an angle of incidence $\Phi = 70^\circ$ and a wavelength range of 380–900 nm.

The morphology and composition the final samples were analyzed in three ways. Fiber size and mat structure pre- and post-carbonization was imaged by scanning electron microscopy at 5 kV using a secondary electron detector (JEOL 6400). A relative comparison of the atomic composition of the fibers, not calibrated against a standard, was conducted via energy dispersive X-ray spectroscopy (EDX) at an accelerating voltage of 10 kV (Hitachi S3200). Absolute aluminum content was determined using inductively coupled plasma mass spectrometry (ICP-MS) with samples digested by ashing. Approximately 0.03 g of sample dried overnight at 500 °C was weighed to an accuracy of $\pm 10 \mu\text{g}$. Each sample was placed in approximately 2 mL of deionized H₂O and 4 mL of 6 N HCL and heated for 45 minutes at 95 °C. Samples were finally filtered through a #41 Whatman paper filter prior to introduction to the ICP-MS.

For electrochemical testing, 1.3-cm circular disks were die-cut from each swatch to be used as anodes. The samples were dried overnight in a vacuum oven at 80 °C prior to

introduction to a high-purity argon filled glove box (Labconco Protector) for coin-cell assembly. Each anode had a mass of approximately 3 mg fiber. A similarly sized copper disc was used at the current collector with contact maintained by the mechanical force of a disc spring. The counter electrode was lithium metal (Sigma Aldrich) and the separator was polypropylene (Celgard). The electrolyte was 1M LiPF₆ in a 1:1 (w:w) solvent mixture of ethylene carbonate (EC) and ethylmethylcarbonate (EMC). All electrochemical data was collected in galvanostatic mode with an Arbin Instruments (BT-2000) battery tester. Cells were cycled at currents of 25, 50, 100, and 200 mA/g. The cut-off voltages used were 25 mV on charge and 2.5 V on discharge.

4.3 Results and Discussion

4.3.1 Fiber Morphology and Composition – The two scanning electron micrographs shown in **Figure 4.1** are typical representations of the fibers used in this work. Prior to carbonization the fibers' diameters ranged between 350 and 550-nm. After carbonization the fibers' diameters had decreased to between 300 and 450-nm. The carbonization process does not create noticeable damage to the non-woven structure or to most individual fibers (**Figure 4.1b**).

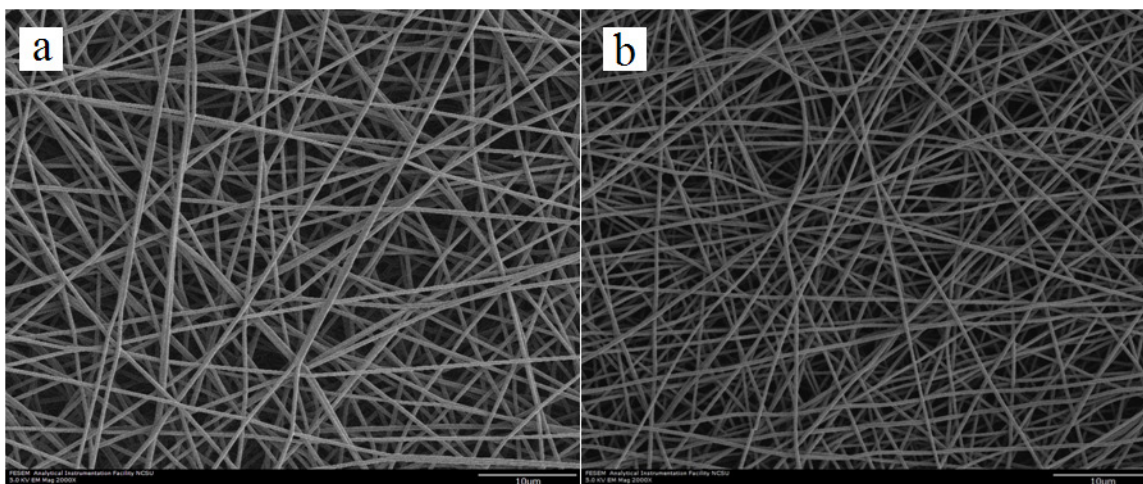


Figure 4.1 – Scanning electron micrographs of nanofibers used for atomic layer deposition as electrospun, (a) and after pyrolysis at 700 °C, (b).

A comparison of the relative atomic composition as measured by EDX of the samples is provided in **Table 4.1**. It is important to note that a calibration standard was not used so the results should be viewed as a relative comparison. As expected the samples subjected to twenty ALD cycles have approximately twice the relative aluminum content when compared to the ten ALD samples. **Table 4.1** also contains the results for the absolute aluminum weight fraction as measured by ICP-MS of samples processed at 90 °C. As expected the sample processed for 20 ALD cycles contains approximately twice the aluminum as one processed for 10 cycles. The ellipsometry results from the silicon reference chips are additional data provided in **Table 4.1**. Of note is the effect of the soak step on the material deposition at 45 °C. There is a significantly higher growth rate of alumina on the silicon reference chips observed at this lowest processing temperature which is attributed to incomplete desorption of adsorbed precursor after the chemical surface reaction has

completed. With the soak step not used in the low temperature process, the amount of alumina deposited at 45 °C became consistent with the other trials.

Table 4.1 – Relative elemental composition by EDX of samples to nearest 0.5%, absolute aluminum mass content as measured by ICP-MS, and thickness of alumina film on silicon measured by ellipsometry.

Sample	Element	Atomic %	Aluminum Wt%	Thickness (Å)
0 ALD	Carbon	98.0	N/A	N/A
	Aluminum	0.0		
	Oxygen	2.0		
90 °C 10 ALD	Carbon	95.0	1.4	24
	Aluminum	3.0		
	Oxygen	2.0		
90 °C 20 ALD	Carbon	90.0	2.9	44
	Aluminum	7.5		
	Oxygen	2.5		
45 °C 10 ALD	Carbon	90.5	7.1	42
	Aluminum	5.0		
	Oxygen	4.5		
45 °C 20 ALD	Carbon	86.0	5.5	72
	Aluminum	8.0		
	Oxygen	6.0		
45 °C 6 ALD (no soak)	Carbon	96.0	1.3	18
	Aluminum	2.0		
	Oxygen	2.0		
45 °C 10 ALD (no soak)	Carbon	94.0	0.9	14
	Aluminum	3.0		
	Oxygen	3.0		
150 °C 10 ALD	Carbon	94	1.6	18
	Aluminum	4.0		
	Oxygen	2.0		

Assessing the uniformity of the deposition throughout the non-woven mat was accomplished by manually separating a portion of the sample processed for 10 ALD cycles at 90 °C into four layers (**Figure 4.2**). Then the relative atomic breakdown of each section was

analyzed by EDX and is reported in **Table 4.2**. The aluminum content is consistent for the top three most layers, but very low for the lowest one. It is likely that this layer was thin enough that additional carbon signal was detected from the carbon tape used to affix the samples upon the SEM sample holder.

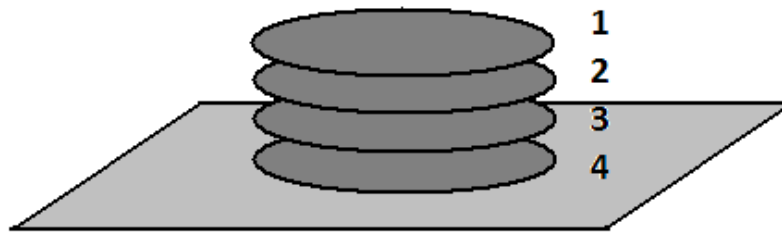


Figure 4.2 – Illustration of the layer-by-layer sectioning of the nanofiber mat used to assess the uniformity of the deposition alumina throughout the non-woven mat.

Table 4.2 – Relative layer-by-layer elemental composition measured by EDX of pyrolyzed fibers coated for 10 alumina ALD cycles at 90 °C from top (1) to bottom (4) as seen in Figure 4.2.

Layer	Element	Atomic %
1	Carbon	95
	Oxygen	2.5
	Aluminum	2.5
2	Carbon	94
	Oxygen	2.5
	Aluminum	3.5
3	Carbon	93.5
	Oxygen	3
	Aluminum	3.5
4	Carbon	95.5
	Oxygen	3.5
	Aluminum	1

4.3.2 *Electrochemical Performance* – The goal of this work was to reduce the irreversible losses of lithium to SEI formation. Results of the first-cycle irreversible capacity of the cells processed at 90 °C are provided in **Figure 4.3**. The data shows an average reduction of irreversible losses of 24% when comparing cells using mats treated with 10 ALD cycles to the uncoated control materials. For cells assembled from the sample processed for 20 ALD cycles the improvement in irreversible losses is an even better 42% relative to the control material.

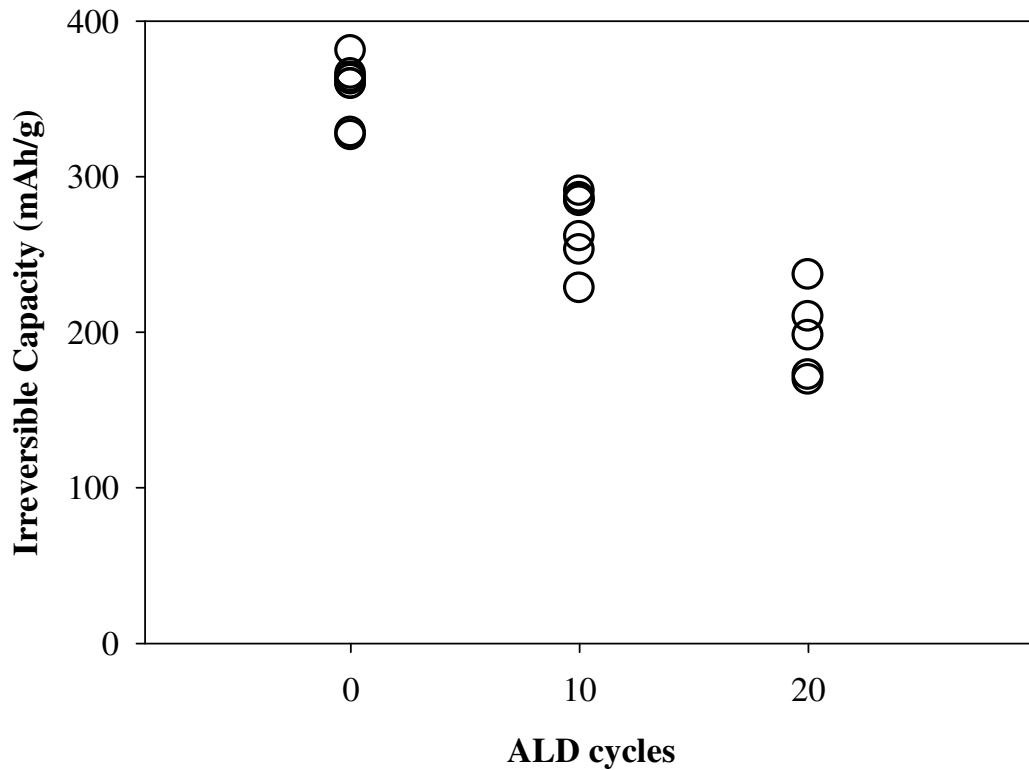


Figure 4.3 – First-cycle irreversible capacity loss of cells using carbon fibers coated with alumina at 90 °C compared to uncoated reference samples.

The deposition of aluminum oxide via ALD proceeds over a wide range of temperatures and additional samples were processed at lower (45 °C) and higher (150 °C) temperatures to investigate the impact of ALD processing temperature on the electrochemical performance. The irreversible capacity losses for these materials are shown in **Figure 4.4**. The cells made from materials processed for ten cycles at a lower temperature with a 60 second soak show a more modest improvement (10%) than the samples processed at 90 °C. Oddly, for 20 cycles of deposition at this low temperature no improvement in the irreversible losses is observed. With the soak step removed the first-cycle irreversible losses were reduced by 17%, but fewer alumina cycles resulted in no average benefit to irreversible capacity loss. Lastly anodes processed for ten cycles at 150 °C also show a 17% improvement in the irreversible losses. This data suggests that any coating which sufficiently covers the surface will show some reduction in irreversible losses, but going beyond that point is not necessarily better.

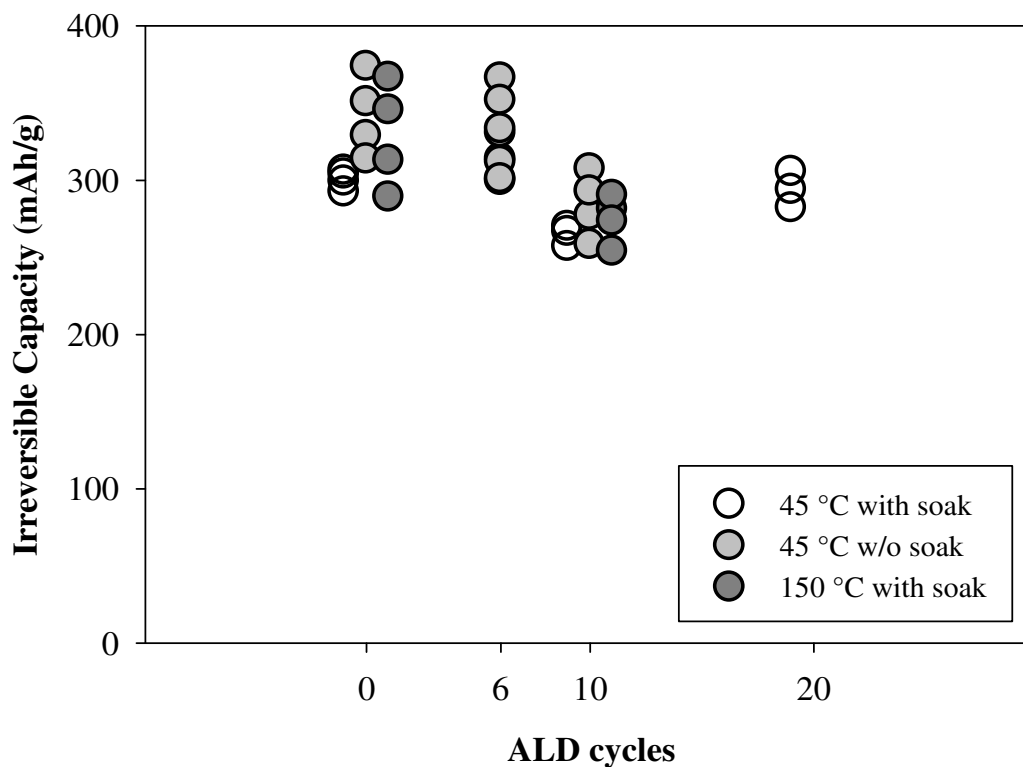


Figure 4.4 – First-cycle irreversible capacity loss of cells using carbon fibers coated with alumina by ALD at 45 °C, both with and without the 60 second soak, and at 150 °C, compared to untreated reference samples.

A comparison of typical charge and discharge curves for electrodes made of carbon fibers processed at 90 °C is provided in **Figure 4.5** and contains features common to hard-carbon materials. Formation of the SEI during the first charge of the untreated controls begins around 0.8 V (**Figure 4.5a**) and closer to 0.7 V for the cell from 10 ALD (**Figure 4.5b**) and the voltage plateau is less distinct. In subsequent cycles the reversible capacity of both cells decreases before stabilizing between cycle 15 and 20. The results from 20 ALD (**Figure 4.5c**) are quite different. No clear plateau representing SEI formation is seen, though the slope of the voltage decrease during the first charge is flatter when compared to

the second charge. Additionally, the reversible capacity of the material is significantly lower than that of the reference or cells made of fibers coated for 10 cycles. The capacity then increases with subsequent cycles before stabilizing around cycle number 5.

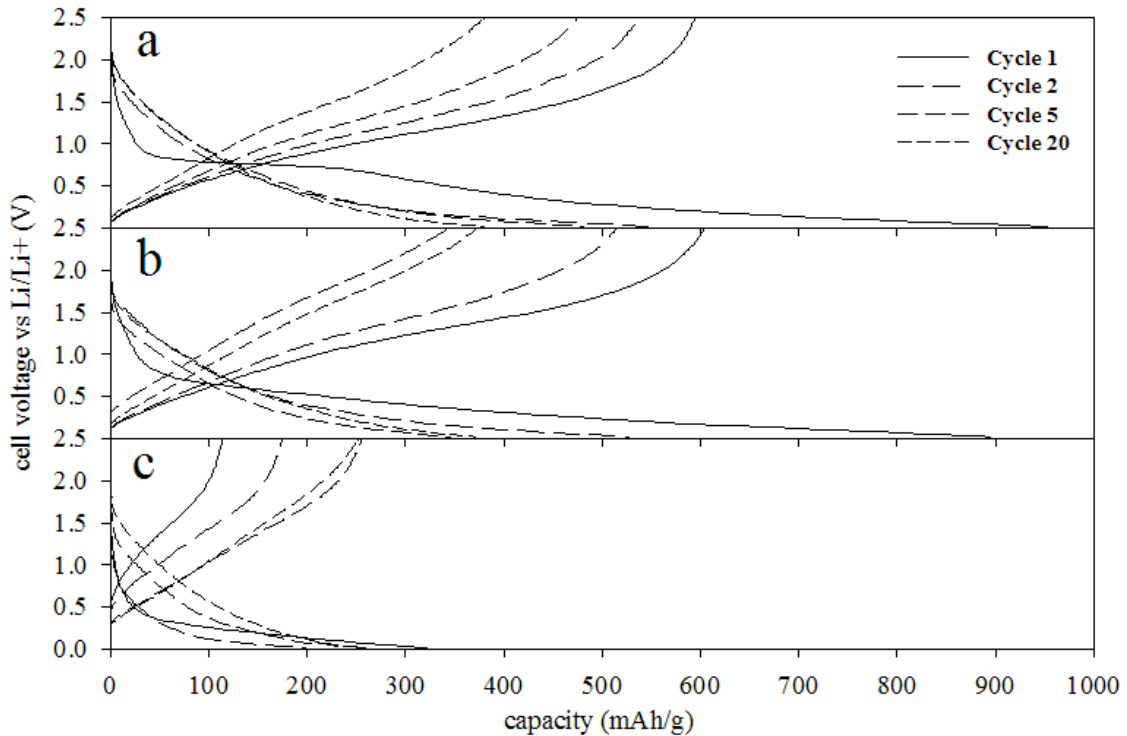


Figure 4.5 – Typical results for cell voltage as a function of capacity at 25 mA/g C/D current for (a) 0 ALD cycles, (b) 10 ALD cycles, (c) 20 ALD cycles.

The data presented in **Figure 4.6** better illustrates the reversible capacity of the materials under study. At low charge and discharge currents, cells coated for 10 cycles have stable reversible specific capacities of just under 400 mAh/g, very similar to the uncoated materials, and greater than the theoretical maximum of graphite. At higher currents the coating on the cell begins to affect the reversible capacity, leaving only 35% capacity

retention at a charge and discharge rate of 200 mA/g compared to 43% retention for the uncoated reference material. Upon returning to the lowest charge and discharge rates the materials recover to the same specific capacities observed at cycle number 20.

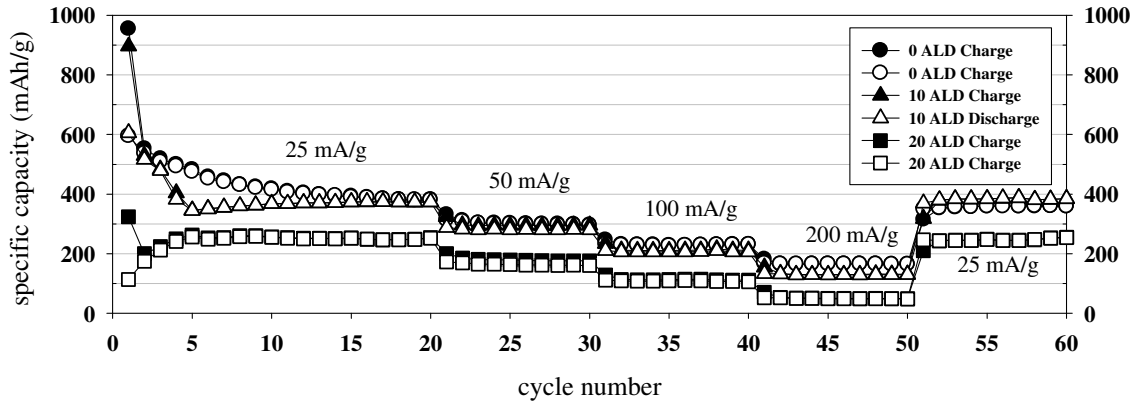


Figure 4.6 – Typical charge and discharge capacities for electrodes coated by ALD at 90 °C over 60 cell cycles with symmetric charge and discharge currents as indicated on the figure.

While the amount of alumina present on electrodes processed for 20 ALD cycles significantly reduces the irreversible capacity losses, the cell performance in **Figure 4.6** shows that this quantity of alumina has a significant detrimental impact on the reversible capacity of the electrode. The cell exhibits only 66% of the reversible capacity of the uncoated materials. Additionally, at all currents the thicker 20 ALD cycle coating results in cells possessing worse capacity retention than both the uncoated reference and 10 ALD cycle material, with only 21% of the cell capacity available at 200 mA/g.

When considering the deposition of alumina at 45 °C, a similar picture emerges. The additional insulating material deposited when the soak was used at low temperatures has a clear negative impact (**Figure 4.7**) on the both the initial capacity and capacity retention of

these electrodes. Only 17% of the reversible capacity remains at a current of 200 mA/g for the sample made from fibers coated for 10 cycles, and virtually none remains for the cells made from the thicker 20 cycle sample. When the soak step was not used the capacity retention for electrodes made from fibers processed for 10 ALD cycles improves to 44% at 200 mA/g (**Figure 4.8**). A coating of only 6 ALD cycles delivers no significant change in performance here, just as it showed no impact on irreversible losses. The reduced capacity retention, regardless of alumina thickness, might be improved if these materials were fabricated in a manner that did not place an insulating layer between the active material and the current collector. The arrangement of a coating upon an already fabricated electrode rather than upon the constituent particles has been superior when applied to more conventional anodes and cathodes ³¹.

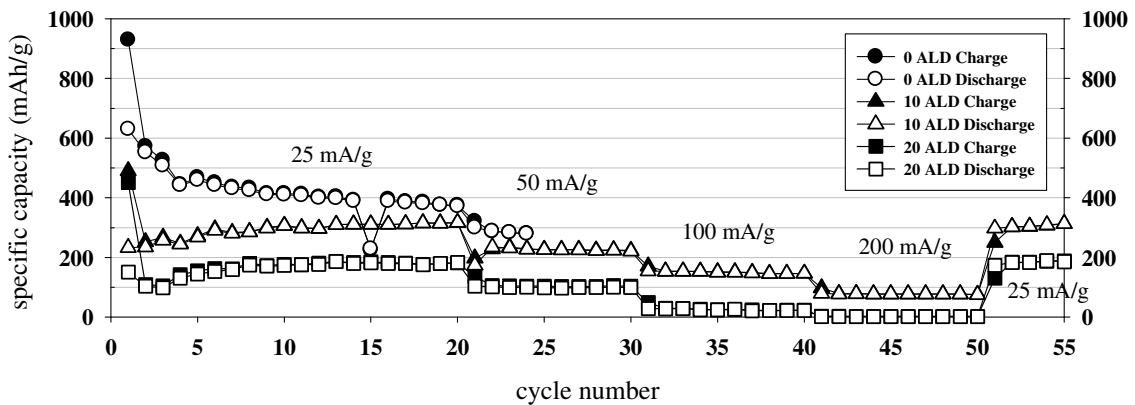


Figure 4.7 – Typical charge and discharge capacities for electrodes coated by ALD- at 45 °C with a soak step during the ALD process. The charge and discharge currents indicated on the figure were symmetric. The 0 ALD reference cell was deliberately stopped after cycle 24 to free up test equipment for other experiments.

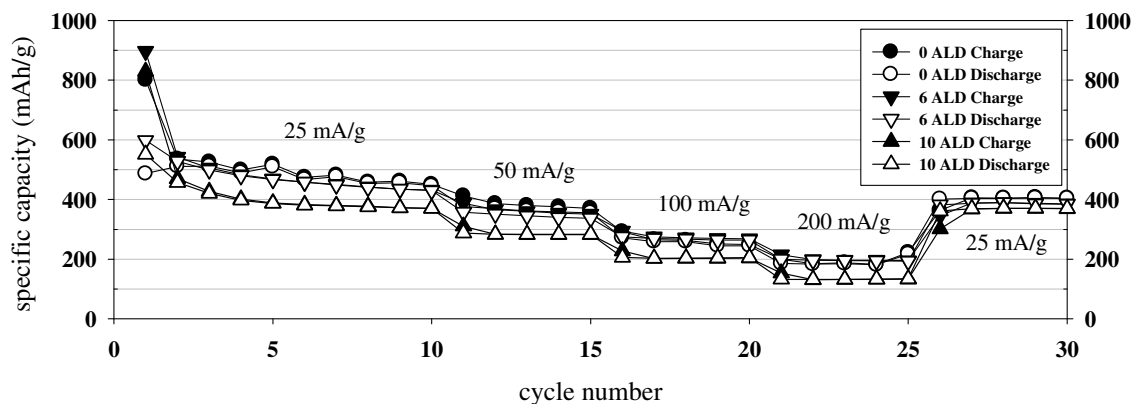


Figure 4.8 – Typical charge and discharge capacities for electrodes coated by ALD at 45 °C without a soak step during the ALD process. The charge and discharge currents indicated on the figure were symmetric.

Samples prepared at the highest ALD processing temperature showed superior capacity retention than all other processing conditions. A typical cell, as seen in **Figure 4.9**, shows capacity retention of 61% at the highest current, and this performance is virtually identical to a typical reference cell. It should be noted that the reference cell used here also shows superior capacity retention to all previous reference materials. While all samples in this study were electrospun and carbonized in a similar manner, day-to-day process variation is clearly evident in the electrochemical data. For that reason each experimental treatment required its own untreated carbon nanofibers reference sample, each labeled as 0 ALD in the preceding graphs.

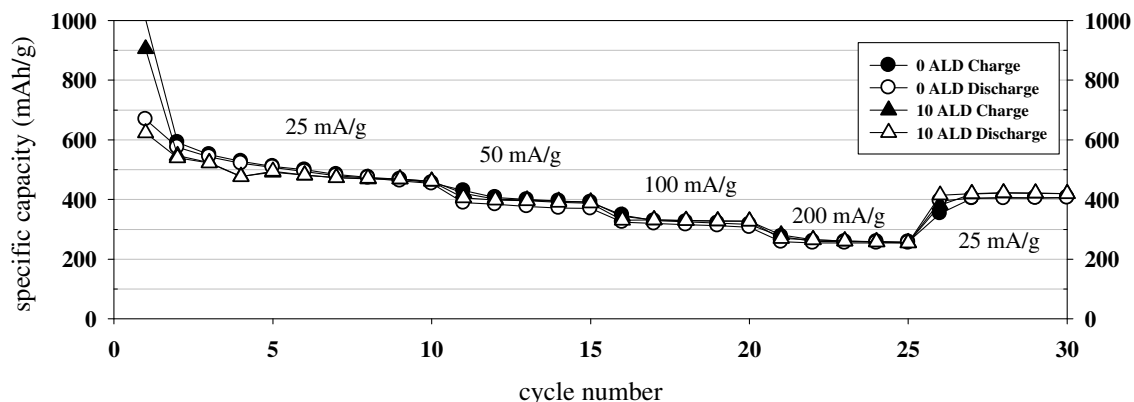


Figure 4.9 – Typical charge and discharge capacities for electrodes coated by ALD at 150 °C. The charge and discharge currents indicated on the figure were symmetric.

The coulombic efficiency at higher currents is affected by the alumina in an unexpected manner as seen in **Figure 4.10**. At low currents the data indicates a thin layer of alumina can improve the efficiency of the cell, with the 10 ALD cell reaching and maintaining better coulombic efficiency than the untreated cell. Upon the first increase of the current, the coulombic efficiency of all cells lowers, with more alumina corresponding to a greater efficiency reduction. But curiously, as the current increases, the gap in coulombic efficiency between cells with and without alumina shrinks. None of the data available suggests a mechanism for this result, which was seen for every cell assembled. For example, a comparison of the charge or discharge curves before and after a current change reveal no clearly identifiable voltage plateaus corresponding to a new reaction occurring.

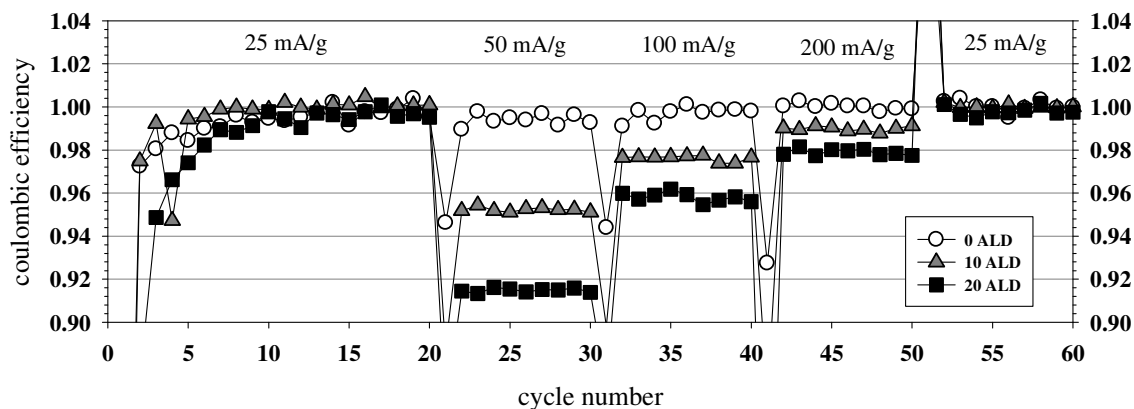


Figure 4.10 – Typical coulombic efficiency over 60 cycles for 90 °C ALD-treated electrodes with symmetric charge and discharge currents indicated on the figure.

Some electrodes were subjected to higher discharge current relative to charge current to demonstrate how utilizing the full charge capacity could improve the reversible capacity retention at higher currents. The resulting data is presented in **Figure 4.11** with the discharge current for each section indicated. As expected all cells show improved capacity retention at all discharge currents. The reversible capacity for the cell containing fibers coated for 10 ALD cycles has improved to 60% from 35% at a specific discharge current of 200 mA/g, and to 84% from 55% at 100 mA/g.

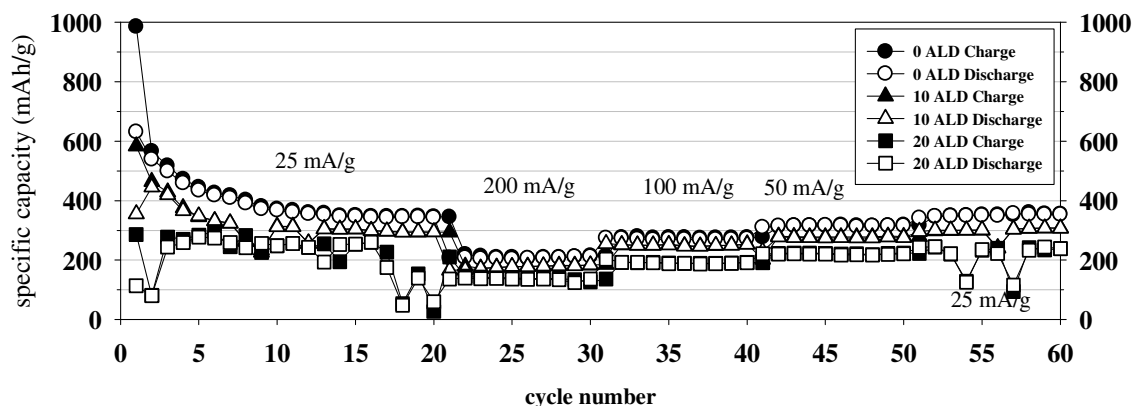


Figure 4.11 – Typical charge and discharge capacities for ALD-treated electrodes processed at 90 °C over 60 cycles with asymmetric current. The charge was conducted at 25 mA/g with discharge current indicated on the figure.

4.4 Conclusion

Thin coatings of alumina were deposited on carbonized nanofibers employed as anodes for potential use in Li-ion batteries. The use of atomic layer deposition to create those alumina films has effected a uniform deposition throughout the entirety of the non-woven structure. The ALD alumina coatings noticeably reduced the first-cycle irreversible capacity of these high-surface area carbon materials. There was an improvement of up to 24% in first-cycle irreversible losses for electrodes undergoing ten deposition cycles at 90 °C when compared to untreated material. These cells also reached coulombic efficiencies exceeding 99% in less cycles the cells based on bare nanofibers. Further, at low currents alumina coating created by 10 ALD cycles did not dramatically affect the reversible capacity. As the current during charge and discharge increased the alumina resulted in lower capacity retention, but under slow-charge with fast-discharge conditions the capacity retention improved. A thicker coating of alumina showed greater irreversible capacity improvement

but demonstrated poor overall reversible performance at all currents. These findings indicate that it may be possible to improve the value of these high-surface area fiber materials via ALD.

Chapter 5

Molecular Layer Deposition of Alucone onto Lithium-ion Carbon Nanofiber Electrodes

5.1 Introduction

Lithium-ion (Li-ion) battery technology has found widespread adoption in the 21st century³⁶⁵. These secondary batteries are now used in applications ranging from mobile phones and computers, to power tools, and recently, electric and hybrid-electric vehicles³⁶⁷. The large energy and power densities of Li-ion cells, double that of previous generation Ni based cells, are the primary reason for the dominant position of this technology¹. Additional benefits often cited include low rates of self-discharge, high operating voltages, and the lack of a memory effect. Despite their prevalence, the cost of Li-ion cells remains high for widespread use in transportation applications. Additionally the cells will need to deliver even higher energy densities to meet future demand across the listed applications³⁶⁵.

Most commercial Li-ion cells are based on the movement of the Li between a metal oxide cathode and a graphitic anode within a mixed organic electrolyte^{48, 376}. There are many potential anode materials known to reversibly store more Li than the theoretical limit of graphitic carbon^{67, 99, 377}. Many of these materials suffer from a critical defect, such as low electronic conductivity¹⁴² or poor mechanical durability⁷⁹ that prevents their adoption as the next anode of choice. A large body of research has been focused on producing composite materials which when considered as a whole will have the right performance and cost to serve as next generation anodes¹⁰⁶. The use of composite nanoscale materials, such as pyrolyzed electrospun nanofibers^{24, 219}, has garnered significant research to create improved battery performance at high loads. At this time commercialization of these one-dimensional composites remains impossible, partly due to irreversible losses of Li during the formation of the solid electrolyte interphase (SEI) layer during the first charge of the battery²⁴.

The formation of the SEI is a well-known and necessary process in stable Li-ion cells. The process is dependent on both surface chemistry^{165, 168} and surface area¹⁶⁶. For example, graphitic electrodes suffer less Li consumption than non-graphitic electrodes during SEI formation²⁵. The hard carbon, high surface-area nanofibers yield particularly large irreversible losses. The SEI layer is composed of the decomposition products of the reduction of the electrolyte salts and organic solvents by lithium at the electrode surface at potentials near 0.8 V vs. Li/Li⁺¹⁶³. These lithium atoms have been irreversibly lost to future electrochemical processes, and accounting for their loss is an important part of producing commercial cells. Investigations of the SEI composition have found a complex mix of organic-inorganic materials¹⁶⁰. Once the SEI has fully passivated the surface, Li ions will continue to diffuse through it, undergo charge transfer at the anode surface, and intercalate into the bulk of the electrode material.

Many approaches have been taken to limit the irreversible losses of Li during SEI formation. Organic molecules used as additives in the electrolyte have been used to polymerize on the electrode surface and form a precursor to the SEI layer^{179, 181}. Some inorganic additives have suppressed the consumption of Li during SEI formation^{182, 183}. Other work has deposited soft graphitic pyrocarbon on hard carbon electrodes to change the chemistry of the electrode surface and make one which suffers less Li consumption during SEI formation^{27, 172, 173}.

One significant advantage of the non-woven structure which results from electrospinning is a large, easily accessible surface. This has led to surface modification by established vapor phase deposition reactions^{28, 234}. When highly conformal, well-controlled,

thin, uniform coatings are desired, either atomic layer deposition^{341, 348} (ALD) or molecular layer deposition (MLD) are employed³⁵¹. These processes commonly rely on a binary self-limiting reaction sequence (A-B), which by repetition builds up a coating layer-by-layer. In some cases ternary sequences are employed³⁵². The key is that each partial-step be a self-limiting reaction, so that the quantity of material deposited depends solely on the number of process cycles.

The primary difference between ALD and MLD is the size of the precursor molecules used, and thus the size of the products left on the surface. Atomic layer deposition is used throughout the microelectronics industry to create thin layers of metals³⁴⁴ and dielectrics^{346,378}. Molecular layer deposition has been used to grow a wide range of polymer materials^{35-37,355} and, more recently, metal-organic hybrid materials containing aluminum³³ and zinc³⁴; commonly referred to as “metal-cones” (*e.g.* alucone). These hybrid materials are created through similar chemistries as ALD. The deposition of alumina proceeds from trimethylaluminum (TMA) and water, versus the deposition of alucone from TMA and ethylene glycol or glycidol³⁵⁸. The resulting alucone material is less dense than ALD alumina, and possesses material properties such as hardness, elastic modulus, and thermal expansion more akin to polymers than to ceramics³⁵⁹.

Both atomic layer deposition and molecular layer deposition have been used to grow coatings on fibers and change the surface properties of those materials^{348,349,375}. Several publications have applied atomic layer deposition to Li-ion electrodes made of traditional micron-sized active materials³⁰⁻³². Thin coatings of aluminum oxide were shown to reduce capacity fade for LiCoO₂ cathodes. Aluminum oxide coatings have also reduced the capacity

fade in both graphite and MoO_3 anodes. To date there are no published reports of MLD alucone or zincone applied to Li-ion cells. These hybrid metal-organic compounds may serve as an artificial SEI layer when applied to non-woven carbonized nanofibers. This work hypothesizes the deposition of the lower density hybrid alucone film will be a better approximation of the natural SEI layer than alumina formed by ALD. The alucone will present less of a diffusion barrier to Li atoms and while still reducing the Li losses during SEI formation.

5.2 Materials and Methods

The polymer nanofibers used as the electrode precursor were made from polyacrylonitrile (PAN) (Sigma Aldrich MW 150,000). The PAN was weighed and dissolved in anhydrous dimethylformamide (Sigma Aldrich) to make a solution of 11 wt% polymer. The mixture was heated to 40 °C and stirred for 24 hours to dissolve the polymer. The final solution was then sealed and stored at room temperature.

For electrospinning the PAN solution was pumped through a 22-gauge stainless-steel needle by a syringe pump at 1 mL/h. The collector was a flat metallic circular disk of 30-cm diameter covered in aluminum foil. The distance from the tip of the needle to the collector plate was 15 cm. The electric field was varied between 0.75 and 1 kV/cm, as needed, to maintain a stable Taylor cone. Electrospinning for approximately 3 hours produced a non-woven mat of about 15-cm diameter and a total mass of around 0.3 g. Swatches were cut from the central portion of the mat and measured approximately 3-cm wide by 12-cm long. These samples were removed from the aluminum foil prior to thermal treatment.

The two-step carbonization process of PAN²²⁷ was performed in a single zone Lindberg Blue tube furnace (model 55322-3) within a 45-mm inner diameter quartz tube. Swatches were loaded upon flat quartz shelves and the processing gasses flowed over the samples down the length of the tube. The stabilization step was conducted under a flow of dry air (National Welders) at 250 °C with a 5 °C/min ramp rate from room temperature and a soak of 2 hours at 250 °C followed by uncontrolled cooling to ambient conditions. The pyrolysis step was performed under a flow of high-purity nitrogen (National Welders) at 700 °C with a 5 °C/min ramp rate from room temperature and a soak of 2 hours at 700 °C followed by uncontrolled cooling to ambient conditions. The carbonization was conducted in

All alucone MLD was conducted in a hot wall reactor described elsewhere³⁷⁵ with samples arranged so the processing gases flowed over the samples and down the length of the tube. The aluminum precursor was trimethylaluminum (TMA, Al(CH₃)₃, Strem) and the oxidant was ethylene glycol (C₂H₆O₂, Sigma-Aldrich). The ethylene glycol source is heated to 80 °C to increase the vapor pressure of the precursor. The MLD process is a repetition of binary self-limiting A/B reaction cycles. The TMA adsorbs and reacts with surface hydroxyl groups (reaction A) to create aluminum-methyl species bound to the oxygen, with methane as a byproduct that is carried away. After the reactor is purged of residual TMA and methane byproducts, the ethylene glycol oxidant is introduced. The ethylene glycol then reacts with the Al-methyl groups producing a monolayer of Al₂(C₂H₄O₂)₃ (reaction B) terminated by hydroxyl groups. Again the byproduct of the reaction is methane, and it and residual water are purged from the reactor to complete one cycle. High-purity nitrogen served as both the purge gas and the carrier for the MLD precursors. The samples were processed between 6

and 40 full A/B cycles at a processing temperature of 100 °C, with untreated samples serving as reference. Each purge cycle was 120 seconds. The TMA precursors was pulsed for 5 seconds while the ethylene glycol pulses lasted 10 seconds. All processing was conducted at a base pressure of 0.8 Torr, with maximum observed pressure of 1 Torr during the TMA doses.

The mass of the non-woven mat was measured before and after deposition on a 5 digit analytical balance to track the mass gained during the deposition process. For reference a small piece of silicon (1 cm by 1 cm) was also placed in the reactor and the thickness of alucone deposited upon it was measured using an Alpha-SE spectroscopic ellipsometer (J.A. Woollam) at an angle of incidence $\Phi = 70^\circ$ and a wavelength range of 380–900 nm. The morphology of the fibers with and without coating was imaged by scanning electron microscopy at 5 kV using a secondary electron detector (JEOL 6400).

For electrochemical testing, 1.3-cm circular disks were die-cut from each fiber swatch to be used as anodes. The samples were introduced to a high-purity argon filled glove box (Labconco Protector) for coin-cell assembly. Each anode had a mass of approximately 4 mg fiber and coating. A similarly sized copper disc was used at the current collector with contact maintained by the mechanical force of a disc spring. The counter electrode was lithium metal (Sigma Aldrich) and the separator was polypropylene (Celgard). The electrolyte was 1M LiPF_6 in a 1:1 (w:w) solvent mixture of ethylene carbonate (EC) and ethylmethylcarbonate (EMC). All electrochemical data were collected in galvanostatic mode with an Arbin Instruments (BT-2000) battery tester. Cells were cycled at symmetric currents

of either 25 or 200 mA/g. The cut-off voltages used were 25 mV on charge and 2 V on discharge.

5.3 Results and Discussion

5.3.1 *Fiber Morphology* – For each deposition there was a measureable increase in the mass of the sample (**Table 5.1**). There is an approximately linear relationship between coating thickness and the number of cycles for between 20 and 40 cycles (**Figure 5.1**). The samples given only 10 and 6 cycles had much lower growth, suggesting incomplete nucleation of the film, and a coating that may not be uniformly conformal.

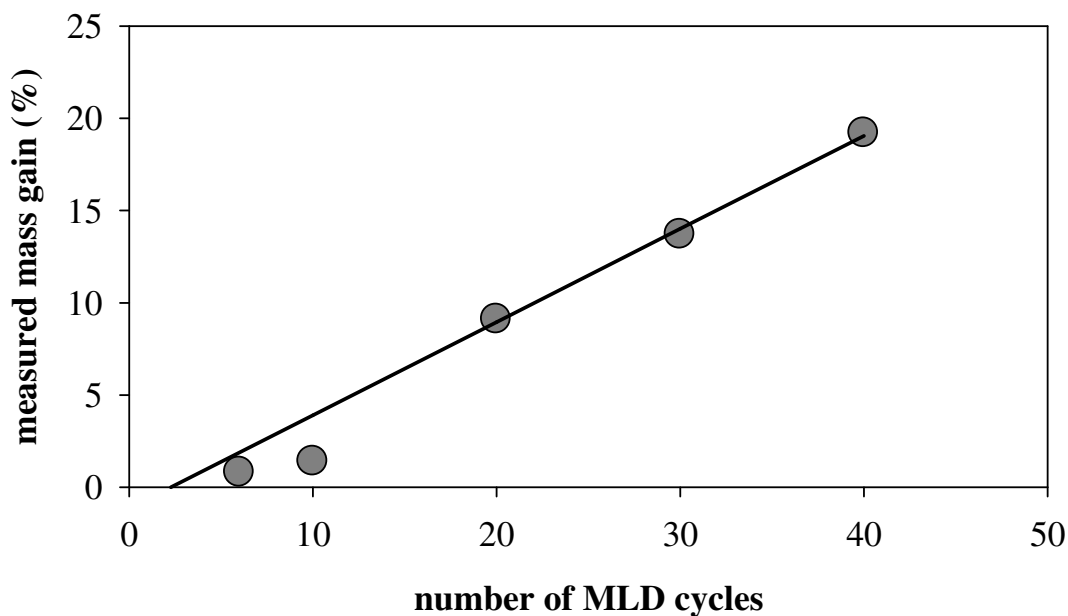


Figure 5.1 – Percentage of mass gain of the pyrolyzed fiber mat as a function of the number of MLD cycles. The trend line is fit to the data for 20 or more cycles.

Using an estimate for the surface area of 150 m²/g based on a BET measurement performed at a previous time and an alucone density set at the average of PEO and alumina (2.5 g/cm³), the deposited thickness on the fibers has been estimated and included in **Table 5.1**.

Table 5.1 – Mass gain during MLD on pyrolyzed PAN nanofibers, estimated thickness of the film, and the film thickness on Si when available.

Number of MLD Cycles	Mass before deposition (mg)	Mass after deposition (mg)	Percent Mass Gain	Estimated thickness (nm)	Ellipsometry Thickness on Si (nm)
40	41.94	49.98	19.2%	51	N/A
30	48.57	55.23	13.7%	37	N/A
20	60.85	66.40	9.1%	24	N/A
10	77.06	78.15	1.4%	4	3.9
6	73.65	74.25	0.8%	2	2.5

The untreated fibers used for this work measured between 390 and 600 nm after pyrolysis with an average of around 430 nm (**Figure 5.2**), and some visible defects were present in the fibers (**Figure 5.2b**). These areas are not bead defects caused when a region of the electrospun fiber has higher surface tension, but may represent a region where the solubility of the polymer was impacted by a contaminant.

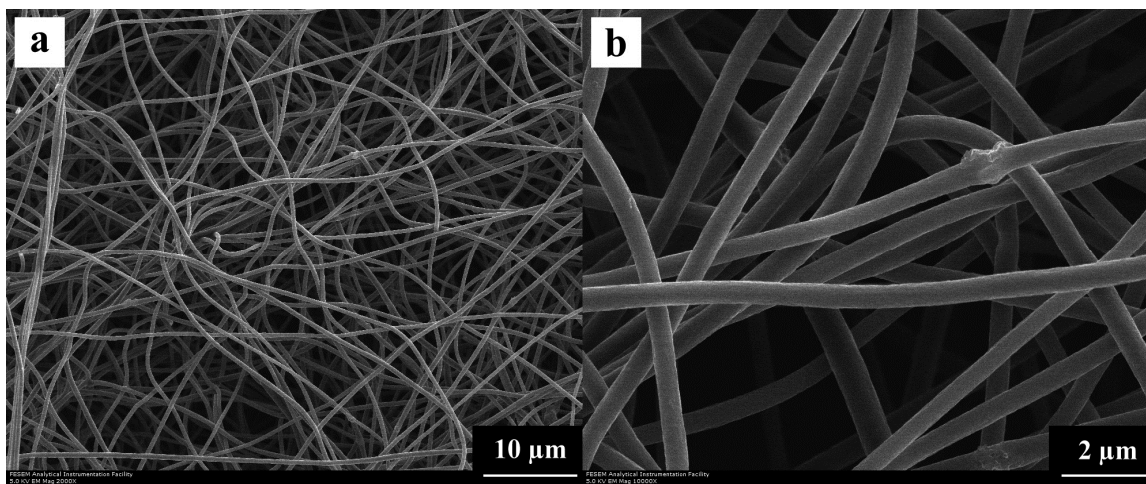


Figure 5.2 – Scanning electron micrograph of untreated fibers, pyrolyzed at 700 °C, used as reference material for comparison to fibers coated with alucone by molecular layer deposition at a) 2,000 x and b) 10,000x.

The fibers coated with 40 MLD cycles are larger in diameter by about 50 nm as measured over several micrographs and have some visible surface texture not present in the untreated or thinner MLD coatings (**Figure 5.3**). The 50 nm diameter increase is less than the estimated thickness of the film, but still a significant addition of material. It is not possible to distinguish changes in fiber diameter for less deposition cycles and those fibers are not shown. The surface of fibers coated for 20 MLD cycles does contain some additional surface texture, but it is less prevalent than for the thicker coatings.

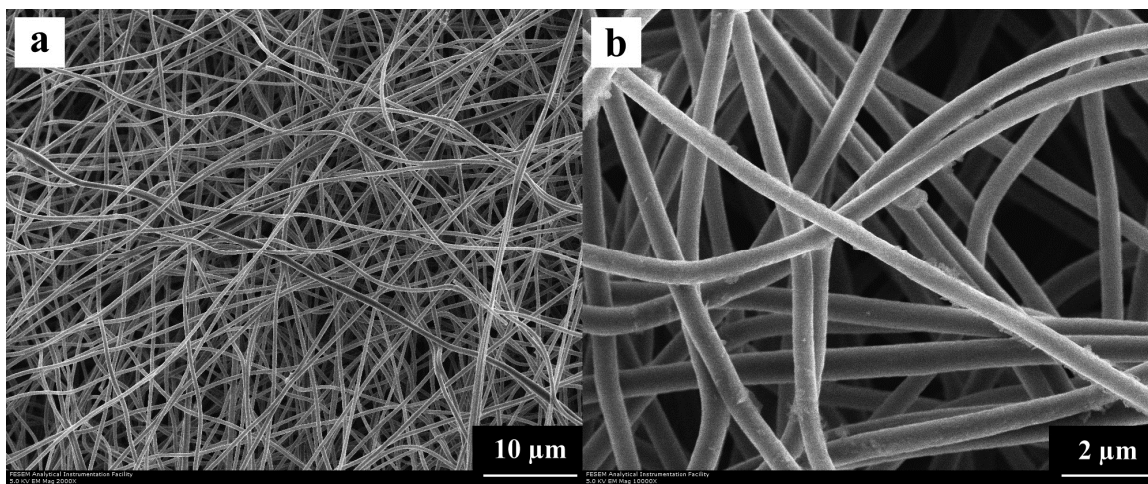


Figure 5.3 – Scanning electron micrograph of fibers coated for 40-cycles with alucone by molecular layer deposition at a) 2,000 x and b) 10,000x.

5.3.2 Electrochemical Performance of MLD Coated Nanofiber Electrodes – The initial cells were fabricated from samples coated with alucone for 40 or 20 MLD cycles. With one exception these cells stored significantly less Li than the uncoated reference materials at low rates (25 mA/g) of charge and discharge (**Figure 5.4**). This lower capacity at low currents is similar to results for 20 cycles of alumina deposited by ALD in **Chapter 5 (Figures 4.6 and 4.7)**, where there was a significant barrier to either electron transport or Li diffusion that resulted in the electrodes not reaching the maximum Li storage. At high currents the electrodes coated with 40 cycles of alucone were incapable of charging or discharging any significant quantity Li prior to reaching the cutoff voltages, an even more dramatic drop off than observed for 20 cycles of alumina. The 20-cycle alucone materials have more variability at all currents, with one cell outperforming the reference material, while the others were worse than the reference and better than the 40-cycle cells. It should be noted that the storage of Li in the reference cells is markedly lower than reference samples used in

Chapters 3 and 4, but the experimental cells from MLD-treated fibers are performing yet more poorly. This reduced capacity is likely due to the combination of a smaller voltage window and the larger diameter fibers not reaching full lithiation before reaching the cutoff voltage.

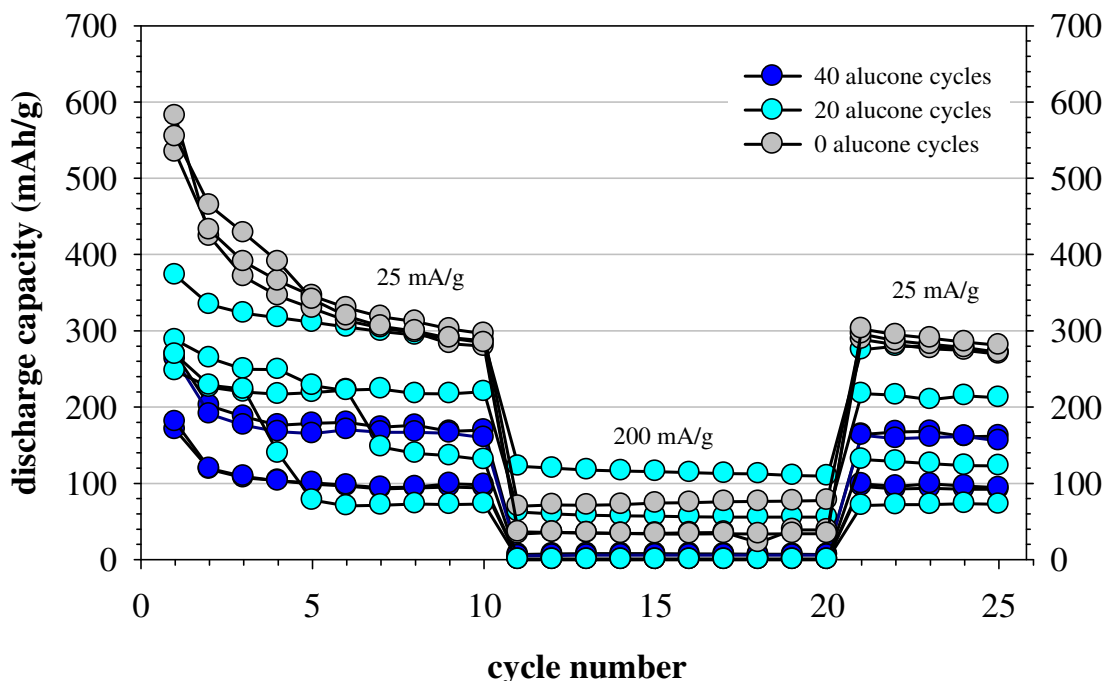


Figure 5.4 – Reversible discharge capacity of materials coated with 40 and 20 alucone MLD cycles, and untreated reference materials, at the indicated symmetric charge and discharge currents.

Both coating thicknesses provided a reduction in first-cycle irreversible capacity losses (Figure 5.5). The improvement relative to the reference materials was 23% for 40 cycles and 20% for 20 cycles of alucone. These quantities of alucone on the samples produce a similar reduction in irreversible capacity as 10 cycles of alumina via ALD (Chapter 4 Figures 4.3 and 4.4), but the capacity retention is noticeably worse.

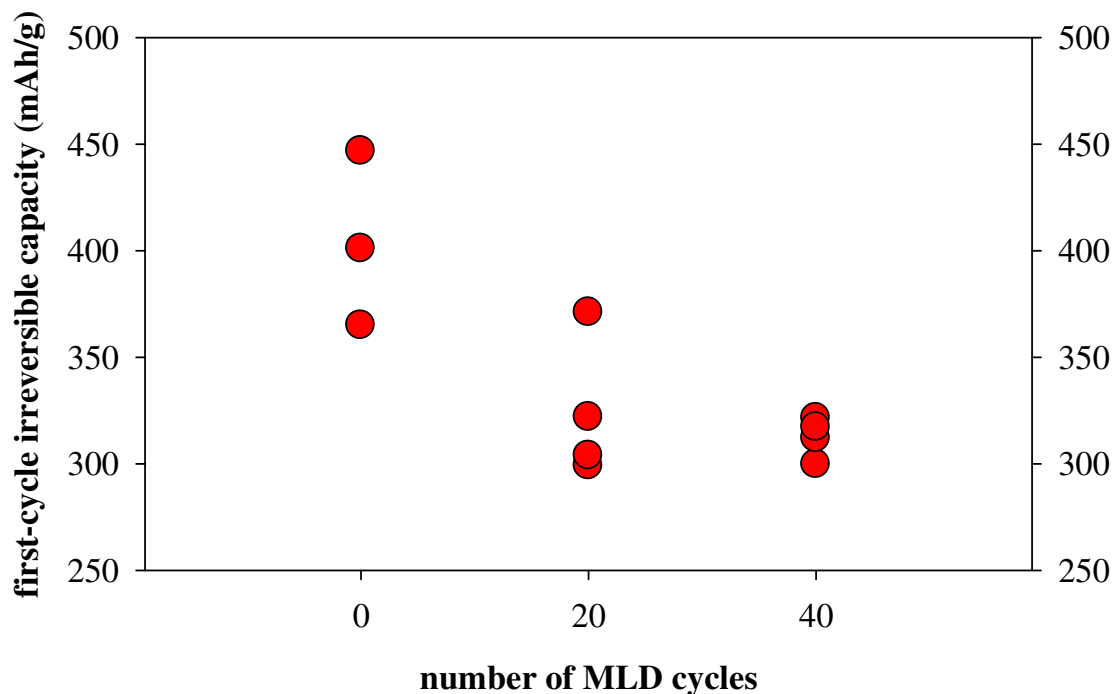


Figure 5.5 – Average reduction in irreversible capacity of 23% for 40 cycles of alucone and 20% for 20 cycles of alucone on electrodes made of pyrolyzed PAN fibers.

To reduce the impact of the coating on reversible capacity, thinner films were deposited, using 10 or 6 MLD cycles. At the low 25mA/g charge and discharge current cells made from these fibers with thinner coatings (**Figure 5.6**) reversibly store almost as much Li as the population of uncoated reference materials. All the cells suffer a large reduction in reversible capacity when the current increases to the higher 200 mA/g charge and discharge. The capacity loss of the cells made of MLD-treated fibers is more variable than the uncoated reference material, but the performance of some cells from the coated material is comparable to the uncoated reference samples.

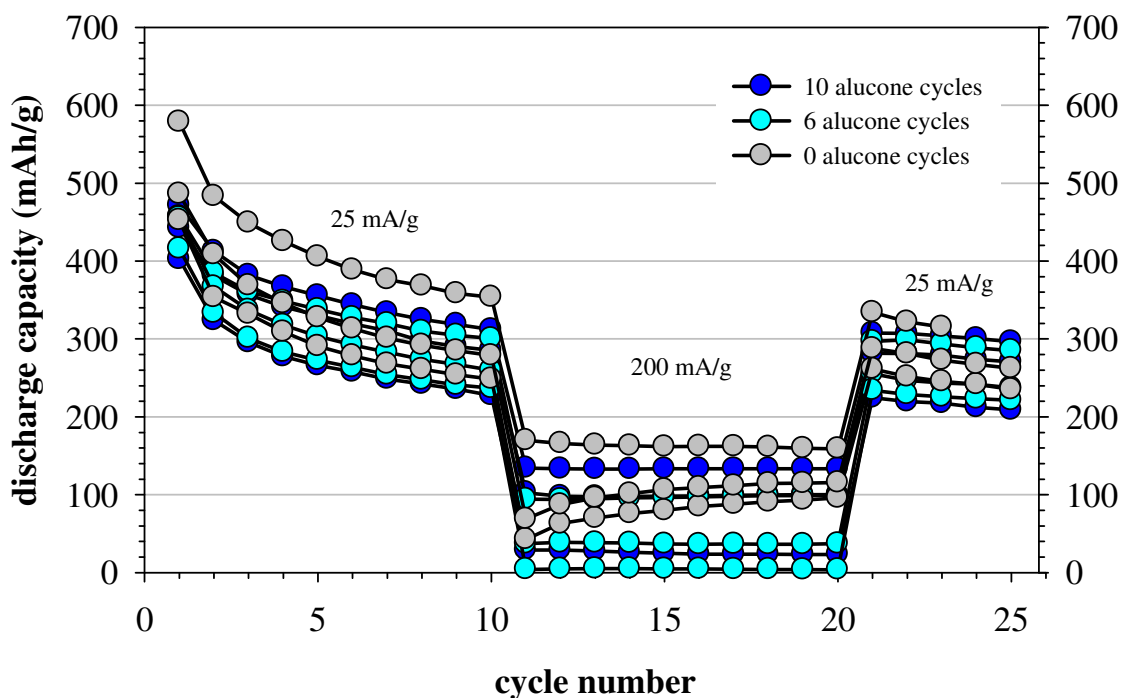


Figure 5.6 – Reversible discharge capacity of materials coated with 10 and 6 alucone cycles, and untreated reference materials, at the indicated symmetric charge and discharge currents.

The cells made from fibers with less alucone deposited realize smaller irreversible capacity improvements than the cells coated with more alucone (**Figure 5.7**). There is a 12% average reduction of the irreversible Li losses with 6 cycles and only a 9% average reduction for 10 cycles. This reversal is a possible indication that the low number of coatings has not completely covered the active surface. There is a significant spread between samples

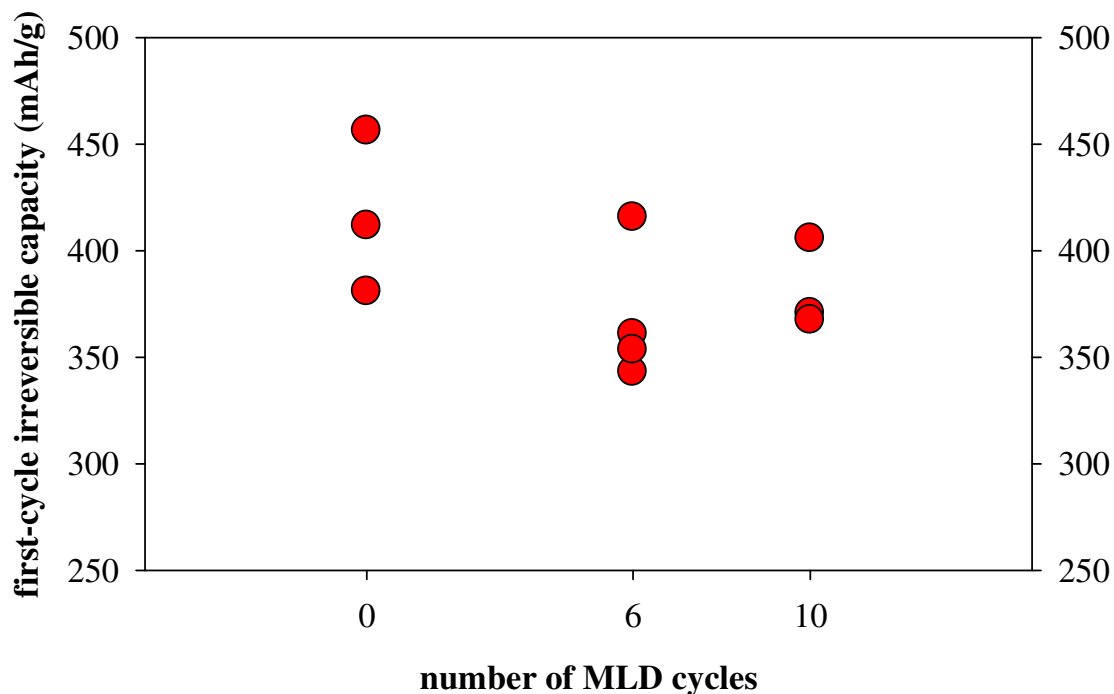


Figure 5.7 –Average reduction in irreversible capacity of 9.4% for 10 cycles of alucone and 12.5% for 6 cycles of alucone on electrodes made of pyrolyzed PAN fibers.

Table 5.2 - Summary of average irreversible capacity improvements produced by MLD of alucone onto pyrolyzed PAN electrodes.

Number of MLD Cycles	Average Reduction in First-cycle Irreversible Capacity
40	22.7%
20	19.9%
10	9.4%
6	12.5%

5.4 Conclusion

Molecular layer deposition successfully deposited between 6 and 40 layers of alucone onto pyrolyzed PAN fiber from TMA and glycerol. The films grown for between 20 and 40

cycles show an approximately linear mass gain. A separate deposition experiment for 6 or 10 cycles had a lower rate of mass gain on the pyrolyzed fiber substrates, suggesting incomplete coverage of the fibers. Silicon reference samples which were present during the 6 and 10 cycle depositions were consistent with the growth of approximately 4 Å per cycle.

The alucone materials successfully served as a partial artificial SEI layer. All coating thicknesses resulted in an average decrease in the first-cycle irreversible capacity losses of the electrodes. The thicker deposits resulted in larger improvements with the maximum benefit being a reduction of 23% for 40 deposition cycles. A greater reduction was found for 6 deposition cycles than for 10, consistent with the assumption of coating non-uniformity below a certain threshold of deposition cycles.

The reversible discharge capacity of the materials trended opposite to the irreversible capacity improvements, with better performance observed for fewer layers of alucone. Cells with 40 layers of alucone had about half the capacity of untreated reference materials at low current rates, and capacity retention of less than 5% at high current rates. The materials processed for 6 or 10 alucone cycles had reversible capacities only slightly reduced from the untreated reference materials at low charge/discharge rates. These alucone coatings show similar performance to alumina coatings by ALD and represent a potential means of improving the value of large surface area anode materials.

Chapter 6

Pyrolyzed Polyimide/Tin Composite Nanofibers as Anodes in Li-ion Batteries

6.1 Introduction

Lithium-ion batteries are the power supply of choice for mobile computing and communications because of high operating voltages, low rates of capacity fade, and large energy densities¹. Most commercialized Li-ion cells are comprised of a graphitic anode and a lithiated metal oxide cathode, and have been since the initial commercialization by Sony^{50, 365}. The commercially available cells have electrodes which contain a significant fraction of inactive materials, added to improve electronic conductivity and to bind the mixture of micron-scale particles together on the current collector^{48, 56}. Continual developments in mobile communications and computing technology, the needs of modern consumers, and the electrification of personal transportation^{2, 3} are driving the need for safer batteries with larger energy densities and higher power ratings. Meeting these needs will require electrodes with a greater lithium loading capacity and a reduction in the inactive materials.

There are many potential anode materials capable of storing more energy than commercialized graphite: pyrolyzed carbons^{70, 172}, alloying materials like tin or silicon^{78, 80}, and conversion materials including iron and cobalt oxides^{91, 379}. Many of these materials suffer from poor mechanical durability in the cycling process^{79, 102}, leading to incomplete utilization of the active material, and a degradation of cell performance. Thus implementation of these alternative anode materials requires engineering solutions to create novel structures or composites^{16, 24, 125, 380}. Efforts have been focused on creating nanoscale materials with the intention of: increasing the reactive surface for electron transfer³⁸¹, limiting the scope of mechanical deformation¹⁰⁹, decreasing the diffusion paths for Li-ions¹²¹, and engineering composite structures from simple building blocks to assemble easy to

implement materials¹¹⁴. An alternative to nano-particulate based composite electrodes are composites made of continuous one-dimensional structures^{22, 24, 115, 382}.

A facile method to create one-dimensional non-woven nanofiber webs is electrospinning¹⁹⁶. The process requires a stable flow of polymer solution through a needle, a high-voltage power supply, and a grounded collector to capture the resulting fibers. When the fibers are made of polymers able to be pyrolyzed, it is possible to thermally treat them into carbon anodes that require no binding materials or conductive additives^{38, 371}.

Additionally, it is possible to produce nanoscale composites via electrospinning. Techniques exist to create nanoparticles embedded in the fibers via *ex situ*^{23, 213} and *in situ*^{24, 271} methods^{23, 213}. Electrospinning solutions of PAN dissolved in dimethylformamide is a straight forward process, and the pyrolysis of PAN is well documented. A wide range of salts have been dissolved into the solution and resulted in nanoparticle condensation during the pyrolysis step^{24, 216, 383}. Some researchers have taken this path to create composite anodes of nanoparticles of lithium storing metals or metal oxides embedded in a continuous one-dimensional nanofiber web. For example, tin oxide nanoparticles have been incorporated into electrospun polyacrylonitrile (PAN), successfully reduced during pyrolysis, and delivered in reversible capacities over 600 mAh/g²⁴.

One barrier to the implementation of these composites as commercial electrodes is the irreversible losses of Li to solid electrolyte interphase formation at the electrode surface during the first charge^{162, 163, 174}. The large surface area of the electrospun fibers increases these losses. It is well known that non-graphitic carbons have larger losses than conventional

graphite-based electrode³⁶⁸. The magnitude of these losses typically decreases with increasing pyrolysis temperature, as the material becomes more ordered²⁷.

Polyacrylonitrile has served as the precursor matrix to make composite-fiber based anodes, but other materials can be used as precursors for a carbonized nanofiber web^{38, 270}. Polyimides are an important family of macromolecules because of their mechanical durability, dielectric properties, and chemical resistance^{40, 238, 244}. They are most commonly formed from the reaction of an aromatic diamine with an aromatic dianhydride in an organic solvent to produce a solution of poly(amic acid) (**Figure 6.1**). The poly(amic acid) precursor is processable and subjected to thermal or chemical dehydration yielding the final polyimide³⁸⁴, which is a thermoset resin.

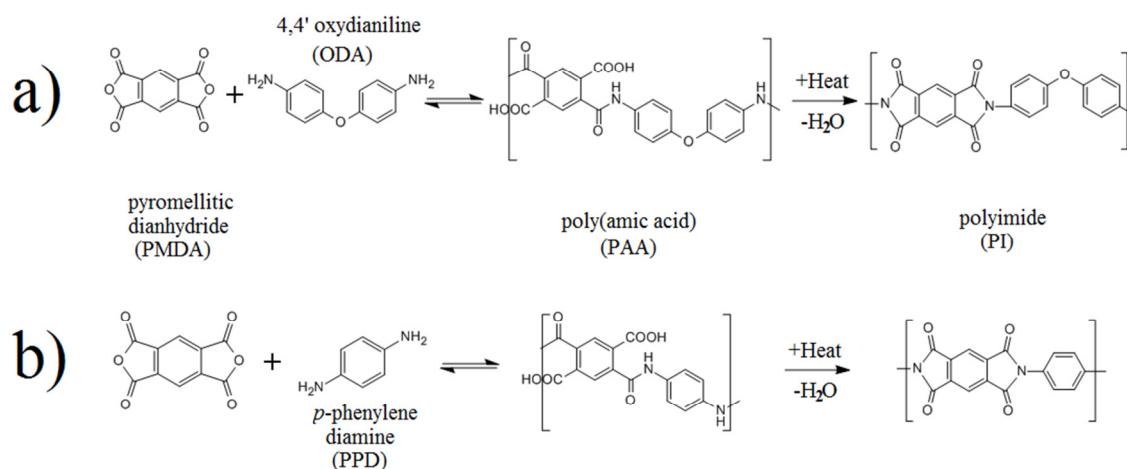


Figure 6.1 – The reactions to form poly(amic acid) and subsequent thermal imidization by dehydration between a) pyromellitic dianhydride and 4,4'-oxydianiline and b) pyromellitic dianhydride and *p*-phenylene diamine.

The polymerization procedure is known to impact the molecular weight (MW) distribution of the resulting polymers, with larger molecules resulting from heterogeneous polymerization

when the dianhydride is added as a solid to a solution already containing a fully dissolved diamine^{243, 244}. The reaction of the diamine and dianhydride is reversible prior to imidization, and studies of mixtures of different poly(amic acids) have shown a redistribution to a random copolymer^{247, 248, 253}. Additionally the reversibility of the reaction often leads to a redistribution of the MW as the resin ages.

By carefully selecting the two monomers used in the reaction it is possible to tailor the final material properties to suit the intended application. The resulting electronic conductivity of pyrolyzed polyimide film can be varied by monomer selection⁴³⁻⁴⁵. Further, the production of polyimide-based, electrospun, carbonized nanofibers based on pyromellitic dianhydride and 4,4'-oxydianiline has been demonstrated by electrospinning the poly(amic acid) form followed by thermal imidization of the non-woven mat^{46, 385}. The *in situ* technique has been used to create composites of ultra-fine polyimide fibers of less than 100 nm in diameter containing silver nanoparticles²⁷¹.

The ability to control the properties of the pyrolyzed material by monomer selection presents an opportunity to engineer improved composite electrodes. It is hypothesized poly(amic acids) will produce more conductive fibers. At high discharge rates this will improve the capacity retention of these composite nanofiber electrodes with high aspect ratios between fiber junctions. Additionally, the more conductive fibers should be more graphitic and the first-cycle irreversible capacity losses should be lower than similar PAN-based fibers.

6.2 Materials and Methods

Pyromellitic dianhydride (PMDA, Evonik), phthalic anhydride (PA, Sigma-Aldrich), 4,4'-Oxydianiline (ODA, Sigma-Aldrich) and p-phenylene diamine (PPD, Sigma-Aldrich) were used as provided. Polyethylene oxide of weight average molecular weight (M_w) of 2 Mg/mol was obtained from Dow (Sentry PolyOX). All of the above were stored in a desiccator to minimize moisture adsorption. The source of tin was either tin acetate (Sigma Aldrich), tin(II) acetylacetonate (Sigma Aldrich) or dimethyldineodecanoate tin (DMDND-tin) (Gelest).

The precursor poly(amic acid) (PAA) was polymerized in between 8 and 15 mL of anhydrous dimethylformamide (DMF) (Sigma Aldrich) to yield solutions between 10 and 30 wt% polymer by one of three procedures. All monomers were used in a 1:1 stoichiometric ratio to maximize molecular weight. The sample vials were heated to approximately 40 °C with moderate stirring. The first method was homogeneous solution polymerization where the monomers were each dissolved in separate vials of DMF and then mixed to yield the final solution. The other two methods were heterogeneous polymerizations, in which one of the two monomers was completely dissolved followed by the addition of the other solid monomer into the solution. If needed, the high molecular weight PEO was dissolved in the DMF overnight with moderate stirring prior to addition of monomer. Unless otherwise noted the tin compound was also added prior to monomer. Solutions were gently mixed during polymerization and usually reacted for 1 hour prior to further use.

The molecular weight distribution for the poly(amic acid) solutions was determined using a Waters 2695 chromatography system. Three Waters Styragel HR4 columns were

used to perform the separation arranged in the following order: WAT045900, WAT045810, and last WAT045885. The columns were maintained at 30 °C. The mobile phase used was a solution of 0.3 M LiBr and 0.3 M H₃PO₄ in HPLC grade DMF (all from Sigma-Aldrich) and the flow rate was 0.5 mL/min. Samples were diluted to 1 mg/mL and 100 µL of sample was injected for each measurement. Differential refractive index (RI) was measured on a Wyatt Optilab rEX at 633 nm. Additional low-angle light scattering data at 690 nm was available from a Wyatt miniDawn. The six calibration standards used were polyethylene oxide with M_w between 660 and 378,000 g/mol. The calibration curve was constructed based upon the differential RI data and was based on a third-order polynomial of the logarithm of the arithmetic mean of the number average (M_n) and weight average (M_w) molecular weights plotted against the elution time at maximum differential refractive index response. After baseline correction of the experimental results the equivalent PEO M_n and M_w of the polyimide samples were calculated from the following equations²⁵⁹:

$$M_n = \frac{\sum D_{RI,i}}{\sum D_{RI,i}/M_i} \quad \text{Equation 10}$$

$$M_w = \frac{\sum (D_{RI,i} M_i)}{\sum D_{RI,i}} \quad \text{Equation 11}$$

where M_i is the calibrated equivalent PEO MW at a given elution time i and $D_{RI,i}$ is the baseline corrected differential RI response at the elution of M_i .

All cone and plate shear viscosity data were collected on a TA Instruments AR2000 rheometer operating in flow mode. The analysis cone was 40 mm in diameter with 2° slope.

The sample was held at 25 °C. The applied shear stress varied between 0.01 and 500 Pa as needed for a given sample, with typical experiments spanning a three decade range in applied stress. A one minute pre-shear below the midpoint of the stress range was used and the samples were given three minutes to equilibrate.

For electrospinning the resulting PAA solution flowed through a 22-gauge stainless-steel needle – unless otherwise noted – from a syringe pump at 1 mL/h. The electrospinning setup was oriented horizontally. The fibers were collected on aluminum foil spread over a flat metallic circular disk of 30-cm diameter. The distance from the tip of the needle to the collector plate was 15 cm. The electric field was varied between 0.5 and 1.67 kV/cm, as needed based on solution properties, to maintain a stable Taylor cone. The length of time for the electrospinning varied, with the end goal being a non-woven mat of about 15-cm diameter and a total mass greater than 0.3 g. Swatches were cut from the central portion of the mat and measured approximately 3-cm wide by 12-cm length.

The poly(amic acid) was thermally converted to polyimide in a single zone Lindberg Blue tube furnace (model 55322-3) within a 45-mm diameter quartz tube. Swatches were on loaded flat quartz shelves and the processing gasses flowed over them down the length of the tube. Imidization occurred under a flow of dry air (National Welders) at 250 °C with a 5 °C/min ramp rate from room temperature and a soak of 2 hours at 250 °C followed by uncontrolled cooling to ambient conditions. After imidization the free-standing non-woven mat was peeled off the aluminum support. The pyrolysis step was done under a flow of high-purity nitrogen (National Welders) at 700 or 900 °C with a 5 °C/min ramp rate from room temperature and a soak of 2 hours followed by uncontrolled cooling to ambient conditions.

Fiber size and mat structure was imaged by scanning electron microscopy at 5 kV using a secondary electron detector (JEOL 6400). The non-pyrolyzed fibers were sputter coated by a palladium and gold alloy to improve conductivity. Absolute tin content was determined using inductively coupled plasma mass spectrometry (ICP-MS) with samples digested by microwave heating. Approximately 0.03 g of sample was weighed to an accuracy of ± 10 μg . Each sample was placed in approximately 4 mL of aqua regia (3:1 HCl:HNO₃) and covered for 16 hours. Samples were heated in a closed vessel to 175 °C for 5 minutes. After cooling the samples were filtered through a #41 Whatman paper filter prior to introduction to the ICP-MS.

Some were subjected to Raman spectroscopy to compare the disorder of the pyrolyzed carbon nanofibers. The instrument was a Horiba-Jobin Yvon LabRAM HS VIS high-resolution confocal Raman microscope using a 632.8 nm laser as the excitation source. The laser was focused normal to the substrate through a 50X objective lens resulting in an approximately 1 μm spot size. The instrument was calibrated using the 520.7 cm^{-1} line of a silicon wafer. LabSpec software (Horiba Scientific, Ltd.) was used to process all spectra.

For electrochemical testing, 1.3-cm circular disks were cut from each swatch to be used as anodes. The samples were dried overnight in a vacuum oven at 80 °C prior to introduction to a high-purity argon filled glove box (Labconco Protector) for coin-cell assembly. Each anode had a mass of approximately 3 mg fiber. A similarly sized copper disc was used at the current collector with contact maintained by the mechanical force of a disc spring. The counter electrode was lithium metal (Sigma Aldrich) and the separator was polypropylene (Celgard). The electrolyte was 1M LiPF₆ in a 1:1 (w:w) solvent mixture of

ethylene carbonate (EC) and ethylmethylcarbonate (EMC). All electrochemical data was collected in galvanostatic mode with an Arbin Instruments (BT-2000) battery tester. Cells were cycled at currents of 25, 50, 100, 200, and 400 mA/g. The cut-off voltages used were 25 mV on charge and 2 V on discharge.

6.3 Results and Discussion

6.3.1 Impact of Polymerization Methods on Solution Properties and Electrospinning

Initially polymer solutions of PMDA and ODA were prepared via homogeneous solution polymerization, whereby both monomers were heated and dissolved in separate vials of DMF. The separate solutions were then combined and stirred to complete the polymerization forming the poly(amic acid), a polyelectrolyte with weakly acidic carboxylic groups. Some of the initial solutions produced and the relevant electrospinning parameters and resulting morphologies are contained in **Table 6.1** with images collected via scanning electron microscopy in **Figure 6.2**.

Table 6.1 – Range of morphologies produced from PMDA-ODA solutions during electrospinning.

Wt % poly(amic acid)	Electrospinning voltage (kV)	Resulting morphology	Observed diameters
22.0	20 kV	Beads	100 nm to 2.5 μm
24.0	20 kV	Beads	200 nm to 4 μm
26.0	20 kV	small fibers and beads	100 and 1 to 2 μm
28.0	25 kV	Fibers	100 to 750 nm
30.2	20 kV	Fibers	1 to 3 μm

The lower two concentration solutions were below the entanglement threshold required for electrospinning and resulted electrospayed beads. At 26 wt% some of the polymer chains

were just entangled and small fibers are formed between large beads. By 28 wt% continuous fibers are formed and a further increase in the amount of polymer in solution widened the fiber diameter.

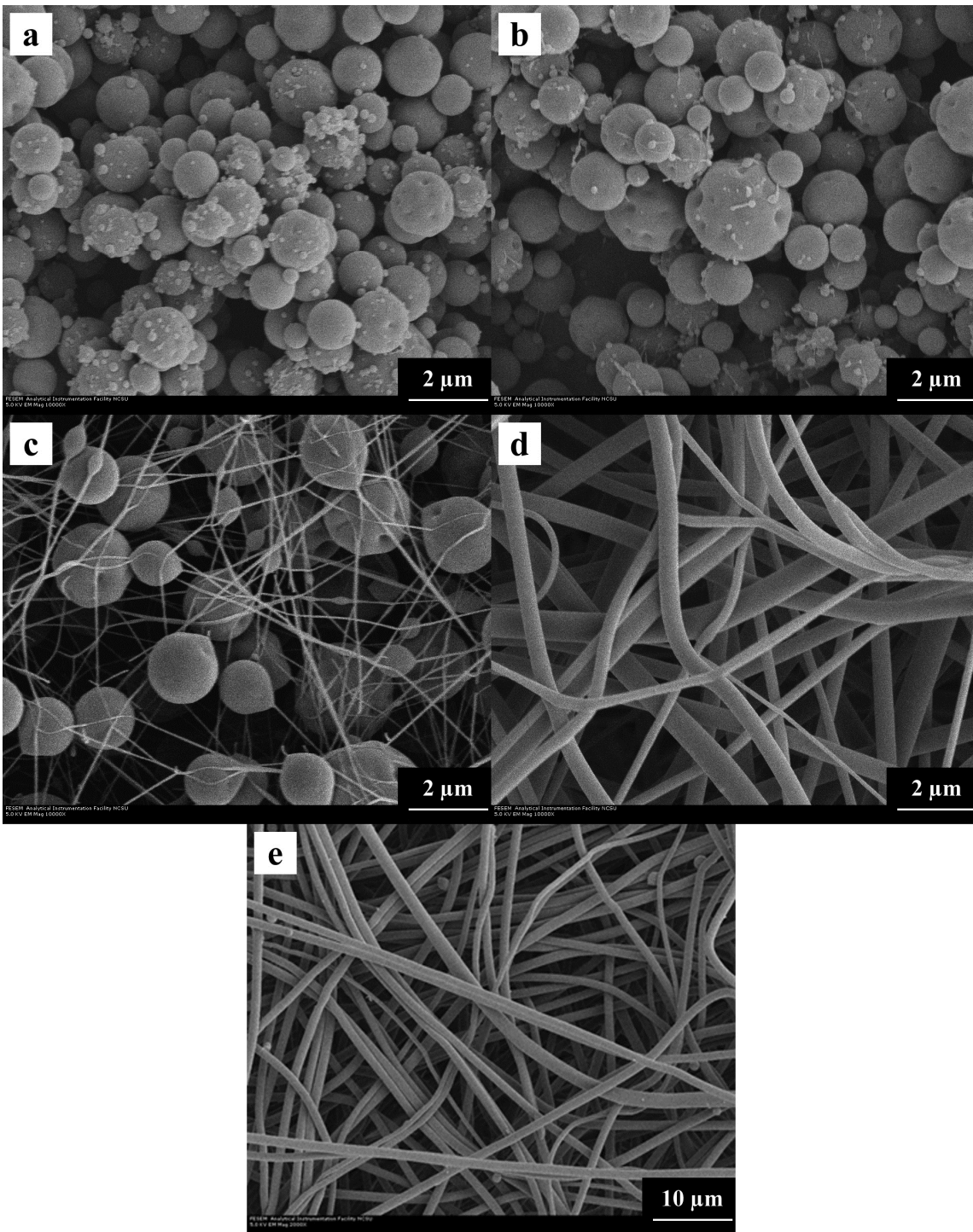


Figure 6.2 – Scanning electron micrograph illustrating the range of morphologies produced from PMDA-ODA solutions during electrospinning, a) 22, b) 24, c) 26, d)28, and e) 30.2 wt% total polymer in DMF.

In contrast, homogeneous polymerization for PAA made from PMDA and PPD was unable to produce continuous fibers at any polymer concentration between 5 and 25 wt%, which is caused by insufficient entanglements. The lack of entanglements is indicated by the very low shear viscosity for solutions as polymerized (**Figure 6.3**, white objects). The shear viscosity of these solutions changed over the over the course of hours for concentrated solutions and days for less concentrated ones (**Figure 6.3**). All solutions developed into gels with noticeable shear thinning behavior. The least concentrated solution (7.5%) shows shear thinning at 24 hours, but by that time the most concentrated solution has gelled and no longer flows at accessible shear rates.

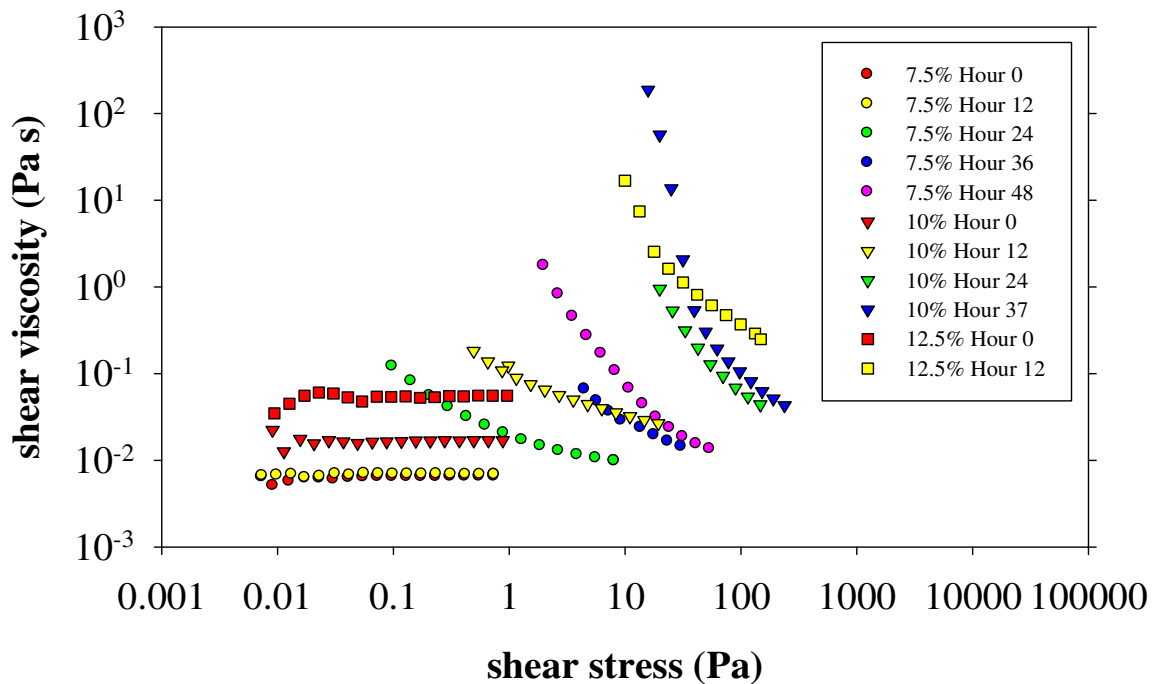


Figure 6.3 - Change in shear viscosity for solutions of PMDA-PPD for 7.5, 10 and 12.5 wt% total polymer measured every 12 hours for up to 48 hours after polymerization.

Around 15 wt% it was possible to produce a mixture of fibers and beads within the first hour (**Figure 6.4**). As the solution aged and the shear viscosity increased the syringe pump became unable to deliver the desired flow rate. When this condition was first noticed the pump was unsuccessfully reset in an attempt to re-establish flow, while unnoticed the pump would reach a safety-error stalled condition. Anytime throughout this chapter where similar behavior occurred will be referred to as a stall, even if it was noticed prior to the pump reaching the stalled condition. More concentrated solutions only resulted in a shorter operating window before the pump stalled. A reduction in the polymer content of the solution would extend the time for which the solution could be pumped, but the solutions would not have sufficient entanglements to electrospin.

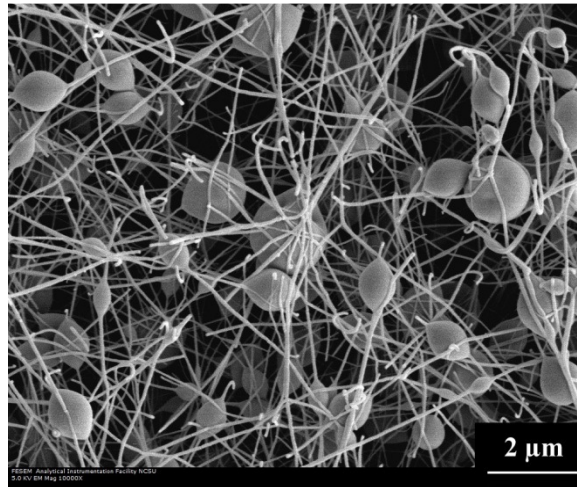


Figure 6.4 – Scanning electron micrograph containing a mixture of fibers and beads produced from a PMDA-PPD solution of 15 wt% total polymer in the first hour after polymerization.

The PMDA-ODA type polyimides did not increase in viscosity like the PPD ones during the time after polymerization and while electrospinning, so random co-polymers were created using some of the ODA monomer in place of PPD. The objectives were to retard the viscosity changes and add additional chain flexibility. For this experiment three solutions were made, all were 10 wt% PAA in DMF. One used entirely PPD as the diamine. The second had a diamine ratio of 85:15 (PPD:ODA) and the final solution used a 70:30 ratio. The rate at which the viscosity changed was dramatically reduced by the inclusion of 15% ODA (**Figure 6.5**). Not shown is the solution with 30% ODA which had no increase in viscosity after a month. The initial viscosity of the solutions was unchanged from the PPD only reference case, and thus the solution was still unable to be electrospun.

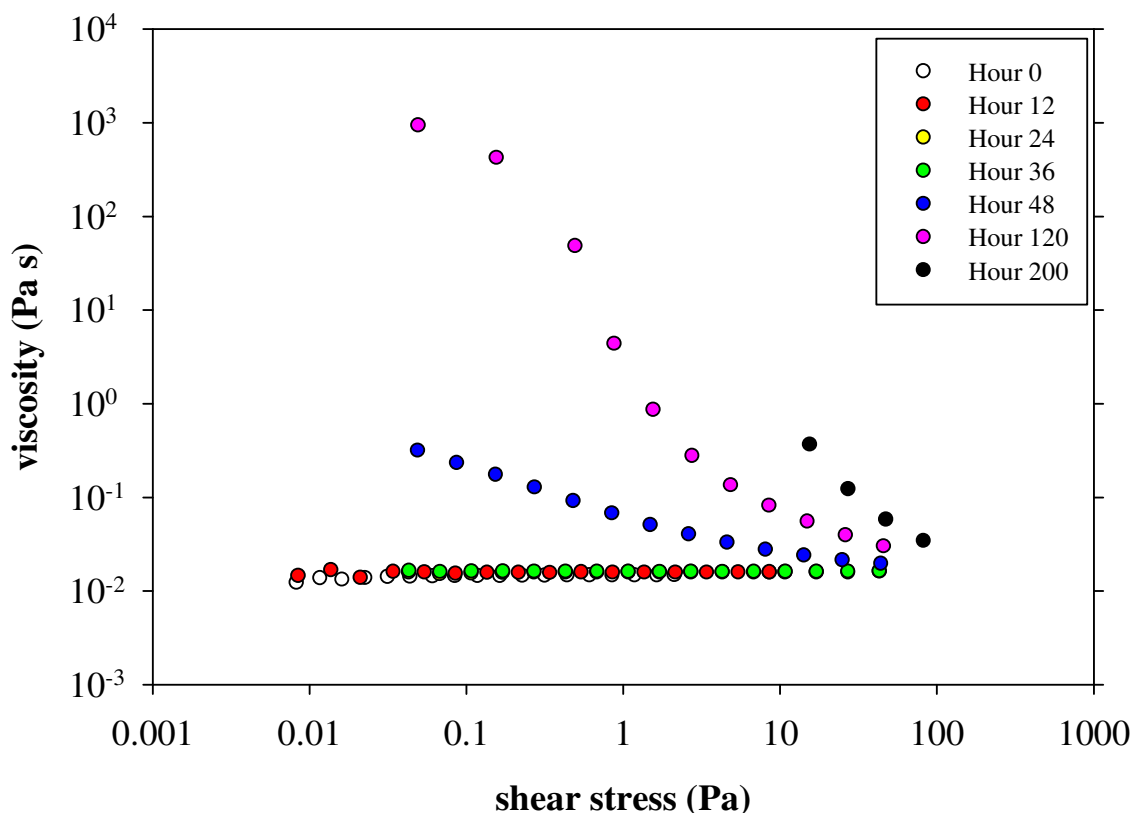


Figure 6.5 - Observed change in shear viscosity for co-polymer of PMDA-PPD/ODA with an 85:15 PPD:ODA ratio for a 15 wt% total polymer solution.

Phthalic anhydride (PA) can serve as a terminating agent to control the M_w of poly(amic acids). When 1% of the dianhydride was replaced with PA in a 15% PPD solution, the viscosity of the solution (**Figure 6.6**) responded with the same gelling and shear thinning behavior, ruling out continued linear chain growth as the potential source of viscosity changes. Used with a 25 wt% solution of ODA based polyimide, the inclusion of 4% phthalic anhydride reduced the solution viscosity by almost one order of magnitude (**Figure 6.7**).

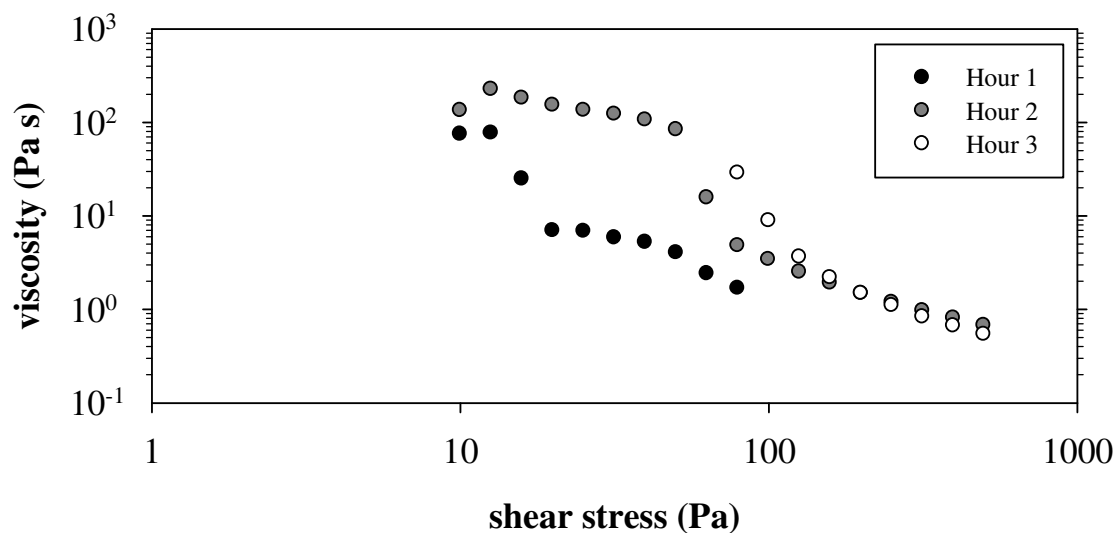


Figure 6.6 - The addition of 1% phthalic anhydride to shorten chain length did not eliminate the gelling and shear thinning for a PMDA-PPD solution with 15 wt% total polymer.

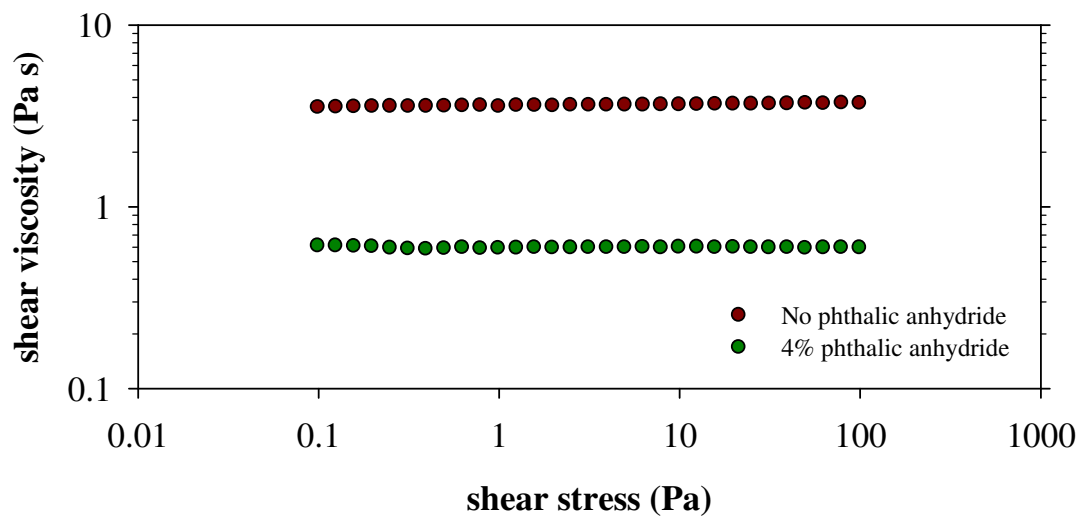


Figure 6.7 - The use of phthalic anhydride with PMDA-ODA solution of 25 wt% total polymer resulted in lower shear viscosity.

The proposed mechanism for the gelling of the PMDA-PPD solutions is cross-linking when a second PPD molecule reacts with the carboxylic group formed during the original amic acid reaction (**Figure 6.8**). Unlike the amic acid formation (**Figure 6.1**), which involves the reversible exchange of a proton, this “double reaction” is a dehydration. After the double reaction the second PPD molecule is then free to react with a different dianhydride group and the chain will have more than two growing ends, creating a networked gel over time. This reaction would be favored in conditions where the diamine is in excess, such as heterogeneous polymerization when the dianhydride is dissolved first, and the interfacial concentration of PPD is high at the solid/solution interface. It would also be favored in the case of very short oligomers, when there are many unreacted groups available. Heterogeneous polymerization performed with the addition of the solid diamine to the already dissolved dianhydride creates a local excess of the dianhydride, making the double reaction less likely.

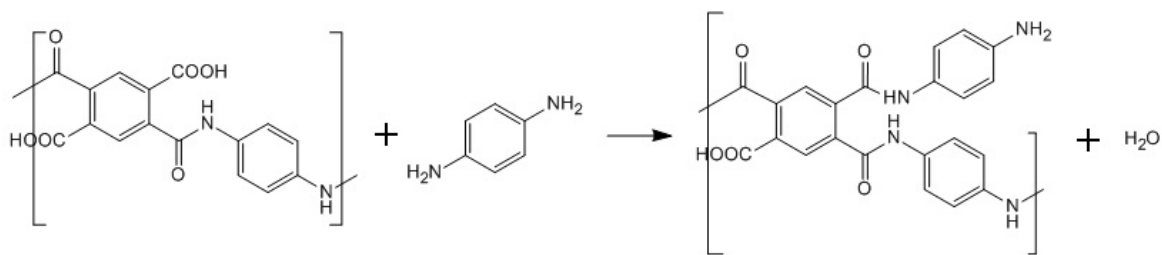


Figure 6.8 – Proposed double reaction mechanism, creating irreversible chemically cross-linked chains in PMDA-PPD solutions.

Successful electrospinning of PMDA-PPD fibers resulted from the addition of a small amount of very high MW PEO (2 Mg/mol). The shear viscosity change for a 15 wt% PAA

solution with 0.25% and 0.5% PEO was small, (Figure 6.9), but the solution produced continuous nanofibers when electrospun (Figure 6.10). The chains of PEO created entanglements with each other and the PAA molecules, preventing bead formation. In Figure 6.10b individual fibers have melded together where they intersect indicating that there was solvent present in the fiber when it deposited unto the collector. The fibers stretched more with greater electric field strength, shrinking the diameter (6.10d and 6.10f) and the DMF remaining upon arrival at the collector was insufficient for the fibers to meld together.

The inclusion of the PEO did not prevent the viscosity changes of the PMDA-PPD solutions. Thus, while continuous fiber formation occurred, it was not possible to spin for a sufficient length of time to create enough material for subsequent processing and use as an electrode.

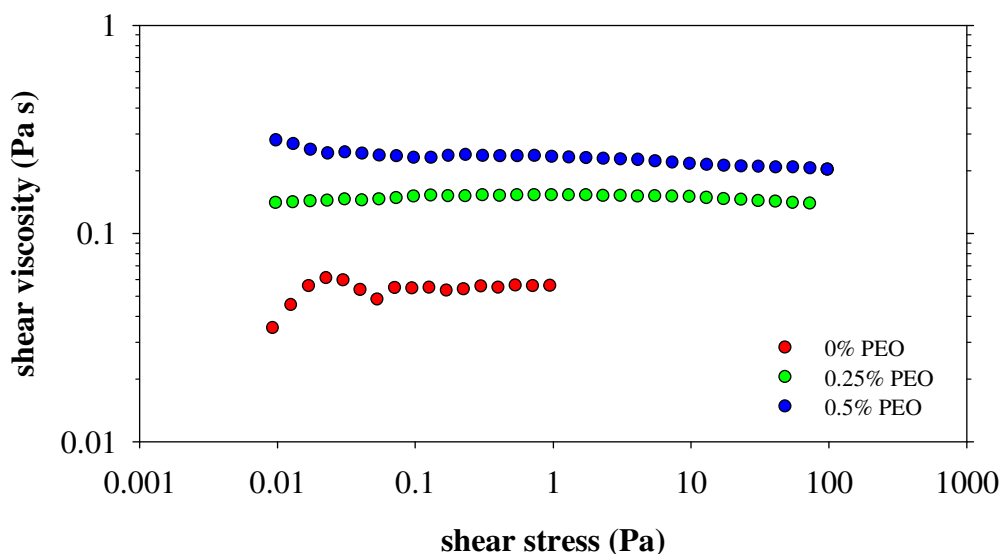


Figure 6.9 – The addition of 2 Mg/mol PEO to PMDA-PPD solutions containing 15 wt% total polymer increased shear viscosity slightly.

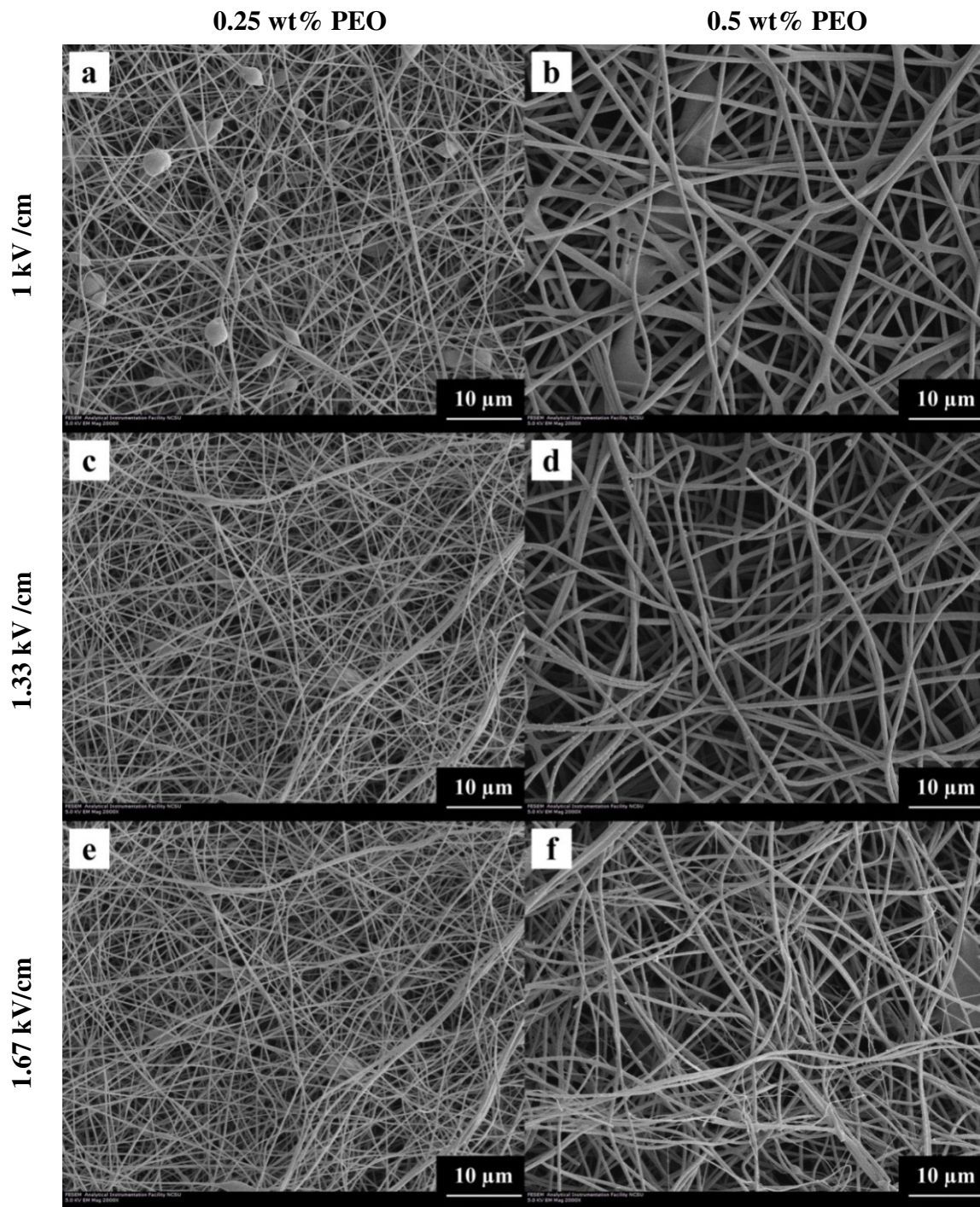


Figure 6.10 – Scanning electron micrographs of fibers electrospun from 15 wt% PMDA-PPD polymer containing an additional 0.25% PEO (a,c,e), 0.5% PEO (d,e,f). The electric field strength was (a,b) 1 kV/cm, (c,d) 1.33 kV/cm, and (e,f) 1.67 kV/cm.

Use of heterogeneous polymerization methods, recommended by books and historical literature, changed the solution properties and impacted the electrospinning of the resulting solutions. Pyromellitic dianhydride takes longer to dissolve in DMF and was added first, followed by addition of the solid diamine. For polyimides using the ODA monomer, there was an increase in the shear viscosity when the heterogeneous method was used (**Figure 6.11**), and electrospinning became possible for less concentrated solutions.

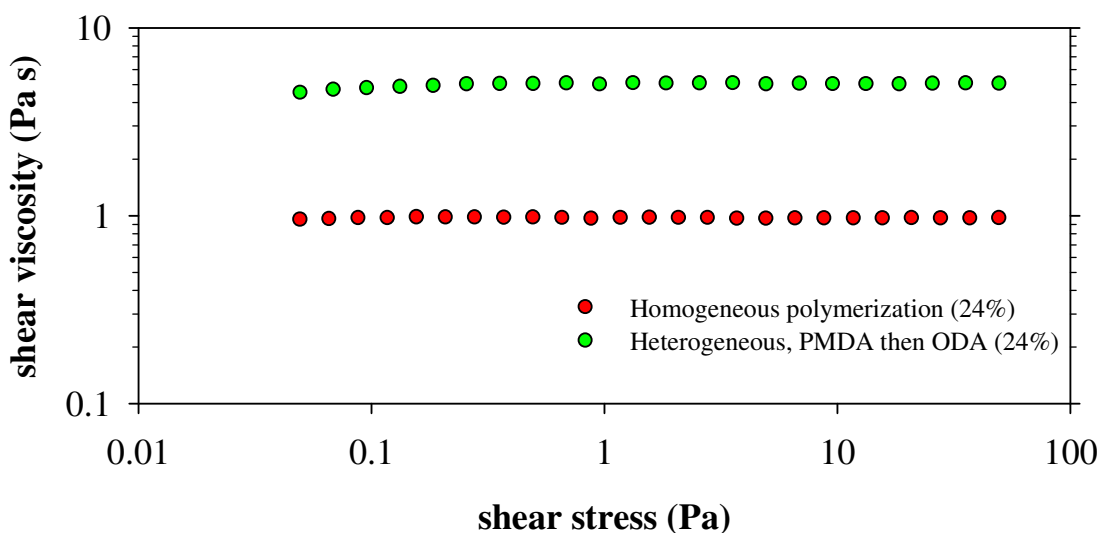


Figure 6.11 - Comparison of the shear viscosity of PMDA-ODA solutions with 24 wt% or 25 wt% total polymer polymerized by homogeneous and heterogeneous methods. Heterogeneous methods began with complete dissolution of one monomer then followed by addition of the second solid monomer to the resulting solution.

For PMDA-PPD solutions the switch to heterogeneous polymerization with the dianhydride dissolved first did not eliminate the gelling or development of a shear-thinning solution (**Figure 6.11**). Similar to the homogeneous polymerization there is an excess of dianhydride molecules in solution so the rapidly dissolving diamine can react to make lots of

small oligomers. Then as with the homogeneous solution, the double reactions described previously can occur and begin the formation of cross-linked gels.

When the order of addition was reversed with PPD dissolved first, followed by the addition of solid PMDA, there was a marked increase in viscosity. No thickening or conversion to shear thinning behavior was observed over the first 24 hours (**Figure 6.12**). In this reaction scheme the diamine is in excess and will immediately react with the slower dissolving dianhydride. This creates a higher effective concentration of dianhydride where the reaction occurs and drives the reaction to larger MW polymers. With less small molecules the likelihood of the double reaction is reduced and the solution viscosity is stable enough to work with for several hours to days. This order of addition was adopted for a majority of subsequent polymerizations. It should be noted that over the course of weeks the samples did gel, but at a much slower rate than the samples polymerized by the other methods.

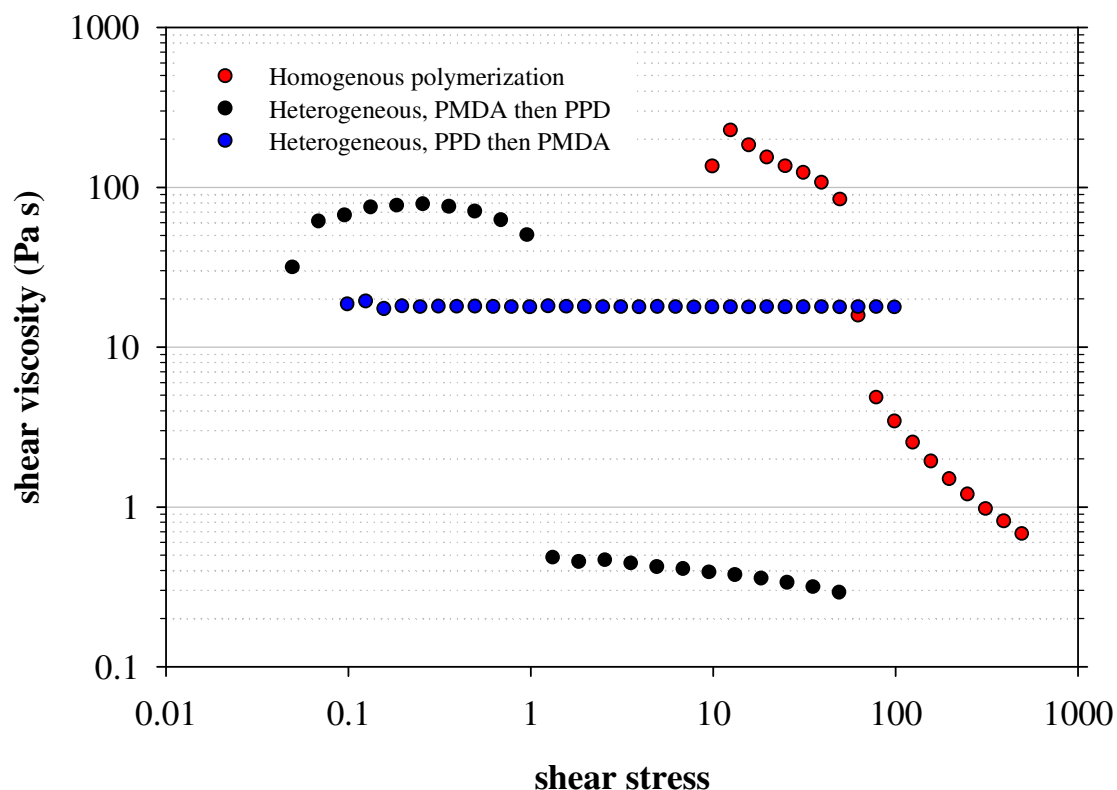


Figure 6.12 - Comparison of the shear viscosity of 15 wt% total polymer PMDA-PPD solutions polymerized by homogeneous and heterogeneous methods. Heterogeneous methods began with complete dissolution of one monomer then followed by addition of the second solid monomer to the resulting solution.

When 2 Mg/mol PEO was included in the heterogeneous polymerization of PMDA-PPD the resulting 15 wt% solution had shear viscosity an order of magnitude lower than a comparable solution without PEO (**Figure 6.13**). This could have been the result of the PEO chains inhibiting mobility of the growing amic acid chains during polymerization. This reduced viscosity was similar to that observed for the addition of PEO to homogeneous polymerization shown earlier (**Figure 6.9**), and resulted in successful electrospinning of

fibers. Electrospinning solutions prepared by the heterogeneous polymerization method required less added PEO than the homogeneous method.

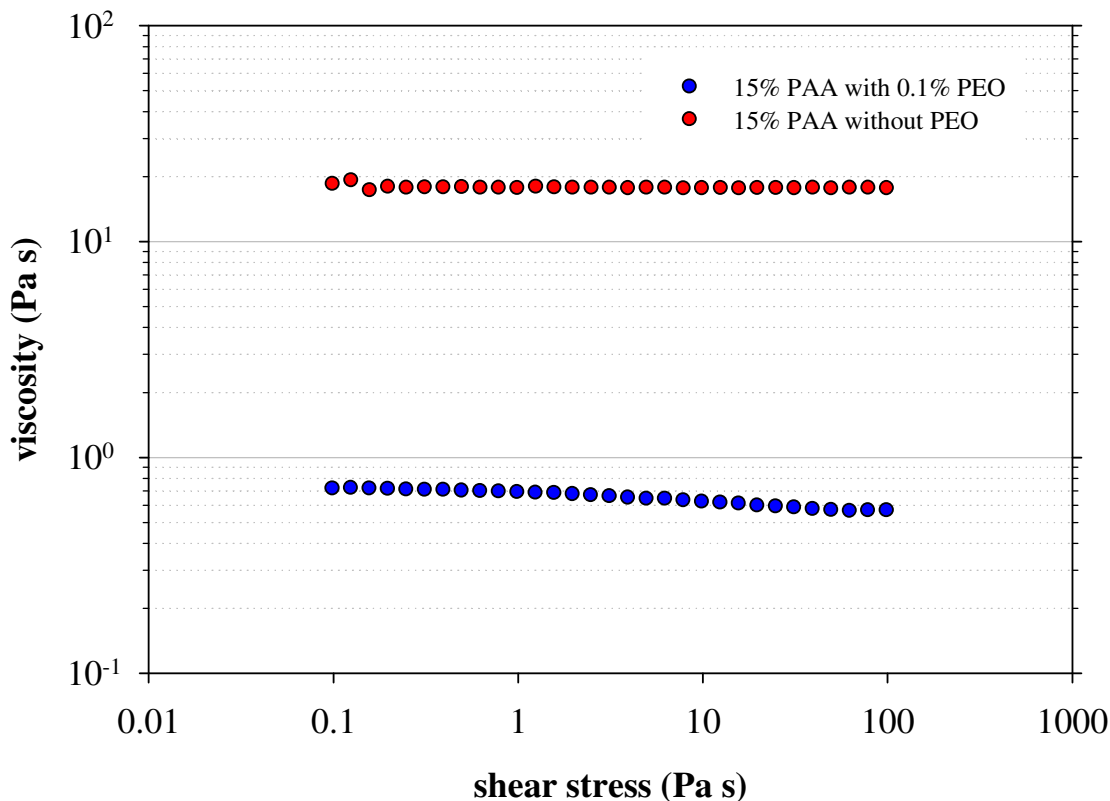


Figure 6.13 - Inclusion of 2 Mg/mol PEO resulted in a lower viscosity solution for the heterogeneous polymerization technique applied to PMDA-PPD solutions of 15 wt% total polymer.

6.3.2 Impact of Tin Complexes on Solution Properties and Electrospinning

Tin salts were introduced to the electrospinning solution to create composite nanofibers capable of storing lithium by the alloying of tin. Given reported success with silver acetate in PMDA-ODA fibers, and other metal acetates in DMF based electrospinning, tin acetate was added to solutions of PMDA-ODA. When the tin acetate ($\text{Sn}(\text{C}_2\text{H}_3\text{O}_2)_2$), 12.5

to 25 wt% with respect to polymer, was dissolved in the DMF prior to polymerization, the final addition of ODA resulted in a phase separation into a clear low viscosity liquid and a yellow-grey high viscosity phase. Continued mixing was unable to recombine these phases. If the polymerization was completed prior to the addition of tin acetate, a similar phase separation occurred during mixing. To reduce the possibility of water contamination the tin acetate was vacuum dried for 48 hours prior to use and no improvement was observed. These effects required the use of other sources of tin.

Alternative tin sources utilized were coordination complexes. In these molecules the metal cation is tightly complexed with one or more organic anions and the species do not dissolve in solvents. These complexes are often completely miscible in organic solvents and some are used as catalysts in organic synthesis. An initial test was conducted adding 0.09 g of palladium acetylacetonate (acac) ($\text{Pd}(\text{C}_5\text{H}_8\text{O}_2)_2$) (acac) dissolved in DMF to a fully polymerized PMDA-ODA solution of 34.2 wt%. The final solution was 24% polymer in DMF and 2% Pd(II) acac, no phase separation occurred, and it was possible to measure the increased shear viscosity (**Figure 6.14**).

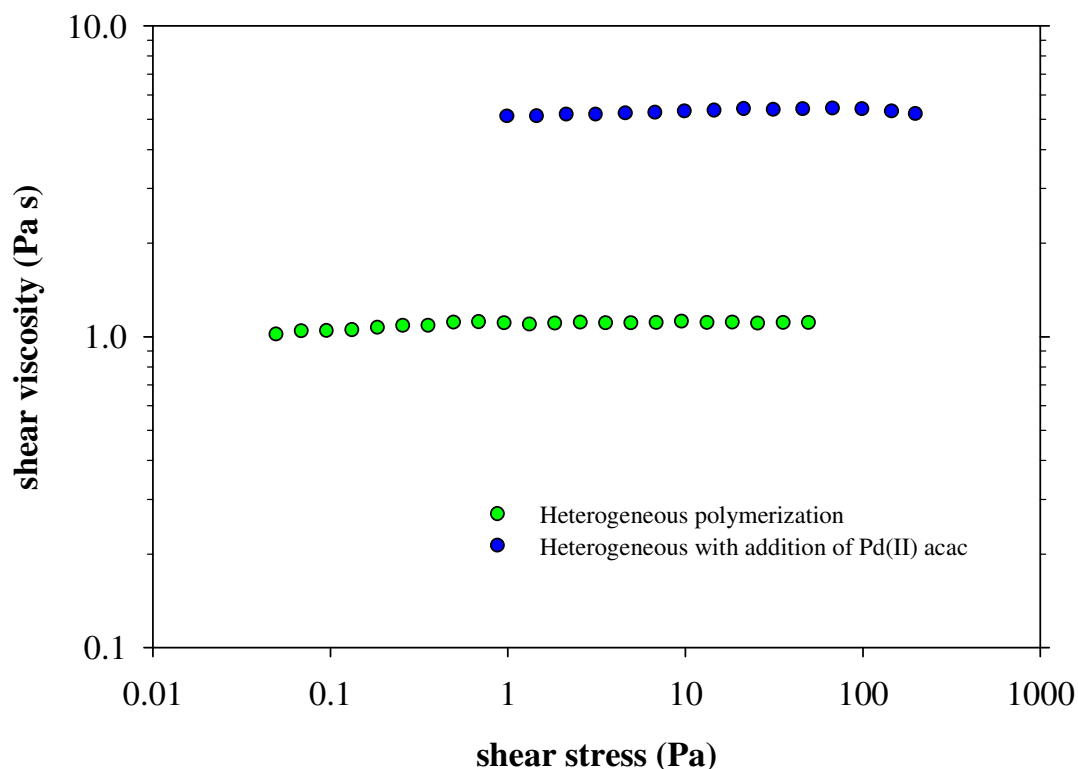


Figure 6.14 – Addition of 2 wt% Pd(II) acac increased viscosity for a PMDA-ODA solution with 24 wt% total polymer.

There were several possible explanations for the viscosity increase, first the heterogeneous polymerization was conducted at a significantly higher total polymer concentration, and in the case of heterogeneous polymerization the MW distribution could favor larger chains. After dilution these longer chains would still yield an increased viscosity. Second, the Pd(II) acac could have catalyzed further polymerization and increased the MW, as acac compounds are used in organic synthesis^{386, 387}. Finally the Pd acac complex could be act as a physical cross-linking agent with the carboxylic groups in the amic acid, causing an increase in viscosity. Physical cross-links would likely cause the solution to

display shear thinning, where high shear rates sever the association of the metal complex with the carboxylic sites on the PAA molecule.

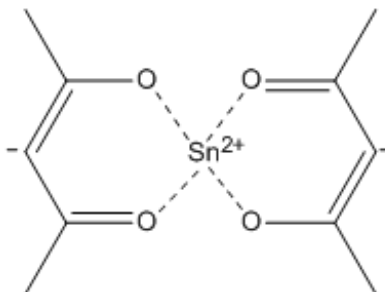


Figure 6.15 – The chemical structure of Sn(II) acetylacetonate.

Tin acetylacetonate is available for the Sn(II) oxidation state (**Figure 6.15**) as a yellow liquid fully miscible in DMF. At least 15 wt% Sn(II) acac with respect to the polymer was added to the solutions. If 50% of the polymer mass remained after pyrolysis, the final fibers would contain at least 10% tin by weight, assuming no tin is lost during thermal processing. The shear viscosity of two PMDA-ODA 28 wt% solutions containing 15 wt% Sn(II) acac relative to the polymer is compared to a reference of 28 wt% without any tin in **Figure 6.16**.

The lowest viscosity sample contained no tin complex. Addition of Sn(II) acac to an already polymerized solution resulted in two regions within the solution due to incomplete mixing, though there was no apparent phase separation, only a viscosity difference. The viscosity was measured for a sample taken from the less viscous region. Addition of the tin complex prior to any monomer created a uniform solution which had the highest shear viscosity of the three samples.

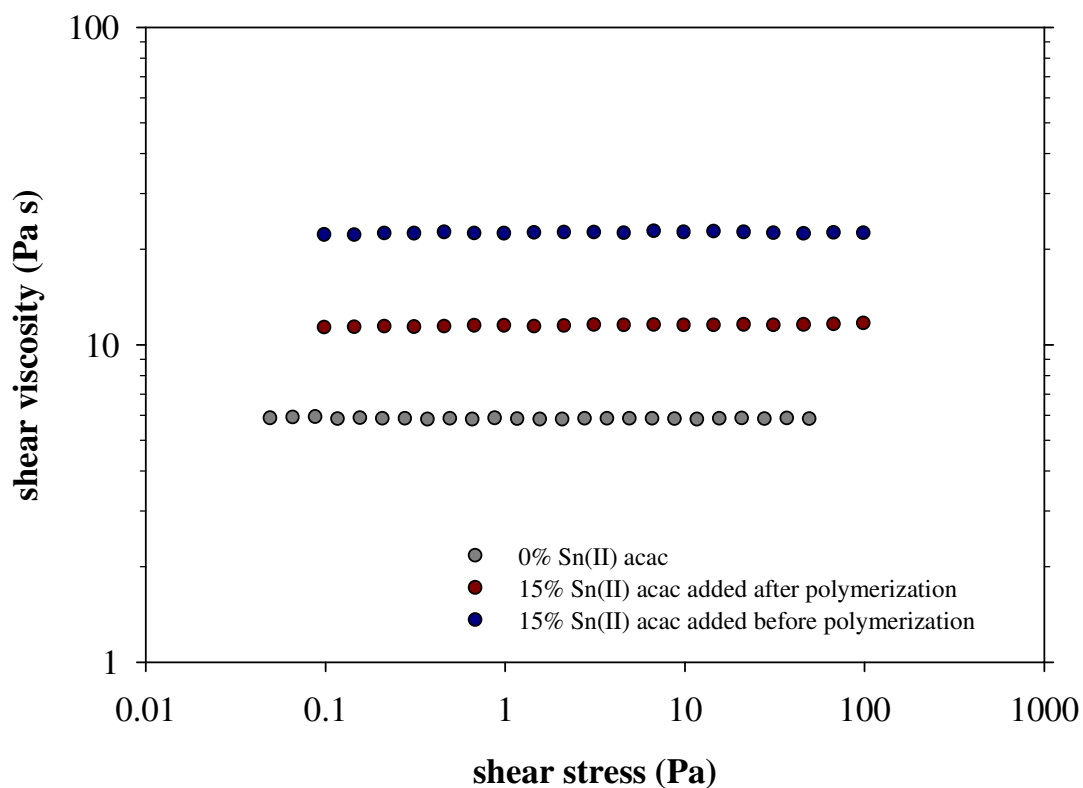


Figure 6.16 - Addition of 15 wt% Sn(II) acac relative to the polymer mass resulted in increased viscosity for PMDA-ODA solutions of 28 wt% total polymer.

The use of Sn(II) acac with 15 wt% PAA solutions based on the PPD monomer resulted in solutions so viscous they were unable to be pumped for electrospinning or measured on the rheometer, so an alternative liquid organometallic tin molecule was used, dimethyldineodecanoate tin (DMDND-tin) (**Figure 6.17**).

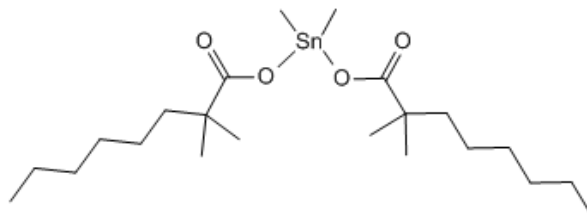


Figure 6.17 – The chemical structure of dimethyldineodecanoate tin.

Dimethyldineodecanoate tin is a more massive molecule per unit Sn than Sn(II) acac, so to maintain a similar theoretical tin loading in fibers requires more of the tin complex, approximately 23.25% would result in the same theoretical yield of tin. When added as the first step in making 15 wt% PAA solutions, the solutions displayed a marked increase in viscosity (**Figure 6.17**). There may be evidence of shear thinning behavior for the most viscous solution suggesting physical cross-linking rather than a real increase in MW. Both solutions were unable to be electrospun because of a stalled syringe.

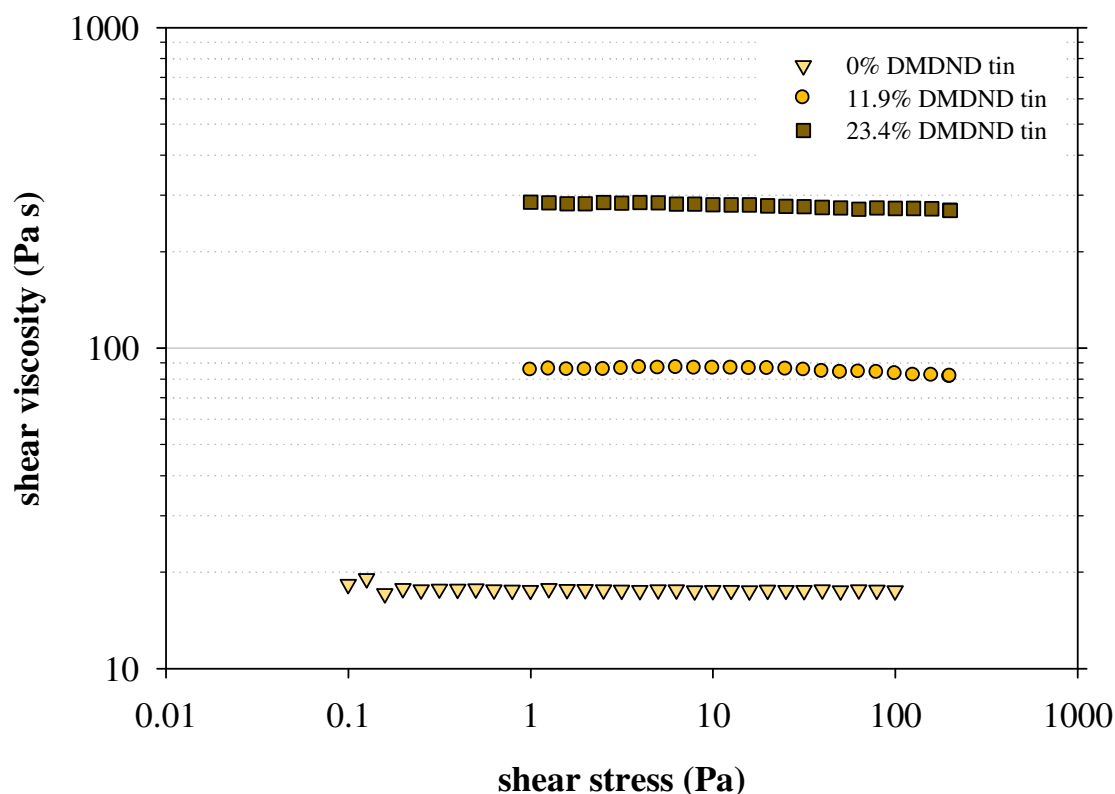


Figure 6.18 – Increased shear viscosity resulting from the addition of DMDND-tin prior to polymerization of PMDA-PPD with 15 wt% total polymer.

Reduction of the PAA content to 12 wt% still produced stalled syringe pumps for a solution with 16.25% DMDND-tin. **Table 6.2** contains a summary of various combinations of polymer, tin complex, and PEO additives and the quantitative and observed results. Most of these solutions show a slight shear-thinning trend for measured shear viscosity, providing evidence of potential physical cross-linking impacting the viscosity behavior. While there may exist a condition at which stable electrospinning of this system is possible, the time, material, and equipment constraints of this work have failed to identify the appropriate conditions.

Table 6.2 – Summary of attempts to utilize dimethyldiiododecanoate tin with low concentrations of PMDA-PPD derived poly(amic acid). Unless otherwise noted, the flow rate for electrospinning was set at 1 mL/h, tip to collector distance was 15 cm, and the needle was 22-gauge.

Sample Name	Wt % Polymer	PEO Wt %	Relative Wt% DMDND-tin	Shear Viscosity* (Pa s)	E-spin result	Notes
PPD36	12	0.1	30.25	300 to 250	Fail	Shear thinning, stalled pump
PPD37	10	0.1	30.25	N/A	Fail	Attempted 12-gauge needle, ended up with wet splatter of resin on the collector
PPD38	12	0.1	23.25	N/A	Fail	Stalled pump
PPD39	9	0.05	21	50 to 45	Electrospray	Shear thinning
PPD40	9	0.1	21	27 to 24	Electrospray	Shear thinning
PPD41	9	0.2	21	33.5 to 30	N/A	Shear thinning, damaged syringe
PPD44	9	0.2	21	36 to 31	Spin/spray mix	Shear thinning, pump stall
PPD46	9	0.3	21	54 to 49	Electrospin	Shear thinning, pump stalled for 22 gauge needle, and a wet splatter was collected for 12-gauge needle, 20 gauge needle suffered pump stall and produced insufficient material to make into cells

*Shear viscosity was highest for low shear stress and slightly decreased as shear stress increased.

6.3.3 Results of Size Exclusion Chromatography

Size exclusion chromatography (SEC) was employed to determine the average MWs of the poly(amic acids) produced for reactions at various polymer and tin compound loadings. Accurate results for poly(amic acid) solutions require the use of buffering chemicals to suppressing dissolution of the polyelectrolyte and interaction with the polystyrene stationary phase contained within the column²⁶⁰. The mobile phase chosen for all SEC measurements was a solution of 0.03 M LiBr and 0.03 M H₃PO₄ in HPLC grade DMF. Calibration of the column was conducted using PEO standards (**Table 6.3**), and all MW distributions reported are equivalent MWs to PEO, an established practice when standards for the polymer under study are not available. Universal calibration of a column is possible if the Mark-Houwink parameters are known for both the polymer standards and experimental polymer in a given solvent²⁵⁹, and has been demonstrated for poly(amic acids)²⁵⁵, but was not possible due to constraints on equipment availability. Additionally, unless otherwise noted all samples presented here were polymerized by the heterogeneous method with the solid dianhydride added to the diamine in solution, and none contained 2 Mg/mol PEO.

Table 6.3 – Reported number average molecular weight (M_n) , weight-average molecular weight (M_w), and polydispersity index (PDI) of the PEO standards used to calibrate the differential RI detector on the size exclusion chromatography column.

Standard	M_n (g/mol)	M_w (g/mol)	PDI
PEO1	600	660	1.10
PEO2	2000	2150	1.08
PEO3	4000	4160	1.04
PEO4	10000	10600	1.06
PEO5	50000	59500	1.19
PEO6	360000	378000	1.05

With narrowly dispersed standards it is common to use the arithmetic or geometric mean of M_n and M_w to identify the peak position. In this work the arithmetic mean was chosen. A plot of the six standards elution time as measured by differential refractive index (RI) is provided in **Figure 6.19**. Response of the detector beyond 21 minutes is ignored as that represents what are commonly referred to as solvent peaks, and are common to every injection of the column, including the solvent blank in **Figure 6.19**. The chromatogram for the four lower MW standards ($M_n = 200, 2,000, 4,000$ and $10,000$ g/mol) are noticeably sharper than the last two, caused by a lower polydispersity index (PDI). The reported PDI for the highest MW sample (360 kg/mol) was labeled as the second smallest of the standards, but the chromatogram indicates the provided PDI value is likely incorrect, thus the calibration at higher molecular weights is less accurate.

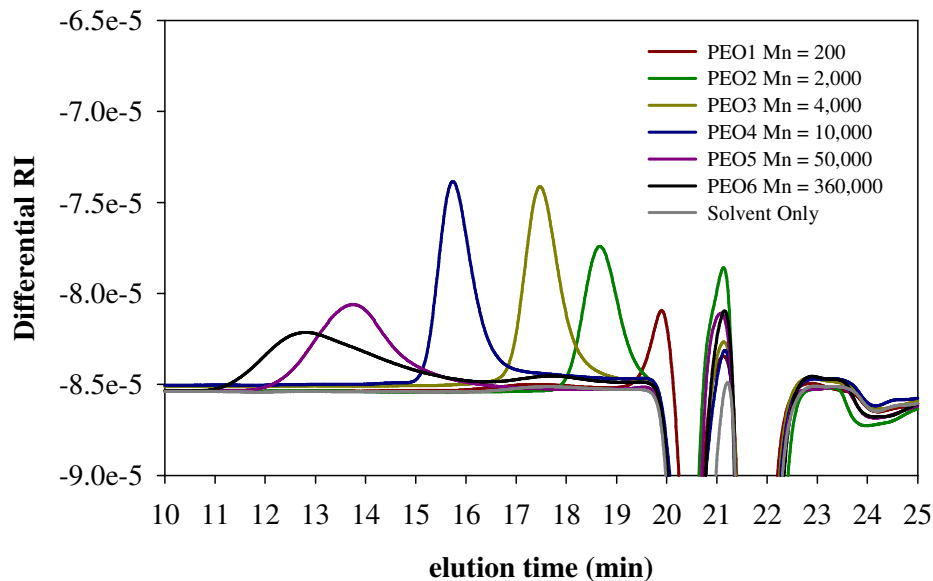


Figure 6.19 – Elution of PEO standards measured by differential refractive index (RI) and used to calibrate the column used for size exclusion chromatography. The high molecular weight standards elute at earlier times than the low molecular weight standards.

Based on the results in **Figure 6.19** the peak response time was assigned the arithmetic mean MW of the standard. The logarithm of this value was then plotted against the response time (**Figure 6.20**). The most commonly used fit to construct a calibration curve is a third order polynomial²⁵⁹, and that produces the best fit of this data, resulting in the calibration equation correlating elution time with $\log(\text{MW})$. This equation is used to convert the elution time for a given the differential RI response to an equivalent molecular weight.

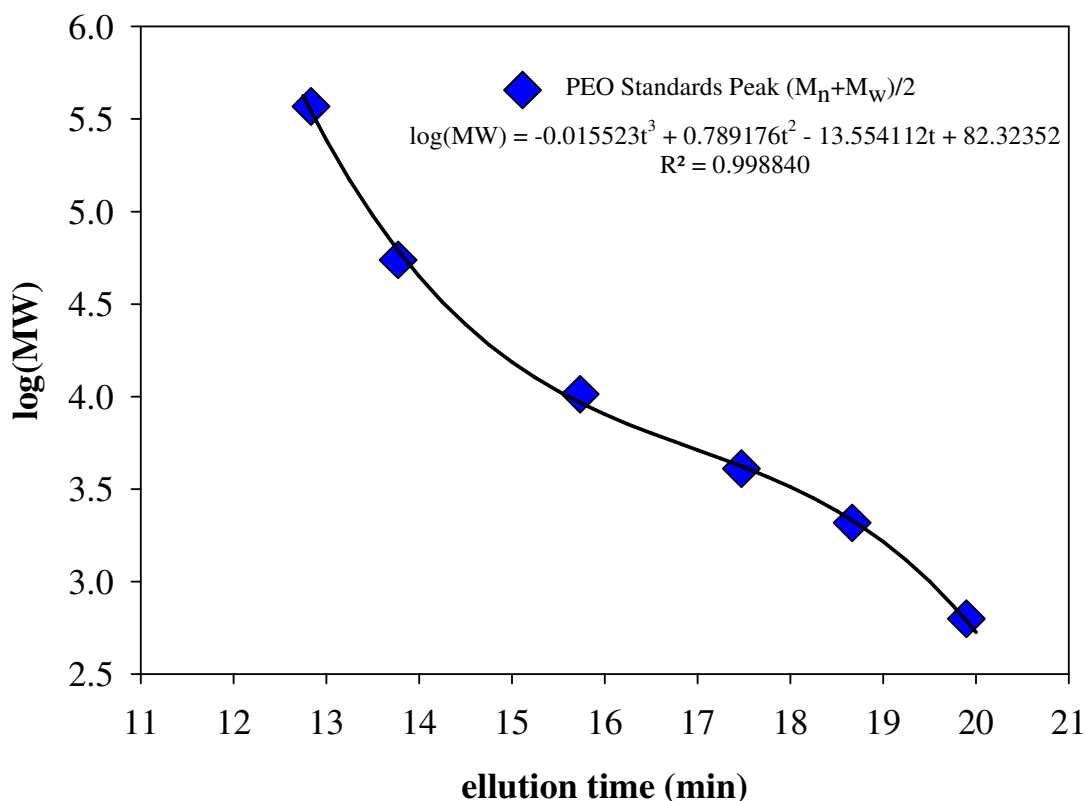


Figure 6.20 – Calibration curve constructed using PEO standards for measuring the equivalent molecular weight of poly(amic acids) based on the differential refractive index response.

The MW distribution of 20 and 25 wt% poly(amic acid) solutions made from PMDA and ODA was measured over the course of 3 days (**Figures 6.21 and 6.22**), beginning with the day of polymerization. There is little change in either sample over the course of three days with calculated values of M_n and M_w displayed in **Table 6.4**, so any equilibration of these solutions is slow. It is important to point out that the MW distribution of these samples exceeds the largest calibration standard ($M_n = 360,000$ g/mol) and thus at the high end of the distribution the results are an extrapolation from the calibration curve. The impact of 4% of

phthalic anhydride terminating agent is also contained in **Table 6.4**, and illustrated in **Figure 6.23**, and the average MW has been significantly lowered.

Table 6.4 – Equivalent number and weight average molecular weight of PMDA-ODA samples as measured by SEC over three days beginning on the day of polymerization.

Sample	M _n (kg/mol)			M _w (kg/mol)		
	Day 1	Day 2	Day 3	Day 1	Day 2	Day 3
20 wt%	13.7	13.0	14.2	50.3	47.9	59.0
25 wt%	15.9	16.1	15.8	72.6	73.4	73.3
25 wt% with 4% PA	8.0	N/A	N/A	18.1	N/A	N/A

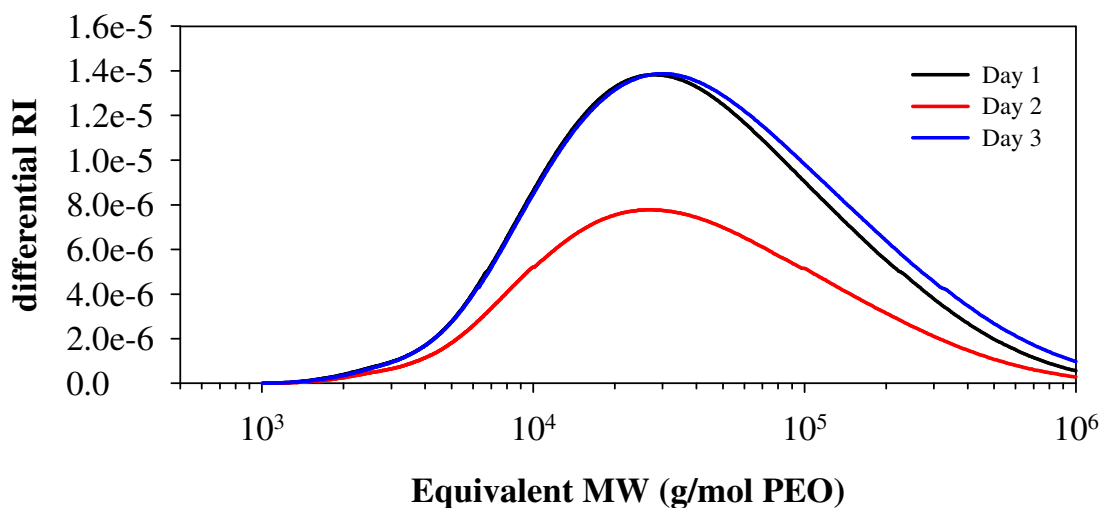


Figure 6.21 – MW distribution of a PMDA-ODA solution of 20 wt% total polymer measured once a day for three days, beginning on the day of polymerization.

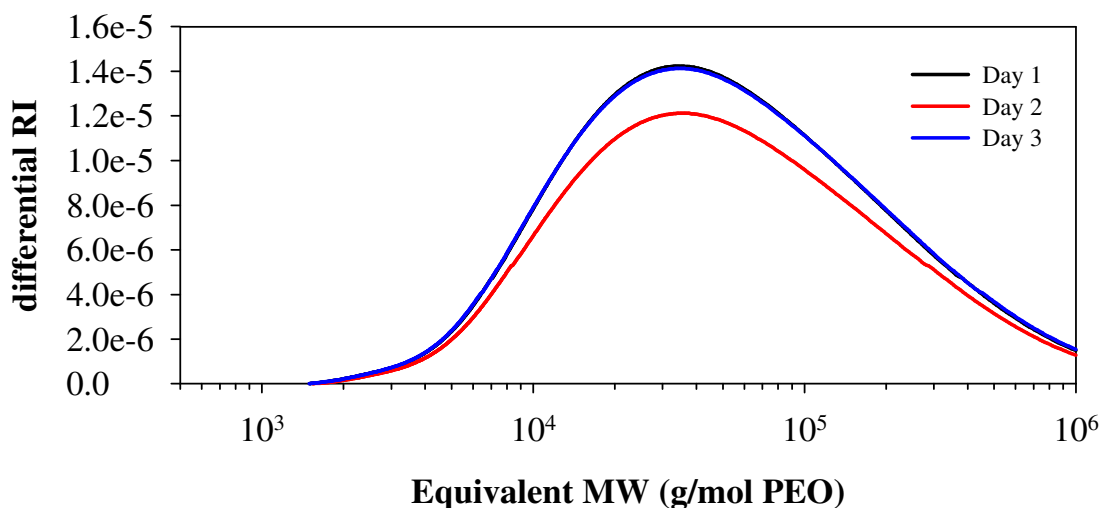


Figure 6.22 – MW distribution of a PMDA-ODA solution of 25 wt% total polymer measured once a day for three days, beginning on the day of polymerization.

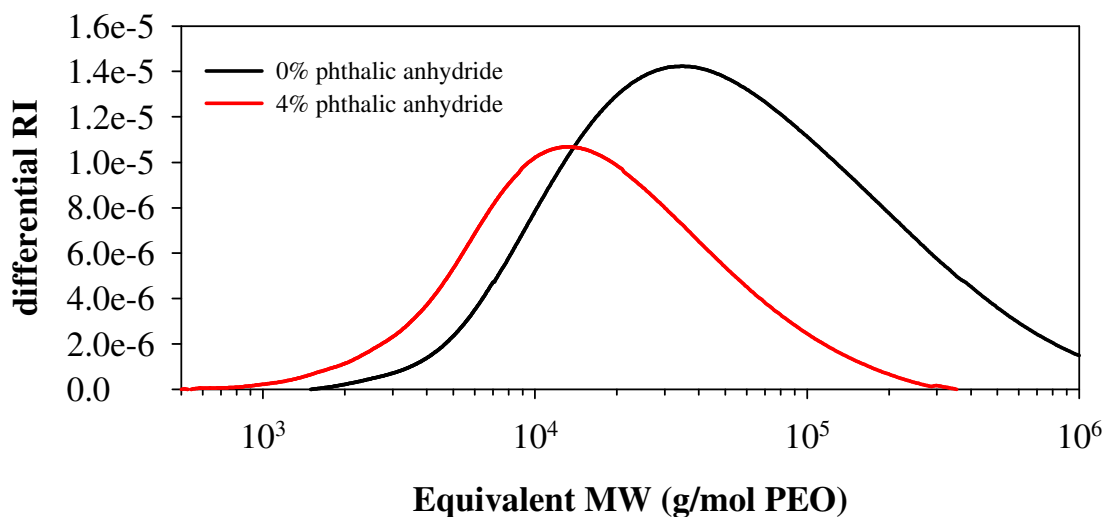


Figure 6.23 – MW distribution of a PMDA-ODA solution of 25 wt% total polymer with and without 4% PA.

The MW distribution of 15 and 20 wt% poly(amic acid) made from PMDA and PPD are presented in **Figures 6.24** and **6.25** and **Table 6.5**. For these samples over half the signal

is located above the highest MW standard, and thus the error from extrapolation is greater than for the PMDA-ODA results. In this case, the less concentrated solution results in the larger MW polymer. It appears that the average MW of the samples is decreasing as the resins equilibrate, but there is an appearance of a very small second peak at very high MW, not shown for the differential RI measurements. The data available from a light scattering detector clearly shows the signal of this very high MW peak (**Figure 6.26**). Thus the long term trend of these samples is the slow conversion of the longer chains into smaller chains by equilibration, but also further reaction to create cross-linked gels.

Table 6.5 – Equivalent number and weight average molecular weight of PMDA-PPD samples as measured by SEC over three days beginning on the day of polymerization.

Sample	M _n (kg/mol)			M _w (kg/mol)		
	Day 1	Day 2	Day 3	Day 1	Day 2	Day 3
15 wt%	45.1	42.5	33.3	2330	1230	605
20 wt%	34.4	25.4	26.4	1507	419	331

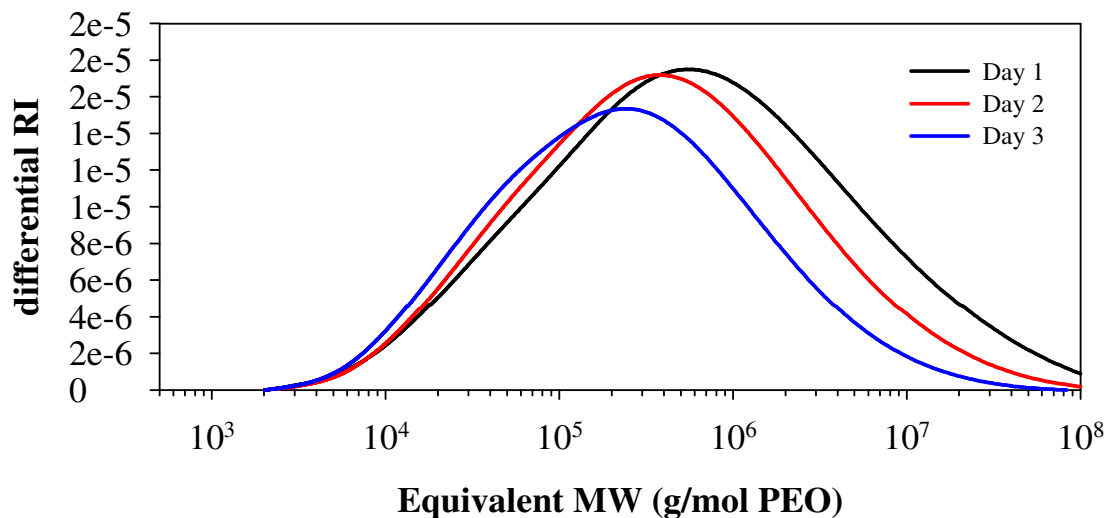


Figure 6.24 - MW distribution of a PMDA-PPD solution 15 wt% total polymer measured once a day for three days, beginning on the day of polymerization (NOTE: the highest MW standard available was ~400 kg/mol).

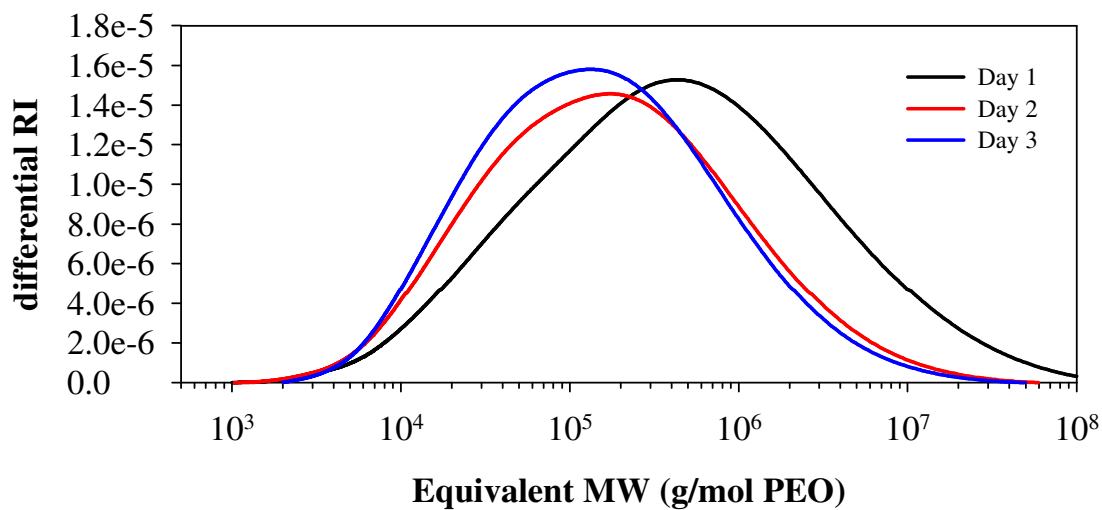


Figure 6.25 - MW distribution of a PMDA-PPD solution of 20 wt% total polymer measured once a day for three days, beginning on the day of polymerization (NOTE: the highest MW standard available was ~400 kg/mol).

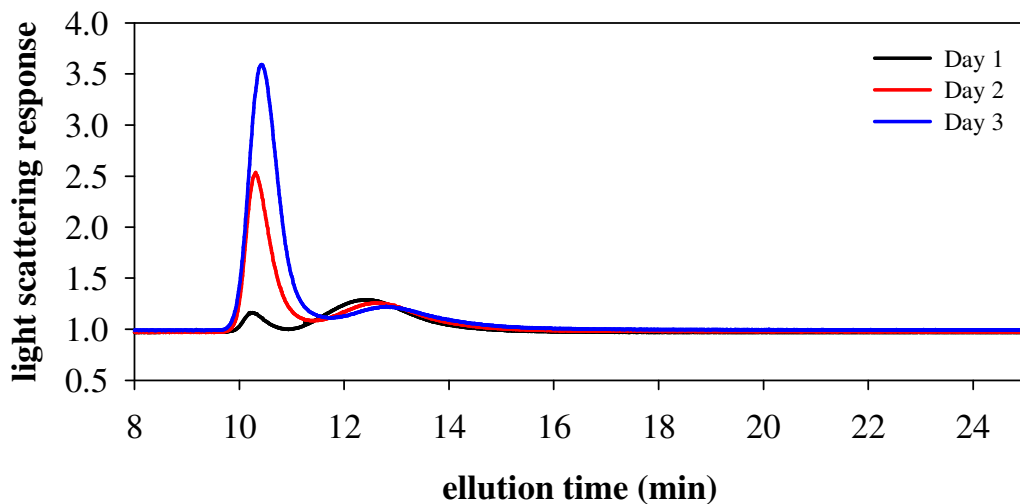


Figure 6.26 – Raw light scattering data shows a strong response to very large molecules, which elute at shorter times, forming in a PMDA-PPD solution of 15 wt% total polymer measured once a day for three days beginning on the day of polymerization.

The mobile phase used for these measurements is DMF buffered with H_3PO_4 and LiBr because the sample is a polyelectrolyte, and as such the dilution to low concentrations in an acidic environment could impact the equilibrium state of these polymers, as explained below. Each diluted sample was at least 1 mL in volume, and of that only 100 μL was injected into the column for a given test. Thus there was extra sample available for measurement on subsequent days (**Figure 6.27**). The peak response for re-injection of 20% PMDA-ODA is shifted to a lower MW each day as the presence of protons in solution shifts the equilibrium of the reaction to more unreacted anhydride and diamine.

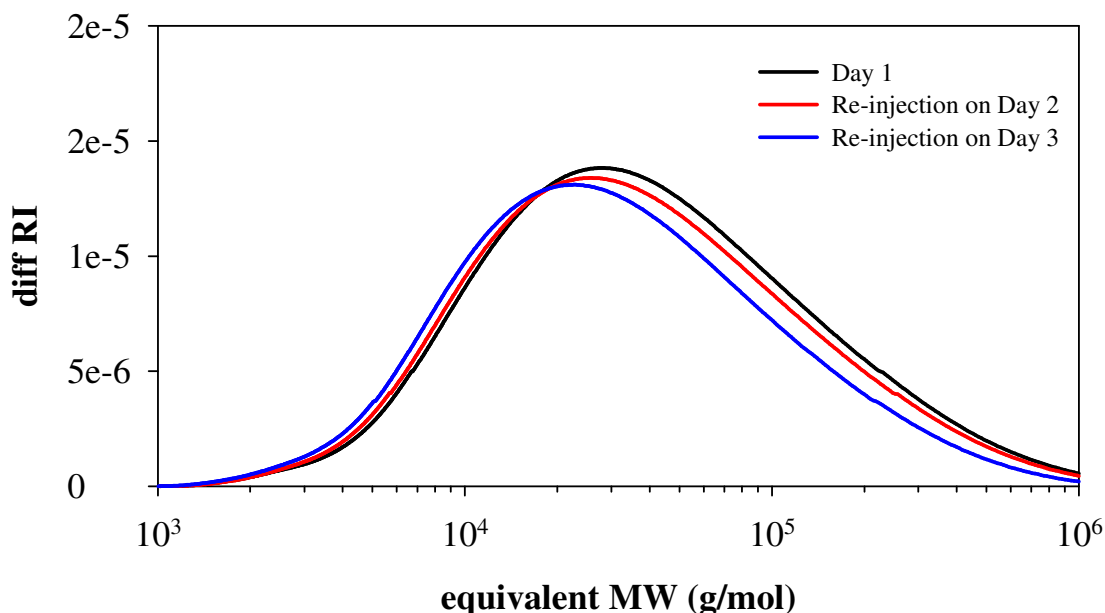


Figure 6.27 – Reduction of average MW for a PMDA-ODA solution of 20 wt% total polymer measured, once each a day for three days by re-injecting the sample diluted in the buffered DMF mobile phase on the day of polymerization.

Similarly the reinjection of the 15 wt% PMDA-PPD sample is shown in **Figure 6.28**, and compared to the sample prepared on the second day. Due to an equipment malfunction data for the on the third day is unavailable. The reduction in MW of this sample in the acidic environment is greater than the reduction in MW of the equilibrating concentrated resin. There is a signal present from the light scattering detector for very large MW molecules (**Figure 6.29**) for both second day samples, but the relative intensity is greater for the sample prepared after the original concentrated resin aged a day.

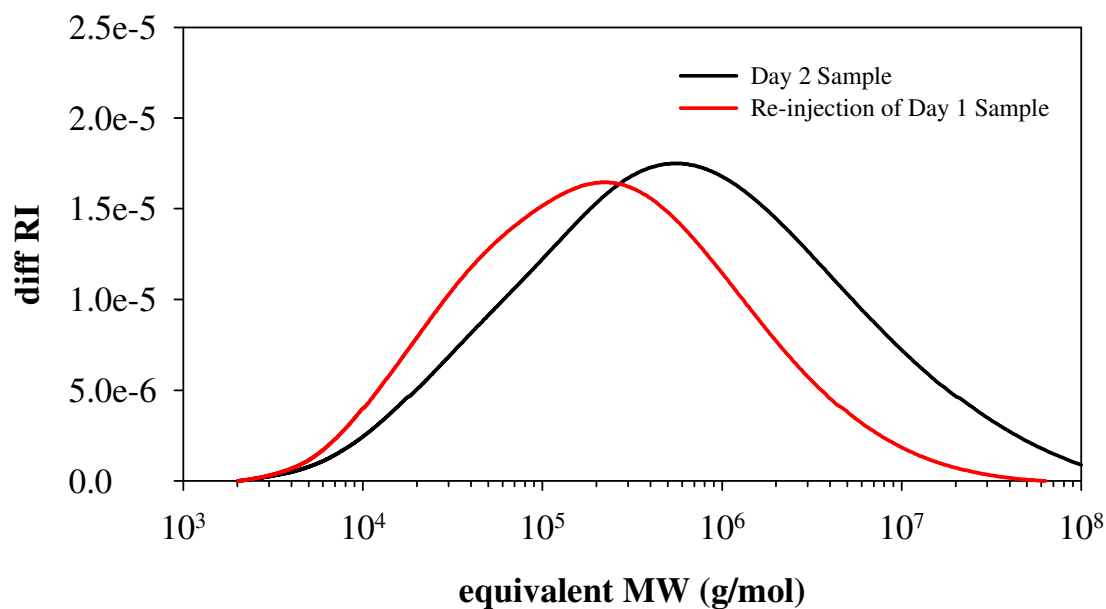


Figure 6.28 – Shift in MW distribution for a PMDA-PPD solution of 15 wt% total polymer, measured by re-injecting the sample diluted in the buffered DMF mobile phase on the day of polymerization the next day. (NOTE: the highest MW standard available was ~400 kg/mol)

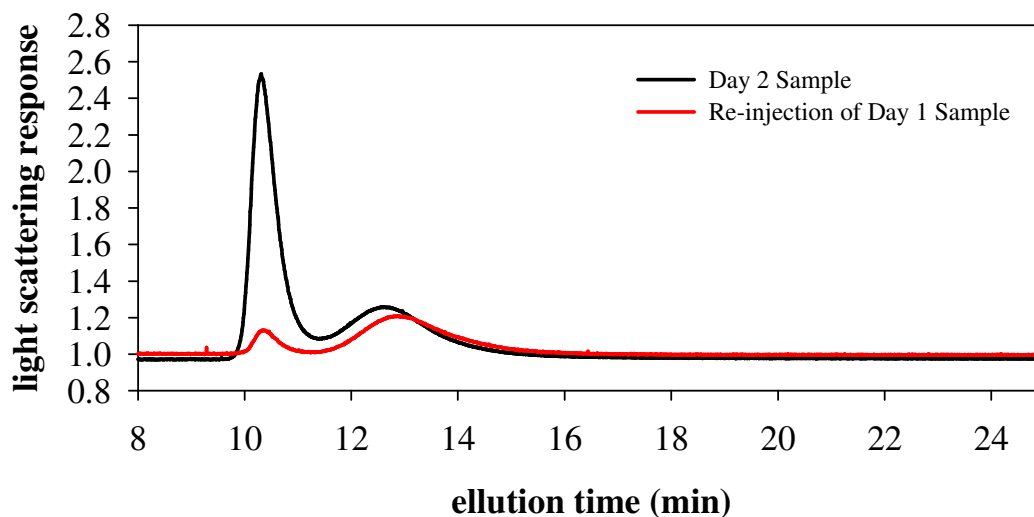


Figure 6.29 – Comparison of raw light scattering response of a sample measured on the second day to a re-injection of the first day sample for a PMDA-PPD solution of 15 wt% total polymer.

The addition of tin complex had a noticeable impact on the MW distribution of both polymers. **Figure 6.30** presents the results for the polymerization of PMDA-ODA solutions containing 25 wt% total polymer. The two tin complexes, based on SEC results, had opposite effects on the MW of this polymer. The addition of the Sn(II) acac has lowered the average MW with M_w dropping from 72.5 kg/mol to 44.3 kg/mol. The dimethyldineodecanoate tin increased to average MW, with M_w now having a value of 255 kg/mol.

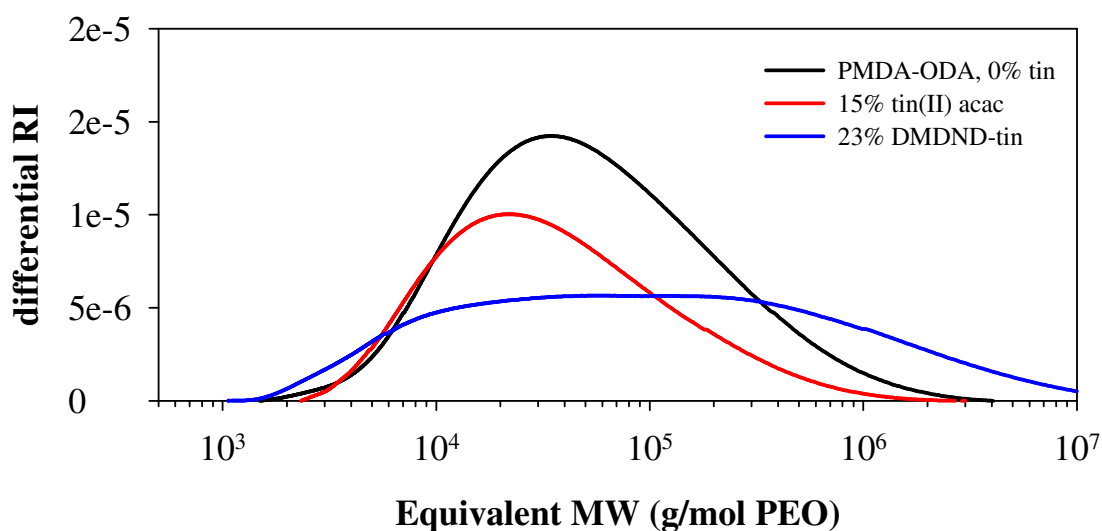


Figure 6.30 – Change in MW distribution for PMDA-ODA solutions of 25 wt% total polymer with the inclusion of Sn(II) acac and DMDND-tin. (NOTE: the highest MW standard available was ~400 kg/mol)

When tin complexes were added to the PMDA-PPD solutions prior to polymerization they both lowered the average MW (**Figure 6.31** and **Table 6.6**). Not only did both complexes lower the MWs of the resin, but increased amounts of tin resulted in even lower MWs. This contrasts with the rheology of these solutions shown in **Figure 6.18**, where the increasing amounts of DMDND-tin increased the solution viscosity by orders of magnitude. Though very little shear thinning was observed, the high viscosity of the concentrated PMDA-PPD solutions containing tin is significant evidence of physical cross-linking. The cross-links are then not present at the dilute, buffered conditions necessary for size exclusion chromatography. Also of note is the similarity of the MW distribution of the samples containing 15% Sn(II) acac and 23.25% DMDND-tin. Those relative fractions of tin

complexes would result in an approximately equivalent amount of tin residing in any electrospun fibers after pyrolysis (~10%).

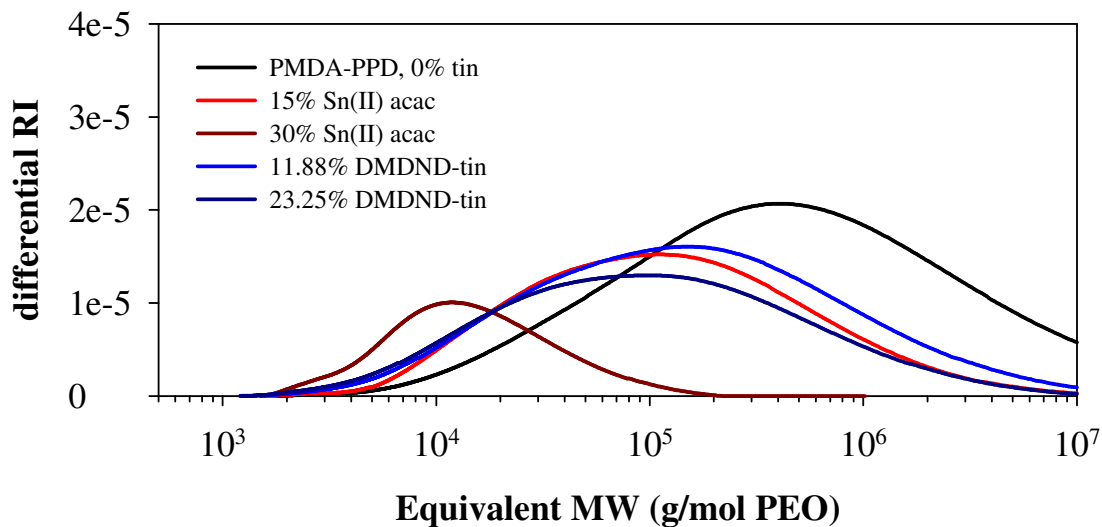


Figure 6.31 – Change in in MW distribution for PMDA-PPD solutions of 15 wt% total polymer polymerized with the inclusion of Sn(II) acac and DMDND-tin. (NOTE: the highest MW standard available was ~400 kg/mol)

Table 6.6 – Equivalent number and weight average molecular weight of 15 wt% PMDA-PPD samples, polymerized with the indicated amount of tin compounds relative to polymer mass, as measured by SEC.

Sample	M_n (kg/mol)	M_w (kg/mol)
15 wt% PMDA-PPD	50.2	1610
with 15% Sn(II) acac	23.8	220
with 30% Sn(II) acac	8.3	15.2
with 11.88% DMDND-tin	22.9	325
with 23.25% DMDND-tin	17.9	193

The combination of concentrated solution rheology and these MW distributions can provide an explanation for the difficulty of producing electrospun fibers from PPD based polyimide. The physical cross-linking occurring in the concentrated solution prevented pumping the solutions through the syringe at low shear rates. The use of larger gauge needles made pumping some solutions easier. The resulting droplets present at the end of the needle did not contain sufficient entanglements, and the stress created in the jet released from the Taylor cone is sufficient to break the physical cross-links. Therefore the jet breaks into droplets and electrosprays onto the collector. Finally, the addition of high MW PEO produced some success in transitioning from electro spraying to electro spinning (**Table 6.2**), but it contributed to the pump stalling. When the resulting Taylor cone was drawn into a fiber, the result was often fibers arriving at the collector still containing significant solvent, and creation of a region in the center of the collector where the polymer is still in solution.

6.3.4 *Electrochemical Performance*

Continuous nanofiber mats were electrospun from PMDA-ODA samples and PMDA-PPD samples with a small quantity of high MW PEO additive. The resulting non-wovens

were imidized at 250 °C and pyrolyzed at either 700 or 900 °C. Similar to the PAN based fibers discussed in Chapters 3, 4, and 5 these materials show a significant capacity fade over the first 10 cycles (**Figure 6.31**). The stable reversible capacity (~300 mAh/g) of the materials at low currents is lower than the PAN based fibers (Chapters 3 and 4) by around 30%, partly explained by the lower cutoff voltage during discharge (2.0 V for PI vs. 2.5 V for PAN). The capacity retention, defined as the percentage of maximum stable reversible discharge capacity available at low current realized at increased currents, of these materials is significantly improved and is provided in **Table 6.7** for comparison to the untreated PAN fibers used in **Chapter 4**. The greater order present in these fibers, indicated by the lower I_D/I_G ratio from Raman spectroscopy, is contributing to an improved electronic conductivity, enabling greater capacity utilization as current increases.

Table 6.7 – Comparison of the capacity retention at the indicated increasing applied currents for the various precursor polymers used in this work.

Sample	Raman				
	I_D/I_G Ratio	50 mA/g	100 mA/g	200 mA/g	400 mA/g
ODA 700 °C	1.34	86.7%	73.9%	62.9%	53.1%
ODA 900 °C	1.19	91.0%	79.9%	69.8%	59.9%
PPD 700 °C	1.22	83.9%	68.7%	54.3%	38.5%
PPD 900 °C	1.26	86.1%	75.2%	66.0%	56.2%
PAN 700 °C	1.42	84.3%	64.2%	46.4%	N/A

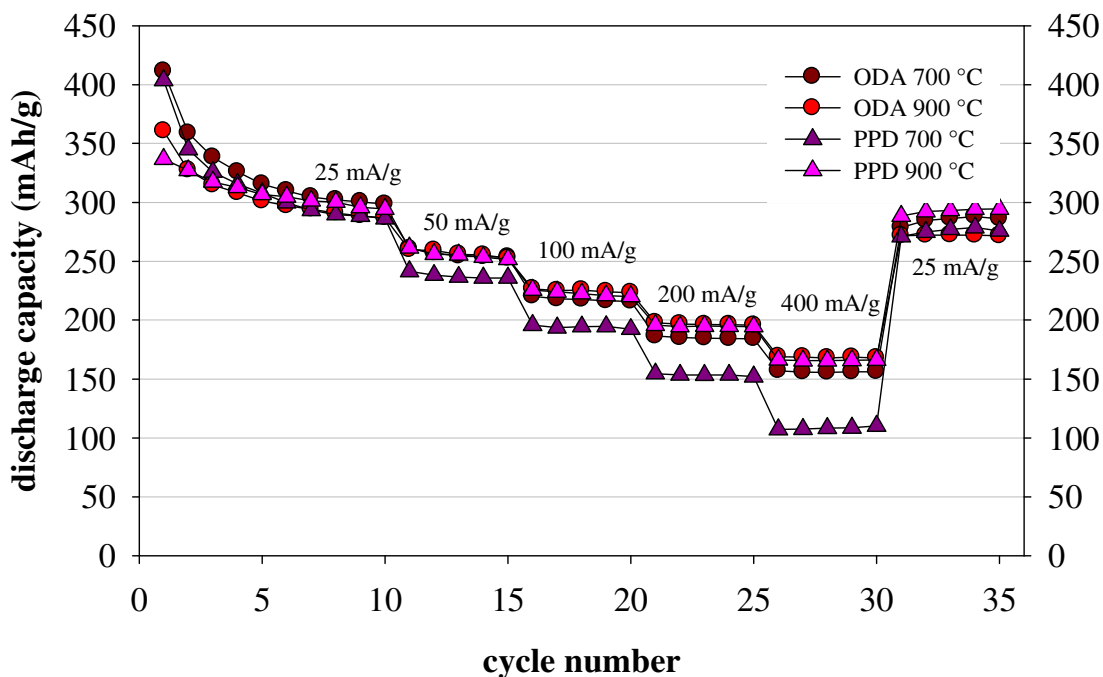


Figure 6.32 – Reversible discharge capacity of polyimide-based nanofiber electrodes. Fibers were pyrolyzed at two different temperatures and then cycled over a range of symmetric currents for charge and discharge.

Equally important to the utility of these polyimide-based electrodes is the first-cycle irreversible capacity (**Figure 6.33**). Electrodes made from both polyimides pyrolyzed at 700 °C would fall in the high range (>400 mAh/g) for irreversible capacity of PAN pyrolyzed at 700 °C, but the PPD-based material suffered smaller losses than the ODA-based cells. At the higher pyrolysis temperature the ODA-based cells fall within the middle of the PAN distribution shown previously in **Figure 3.1**. The PPD-based cells all suffer lower losses than any of the PAN cells pyrolyzed at 900 °C. For PAN electrodes pyrolyzed at either 700 and 800 °C, only one cell from each population ($n_{\text{total}} = 44$ and 34 respectively) showed a lower irreversible capacity than the cells made with electrodes of PMDA-PPD fibers

pyrolyzed at 900 °C. This data illustrates the two potential advantages of using pyrolyzed PMDA-PPD fibers as the host matrix for high-capacity Li storing nanoparticles. The materials will have better capacity retention and less irreversible losses than PAN derived alternatives processed under similar conditions.

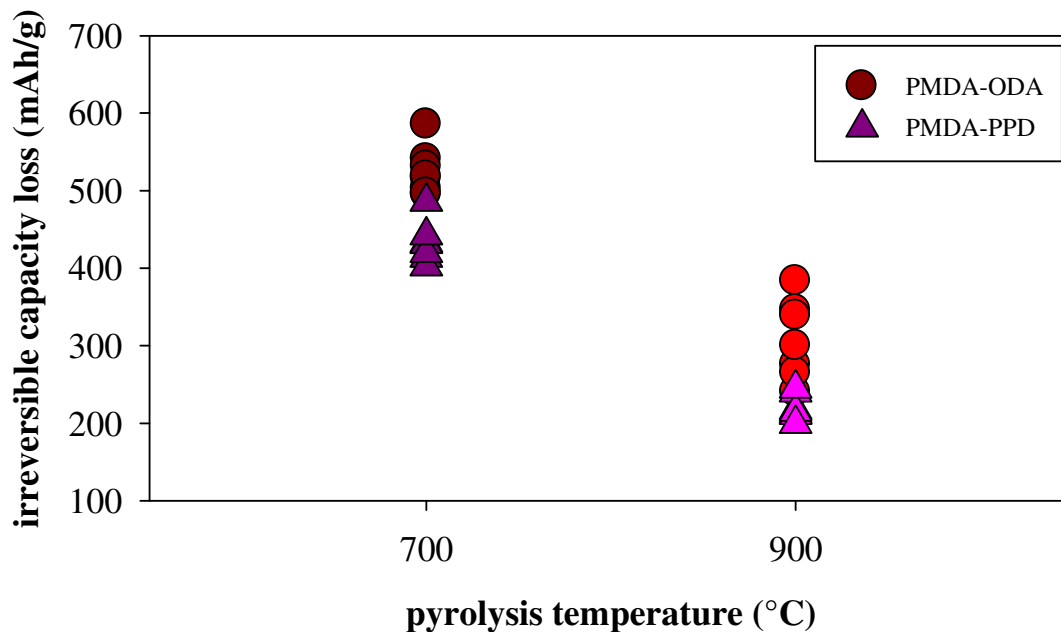


Figure 6.33 - First-cycle irreversible capacity losses of polyimide-based nanofiber electrodes.

Attempts to produce carbon-tin composite nanofibers using the PPD monomer were unsuccessful, but electrospinning PMDA-ODA resins with both Sn(II) acac and DMDND-tin was accomplished. There were two solutions electrospun containing Sn(II) acac, 26 and 28 wt% resin and 15% tin complex with respect to the total polymer mass. The pyrolysis temperature was 700 °C, and 60% of the mass of the mat remained after pyrolysis. The average fiber diameters were approximately 530 and 610 nm (**Figure 6.34**). Of note are the

SnO₂ particles decorating the exterior of the fibers in a few locations, as inferred from EDS analysis of other samples described later. These particles were more prevalent in the 26 wt% sample (**Figure 6.34a** and **6.34c**) than in the fibers spun from the 28 wt% solution (**Figure 6.34b** and **6.34d**), though the region featured was the most dramatically decorated area found. Based on the initial tin loading in the resin, these fibers should contain approximately 8.7% tin, assuming none is lost during thermal processing. Inductively coupled plasma mass spectrometry (ICP-MS) was used to determine the tin content in the fibers after pyrolysis. The smaller diameter fibers contained 6.52 wt% tin and the larger fibers contained 7.27 wt% tin. The cycling data for these cells is not reported because the battery test stand was out of calibration, underestimating the current during charging and overestimating it during discharge, resulting in electrodes that were reporting well over 100% coulombic efficiency. An inspection of the charge and discharge curves reveals no features between 0.6 and 0.4 V that would correspond to alloying of Li with Sn (**Figures 6.35** and **6.36**).

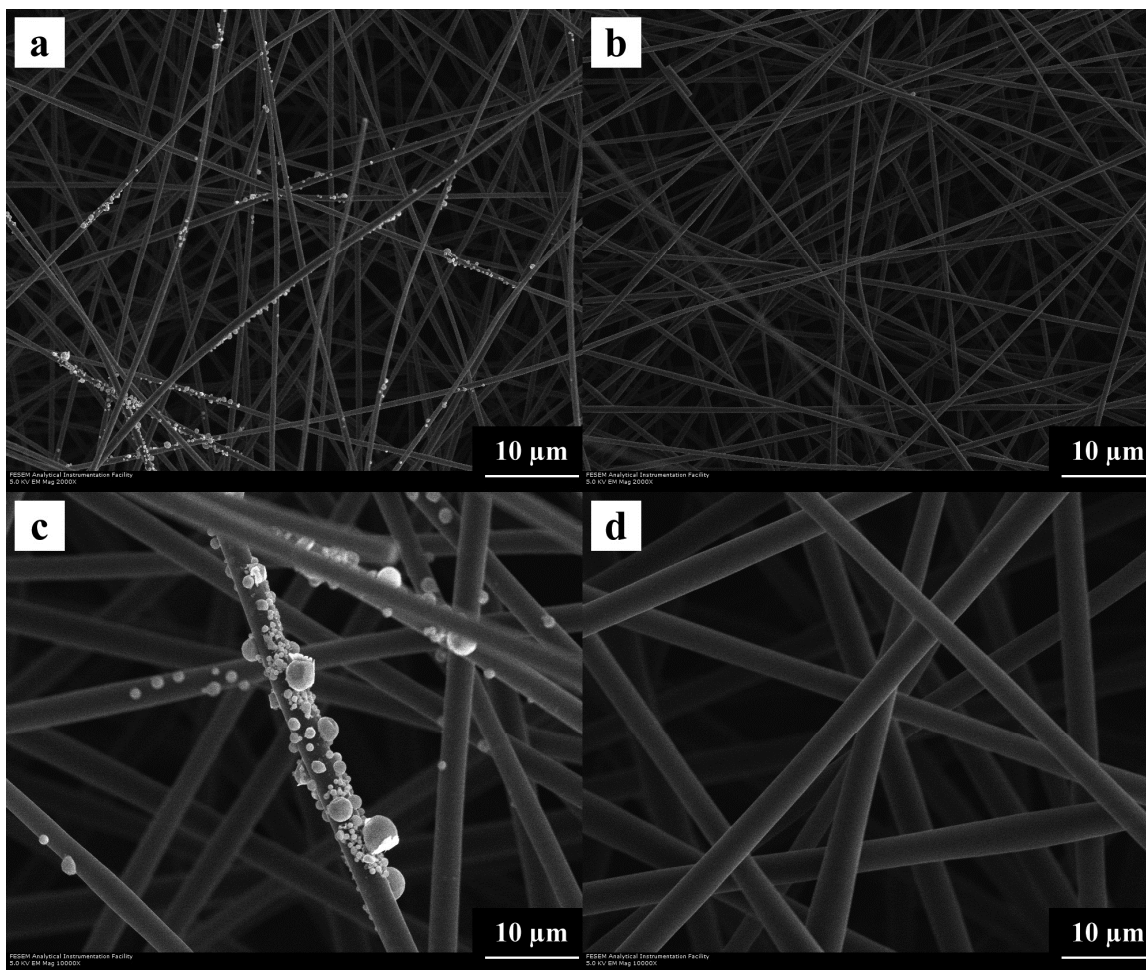


Figure 6.34 – Scanning electron micrograph of PMDA-ODA fibers pyrolyzed at 700 °C, with visible tin oxide particles. Samples were electrospun from a 26 wt% solution (a,c) and a 28wt% solution (b,d) containing 15 wt% Sn(II) acac relative to the polymer mass. Imaged at 2,000x (a,b) and 10,000x (c,d).

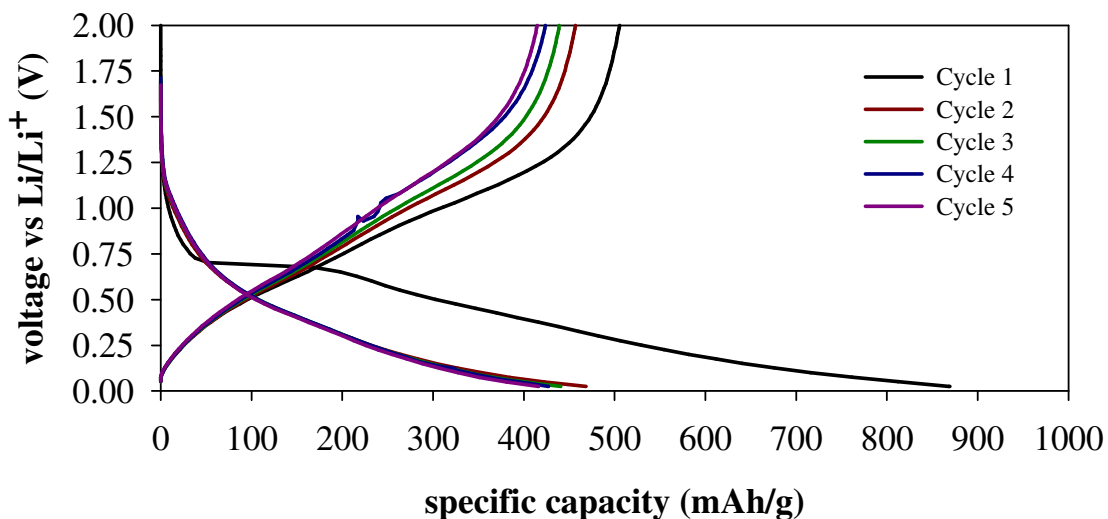


Figure 6.35 – Voltage profiles during charge and discharge for a typical electrode made of fibers spun from a PMDA-ODA solution of 26 wt% polymer, containing 15 wt% Sn(II) acac with respect to polymer mass, pyrolyzed at 700 °C and containing tin oxide. No feature corresponding to reversible Li alloying with Sn is observed near 0.4 V^{1, 129}.

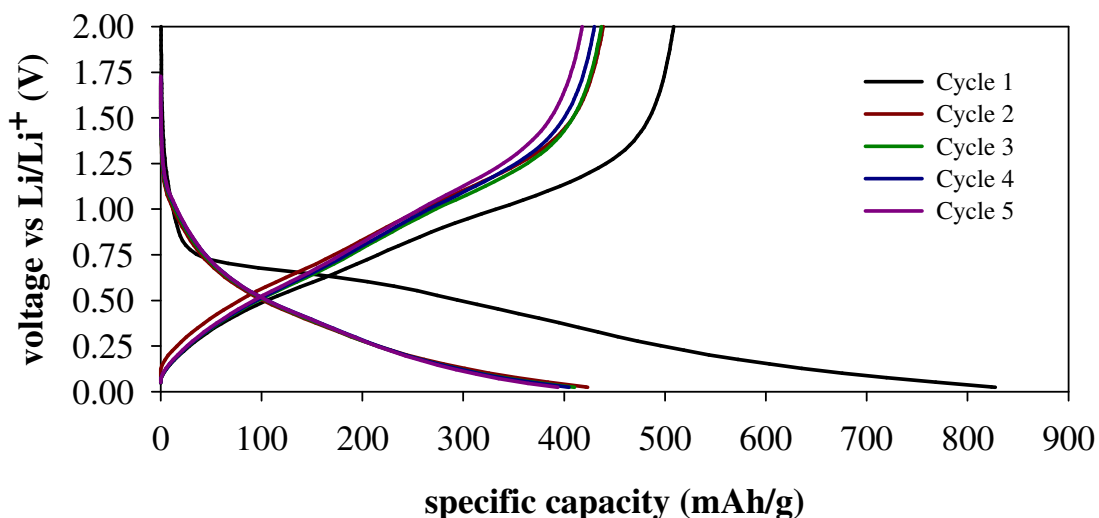


Figure 6.36 – Voltage profiles during charge and discharge for a typical electrode made of fibers spun from a PMDA-ODA solution of 28 wt% polymer, containing 15 wt% Sn(II) acac with respect to polymer mass, pyrolyzed at 700 °C and containing tin oxide. No feature corresponding to reversible Li alloying with Sn is observed near 0.4 V.

Additional fibers were prepared by electrospinning a PMDA-ODA solution containing 22 wt% polymer and 23.25% DMDND-tin complex with respect to the total polymer mass. Samples were pyrolyzed at either 700 or 900 °C. The fibers ranged between 0.75 and 1 μm for fibers pyrolyzed at 700 °C (**Figure 6.37**). The higher carbonization temperature reduced the fiber diameters by about 50 nm (**Figure 6.38**). Particles of tin oxide, confirmed by energy dispersive X-ray spectroscopy (**Figure 6.39**), are visible dispersed throughout the non-woven structure upon the fibers pyrolyzed at 900 °C. The observed particle diameters ranged between 300 nm and 2 μm. These particles were rare in the fibers pyrolyzed at only 700 °C. Based on ICP-MS the fibers contain 5.95 and 6.14 wt% tin.

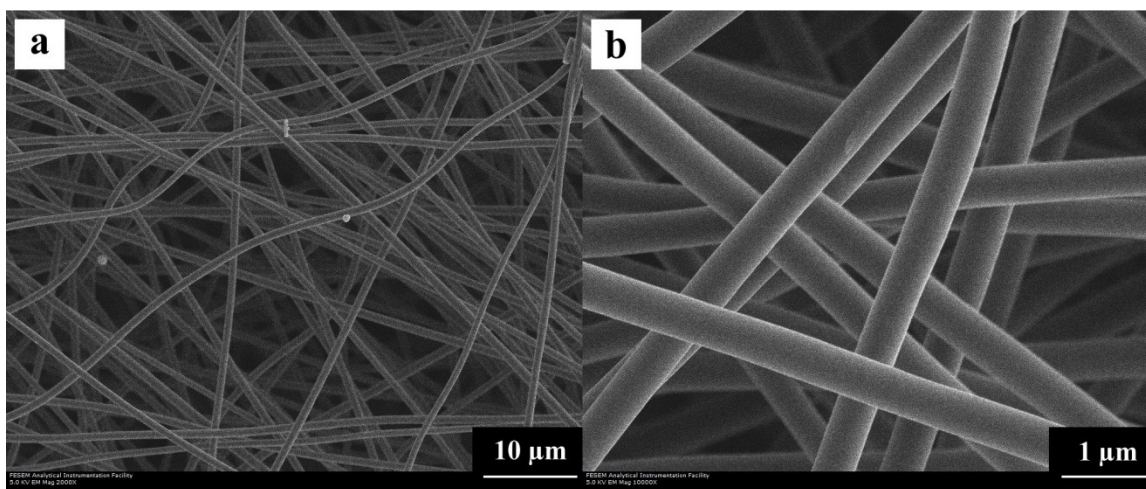


Figure 6.37 – Scanning electron micrograph of PMDA-ODA fibers produced from a 22 wt% polymer solution containing 23.25% DMDND-tin pyrolyzed at 700 °C.

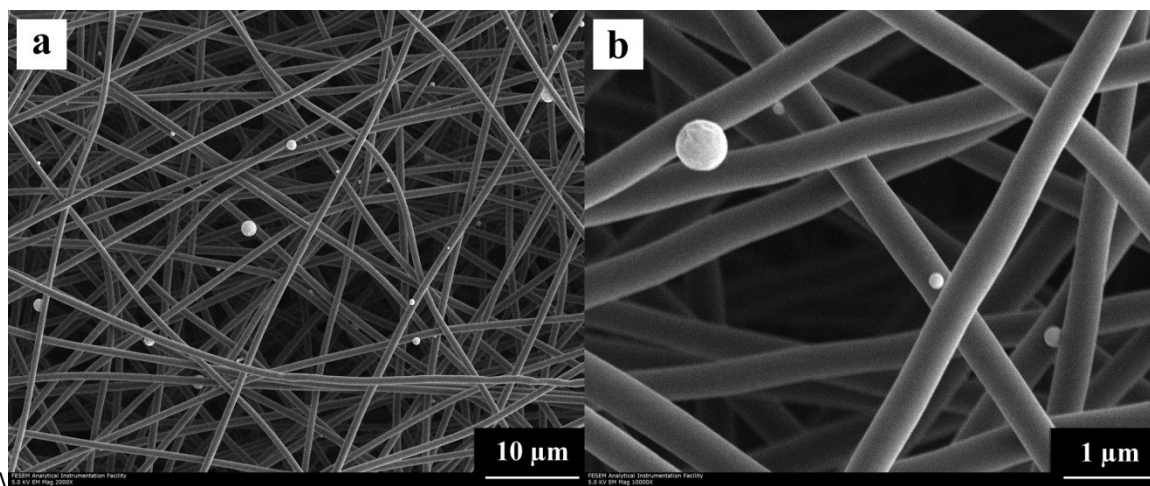


Figure 6.38 – Scanning electron micrograph of PMDA-ODA fibers produced from a 22 wt% polymer solution containing 23.25% DMDND-tin pyrolyzed at 900 °C. A significant number of micron-sized tin oxide particles are visible decorating the surface of the fibers.

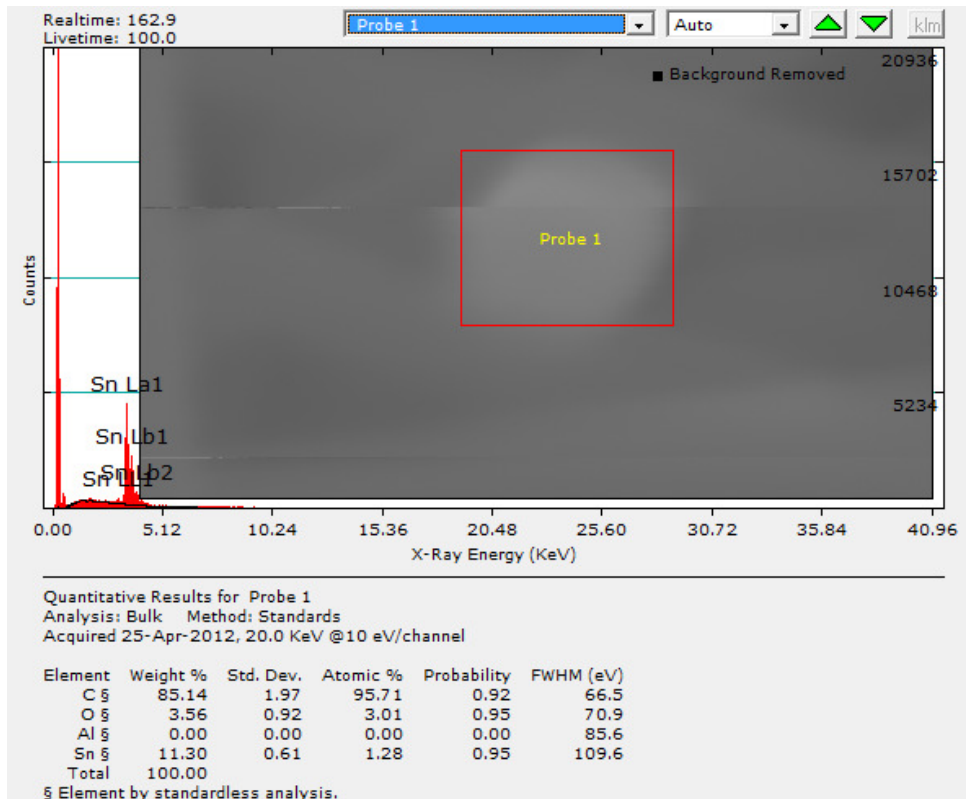


Figure 6.39 – Energy dispersive X-ray spectra obtained for a particle similar to the one seen in Figure 6.38b. The elemental ratio of Sn to O (1.28:3.01) confirms the particles are made of SnO₂.

The irreversible capacities are large (**Figure 6.40**) but similar to the observed losses for PI-based electrodes without tin. This suggests no conversion of tin oxide to metallic tin occurred through the consumption of lithium.

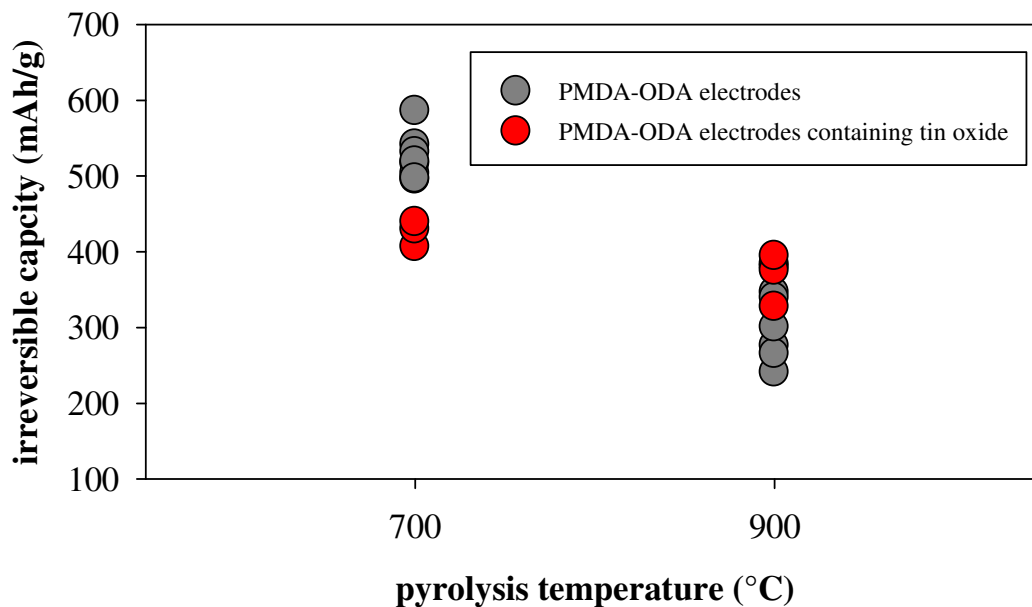


Figure 6.40 – First-cycle irreversible capacity losses of PMDA-ODA derived nanofiber electrodes with and without tin oxide.

These electrodes under cycling display behavior typical of carbonized nanofiber electrodes (**Figure 6.39**) with significant capacity fading during the first 5 to 10 cycles. The reversible capacity of the fibers pyrolyzed at 700 °C is approximately 25% larger than similar fibers presented in presented in **Figure 6.31**, however there is no evidence in the voltage curves over the first 5 cycles (**Figure 6.40**) to suggest the alloying of tin and lithium, elsewhere observed between 400 mV versus Li/Li⁺ in pyrolyzed fibers^{1, 129}.

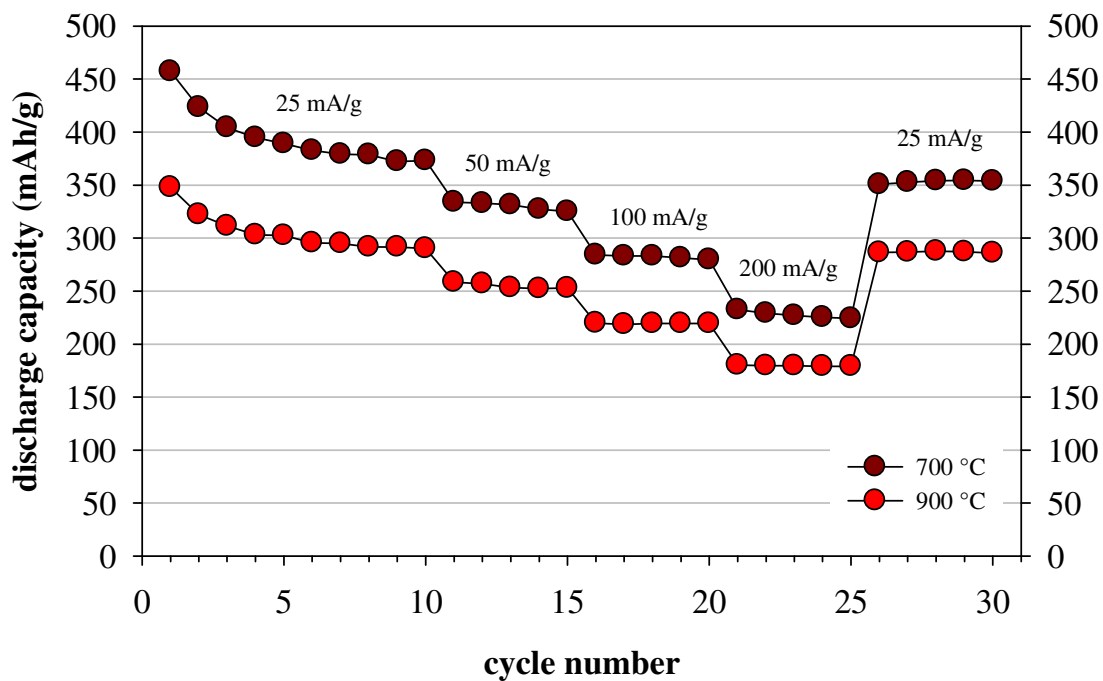


Figure 6.41 – Reversible discharge capacity of PMDA-ODA derived nanofiber electrodes containing tin oxide. Fibers were pyrolyzed at two different temperatures and cycled over a range of indicated symmetric currents for charge and discharge.

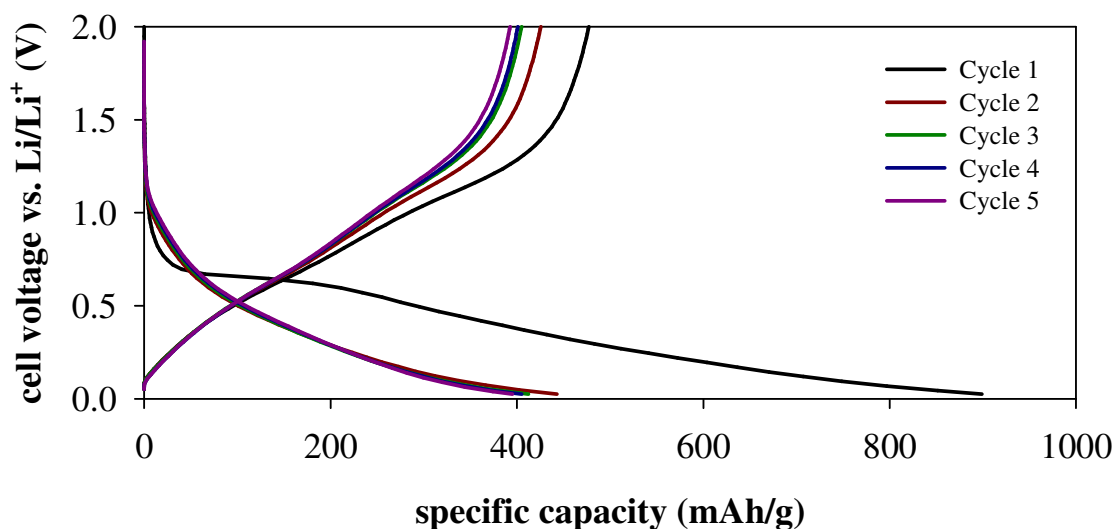


Figure 6.42 – Voltage profiles during charge and discharge for a typical PMDA-ODA electrode, pyrolyzed at 700 °C and containing tin oxide. No feature corresponding to reversible Li alloying with Sn is observed near 0.4 V.

6.4 Conclusion

Nanofibers based on two different polyimides were produced by electrospinning of poly(amic acids) and were subjected to further processing prior to use as anodes in Li-ion cells. The fibers made of PMDA and ODA resulted from solutions of between 24 and 30 wt% in DMF depending on the polymerization method. Successful electrospinning of significant quantity of fibers made of PMDA and PPD required heterogeneous polymerization, with the solid dianhydride added to a solution already containing the diamine, and the addition of small amounts of high M_w PEO. Other methods resulted in solutions whose rheological properties changed over several hours, leading to unsuccessful attempts to electrospin non-woven nanofibers.

Incorporation of tin salts, complexes, or organometallics into the solutions of both polymers had measurable impacts on the solution properties. The addition of tin acetate caused phase separation in all cases. The use of both tin(II) acetylacetonate and dimethyldineodecanoate tin created highly viscous solutions. In the case of PMDA-ODA these solutions could be electrospun. Solutions of PMDA-PPD with tin acac were too viscous for further processing. The use of dimethyldineodecanoate tin with PMDA-PPD made further processing possible, but resulted in an insufficient quantity of non-woven mat for further use.

The combination of shear rheology and size exclusion chromatography was employed to better understand impact of the tin sources on the polymer systems. Size exclusion chromatography demonstrated that the use of tin(II) acetylacetonate and dimethyldineodecanoate tin generally lowered the M_w of the polymers. The shear viscosity of these same solutions was noticeably higher than those without the tin additives. The solutions containing tin additives are weakly shear thinning. The combination of low M_w measured in dilute conditions and high viscosity in concentrated conditions, and slight shear thinning behavior, suggests that the tin additives are acting as physical cross-links through association with the carboxylic groups in the amic acid chains.

The non-woven mats produced were imidized at 250 °C and pyrolyzed at either 700 or 900 °C. The benefits of using polyimide as the basis for the fiber were improved capacity retention at current rates up to 400 mA/g when compared to PAN-based electrodes. Cells derived from PMDA-PPD and pyrolyzed at 900 °C suffered lower first cycle irreversible

losses than either PAN or PMDA-ODA electrodes. All PI-based electrodes that did not contain tin possessed lower reversible capacities than similar PAN-based fibers.

The inclusion of tin resulted in the formation of SnO₂ particles distributed upon the PMDA-ODA fibers for samples pyrolyzed at 900 °C. No surface particles of SnO₂ were observed for the lower pyrolysis temperature. There is no data to indicate utilization of the added tin in the storage of energy. Electrodes made of pyrolyzed PMDA-ODA fibers containing tin possessed irreversible capacities that are not consistent with conversion of the SnO₂ to metallic tin by the consumption of Li. The charge and discharge curves for these materials possess no features that would correspond to the alloying of Sn with Li.

Chapter 7
Summary and Conclusions

This dissertation was focused on using a multidisciplinary approach to engineering pyrolyzed carbon nanofibers employed as anodes in lithium-ion batteries. The resulting work had two major objectives: (1) The of three vapor-phase deposition schemes to create an engineered surface at the interface of PAN-based electrodes and the electrolyte. These new surfaces were hypothesized to reduce the irreversible losses of lithium suffered at the anode during the first charging cycle; and (2) the use of polyimide-based nanofibers to study the impact of the pyrolyzed fiber precursor on electrochemical performance as an anode in Li-ion batteries. The polyimide derived fibers were hypothesized to be more graphitic than fibers based on PAN. This difference would result in fibers with improved capacity retention at high currents and potentially lower irreversible losses.

The first surface modification technique used was plasma enhanced chemical vapor deposition of carbon onto the surface of PAN fibers pyrolyzed at either 700 or 900 °C. The objective was to create a more graphitic surface than existed after pyrolysis. At the lowest temperatures and plasma power (600 W), and in the absence of H₂, the carbon material created was highly amorphous and primarily grew in the spaces between the fibers rather than upon them. Reduction of the chamber pressure from 350 mTorr to 50 mTorr and a majority H₂ (70%) feed gas resulted in no observed material growth or mass change for the samples. The use of higher plasma powers (1200 and 800 W) with hydrogen to methane ratios of 2:1 or 1:1, at operating pressures of 150 and 100 mTorr respectively, led to significant loss of fiber mass during plasma processing resulting in nanofibers damaged by etching. In regions located nearest the heating element, deposition of carbon nanowalls occurred on the fiber surface. This deposition existed in competition with the plasma etch

that was consuming the fibers. The result was an advancing deposition profile into the mat, with concurrent destruction of the outermost fibers and nanowalls. The plasma processing, while having a morphological effect on the fibers, had no impact on the performance of the materials as anodes. Electrochemical testing of the electrodes showed no improvement in lowering irreversible Li losses, and no degradation of the reversible capacity. The interesting structures of high-surface carbon nano-walls secured to a continuous nanofiber network could find application in other energy storage or conversion materials, such as ultra-capacitors and fuel cell catalysis.

Amorphous aluminum oxide deposited by atomic layer deposition (ALD) from trimethylaluminum and water was the second engineered surface employed to reduce irreversible losses of Li. This film was chosen to act as a passivation layer at the pyrolyzed PAN surface, helping suppress the irreversible Li losses. The films were deposited at temperatures of 45, 90, and 150 °C for 6, 10 or 20 cycles. The irreversible capacity losses sustained by the electrodes were reduced by up to 24% for 10 alumina deposition cycles at 90 °C. Paired with this improvement was a slight reduction in reversible capacity and capacity retention as the charge and discharge currents were increased. The undesired reduction in reversible capacity was largest at the lowest deposition temperatures and was barely present for electrodes coated with alumina at 150 °C. The thicker coating for 20 cycles at 90 °C coating showed a 42% reduction in first-cycle irreversible capacity, but greatly reduced the reversible capacity of the material. Additionally the capacity retention at increasing currents (higher C-rates) was much lower, with the 42 Å alumina coating serving as a transport barrier for Li⁺ ions and an insulating barrier for electron flow. The thinnest coatings of alumina had

no significant impact on either reversible or irreversible capacity, suggesting incomplete surface coverage.

The final engineered surface was created by molecular layer deposition (MLD) of metal-organic hybrid alucone films at 100 °C. The precursor chemicals used were trimethylaluminum and ethylene glycol and films were grown using 6 to 40 cycles. There was an observable mass gain for all depositions attempted, with a linear relationship between total cycles and mass gain for 20 or more MLD cycles. This demonstrates a commonly seen period of incomplete coverage for a low number of cycles, followed by steady state growth. All deposition thicknesses produced a reduction in irreversible capacity losses, with the thickest alucone films – 40 cycles – producing a 23% improvement. Similar to the work with amorphous alumina an increase in the thickness of the deposited film correlated to a reduction in the reversible charge capacity of the electrodes, especially at high rates of charge and discharge. The electrodes covered by 40 cycles would store and extract almost no lithium before reaching the cutoff voltages in the cell cycling test. For 10 MLD cycles or less the impact on reversible capacity is small at low currents, and similar to alumina coatings at high currents. Based on the tradeoff between irreversible capacity and coating thickness the “ideal” number of depositions at this temperature is between 10 and 20 cycles.

The impact of fiber precursor was evaluated using nanofibers based on two different polyimides produced by electrospinning of poly(amic acids). The specifics of the polymerization procedure had a significant impact on the shear rheology of PMDA-PPD solutions and hence their ability to be electrospun. The best method to obtain PMDA-PPD solutions for successful electrospinning was a heterogeneous polymerization, where the solid

dianhydride was added to the diamine already completely dissolved in solution with a small quantity of high M_w PEO. Other methods resulted in solutions whose rheological properties changed over a period of hours, leading to unsuccessful attempts to electrospin non-woven nanofibers. There was little change in the properties of PMDA-ODA solutions with polymerization technique, but for consistency the best-method for PMDA-PPD solutions was adopted for this polymer.

Attempts to incorporate tin into the solutions of both pyrolyzed polyimide fibers via various chemicals had measureable impacts on the solution properties. Composite fibers were successfully produced from PMDA-ODA in solution with two tin compounds. Electrospinning of dimethyldineodecanoate tin with PMDA-PPD was possible but, before a sufficient quantity of nanofibers were collected for further processing; the high viscosity solution caused the pump to stall. The use of size exclusion chromatography demonstrated that the M_w of polymers produced with tin in solution was typically lower than similar solutions without tin. This data indicates the tin compounds are serving as physical cross-links in the concentrated solutions used for electrospinning, increasing the shear viscosity leading to stalled pumps.

When pyrolyzed and used as electrodes the PI-based electrodes possessed lower reversible capacities than similar PAN-based fibers. One benefit of using polyimide as the basis for the fiber were improved capacity retention at current rates of 200 and 400 mA/g compared to PAN-based electrodes. Additionally cells derived from PMDA-PPD and pyrolyzed at 900 °C suffered lower first cycle irreversible losses (225 mAh/g) than either

PAN (325 mAh/g) or PMDA-ODA (300 mAh/g) electrodes pyrolyzed under similar conditions.

Chapter 8
Proposed Future Research

8.1 ALD/MLD of Lithium-Organic Films as an Artificial SEI Layer on Electrospun Carbon Nanofiber Anodes

The use of amorphous alumina and alucone have been demonstrated as a means of providing some reduction of the irreversible capacity losses during the first cycle of anodes made from both graphite³⁷⁴ and carbonized electrospun fibers. Additionally, the alumina coatings have a stabilizing effect on the performance of these electrodes as seen from improved coulombic efficiency and capacity retention. The controlled deposition of lithium containing films has been demonstrated from both lithium 2,2,6,6-tetramethyl-3,5-heptanedionate (Li thd) and lithium *tert*-butoxide^{343, 388}. These films are predominantly composed of lithium carbonate (Li_2CO_3), which has been shown to be one component of the solid electrolyte interphase (SEI) responsible for the majority of the first-cycle irreversible capacity in carbon-based anodes¹⁶⁰. Additionally the inclusion of Li_2CO_3 as an electrolyte additive has produced safer batteries and reduced losses of Li during SEI formation³⁸⁹. Given the large surface area and irreversible capacity losses of electrospun carbonized anodes, and the relative success of using alumina ALD and alucone MLD with electrospun fibers, the use of lithium containing ALD films on these anodes should produce even better results.

The lithium ALD films would be deposited on electrospun PAN nanofibers spun from an 11 wt% solution in DMF for 3 or 4 hours in the same procedure as used for both the PECVD, alumina ALD, and alucone MLD work. These fibers would then be stabilized at 250 °C and pyrolyzed at 700 °C. Each electrospinning and carbonization batch would

produce three 30 x 120 mm swatches of carbonized fiber. One of the swatches from each would be reserved as an experimental control during electrochemical testing.

The initial experimental objective would be the deposition of lithium containing films onto the nanofibers substrates at temperatures ranging from 200 to 300 C°. The lithium precursors proposed are Li-thd and cyclopentadienyllithium (Li-cp). The elevated temperature, when compared to the alumina work, is required to properly sublime the solid Li precursors³⁸⁸. These precursors are very moisture sensitive, so it is advised to transfer them into the sample holders for the ALD reactor while in the argon-filled glove box. Given the morphology and chemistry of the substrate, the three-step ALD procedure demonstrated for the deposition from Li *t*-butoxide would be a likely starting point. As with the alumina coated fibers, the mass of the nanofibers mat would be weighed before and after deposition. The use of ICP-MS would be the most readily available means to quantify the lithium deposition. Imaging with electron microscopy would also be necessary to verify the morphology of the fiber mat was not altered by the deposition or that the deposition was not proceeding from nucleation sites to produce non-conformal crystallites.

After suitable deposition conditions had been identified the optimization of the ALD process with respect to electrochemical performance would be the primary objective of this work. Coin cells would be constructed using lithium foil as the counter electrode, LiPF₆ as the electrolyte in EC:EMC and cycled at currents ranging from 25 to 400 mA/g (approximately C/16 to 1C) to investigate the reduction in irreversible losses and the impact of the coating on capacity retention and long term stability.

A potential variation on this work would be the use of MLD techniques to create more complex lithium containing films. While Li_2CO_3 is a component of the naturally formed SEI, and could serve as an approximation, the natural SEI films tend to have a more complex and varied organic structure¹⁶⁰. The use of small molecules such as ethylene glycol and glycidol to produce the “metal”-cone MLD^{33, 358} films might reduce the three-step sequence of lithium precursor, CO_2 , and water to a two-step sequence. The resulting film, if thermodynamically stable during transfer to the glove box for cell assembly, would better approximate the natural SEI.

8.2 Vapor Phase MLD of PMDA-PPD Polyimide on PAN-based Nanofibers

Some of the initial reports of what is now referred to as molecular layer deposition used descriptors like “vapor deposition polymerization³⁵³” and “alternating vapour deposition polymerization³⁵⁴” and were concerned with the heterogeneous polymerization from the vapor phase onto a solid substrate. There are published examples of the MLD of polyamides³⁷, polyimides³⁵⁶, and polyureas³⁵. Of particular interest is the MLD of polyimides based on both the PMDA-ODA³⁵⁵ and PMDA-PPD³⁶ chemistries studied in this dissertation.

Carbonized nanofibers based on both of those polyimides presented in this work as Chapter 6 showed better capacity retention than PAN-based fibers at the same carbonization temperature. Additionally the PMDA-PPD fibers showed lower irreversible capacity losses than similar PAN fibers. It is hypothesized that the molecular layer deposition of polyimides onto PAN fibers will, after carbonization; result in fibers created with the easier PAN-based

electrospinning, but with better surface properties (*i.e.* less C_{irr}) and greater electronic conductivity to help maintain higher reversible capacities at high currents.

There exist two potential pathways to follow for this experiment. The simpler processing route would be as follows: electrospinning of the PAN-based solution with or without metal-complexes, followed by MLD, then the simultaneous thermal stabilization/imidization of the fiber. At this point the carbonization would then be conducted as normal and cells would be tested as in previous studies to compare reversible and irreversible capacity, and the impact of high current on reversible capacity retention. This pathway would be recommended if the sample contraction of the PAN and PI components during the thermal processing was similar enough to prevent delamination or significant cracking. Since the MLD deposited polymer will be pyrolyzed, it will not be an insulating material as in the alumina or alucone cases (Chapters 4 and 5). The added polymer thus can be thicker to ensuring a uniform coating after sample contraction during carbonization. Given the potential reactivity of the acrylonitrile group the best film formation would likely result from the use of the dianhydride monomer as the first precursor, followed by the diamine.

If there were significant difficulties with the PI-based film integrity during carbonization the PAN fibers could be completely carbonized, and then placed into the MLD reactor for surface coating. As the surface chemistry of the carbonized PAN will be significantly different, it may be necessary to reverse the order the precursors are introduced to the reactor. The deposition of alumina and alucone from trimethylaluminum (TMA), reactions which require hydroxyl or unsaturated surface oxygen proceeded without additional

surface oxidation for PAN fibers, and thus it would be likely the diamine could react with existing surface functionality, followed by the dianhydride. If greater oxidation of the surface is required to initiate the deposition a single ozone exposure could be added before any of the polymer precursors were introduced. After the deposition was completed the fibers, would then need to be thermally processed a second time to imidize and pyrolyze the surface poly(amic acid). At this point the material is ready to be cut into electrodes and assembled into coin cells for testing.

8.3 Anodes made by chemical vapor deposition of silicon onto electrospun carbonized-nanofibers

Producing a composite material of silicon and carbon is a well-documented means of producing Li-ion anodes with a high specific capacity^{4, 94, 100, 390}. Of particular success have been one-dimensional materials¹¹³ with reported reversible capacities in excess of 1500 mAh/g^{99, 115}. Carbonized electrospun nanofibers represent a potentially useful material for constructing these composites by depositing a layer of Si on the outside of the fiber by low pressure chemical vapor deposition to create a carbon-core, silicon-shell material¹¹³. In composites of this kind, the carbon fibers will be acting as a material support for the Si and conductive pathway, and their lithium insertion capacity will be of negligible importance. A previous study used commercially purchased carbon fibers and dispensed them onto a stainless steel current collector from solution prior to silicon deposition¹¹³. The free-standing nature of the non-woven structure; the long, continuous electrical pathways of the fibers; and the diameter control available in the electrospinning process make these nanofibers an ideal substrate for this kind of composite. The nanofibers would be prepared by electrospinning

from both PAN and PMDA-PPD solutions. Solutions of 7 and 11 weight % PAN would be spun to test the impact of fiber diameter on the electrochemical performance and durability. Polyacrylonitrile would be chosen for this portion of the experiment because it is an easier, more predictable polymer to electrospin; simplifying the process of preparing different diameter fibers. It is recommended that the materials all be carbonized at 1100 °C to maximize the conductivity of the carbon core. The use of two different polymers is proposed so it will be possible to investigate the impact of the electronic conductivity of the carbon backbone on the rate capability of the composite anodes since carbonized PMDA-PPD type polyimide has a demonstrably higher electronic conductivity than other pyrolyzed materials⁴⁵.

The deposition of the silicon would be conducted in a standard CVD reactor using silane (SiH_4) diluted in argon (Ar). Because the fibers will have been carbonized at 1100 °C there will be no restriction on the deposition conditions used to create the silicon film. Obtaining a uniform coating throughout the entirety of the non-woven structure is anticipated to be the most difficult part of creating these materials. The pyrolyzed non-woven mats are typically hundreds of microns in depth, and determining the proper reaction conditions to ensure full infiltration of the mat will be challenging. Based on previous studies and other available literature, a suitable starting point would be temperatures around 600 °C, a total pressure of 100 Pa, and a SiH_4 :Ar ratio of 1:50³⁹¹. If the LPCVD is incapable of producing an appropriately uniform coating throughout the non-woven mat, there exist methods to produce Si films by atomic layer deposition from SiH_4 . These methods are not desirable because they greatly increase the complexity of the process by requiring low-temperature

adsorption followed by a high temperature decomposition of the silane³⁹². Thus the reactor would have to be repeatedly heated and cooled for each cycle of the process. Beyond the electrochemical testing in coin-cells, the materials would be characterized by SEM and TEM to investigate the quality and thickness of the Si coating before and after cycling.

Once the proper reaction conditions to produce a uniform coating are established, the relationship between electrochemical performance and Si thickness can be determined. If the Si coating is too thick the volume expansion will be too large and the film will pulverize or delaminate from the substrate⁷⁹. If the coating is too thin the lithium storage capacity on a gravimetric or volumetric basis will not be maximized. Good results in the literature would indicate that the ideal coating thickness may be between 50 and 100 nm^{99, 113, 393}.

8.4 Ultra-capacitors made from electrospun fibers coated with carbon nanowalls by PECVD and potential role of ALD in further performance increases.

The use of PECVD methods to create graphitic carbon coatings was not successful, but the processing conditions with the highest temperatures and plasma powers demonstrated an ability to deposit graphene-like ribbons or carbon nanowalls onto the areas with the hottest fiber surfaces. These structures create the possibility to increase the surface area of the non-woven nanofiber structure given the very high surface area of graphene or graphene-like materials³⁹⁴. A very large increase in surface area would not be ideal for carbon-based Li-ion anodes as this would result in a further increase of irreversible capacity losses⁷⁴.

Ultra-capacitors represent an electrochemical device in which very-high surface areas are desirable to increase the double-layer charging these devices rely on to rapidly store and deliver charge³⁹⁵. Ultra-capacitors also represent a complementary technology to batteries in

hybrid and electric vehicle applications². Additionally, the freestanding nature of the non-woven nanofibers substrate presents an ideal platform for these materials, as there is a clearly defined high conductivity pathway for the electrons to travel along during charging and discharging²³¹. Further improvement of the energy and power storage of the composite graphene/nanofiber materials should be possible with the use of atomic layer deposition to create thin metal-oxide layers whose pseudo-capacitance would add to the double-layer charging as recently demonstrated for TiO₂-graphene composite electrodes.³⁹⁶

The initial difficulty with this work will be the uniform creation of the graphene/carbon nanowalls³⁷⁰ throughout the volume of the non-woven fiber mat. The reaction conditions explored in the work outlined in Chapter 3, which created these graphene-on-fiber structures (see **Figures 3.11, 3.12, and 3.21**) all resulted in a simultaneous etch of the fiber substrate. Optimization of this process will likely require one or more of the following recommended modifications.

First, since the deposition of the graphene ribbons and carbon nanowalls was observed on the areas of the mat closest to the heater; it is necessary to ensure uniform heating to a high temperature throughout the non-woven mat. It would be advised to assess if a longer heating period prior to initiation of the plasma results in carbon deposition over the whole sample. An alternative would be modification of the chamber to directly connect the fibers to the controller for the heating, rather than simply resting upon the heated surface. If the sample is uniformly heated to the desired temperature, the ignition of the plasma may create growth throughout the mat.

Second, the deposition time of ten minutes used in the battery work is clearly far too long given the competing deposition and etching of the processing conditions, and might result in total consumption of the carbon precursor deep within void space of the non-woven structure in the case of completely uniform heating. Short deposition times of a minute or less should be studied, and if growth is occurring, it may be advantageous to use a sequence of pulsed plasma deposition followed by an equilibration time to replenish the carbon precursor within the mat.

Additionally to promote greater growth, the partial pressure of the CH₄ precursor should be increased rather than a decrease of the H₂ to study the impact of the gas ratio on the deposited materials³⁰⁷. The effect was subtle, but as seen in Table 7 the lower chamber pressure of samples 8 and 9 produced a greater mass loss than the higher chamber pressure which contained more H₂. Again the goal will be to find a gas mixture and pressure that significantly favors growth of the graphene-like structures over the simultaneous plasma etch of the carbon nano-fiber substrate.

The processing conditions used to create the fiber substrate may require modification to produce the best performing material. Lower pyrolysis temperatures were used for the battery work to maximize Li storage of the carbon material. In an ultra-capacitor application the fibers will not be storing any charge within the bulk volume and the fiber size and electronic conductivity of the fibers will be the more important parameters. As such, the use of polyimide (PMDA-PPD) based nanofibers as the substrate may be advantageous due to the higher electronic conductivity of these materials when pyrolyzed⁴⁵. The ideal fiber diameter for the application will likely be influenced by on the ratio of growth to etch during

plasma processing, with larger fibers taking longer to etch away, but smaller fibers creating a higher initial surface area for deposition.

After the key electrospinning, thermal, and plasma processing conditions have been identified to produce the highest practical surface area material, these material could be used “as is” to study the specific capacitance over a range of voltage scan rates in typical basic media. The impact of the pseudo-capacitance of ALD TiO₂ could then build upon this baseline data. The deposition of thin layers of TiO₂ upon graphene and carbonized fiber surfaces has been demonstrated using TiCl₄ and H₂O as the precursors³⁹⁷.

8.5 Electrospun ALD/MLD coated electrodes with an embedded mesh current collector

A large part of my testing of alumina and alucone treated electrospun anodes focused on the impact of the coating on the capacity retention at charging rates near $C/2$. In general, the fibers coated with ALD or MLD films showed lower capacities than the untreated fibers as the current increased. There are at least two potential causes of this difference: electron transfer and lithium diffusion.

The films represent a region through which Li must diffuse prior to undergoing charge transfer at the carbon surface, just like the SEI. The ability of the anode to intercalate Li will be impaired at higher rates of charge and discharge if the rate of Li diffusion in the alumina or alucone film is slower than through the natural SEI. Alternatively, the films are electrical insulators which will represent a barrier to transfer from the current collector to the electrode. In this case it is not the Li diffusion that limits the cell capacity, but the fact that the voltage required to drive the electrons across the ALD film pushes the overall cell voltage

to the cutoff limit prior to full utilization of the material's capacity. This kind of behavior has already been observed for conventional electrodes made from ALD coated graphite³⁷⁴. When the powder was coated before the electrodes were cast, the resulting anodes showed rapid loss of capacity attributed to the insulating layer and loss of conductive pathways upon repeated expansion and contraction during cycling. Coating of the anode after the slurry was cast produced electrodes that showed between 5% and 7% capacity fade over 200 cycles.

It is likely that both processes contribute a decrease in utilized capacity of the nanofiber anodes as current increases. Determining if one or the other dominates the behavior of the electrospun anodes could lead to better engineering choices when designing electrodes. The nanofiber electrodes do not show the rapid capacity fade like the powder coated electrodes, likely because, similar to the anodes coated after casting, the conductive pathways of the nanofibers are not interrupted during cycling. The overall rate of electron transfer between the copper current collector and the nanofibers is likely impacted by the insulating film, and it can be hypothesized that eliminating this transfer barrier would boost capacity at higher currents. A means of testing this would be to directly electrospin the nanofibers onto the current collector prior to carbonization and ALD treatment.

Simply replacing the aluminum foil used to collect the nanofibers during electrospinning with a copper foil might be a simple first step. The melting point of copper is sufficiently high (1084 °C) to permit direct carbonization. But the resulting contraction of the nanofiber mat during stabilization and carbonization would likely de-laminate the electrode from the copper. Instead it is proposed to electrospin the nanofibers onto a mesh structure such as expanded metal³⁹⁸. These materials are available in a range of thickness

and open areas and are fabricated from many different metals including copper, nickel, or alloys of the two³⁹⁹. Both copper and nickel meshes have found use as the current collectors in traditional cast electrodes pressed into pellets prior to use electrochemical cells.

Preparation of the bonded structure would begin by securing a sheet of expanded metal to the collector prior to electrospinning. It may be advisable to spray a fine mist of the electrospinning solvent, DMF, prior to beginning the electrospinning, in that way some of the initial fibers that reach the collector would be slightly wetted and “melt” unto the mesh structure. Half-way through the electrospinning process the expanded metal sheet could be flipped over to bond fibers to both sides. It should be noted that this approach of electrospinning onto a mesh electrode could also be applicable in the case of TiO₂ coated ultra-capacitor materials, should electron transfer to the electrode be sufficiently impaired by the coating.

The resulting bonded mats would then be cut into swatches and thermally processed through the stabilization and carbonization steps together. There would likely be some contraction of the fiber structure as it lost between 40 and 50% of its mass through the thermal treatment up to 900 °C for copper mesh, but given the improved flexibility of the expanded metal sheets when compared to metal foils the degree of de-lamination should be significantly less. At this point some of the swatches could be loaded into the ALD reactor and coated with a fine layer of alumina, alucone, or potentially a lithium containing film. Finally discs could be die-cut from the final products, weighed, and assembled into Li-ion coin cells for testing at low (C/16) and high (1C or C/2) currents for a number of cycles. Cutting the discs last would ensure that at the exposed copper mesh surface was not covered

with the ALD or MLD film and thus would not have this electronic barrier. The capacity retention could then be studied on a normalized basis, or the cells could be broken open after testing the active material removed from the metal mesh, and the mass of the mesh could be subtracted from the initial mass to get a specific capacity of the materials.

8.6 Thermochemical Reduction of SnO₂ Nanoparticles in Nanofibers via a Hydrogen Containing Atmosphere

All of the attempts to incorporate Sn into the nanofibers attempted as part of this work failed to result in any utilization of the alloying properties of Sn. In the case of tin acetate added to PAN solutions the resulting fibers were clearly decorated by SnO₂ nanoparticles but no additional features were visible in the voltage curves to indicate the reduction of **Equation 12**, nor was there a dramatic increase in the irreversible capacity that would correspond to this consumption of Li.



Similarly the inclusion of tin in the polyimide based nanofibers did not show any increase in the reversible capacity or irreversible capacity due to the SnO₂ conversion reaction. Though there are reports indicating that the pyrolysis of Sn/C composite fibers results in both SnO₂ and Sn phases, the best published result for the use of Sn in porous pyrolyzed nanofibers was accomplished when the pyrolysis was conducted in an Ar and H₂ mixture²⁴, rather than the inert N₂. During the stabilization process of that work the tin octanoate was converted to SnO₂ and the PMMA phase in which the tin complex was included thermally decomposed to create a porous internal structure. Adopting an Ar/H₂

mixture to improve the reducing potential of the atmosphere within the tube furnace is expected to have a similar impact on the SnO₂ present in fibers produced from the polyimide precursors. Use of an Ar/H₂ or forming gas mixture would also be marginally safer than the use of a pure H₂ process flow.

References

1. Tarascon J-, Armand M. Issues and challenges facing rechargeable lithium batteries. *Nature* 2001; 414(6861):359-67.
2. Burke AF. Batteries and ultracapacitors for electric, hybrid, and fuel cell vehicles. *Proc IEEE* 2007; 95(4):806-20.
3. Goodenough JB, Kim Y. Challenges for rechargeable li batteries. *Chem Mat* 2010; 22(3):587-603.
4. Il-Seok Kim, Kumta PN. High capacity Si/C nanocomposite anodes for li-ion batteries. *J Power Sources* 2004; 136(1):145-9.
5. Heon-Young Lee, Sung-Man Lee. Carbon-coated nano-si dispersed oxides/graphite composites as anode material for lithium ion batteries. *Electrochemistry Communications* 2004 05; 6(5):465-9.
6. Chen JS, Cheah YL, Chen YT, Jayaprakash N, Madhavi S, Yang YH, Lou XW. SnO(2) nanoparticles with controlled carbon nanocoating as high-capacity anode materials for lithium-ion batteries. *Journal of Physical Chemistry C* 2009 NOV 26;113(47):20504-8.
7. Zhang W, Wu X, Hu J, Guo Y, Wan L. Carbon coated fe(3)O(4) nanospindles as a superior anode material for lithium-ion batteries. *Advanced Functional Materials* 2008; 18(24):3941-6.
8. Guo ZP, Milin E, Wang JZ, Chen J, Liu HK. Silicon/disordered carbon nanocomposites for lithium-ion battery anodes. *J Electrochem Soc* 2005; 152(11):2211-6.
9. Niu J, Lee JY. Improvement of usable capacity and cyclability of silicon-based anode materials for lithium batteries by sol-gel graphite matrix. *Electrochemical and Solid-State Letters* 2002; 5(6):107-10.
10. Zeng ZY, Tu JP, Huang XH, Wang XL, Zhao XB, Li KF. Electrochemical properties of a mesoporous Si/TiO₂ nanocomposite film anode for lithium-ion batteries. *Electrochemical and Solid-State Letters* 2008; 11(6):105-7.
11. Kim T, Mo YH, Nahm KS, Oh SM. Carbon nanotubes (CNTs) as a buffer layer in silicon/CNTs composite electrodes for lithium secondary batteries. *J Power Sources* 2006; 162(2):1275-81.

12. Ishihara T, Nakasu M, Yoshio M, Nishiguchi H, Takita Y. Carbon nanotube coating silicon doped with cr as a high capacity anode. *J Power Sources* 2005; 146(1-2):161-5.
13. Wang W, Kumta PN. Reversible high capacity nanocomposite anodes of Si/C/SWNTs for rechargeable li-ion batteries. *J Power Sources* 2007; 172(2):650-8.
14. Zhou G, Wang D, Li F, Zhang L, Li N, Wu Z, Wen L, Lu GQ, Cheng H. Graphene-wrapped fe(3)O(4) anode material with improved reversible capacity and cyclic stability for lithium ion batteries. *Chemistry of Materials* 2010; 22(18):5306-13.
15. Wang H, Cui L, Yang Y, Casalongue HS, Robinson JT, Liang Y, Cui Y, Dai H. Mn(3)O(4)-graphene hybrid as a high-capacity anode material for lithium ion batteries. *J Am Chem Soc* 2010; 132(40):13978-80.
16. Wang X, Zhou X, Yao K, Zhang J, Liu Z. A SnO(2)/graphene composite as a high stability electrode for lithium ion batteries. *Carbon* 2011; 49(1):133-9.
17. Zhu X, Zhu Y, Murali S, Stoller MD, Ruoff RS. Reduced graphene oxide/tin oxide composite as an enhanced anode material for lithium ion batteries prepared by homogenous coprecipitation. *J Power Sources* 2011; 196(15):6473-7.
18. Chou S, Wang J, Choucair M, Liu H, Stride JA, Dou S. Enhanced reversible lithium storage in a nanosize silicon/graphene composite. *Electrochemistry Communications* 2010; 12(2):303-6.
19. Lee JK, Smith KB, Hayner CM, Kung HH. Silicon nanoparticles-graphene paper composites for li ion battery anodes. *Chemical Communications* 2010; 46(12):2025-7.
20. Aussawasathien D, Sancaktar E. Electrospun polyacrylonitrile-based carbon nanofibers and their silver modifications: Surface morphologies and properties. *Current Nanoscience* 2008; 4(2):130-7.
21. Wang L, Yu Y, Chen P, Chen C. Electrospun carbon-cobalt composite nanofiber as an anode material for lithium ion batteries. *Scr Mater* 2008; 58(5):405-8.
22. Ji L, Zhang X. Manganese oxide nanoparticle-loaded porous carbon nanofibers as anode materials for high-performance lithium-ion batteries. *Electrochemistry Communications* 2009; 11(4):795-8.
23. Ji L, Zhang X. Fabrication of porous carbon/Si composite nanofibers as high-capacity battery electrodes. *Electrochemistry Communications* 2009; 11(6):1146-9.

24. Yu Y, Gu L, Zhu C, Van Aken PA, Maier J. Tin nanoparticles encapsulated in porous multichannel carbon microtubes: Preparation by single-nozzle electrospinning and application as anode material for high-performance li-based batteries. *J Am Chem Soc* 2009; 131(44):15984-5.
25. Buiel E, George AE, Dahn JR. On the reduction of lithium insertion capacity in hard-carbon anode materials with increasing heat-treatment temperature. *J Electrochem Soc* 1998; 145(7):2252-7.
26. Beguin F, Metenier K, Chevallier F, Azais P, Pellenq R, Bonnamy S, Duclaux L, Rouzaud J-, Frackowiak E. Designing nanostructured carbons for the negative electrode of lithium batteries. *Molecular Crystals and Liquid Crystals* 2002; 386:151-7.
27. Buiel E, Dahn JR. Reduction of the irreversible capacity in hard-carbon anode materials prepared from sucrose for li-ion batteries. *J Electrochem Soc* 1998; 145(6):1977-81.
28. Peng Q, Sun X, Spagnola JC, Hyde GK, Spontak RJ, Parsons GN. Atomic layer deposition on electrospun polymer fibers as a direct route to Al₂O₃ microtubes with precise wall thickness control. *Nano Letters* 2007; 7(3):719-22.
29. Spagnola JC, Gong B, Arvidson SA, Jur JS, Khan SA, Parsons GN. Surface and sub-surface reactions during low temperature aluminium oxide atomic layer deposition on fiber-forming polymers. *Journal of Materials Chemistry* 2010; 20(20):4213-22.
30. Jung YS, Cavanagh AS, Dillon AC, Groner MD, George SM, Lee S. Enhanced stability of LiCoO₂ cathodes in lithium-ion batteries using surface modification by atomic layer deposition. *J Electrochem Soc* 2010; 157(1):A75-81.
31. Jung YS, Cavanagh AS, Riley LA, Kang S, Dillon AC, Groner MD, George SM, Lee S. Ultrathin direct atomic layer deposition on composite electrodes for highly durable and safe li-ion batteries. *Adv Mater* 2010; 22(19):2172.
32. Riley LA, Cavanagh AS, George SM, Jung YS, Yan Y, Lee S, Dillon AC. Conformal surface coatings to enable high volume expansion li-ion anode materials. *Chemphyschem* 2010; 11(10):2124-30.
33. Dameron AA, Seghete D, Burton BB, Davidson SD, Cavanagh AS, Bertrand JA, George SM. Molecular layer deposition of alucone polymer films using trimethylaluminum and ethylene glycol. *Chemistry of Materials* 2008; 20(10):3315-26.
34. Peng Q, Gong B, VanGundy RM, Parsons GN. "Zincone" zinc oxide - organic hybrid polymer thin films formed by molecular layer deposition. *Chemistry of Materials* 2009; 21(5):820-30.

35. Zhou H, Bent SF. Molecular layer deposition of functional thin films for advanced lithographic patterning. *ACS Appl Mater Interfaces* 2011; 3(2):505-11.
36. Adarnczyk NM, Dameron AA, George SM. Molecular layer deposition of poly(p-phenylene terephthalamide) films using terephthaloyl chloride and p-phenylenediamine. *Langmuir* 2008; 24(5):2081-9.
37. Du Y, George SM. Molecular layer deposition of nylon 66 films examined using in situ FTIR spectroscopy. *Journal of Physical Chemistry C* 2007; 111(24):8509-17.
38. Park SH, Kim C, Yang KS. Preparation of carbonized fiber web from electrospinning of isotropic pitch. *Synth Met* 2004; 143(2):175-9.
39. Edie DD, Yang KS, Lim DY, Kim YM, Choi YO. Preparation of carbon fiber web from electrostatic spinning of PMDA-ODA poly(amic acid) solution. *Carbon* 2003; 41(11):2039-46.
40. Goeschel U, Lee H, Yoon D, Siemens R, Smith B, Volksen W. Effects of chemical-structure and precursor on optical-properties, thermomechanical properties, and molecular-orientation and order of thin-films of stiff aromatic polyimides. *Colloid Polym Sci* 1994; 272(11):1388-95.
41. Burgman H, Freeman J, Frost L, Bower G, Traynor E, Ruffing C. Aromatic imide polymers for high-temperature adhesives. *J Appl Polym Sci* 1968;12(4):805,&.
42. Wallach M. Structure-property relations of polyimide films. *Journal of Polymer Science Part A-2-Polymer Physics* 1968;6(5PA2):953.
43. Hishiyama Y, Nakamura M, Nagata Y, Inagaki M. Graphitization behavior of carbon film prepared from high modulus polyimide film: Synthesis of high-quality graphite film. *Carbon* 1994; 32(4):645-50.
44. Inagaki M, Takeichi T, Hishiyama Y, Oberlin A. High quality graphite films produced from aromatic polyimides. *Chemistry and Physics of Carbon*, 1999; 26:245-333.
45. Inagaki M, Ibuki T, Takeichi T. Carbonization behavior of polyimide films with various chemical structures. *J Appl Polym Sci* 1992; 44(3):521-5.
46. Liu J, Min Y, Chen J, Zhou H, Wang C. Preparation of the ultra-low dielectric constant polyimide fiber membranes enabled by electrospinning. *Macromolecular Rapid Communications* 2007; 28(2):215-9.

47. Eweka E. Electrolytes and additives for high efficiency lithium cycling. *Journal of Power Sources*; 65(1):247 .
48. Zhang SS, Xu K, Jow TR. Study of the charging process of a LiCoO₂-based li-ion battery. *J Power Sources* 2006; 160(2):1349-54.
49. Sun X, Lee H, Yang X, McBreen J. Improved elevated temperature cycling of LiMn₂O₄ spinel through the use of a composite LiF-based electrolyte. *Electrochemical and Solid State Letters* 2001; 4(11):A184-6.
50. Wang Y, Cao G. Developments in nanostructured cathode materials for high-performance lithium-ion batteries. *Adv Mater* 2008;20(12):2251-69.
51. Wang H, Jang Y, Huang B, Sadoway DR, Chiang Y. TEM study of electrochemical cycling-induced damage and disorder in LiCoO₂ cathodes for rechargeable lithium batteries. *J Electrochem Soc* 1999;146(2):473-80.
52. Pan Q, Guo K, Wang L, Fang S. Novel modified graphite as anode material for lithium-ion batteries. *J Electrochem Soc* 2002; 149(9):A1218-23.
53. Hossain S, Kim Y-, Saleh Y, Loutfy R. Overcharge studies of carbon fiber composite-based lithium-ion cells. *J Power Sources* 2006;161(1):640-7.
54. Endo M, Kim Y, Hayashi T, Nishimura K, Matusita T, Miyashita K, Dresselhaus M. Vapor-grown carbon fibers (VGCFs) - basic properties and their battery applications. *Carbon* 2001;39(9):1287-97.
55. Fu LJ, Endo K, Sekine K, Takamura T, Wu YP, Wu HQ. Studies on capacity fading mechanism of graphite anode for li-ion battery. *J Power Sources* 2006;162(1):663-6.
56. Markevich E, Salitra G, Aurbach D. Influence of the PVdF binder on the stability of LiCoO₂ electrodes. *Electrochemistry Communications* 2005;7(12):1298-304.
57. Aurbach D, Talyosef Y, Markovsky B, Markevich E, Zinigrad E, Asraf L, Gnanaraj JS, Kim H. Design of electrolyte solutions for li and li-ion batteries: A review. *Electrochim Acta* 2004; 50(2-3):247-54.
58. Aurbach D, Zaban A, Schechter A, Eineli Y, Zinigrad E, Markovsky B. The study of electrolyte-solutions based on ethylene and diethyl carbonates for rechargeable Li batteries .1. Li metal anodes. *J Electrochem Soc* 1995; 142(9):2873-82.

59. Aurbach D, Eineli Y, Markovsky B, Zaban A, Luski S, Carmeli Y, Yamin H. The study of electrolyte-solutions based on ethylene and diethyl carbonates for rechargeable Li batteries .2. Graphite-electrodes. *J Electrochem Soc* 1995; 142(9):2882-90.
60. EinEli Y, Thomas S, Koch V, Aurbach D, Markovsky B, Schechter A. Ethylmethylcarbonate, a promising solvent for li-ion rechargeable batteries. *J Electrochem Soc* 1996; 143(12):L273-7.
61. Aurbach D, Eineli Y. The study of li-graphite intercalation processes in several electrolyte systems using in-situ X-ray-diffraction. *J Electrochem Soc* 1995; 142(6):1746-52.
62. Manuel Stephan A, Nahm KS. Review on composite polymer electrolytes for lithium batteries. *Polymer* 2006;47(16):5952-64.
63. Cao F, Barsukov IV, Bang HJ, Zaleski P, Prakash J. Evaluation of graphite materials as anodes for lithium-ion batteries. *J Electrochem Soc* 2000;147(10):3579-83.
64. Tetsumi K, Zaghbi K, Suwada Y, Abe H, Ohsaki T. Anode performance of vapor-grown carbon fibers in secondary lithium-ion batteries. *J Electrochem Soc* 1995; 142(4):1090.
65. Chang Y, Sohn H, Ku C, Wang Y, Korai Y, Mochida I. Anodic performances of mesocarbon microbeads (MCMB) prepared from synthetic naphthalene isotropic pitch. *Carbon* 1999; 37(8):1285-97.
66. Takami N, Satoh A, Hara M, Ohsaki T. Rechargeable lithium-ion cells using graphitized mesophase-pitch-based carbon fiber anodes. *J Electrochem Soc* 1995; 142(8):2564-71.
67. Oumellal Y, Rougier A, Nazri GA, Tarascon J, Aymard L. Metal hydrides for lithium-ion batteries. *Nature Materials* 2008; 7(11):916-21.
68. Sato Y, Nakano T, Kobayakawa K, Kawai T, Yokoyama A. Particle-size effect of carbon powders on the discharge capacity of lithium ion batteries. *J Power Sources* 1998;75(2):271-7.
69. Ahn S, Kim Y, Kim KJ, Kim TH, Lee H, Kim MH. Development of high capacity, high rate lithium ion batteries utilizing metal fiber conductive additives. *J Power Sources* 1999;81:869-901.
70. Buiel E, Dahn JR. Li-insertion in hard carbon anode materials for li-ion batteries. *Electrochim Acta* 1999;45(1-2):121-30.

71. Cuesta A, Dhamelincourt P, Laureyns J, Martinezalonso A, Tascon J. Raman microprobe studies on carbon materials. *Carbon* 1994;32(8):1523-32.
72. Xing W, Xue JS, Dahn JR. Optimizing pyrolysis of sugar carbons for use as anode materials in lithium-ion batteries. *J Electrochem Soc* 1996;143(10):3046-52.
73. Tokumitsu K, Mabuchi A, Fujimoto H, Kasuh T. Electrochemical insertion of lithium into carbon synthesized from condensed aromatics. *J Electrochem Soc* 1996;143(7):2235-9.
74. Stephan AM, Kumar TP, Ramesh R, Thomas S, Jeong SK, Nahm KS. Pyrolytic carbon from biomass precursors as anode materials for lithium batteries. *Materials Science and Engineering A* 2006;430(1-2):132-7.
75. Tatsumi K, Kawamura T, Higuchi S, Hosotubo T, Nakajima H, Sawada Y. Anode characteristics of non-graphitizable carbon fibers for rechargeable lithium-ion batteries. *J Power Sources* 1997;68(2):263-6.
76. Tokumitsu K, Mabuchi A, Fujimoto H, Kasuh T. Electrochemical insertion of lithium into carbon synthesized from condensed aromatics. *J Electrochem Soc* 1996;143(7):2235-9.
77. Matsumura Y, Wang S, Mondori J. Interactions between disordered carbon and lithium in lithium ion rechargeable batteries. *Carbon* 1995;33(10):1457-62.
78. Zhang W. A review of the electrochemical performance of alloy anodes for lithium-ion batteries. *J Power Sources* 2011;196(1):13-24.
79. Beaulieu LY, Eberman KW, Turner RL, Krause LJ, Dahn JR. Colossal reversible volume changes in lithium alloys. *Electrochemical and Solid-State Letters* 2001;4(9):137-40.
80. Park C, Kim J, Kim H, Sohn H. Li-alloy based anode materials for li secondary batteries. *Chem Soc Rev* 2010;39(8):3115-41.
81. Winter M, Besenhard JO, Sphar MS, Novak P. Insertion electrode materials for rechargeable lithium batteries. *Adv Mater* 1998;10(10):725-63.
82. Ji L, Lin Z, Alcoutlabi M, Zhang X. Recent developments in nanostructured anode materials for rechargeable lithium-ion batteries. *Energy & Environmental Science* 2011; 4(8):2682-99.
83. Sharma RA, Seefurth RN. Thermodynamic properties of the lithium-silicon system. *J Electrochem Soc* 1976 12; 123(12):1763-8.

84. Rom I, Wachtler M, Papst I, Schmied M, Besenhard JO, Hofer F, Winter M. Electron microscopical characterization of Sn/SnSb composite electrodes for lithium-ion batteries. *Solid State Ionics, Diffusion & Reactions* 2001 07;143(3-4):329-36.
85. Liu J, Li Y, Ding R, Jiang J, Hu Y, Ji X, Chi Q, Zhu Z, Huang X. Carbon/ZnO nanorod array electrode with significantly improved lithium storage capability. *Journal of Physical Chemistry C* 2009; 113(13):5336-9.
86. Yang Z, Choi D, Kerisit S, Rosso KM, Wang D, Zhang J, Graff G, Liu J. Nanostructures and lithium electrochemical reactivity of lithium titanates and titanium oxides: A review. *J Power Sources* 2009; 192(2):588-98.
87. Gillot F, Boyanov S, Dupont L, Doublet M, Morcrette A, Monconduit L, Tarascon J. Electrochemical reactivity and design of NiP₂ negative electrodes for secondary li-ion batteries. *Chemistry of Materials* 2005; 17(25):6327-37.
88. Hwang H, Kim MG, Kim Y, Martin SW, Cho J. The electrochemical lithium reactions of monoclinic ZnP₂ material. *Journal of Materials Chemistry* 2007;17(30):3161-6.
89. Pralong V, Souza D, Leung K, Nazar L. Reversible lithium uptake by CoP₃ at low potential: Role of the anion. *Electrochemistry Communications* 2002; 4(6):516-20.
90. Lee YH, Leu IC, Liao CL, Chang ST, Wu MT, Yen JH, Fung KZ. Fabrication and characterization of Cu₂O nanorod arrays and their electrochemical performance in li-ion batteries. *Electrochemical and Solid-State Letters* 2006; 9(4):207-10.
91. Li Y, Tan B, Wu Y. Mesoporous CO₃O₄ nanowire arrays for lithium ion batteries with high capacity and rate capability. *Nano Letters*; 8(1):265-70.
92. He Y, Huang L, Cai J, Zheng X, Sun S. Structure and electrochemical performance of nanostructured Fe₃O₄/carbon nanotube composites as anodes for lithium ion batteries. *Electrochim Acta* 2010; 55(3):1140-4.
93. Hong L, Lihon S, Qing W, Liquan L, Xuejie H. Nano-alloy anode for lithium ion batteries. Symposium on materials for advanced batteries and fuel cells in conjunction with the international conference on materials for advanced technologies (ICMAT 2001); 06; Netherlands: Elsevier; 2002.
94. Hwang TH, Lee YM, Kong B, Seo J, Choi JW. Electrospun core-shell fibers for robust silicon nanoparticle-based lithium ion battery anodes. *Nano Letters* 2012; 12(2):802-7.
95. Green M, Fielder E, Scrosati B, Wachtler M, Moreno JS. Structured silicon anodes for lithium battery applications. *New trends in intercalation compounds for energy storage*

and conversion - proceedings of the international symposium; Apr 30-May 2 2003; Pennington, United States: Electrochemical Society Inc; 2003.

96. Kim I, Blomgren GE, Kumta PN. Si-SiC nanocomposite anodes synthesized using high-energy mechanical milling. *J Power Sources* 2004;130(1-2):275-80.
97. Park M, Kim MG, Joo J, Kim K, Kim J, Ahn S, Cui Y, Cho J. Silicon nanotube battery anodes. *Nano Letters* 2009; 9(11):3844-7.
98. Peng K, Jie J, Zhang W, Lee S. Silicon nanowires for rechargeable lithium-ion battery anodes. *Appl Phys Lett* 2008; 93(3):033105.
99. Chan CK, Peng H, Liu G, McIlwrath K, Zhang XF, Huggins RA, Cui Y. High-performance lithium battery anodes using silicon nanowires. *Nature Nanotechnology* 2008; 3(1):31-5.
100. Chen L, Xie X, Wang B, Wang K, Xie J. Spherical nanostructured Si/C composite prepared by spray drying technique for lithium ion batteries anode. *Materials Science and Engineering B: Solid-State Materials for Advanced Technology* 2006;131(1-3):186-90.
101. Li H, Huang X, Chen L, Wu Z, Liang Y. A high capacity nano-si composite anode material for lithium rechargeable batteries. *Electrochemical and Solid-State Letters* 1999 11;2(11):547-9.
102. Liu W, Guo Z, Young W, Shieh D, Wu H, Yang M, Wu N. Effect of electrode structure on performance of si anode in li-ion batteries: Si particle size and conductive additive. *J Power Sources* 2005;140(1):139-44.
103. Holzapfel M, Buqa H, Scheifele W, Novak P, Petrat FM. A new type of nano-sized silicon. *Chemical Communications* 2005(12):1566-8.
104. Eom JY, Park JW, Kwon HS, Rajendran S. Electrochemical insertion of lithium into multiwalled carbon nanotube/silicon composites produced by ballmilling. *J Electrochem Soc* 2006;153(9):1678-84.
105. Zhang X, Patil PK, Wang C, Appleby AJ, Little FE, Cocco DL. Electrochemical performance of lithium ion battery, nano-silicon-based, disordered carbon composite anodes with different microstructures. *J Power Sources* 2004;125(2):206-13.
106. Datta MK, Kumta PN. Silicon and carbon based composite anodes for lithium ion batteries. *J Power Sources* 2006;158(1):557-63.

107. Zeng ZY, Tu JP, Wang XL, Zhao XB. Electrochemical properties of Si/LiTi₂O₄ nanocomposite as anode materials for li-ion secondary batteries. *J Electroanal Chem* 2008;616(1-2):7-13.
108. Shi DQ, Tu JP, Yuan YF, Wu HM, Li Y, Zhao XB. Preparation and electrochemical properties of mesoporous Si/ZrO₂ nanocomposite film as anode material for lithium ion battery. *Electrochemistry Communications* 2006;8(10):1610-4.
109. Patel P, Kim I, Kumta PN. Nanocomposites of silicon/titanium carbide synthesized using high-energy mechanical milling for use as anodes in lithium-ion batteries. *Materials Science and Engineering B: Solid-State Materials for Advanced Technology* 2005;116(3):347-52.
110. Guo ZP, Zhao ZW, Liu HK, Dou SX. Lithium insertion in si-TiC nanocomposite materials produced by high-energy mechanical milling. *J Power Sources* 2005; 146(1-2):190-4.
111. Wang GX, Sun L, Bradhurst DH, Zhong S, Dou SX, Liu HK. Nanocrystalline NiSi alloy as an anode material for lithium-ion batteries. *J Alloys Compounds* 2000; 306(1-2):249-52.
112. Graetz J, Ahn CC, Yazami R, Fultz B. Highly reversible lithium storage in nanostructured silicon. *Electrochemical and Solid-State Letters* 2003;6(9):194-7.
113. Cui L, Yang Y, Hsu C, Cui Y. Carbon-silicon core-shell nanowires as high capacity electrode for lithium ion batteries. *Nano Letters* 2009; 9(9):3370-4.
114. Magasinski A, Dixon P, Hertzberg B, Kvit A, Ayala J, Yushin G. High-performance lithium-ion anodes using a hierarchical bottom-up approach. *Nature Materials* 2010; 9(4):353-8.
115. Chan CK, Patel RN, O'Connell MJ, Korgel BA, Cui Y. Solution-grown silicon nanowires for lithium-ion battery anodes. *Acs Nano* 2010; 4(3):1443-50.
116. Song T, Xia J, Lee J, Lee DH, Kwon M, Choi J, Wu J, Doo SK, Chang H, Il Park W, et al. Arrays of sealed silicon nanotubes as anodes for lithium ion batteries. *Nano Lett* 2010; 10(5):1710-6.
117. Ji L, Jung K, Medford AJ, Zhang X. Electrospun polyacrylonitrile fibers with dispersed si nanoparticles and their electrochemical behaviors after carbonization. *Journal of Materials Chemistry* 2009; 19(28):4992-7.

118. Kim H, Han B, Choo J, Cho J. Three-dimensional porous silicon particles for use in high-performance lithium secondary batteries. *Angewandte Chemie-International Edition* 2008;47(52):10151-4.
119. Brousse T, Retoux R, Herterich U, Schleich D. Thin-film crystalline SnO₂-lithium electrodes. *J Electrochem Soc* 1998; 145(1):1-4.
120. Ayouchi R, Martin F, Barrado J, Martos M, Morales J, Sanchez L. Use of amorphous tin-oxide films obtained by spray pyrolysis as electrodes in lithium batteries. *J Power Sources* 2000; 87(1-2):106-11.
121. Yang Z, Du G, Feng C, Li S, Chen Z, Zhang P, Guo Z, Yu X, Chen G, Huang S, et al. Synthesis of uniform polycrystalline tin dioxide nanofibers and electrochemical application in lithium-ion batteries. *Electrochim Acta* 2010; 55(19):5485-91.
122. Foster D, Wolfenstine J, Read J, Behl W. Nanocomposites of Sn and Li₂O formed from the chemical reduction of SnO as negative electrode material for lithium-ion batteries. *Electrochemical and Solid State Letters* 2000; 3(5):203-4.
123. Hassoun J, Derrien G, Panero S, Scrosati B. A nanostructured Sn-C composite lithium battery electrode with unique stability and high electrochemical performance. *Adv Mater* 2008; 20(16):3169-75.
124. Deng D, Kim MG, Lee JY, Cho J. Green energy storage materials: Nanostructured TiO₂ and Sn-based anodes for lithium-ion batteries. *Energy & Environmental Science* 2009; 2(8):818-37.
125. An G, Na N, Zhang X, Miao Z, Miao S, Ding K, Liu Z. SnO₂/carbon nanotube nanocomposites synthesized in supercritical fluids: Highly efficient materials for use as a chemical sensor and as the anode of a lithium-ion battery. *Nanotechnology* 2007; 18(43):435707.
126. Wang C, Zhou Y, Ge M, Xu X, Zhang Z, Jiang JZ. Large-scale synthesis of SnO₂ nanosheets with high lithium storage capacity. *J Am Chem Soc* 2010; 132(1):46,+.
127. Kim W, Lee B, Kim D, Kim H, Yu W, Hong S. SnO₂ nanotubes fabricated using electrospinning and atomic layer deposition and their gas sensing performance. *Nanotechnology* 2010; 21(24):245605.
128. Yu Y, Yang Q, Teng D, Yang X, Ryu S. Reticular Sn nanoparticle-dispersed PAN-based carbon nanofibers for anode material in rechargeable lithium-ion batteries. *Electrochemistry Communications* 2010 SEP;12(9):1187-90.

129. Mi H, Xu Y, Shi W, Yoo H, Park S, Park Y, Oh SM. Polymer-derived carbon nanofiber network supported SnO(2) nanocrystals: A superior lithium secondary battery material. *J Mater Chem* 2011;21(48):19302-9.
130. Wang H, Gao P, Lu S, Liu H, Yang G, Pinto J, Jiang X. The effect of tin content to the morphology of Sn/carbon nanofiber and the electrochemical performance as anode material for lithium batteries. *Electrochim Acta* 2011; 58:44-51.
131. Li L, Yin X, Liu S, Wang Y, Chen L, Wang T. Electrospun porous SnO(2) nanotubes as high capacity anode materials for lithium ion batteries. *Electrochemistry Communications* 2010; 12(10):1383-6.
132. Armstrong A, Armstrong G, Canales J, Bruce P. TiO₂-B nanowires as negative electrodes for rechargeable lithium batteries. *J Power Sources* 2005; 146(1-2):501-6.
133. Ding S, Chen JS, Luan D, Boey FYC, Madhavi S, Lou XW(. Graphene-supported anatase TiO(2) nanosheets for fast lithium storage. *Chemical Communications* 2011;47(20):5780-2.
134. Peramunage D, Abraham K. Preparation of micron-sized Li₄Ti₅O₁₂ and its electrochemistry in polyacrylonitrile electrolyte-based lithium cells. *J Electrochem Soc* 1998; 145(8):2609-15.
135. Hibino M, Abe K, Mochizuki M, Miyayama M. Amorphous titanium oxide electrode for high-rate discharge and charge. *J Power Sources* 2004; 126(1-2):139-43.
136. Zhu N, Liu W, Xue M, Xie Z, Zhao D, Zhang M, Chen J, Cao T. Graphene as a conductive additive to enhance the high-rate capabilities of electrospun li(4)ti(5)O(12) for lithium-ion batteries. *Electrochim Acta* 2010; 55(20):5813-8.
137. Shen L, Yuan C, Luo H, Zhang X, Yang S, Lu X. In situ synthesis of high-loading li(4)ti(5)O(12)-graphene hybrid nanostructures for high rate lithium ion batteries. *Nanoscale* 2011;3(2):572-4.
138. Panda SK, Yoon Y, Jung HS, Yoon W, Shin H. Nanoscale size effect of titania (anatase) nanotubes with uniform wall thickness as high performance anode for lithium-ion secondary battery. *J Power Sources* 2012; 204:162-7.
139. Wang D, Choi D, Li J, Yang Z, Nie Z, Kou R, Hu D, Wang C, Saraf LV, Zhang J, et al. Self-assembled TiO(2)-graphene hybrid nanostructures for enhanced Lli-ion insertion. *Acs Nano* 2009; 3(4):907-14.

140. Liu H, Bi Z, Sun X, Unocic RR, Paranthaman MP, Dai S, Brown GM. Mesoporous TiO₂-B microspheres with superior rate performance for lithium ion batteries. *Adv Mater* 2011; 23(30):3450.
141. Wang Q, Jiao L, Du H, Peng W, Han Y, Song D, Si Y, Wang Y, Yuan H. Novel flower-like CoS architectures: One-pot synthesis and electrochemical properties. *J Mater Chem* 2011;21(2):327-9.
142. Ban C, Wu Z, Gillaspie DT, Chen L, Yan Y, Blackburn JL, Dillon AC. Nanostructured Fe₃O₄/SWNT electrode: Binder-free and high-rate li-ion anode. *Adv Mater* 2010; 22(20):E145.
143. Lee S, Kim Y, Deshpande R, Parilla PA, Whitney E, Gillaspie DT, Jones KM, Mahan AH, Zhang S, Dillon AC. Reversible lithium-ion insertion in molybdenum oxide nanoparticles. *Adv Mater* 2008; 20(19):3627,+.
144. Lu Y, Wang Y, Zou Y, Jiao Z, Zhao B, He Y, Wu M. Macroporous co₃O₄ platelets with excellent rate capability as anodes for lithium ion batteries. *Electrochemistry Communications* 2010; 12(1):101-5.
145. Boyanov S, Zitoun D, Menetrier M, Jumas JC, Womes M, Monconduit L. Comparison of the electrochemical Lithiation/Delithiation mechanisms of FeP_x (x=1, 2, 4) based electrodes in li-ion batteries. *J Phys Chem C* 2009; 113(51):21441-52.
146. Alcantara R, Tirado J, Jumas J, Monconduit L, Olivier-Fourcade J. Electrochemical reaction of lithium with CoP₃. *J Power Sources* 2002; 109(2):308-12.
147. Boyanov S, Gillot F, Monconduit L. The electrochemical reactivity of the NiP₃ skutterudite-type phase with lithium. *Ionics* 2008; 14(2):125-30.
148. Kang Y, Song M, Kim J, Kim H, Park M, Lee J, Liu HK, Dou SX. A study on the charge-discharge mechanism of Co₃O₄ as an anode for the li ion secondary battery. *Electrochim Acta* 2005;50(18):3667-73.
149. Sun Ke, Lu Hai-Wei, Li Da, Zeng Wei, Li Yue-Sheng, Fu Zheng-Wen. Electrospun manganese oxides nanofibers electrode for lithium ion batteries. *Journal of Inorganic Materials* 2009; 24(2):357-60.
150. Zhu X, Zhu Y, Murali S, Stollers MD, Ruoff RS. Nanostructured reduced graphene Oxide/Fe₂O₃ composite as a high-performance anode material for lithium ion batteries. *Acs Nano* 2011; 5(4):3333-8.

151. Wu Z, Ren W, Wen L, Gao L, Zhao J, Chen Z, Zhou G, Li F, Cheng H. Graphene anchored with Co_3O_4 nanoparticles as anode of lithium ion batteries with enhanced reversible capacity and cyclic performance. *ACS Nano* 2010; 4(6):3187-94.
152. Ji L, Tan Z, Kuykendall TR, Aloni S, Xun S, Lin E, Battaglia V, Zhang Y. Fe_3O_4 nanoparticle-integrated graphene sheets for high-performance half and full lithium ion cells. *Physical Chemistry Chemical Physics* 2011;13(15):7139-46.
153. Ma S, Nam K, Yoon W, Yang X, Ahn K, Oh K, Kim K. Electrochemical properties of manganese oxide coated onto carbon nanotubes for energy-storage applications. *J Power Sources* 2008; 178(1):483-9.
154. Liu J, Xia H, Xue D, Lu L. Double-shelled nanocapsules of V_2O_5 -based composites as high-performance anode and cathode materials for li ion batteries. *J Am Chem Soc* 2009; 131(34):12086,+.
155. Lou XW, Deng D, Lee JY, Feng J, Archer LA. Self-supported formation of needlelike Co_3O_4 nanotubes and their application as lithium-ion battery electrodes. *Adv Mater* 2008; 20(2):258.
156. Yuan L, Guo ZP, Konstantinov K, Munroe P, Liu HK. Spherical clusters of NiO nanoshafths for lithium-ion battery anodes. *Electrochemical and Solid-State Letters* 2006;9(11):524-8.
157. Aurbach D, Markovsky B, Shechter A, EinEli Y, Cohen H. A comparative study of synthetic graphite and li electrodes in electrolyte solutions based on ethylene carbonate dimethyl carbonate mixtures. *J Electrochem Soc* 1996; 143(12):3809-20.
158. Agrawal RC, Pandey GP. Solid polymer electrolytes: Materials designing and all-solid-state battery applications: An overview. *Journal of Physics D-Applied Physics* 2008; 41(22):223001.
159. Abe K, Yoshitake H, Kitakura T, Hattori T, Wang H, Yoshio M. Additives-containing functional electrolytes for suppressing electrolyte decomposition in lithium-ion batteries. *Electrochim Acta* 2004;49(26):4613-22.
160. Aurbach D, Zaban A, Ein-Eli Y, Weissman I, Chusid O, Markovsky B, Levi M, Levi E, Schechter A, Granot E. Recent studies on the correlation between surface chemistry, morphology, three-dimensional structures and performance of li and li-C intercalation anodes in several important electrolyte systems. *J Power Sources* 1997;68(1):91-8.

161. van Schalkwijk WA, Scrosati B, NetLibrary I. *Advances in lithium-ion batteries*. New York, NY: Kluwer Academic/Plenum Publishers; 2002. 019: 50102327; edited by Walter A. van Schalkwijk and Bruno Scrosati.
162. Zheng M, Dong Q, Cai H, Jin M, Lin Z, Sun S. Formation and influence factors of solid electrolyte interphase film on the negative electrode surface in lithium-ion batteries. *J Electrochem Soc* 2005;152(11):2207-10.
163. Zhang S, Ding M, Xu K, Allen J, Jow T. Understanding solid electrolyte interface film formation on graphite electrodes. *Electrochemical and Solid State Letters* 2001; 4(12):A206-8.
164. Zhang S, Xu K, Jow T. EIS study on the formation of solid electrolyte. *Electrochim Acta* 2006; 51(8-9):1636-40.
165. Chung G, Jun S, Lee K, Kim M. Effect of surface structure on the irreversible capacity of various graphitic carbon electrodes. *J Electrochem Soc* 1999;146(5):1664-71.
166. Zaghbi K, Nadeau G, Kinoshita K. Effect of graphite particle size on irreversible capacity loss. *J Electrochem Soc* 2000;147(6):2110-5.
167. Fujimoto H, Mabuchi A, Tokumitsu K, Kasuh T. Irreversible capacity of lithium secondary battery using meso-carbon micro beads as anode material. *J Power Sources* 1995;54(2):440-3.
168. Tran T, Yebka B, Song X, Nazri G, Kinoshita K, Curtis D. Thermal and electrochemical studies of carbons for li-ion batteries. 2. correlation of active sites and irreversible capacity loss. *J Power Sources* 2000;85(2):269-78.
169. Xie H, Zhou Z. Physical and electrochemical properties of mix-doped lithium iron phosphate as cathode material for lithium ion battery. *Electrochim Acta* 2006; 51(10):2063-7.
170. Peled E, Menachem C, BarTow D, Melman A. Improved graphite anode for lithium-ion batteries - chemically bonded solid electrolyte interface and nanochannel formation. *J Electrochem Soc* 1996; 143(1):L4-7.
171. Cao Y, Xiao L, Ai X, Yang H. Surface-modified graphite as an improved intercalating anode for lithium-ion batteries. *Electrochemical and Solid State Letters* 2003; 6(2):A30.
172. Lee J, Lee H, Oh S, Lee S, Lee K, Lee S. Effect of carbon coating on electrochemical performance of hard carbons as anode materials for lithium-ion batteries. *J Power Sources* 2007;166(1):250-4.

173. Yoon S, Kim H, Oh SM. Surface modification of graphite by coke coating for reduction of initial irreversible capacity in lithium secondary batteries. *J Power Sources* 2001;94(1):68-73.
174. Beguin F, Chevallier F, Vix-Guterl C, Saadallah S, Bertagna V, Rouzaud JN, Frackowiak E. Correlation of the irreversible lithium capacity with the active surface area of modified carbons. *Carbon* 2005;43(10):2160-7.
175. Laine NR, Vastola FJ, Walker PL. Importance of active surface area in carbon-oxygen reaction. *J Phys Chem* 1963;67(10):2030.
176. Chung K, Park J, Kim W, Sung Y, Choi Y. Suppressive effect of lithium phosphorous oxynitride at carbon anode on solvent decomposition in liquid electrolyte. *J Power Sources* 2002;112(2):626-33.
177. Zhang SS. A review on electrolyte additives for lithium-ion batteries. *J Power Sources* 2006; 162(2):1379-94.
178. Aurbach D, Gnanaraj J, Geissler W, Schmidt M. Vinylene carbonate and lithium salicylatoborate as additives in $\text{LiPF}_3(\text{CF}_2\text{CF}_3)_3$ solutions for rechargeable lithium-ion batteries. *J Electrochem Soc* 2004; 151(1):A23-30.
179. Aurbach D, Gamolsky K, Markovsky B, Gofer Y, Schmidt M, Heider U. On the use of vinylene carbonate (VC) electrolyte solutions for lithium-ion as an additive to batteries. *Electrochim Acta* 2002; 47(9):1423-39.
180. Lee J, Lin Y, Jan Y. Allyl ethyl carbonate as an additive for lithium-ion battery electrolytes. *J Power Sources* 2004; 132(1-2):244-8.
181. Santner H, Moller K, Ivanco J, Ramsey M, Netzer F, Yamaguchi S, Besenhard J, Winter M. Acrylic acid nitrile, a film-forming electrolyte component for lithium-ion batteries, which belongs to the family of additives containing vinyl groups. *J Power Sources* 2003; 119:368-72.
182. Besenhard J, Wagner M, Winter M, Jannakoudakis A, Jannakoudakis P, Theodoridou E. Inorganic film-forming electrolyte additives improving the cycling behavior of metallic lithium electrodes and the self-discharge of carbon lithium electrodes. *J Power Sources* 1993; 44(1-3):413-20.
183. Shin J, Han C, Jung U, Lee S, Kim H, Kim K. Effect of Li_2CO_3 additive on gas generation in lithium-ion batteries. *J Power Sources* 2002; 109(1):47-52.

184. Choi YK, Chung KI, Kim WS, Sung YE, Park SM. Suppressive effect of Li_2CO_3 on initial irreversibility at carbon anode in li-ion batteries. *J Power Sources* 2002; 104(1):132-9.
185. Komaba S, Itabashi T, Kaplan B, Groult H, Kumagai N. Enhancement of li-ion battery performance of graphite anode by sodium ion as an electrolyte additive. *Electrochemistry Communications* 2003; 5(11):962-6.
186. Zheng H, Fu Y, Zhang H, Abe T, Ogumi Z. Potassium salts - electrolyte additives for enhancing electrochemical performances of natural graphite anodes. *Electrochemical and Solid State Letters* 2006; 9(3):A115-9.
187. Xu K, Zhang S, Poese B, Jow T. Lithium bis(oxalato)borate stabilizes graphite anode in propylene carbonate. *Electrochemical and Solid State Letters* 2002; 5(11):A259-62.
188. Zhang SS. An unique lithium salt for the improved electrolyte of li-ion battery. *Electrochemistry Communications* 2006; 8(9):1423-8.
189. Narayanan S, Surampudi S, Attia A, Bankston C. Analysis of redox additive-based overcharge protection for rechargeable lithium batteries. *J Electrochem Soc* 1991; 138(8):2224-9.
190. Buhrmester C, Chen J, Moshurchak L, Jiang J, Wang R, Dahn J. Studies of aromatic redox shuttle additives for LiFePO_4 -based li-ion cells. *J Electrochem Soc* 2005; 152(12):A2390-9.
191. Adachi M, Tanaka K, Sekai K. Aromatic compounds as redox shuttle additives for 4 V class secondary lithium batteries. *J Electrochem Soc* 1999 APR; 146(4):1256-61.
192. Dantsin G, Jambunathan K, Ivanov SV, Casteel WJ, Amine K, Liu J, Jansen AN. Advance electrolyte salts with inherent overcharge protection for lithium ion batteries. October 16-21; Los Angeles, CA: ECS 2005.
193. Andraday AL. Science and technology of polymer nanofibers. Hoboken, N.J.: Wiley; 2008.
194. Wannatong L, Sirivat A, Supaphol P. Effects of solvents on electrospun polymeric fibers: Preliminary study on polystyrene. *Polym Int* 2004; 53(11):1851-9.
195. Frenot A, Henriksson MW, Walkenstrom P. Electrospinning of cellulose-based nanofibers. *J Appl Polym Sci* 2007; 103(3):1473-82.

196. Li D, Xia Y. Electrospinning of nanofibers: Reinventing the wheel? *Adv Mater* 2004; 16(14):1151-70.
197. Zuo W, Zhu M, Yang W, Yu H, Chen Y, Zhang Y. Experimental study on relationship between jet instability and formation of beaded fibers during electrospinning. *Polym Eng Sci* 2005;45(5):704-9.
198. Yarin AL, Koombhongse S, Reneker DH. Bending instability in electrospinning of nanofibers. *J Appl Phys* 2001;89(5):3018-26.
199. Thompson CJ, Chase GG, Yarin AL, Reneker DH. Effects of parameters on nanofiber diameter determined from electrospinning model. *Polymer* 2007;48(23):6913-22.
200. Spivak AF, Dzenis YA, Reneker DH. Model of steady state jet in the electrospinning process. *Mech Res Commun* 2000;27(1):37-42.
201. Yang D, Zhang J, Zhang J, Nie J. Aligned electrospun nanofibers induced by magnetic field. *J Appl Polym Sci* 2008;110(6):3368-72.
202. Wang T, Kumar S. Electrospinning of polyacrylonitrile nanofibers. *J Appl Polym Sci* 2006;102(2):1023-9.
203. Lannutti J, Reneker D, Ma T, Tomasko D, Farson D. Electrospinning for tissue engineering scaffolds. *Materials Science and Engineering C* 2007;27(3):504-9.
204. Ramachandran K, Gouma P. Electrospinning for bone tissue engineering. *Recent Patents on Nanotechnology* 2008;2(1):1-7.
205. Cui W, Li X, Zhu X, Yu G, Zhou S, Weng J. Investigation of drug release and matrix degradation of electrospun poly(DL-lactide) fibers with paracetamol inoculation. *Biomacromolecules* 2006;7(5):1623-9.
206. Piras AM, Chiellini F, Chiellini E, Nikkola L, Ashammakhi N. New multicomponent bioerodible electrospun nanofibers for dual-controlled drug release. *J Bioact Compatible Polym* 2008;23(5):423-43.
207. Kim SJ, Nam YS, Rhee DM, Park H, Park WH. Preparation and characterization of antimicrobial polycarbonate nanofibrous membrane. *European Polymer Journal* 2007;43(8):3146-52.
208. Ma Z, Kotaki M, Ramakrishna S. Surface modified nonwoven polysulphone (PSU) fiber mesh by electrospinning: A novel affinity membrane. *J Membr Sci* 2006;272(1-2):179-87.

209. Ju Y, Choi G, Jung H, Lee W. Electrochemical properties of electrospun PAN/MWCNT carbon nanofibers electrodes coated with polypyrrole. *Electrochim Acta* 2008;53(19):5796-803.
210. Taylor G. Disintegration of water drops in electric field. *Royal Society -- Proceedings Series A* 1964;280(1382):383-7.
211. Kessick R, Fenn J, Tepper G. The use of AC potentials in electrospraying and electrospinning processes. *Polymer* 2004;45(9):2981-4.
212. Moon S, Choi J, Farris RJ. Preparation of aligned polyetherimide fiber by electrospinning. *J Appl Polym Sci* 2008;109(2):691-4.
213. Ji L, Lin Z, Medford AJ, Zhang X. Porous carbon nanofibers from electrospun polyacrylonitrile/SiO₂ composites as an energy storage material. *Carbon* 2009;47(14):3346-54.
214. Kim G, Wutzler A, Radusch H, Michler GH, Simon P, Sperling RA, Parak WJ. One-dimensional arrangement of gold nanoparticles by electrospinning. *Chemistry of Materials* 2005;17(20):4949-57.
215. Graberg TV, Thomas A, Antonietti M, Weber J, Greiner A. Electrospun silica-polybenzimidazole nanocomposite fibers. *Macromolecular Materials and Engineering* 2008;293(10):815-9.
216. Preparation and characterization of a PAN nanofibre containing Ag nanoparticles via electrospinning. *ICSM 2002; Jun 29-Jul 5 2002; Elsevier Ltd; 2003.*
217. Yu J, Liu T. Preparation of a fibrous catalyst containing palladium nanoparticles and its application in hydrogenation of olefins. *Polymer Composites* 2008;29(12):1346-9.
218. Kim C, Cho YJ, Yun WY, Ngoc BTN, Yang KS, Chang DR, Lee JW, Kojima M, Kim YA, Endo M. Fabrications and structural characterization of ultra-fine carbon fibres by electrospinning of polymer blends. *Solid State Commun* 2007;142(1-2):20-3.
219. Ji L, Medford AJ, Zhang X. Porous carbon nanofibers loaded with manganese oxide particles: Formation mechanism and electrochemical performance as energy-storage materials. *Journal of Materials Chemistry* 2009;19(31):5593-601.
220. Zhang Q, Chang Z, Zhu M, Mo X, Chen D. Electrospun carbon nanotube composite nanofibres with uniaxially aligned arrays. *Nanotechnology* 2007;18(11):115611.

221. Choi S, Lee Y, Joo C, Lee S, Park J, Han K. Electrospun PVDF nanofiber web as polymer electrolyte or separator. *Electrochim Acta* 2004; 50(2-3):339-43.
222. Cheruvally G, Kim J, Choi J, Ahn J, Shin Y, Manuel J, Raghavan P, Kim K, Ahn H, Choi DS, et al. Electrospun polymer membrane activated with room temperature ionic liquid: Novel polymer electrolytes for lithium batteries. *J Power Sources* 2007; 172(2):863-9.
223. Choi S, Jo S, Lee W, Kim Y. An electrospun poly(vinylidene fluoride) nanofibrous membrane and its battery applications. *Adv Mater* 2003; 15(23):2027-32.
224. Lee SW, Choi SW, Jo SM, Chin BD, Kim DY, Lee KY. Electrochemical properties and cycle performance of electrospun poly(vinylidene fluoride)-based fibrous membrane electrolytes for li-ion polymer battery. *J Power Sources* 2006; 163(1):41-6.
225. Liang Y, Ji L, Guo B, Lin Z, Yao Y, Li Y, Alcoutlabi M, Qiu Y, Zhang X. Preparation and electrochemical characterization of ionic-conducting lithium lanthanum titanate oxide/polyacrylonitrile submicron composite fiber-based lithium-ion battery separators. *J Power Sources* 2011; 196(1):436-41.
226. Choi S, Kim J, Jo S, Lee W, Kim Y. Electrochemical and spectroscopic properties of electrospun PAN-based fibrous polymer electrolytes. *J Electrochem Soc* 2005;152(5):A989-95.
227. Inagaki M. *New carbons : Control of structure and functions*. 1st ed. Amsterdam ; New York: Elsevier; 2000.
228. Jing M, Wang C, Wang Q, Bai Y, Zhu B. Chemical structure evolution and mechanism during pre-carbonization of PAN-based stabilized fiber in the temperature range of 350-600° C. *Polym Degrad Stab* 2007;92(9):1737-42.
229. Wang Y, Serrano S, Santiago-Aviles J. Raman characterization of carbon nanofibers prepared using electrospinning. *Synth Met* 2003;138(3):423-7.
230. Zhang W, Wang Y, Sun C. Characterization on oxidative stabilization of polyacrylonitrile nanofibers prepared by electrospinning. *Journal of Polymer Research* 2007;14(6):467-74.
231. Kim C, Yang KS. Electrochemical properties of carbon nanofiber web as an electrode for supercapacitor prepared by electrospinning. *Appl Phys Lett* 2003;83(6):1216-8.
232. Borhani S, Hosseini SA, Etemad SG, Militky J. Structural characteristics and selected properties of polyacrylonitrile nanofiber mats. *J Appl Polym Sci* 2008;108(5):2994.

233. Zhang L, Hsieh Y. Nanoporous ultrahigh specific surface polyacrylonitrile fibres. *Nanotechnology* 2006;17(17):4416-23.
234. McCann JT, Lim B, Ostermann R, Rycenga M, Marquez M, Xia Y. Carbon nanotubes by electrospinning with a polyelectrolyte and vapor deposition polymerization. *Nano Letters* 2007;7(8):2470-4.
235. Ge JJ, Hou H, Li Q, Graham MJ, Greiner A, Reneker DH, Harris FW, Cheng SZD. Assembly of well-aligned multiwalled carbon nanotubes in confined polyacrylonitrile environments: Electrospun composite nanofiber sheets. *J Am Chem Soc* 2004;126(48):15754-61.
236. Hou H, Ge JJ, Zeng J, Li Q, Reneker DH, Greiner A, Cheng SZD. Electrospun polyacrylonitrile nanofibers containing a high concentration of well-aligned multiwall carbon nanotubes. *Chemistry of Materials* 2005;17(5):967-73.
237. Ji L, Zhang X, Carbonized PAN nanofibers containing Mn nanoparticles as anodes for li-ion batteries (2008, unpublished) .
238. Hergenrother PM. The use, design, synthesis, and properties of high performance/high temperature polymers: An overview. *High Perform Polymers* 2003;15(1):3-45.
239. Volksen W, Cotts P, Yoon D. Molecular-weight dependence of mechanical-properties of poly(p,p'-oxydiphenylene pyromellitimide) films. *J Polym Sci Pt B-Polym Phys* 1987; 25(12):2487-95.
240. Volksen W, Yoon D, Hendrick J. Polyamic alkyl esters - versatile polyimide precursors for improved dielectric coatings. *Ieee Transactions on Components Hybrids and Manufacturing Technology* 1992; 15(1):107-13.
241. Singh BP, Singh D, Mathur RB, Dhama TL. Influence of surface modified MWCNTs on the mechanical, electrical and thermal properties of polyimide nanocomposites. *Nanoscale Research Letters* 2008;3(11):444-53.
242. Stoffel N, Hsieh M, Kramer E, Volksen W. Adhesion enhancement and lamination of polyimide films. *IEEE Trans Compon Packag Manuf Technol Part B-Adv Packag* 1996; 19(2):417-22.
243. Dinhart R, Wright W. Preparation and fabrication of aromatic polyimides. *J Appl Polym Sci* 1967;11(5):609.
244. Mittal KL, Society of Plastics Engineers. Mid-Hudson Section. *Polyimides: Synthesis, characterization, and applications*. New York: Plenum; 1984.

245. Cotts P. Polyelectrolyte effects in low-angle light-scattering from solutions of polyamic acid in organic-solvents. *J Polym Sci Pt B-Polym Phys* 1986; 24(4):923-30.
246. Bower G, Frost L. Aromatic polyimides. *Journal of Polymer Science Part A-General Papers* 1963;1(10):3135,&.
247. Cotts P, Volksen W, Ferline S. Equilibration of mixtures of polyamic acids studied using size-exclusion chromatography and light-scattering. *J Polym Sci Pt B-Polym Phys* 1992; 30(4):373-9.
248. Fjare D. Amic acid redistribution reactions - substituent effects. *Macromolecules* 1993; 26(19):5143-8.
249. Echigo Y, Iwaya Y, Tomioka I, Furukawa M, Okamoto S. Novel polymerization process of poly(4,4 prime -oxydiphenylenepyromellitic acid). *Macromolecules* 1995;28(8):3000-1.
250. Wallach M. Aromatic poly(amic acids) - fundamental structural studies. *Journal of Polymer Science Part A-2-Polymer Physics* 1967;5(4PA2):653,&.
251. Volksen W. Condensation polyimides - synthesis, solution behavior, and imidization characteristics. *High Perform Polymers* 1994;117:111-64.
252. Cotts P, Volksen W. Solution characterization of polyamic acids and polyimides. *ACS Symp Ser* 1984;242:227-37.
253. Ree M, Yoon D, Volksen W. Miscibility behavior and reequilibration of binary poly(amic acid) mixtures. *J Polym Sci Pt B-Polym Phys* 199; 29(10):1203-13.
254. Mukoyama Y, Shimizu N, Sakata T, Mori S. Elution behavior of polyamic acid and polyamide imide in size-exclusion chromatography. *J Chromatogr* 1991; 588(1-2):195.
255. Konas M, Moy T, Rogers M, Shultz A, Ward T, McGrath J. Molecular-weight characterization of soluble high-performance polyimides .2. validity of universal sec calibration and absolute molecular-weight calculation. *J Polym Sci Pt B-Polym Phys* 1995; 33(10):1441-8.
256. Kim S, Cotts P, Volksen W. Online measurement of the rms radius of gyration and molecular-weight of polyimide precursor fractions eluting from a size-exclusion chromatograph. *J Polym Sci Pt B-Polym Phys* 1992 FEB;30(2):177-83.
257. Kim S, Cotts P. Light-scattering and size exclusion chromatography of semiflexible polyimide precursors. *J Polym Sci Pt B-Polym Phys* 1991 JAN;29(1):109-17.

258. Barth H, Boyes B. Size exclusion chromatography. Anal Chem 1990 JUN 15;62(12):R381-94.
259. Mori S, 1935-. Size exclusion chromatography. Berlin ; New York: Springer; 1999.
260. Konas M, Moy T, Rogers M, Shultz A, Ward T, McGrath J. Molecular-weight characterization of soluble high-performance polyimides .1. polymer-solvent-stationary phase interactions in size-exclusion chromatography. J Polym Sci Pt B-Polym Phys 1995; 33(10):1429-39.
261. Mori S. Calibration of size exclusion chromatography columns for molecular-weight determination of poly(acrylonitrile) and poly(vinylpyrrolidone) in N,n-dimethylformamide. Anal Chem 1983;55(14):2414-6.
262. Krishnan P, Veeramani S, Vora R, Chung T, Uchimura S, Sugitani H. Molecular mass determination of polyamic acid ionic salt by size-exclusion chromatography. J Chromatogr A 2002 ; 977(2):207-12.
263. Kotera M, Nishino T, Nakamae K. Imidization processes of aromatic polyimide by temperature modulated DSC. Polymer 2000;41(10):3615-9.
264. Konno H, Shiba K, Tachikawa H, Nakahashi T, Oka H, Inagaki M. Nanospace due to the presence of boron and nitrogen in carbon films prepared from polyimide. Synth Met 2001; 125(2):189-96.
265. Sysel P, Konecna V, Volka K. Structure-curing relation for polyamic acids. European Polymer Journal 1996;32(3):317-20.
266. Su J, Lua AC. Effects of carbonisation atmosphere on the structural characteristics and transport properties of carbon membranes prepared from kapton [registered trademark] polyimide. J Membr Sci 2007;305(1-2):263-70.
267. Griбанov AV, Sazanov YN, Mokeev MV. Role of structural characteristics of aromatic polyimides in carbonization. Russian Journal of Applied Chemistry 2002; 75(4):606-10.
268. Burger A, Fitzer E, Heym M, Terwiesch B. Polyimides as precursors for artificial carbon. Carbon 1975;13(3):149-57.
269. Nah C, Han SH, Lee M, Kim JS, Lee DS. Characteristics of polyimide ultrafine fibers prepared through electrospinning. Polym Int 2003;52(3):429-32.

270. Xuyen NT, Ra EJ, Geng H, Kim KK, An KH, Lee YH. Enhancement of conductivity by diameter control of polyimide-based electrospun carbon nanofibers. *J Phys Chem B* 2007;111(39):11350-3.
271. Zhang Q, Wu D, Qi S, Wu Z, Yang X, Jin R. Preparation of ultra-fine polyimide fibers containing silver nanoparticles via in situ technique. *Mater Lett* 2007;61(19-20):4027.
272. Hampdensmith M, Kudas T. Chemical-vapor-deposition of metals .1. an overview of cvd processes. *Chemical Vapor Deposition* 1995; 1(1):8-23.
273. Fujino K, Nishimoto Y, Tokumasu N, Maeda K. Dependence of deposition characteristics on base materials in teos and ozone cvd at atmospheric-pressure. *J Electrochem Soc* 1991; 138(2):550-4.
274. Deshmukh S, Aydil E. Low-temperature plasma-enhanced chemical-vapor-deposition of SiO_2 . *Appl Phys Lett* 1994; 65(25):3185-7.
275. Habraken F, Kuiper A. Silicon-nitride and oxynitride films. *Materials Science & Engineering R-Reports* 1994; 12(3):123-75.
276. Islamraja M, Cappelli M, McVittie J, Saraswat K. A 3-dimensional model for low-pressure chemical-vapor-deposition step coverage in trenches and circular vias. *J Appl Phys* 1991; 70(11):7137-40.
277. Martinet C, Paillard V, Gagnaire A, Joseph J. Deposition of SiO_2 and TiO_2 thin films by plasma enhanced chemical vapor deposition for antireflection coating. *J Non Cryst Solids* 1997; 216:77-82.
278. Ray S, Maiti C, Lahiri S, Chakrabarti N. TEOS-based PECVD of silicon dioxide for VLSI applications. *Adv Mater Opt Electron* 1996; 6(2):73-82.
279. Tochtani G, Shimosuma M, Tagashira H. Deposition of silicon-oxide films from teos by low-frequency plasma chemical vapor-deposition. *Journal of Vacuum Science & Technology A-Vacuum Surfaces and Films* 1993; 11(2):400-5.
280. Parsons G, Souk J, Batey J. Low hydrogen content stoichiometric silicon-nitride films deposited by plasma-enhanced chemical vapor-deposition. *J Appl Phys* 1991; 70(3):1553-60.
281. Fix R, Gordon R, Hoffman D. Chemical vapor-deposition of titanium, zirconium, and hafnium nitride thin-films. *Chemistry of Materials* 1991; 3(6):1138-48.

282. Kobayashi T, Hirakuri K, Mutsukura N, Machi Y. Synthesis of CVD diamond at atmospheric pressure using the hot-filament CVD method. *Diamond and Related Materials* 1999 ; 8(6):1057-60.
283. Fitzgerald E, Samavedam S. Line, point and surface defect morphology of graded, relaxed GeSi alloys on si substrates. *Thin Solid Films* 1997; 294(1-2):3-10.
284. Rausch N, Burte E. Thin Tio₂ films prepared by low-pressure chemical vapor-deposition. *J Electrochem Soc* 1993 JAN;140(1):145-9.
285. Kim M, Bang Y, Park N, Choi C, Seong T, Park S. Growth of high-quality GaN on si(111) substrate by ultrahigh vacuum chemical vapor deposition. *Appl Phys Lett* 2001; 78(19):2858-60.
286. Hu Z, Huttinger KJ. Chemistry and kinetics of chemical vapor deposition of pyrocarbon. VIII. carbon deposition from methane at low pressures. *Carbon* 2001;39(3):433-41.
287. Haubner R, Lux B. Diamond growth by hot-filament chemical vapor deposition: State of the art. *Diamond and Related Materials* 1993;2(9):1277-94.
288. Kawase M, Miura K. Pyrocarbon growth from allene and allylene by chemical vapor deposition. Electrochemical Society Inc, high temperature materials division, May 7, 2006 - May 12; 2006; Denver, CO, United states: Electrochemical Society Inc; 2007.
289. Bae S, Kim H, Lee Y, Xu X, Park J, Zheng Y, Balakrishnan J, Lei T, Kim HR, Song YI, et al. Roll-to-roll production of 30-inch graphene films for transparent electrodes. *Nature Nanotechnology* 2010; 5(8):574-8.
290. Andrews R, Jacques D, Qian DL, Rantell T. Multiwall carbon nanotubes: Synthesis and application. *Acc Chem Res* 2002 DEC;35(12):1008-17.
291. Becker A, Huttinger KJ. Chemistry and kinetics of chemical vapor deposition of pyrocarbon - IV pyrocarbon deposition from methane in the low temperature regime. *Carbon* 1998;36(3):213-24.
292. Becker A, Huttinger KJ. Chemistry and kinetics of chemical vapor deposition of pyrocarbon - II pyrocarbon deposition from ethylene, acetylene and 1,3-butadiene in the low temperature regime. *Carbon* 1998;36(3):177-99.
293. Becker A, Huttinger KJ. Chemistry and kinetics of chemical vapor deposition of pyrocarbon - III pyrocarbon deposition from propylene and benzene in the low temperature regime. *Carbon* 1998;36(3):201-11.

294. Chen C, Back M, Back R. Thermal-decomposition of methane. 2. secondary reactions, autocatalysis and carbon formation - non-arrhenius behavior in reaction of CH_3 with ethane. *Canadian Journal of Chemistry-Revue Canadienne De Chimie* 1976;54(20):3175-84.
295. Wu X, Luo R, Zhang J, Xiang Q, Ni Y. Deposition mechanism and microstructure of pyrocarbon prepared by chemical vapor infiltration with kerosene as precursor. *Carbon* 2009;47(6):1429-35.
296. Benzinger W, Becker A, Huettinger KJ. Chemistry and kinetics of chemical vapour deposition of pyrocarbon: I. fundamentals of kinetics and chemical reaction engineering. *Carbon* 1996;34(8):957-66.
297. Lieberman M, Pierson H. Effect of gas-phase conditions on resultant matrix pyrocarbons in carbon-carbon composites. *Carbon* 1974;12(3):233-41.
298. Bruggert M, Hu Z, Huttlinger KJ. Chemistry and kinetics of chemical vapor deposition of pyrocarbon. VI. influence of temperature using methane as a carbon source. *Carbon* 1999;37(12):2021-30.
299. Fukuda M, Mizogami S, Yoshino K. Properties of high-quality flexible graphite film and its preparation by the pyrolytic cvd method. *Jpn J Appl Phys Part 1 - Regul Pap Short Notes Rev Pap* 1989; 28(1):122-4.
300. Benzinger W, Huettinger KJ. Chemical vapor infiltration of pyrocarbon: I. some kinetic considerations. *Carbon* 1996;34(12):1465-71.
301. Dupel P, Bourrat X, Paillet R. Structure of pyrocarbon infiltrated by pulse-cvi. *Carbon* 1995;33(9):1193-204.
302. McAllister P, Hendricks J, Wolf E. The infiltration of carbon-fiber felts and composites by pyrolytic carbon deposition from propylene. *Carbon* 1990;28(4):579-88.
303. Benzinger W, Huttlinger K,J. Chemistry and kinetics of chemical vapor infiltration of pyrocarbon - VI. mechanical and structural properties of infiltrated carbon fiber felt. *Carbon* 1999;37(8):1311-22.
304. Benzinger W, Huttlinger KJ. Chemistry and kinetics of chemical vapor infiltration of pyrocarbon-V. infiltration of carbon fiber felt. *Carbon* 1999;37(6):941-6.
305. Benzinger W, Huttlinger K. Chemical vapor infiltration of pyrocarbon - II. the influence of increasing methane partial pressure at constant total pressure on infiltration rate and degree of pore filling. *Carbon* 1998;36(7-8):1033-42.

306. Benzinger W, Huttinger K. Chemical vapor infiltration of pyrocarbon - III: The influence of increasing methane partial pressure at increasing total pressure on infiltration rate and degree of pore filling. *Carbon* 1999;37(2):181-93.
307. Benzinger W, Huttinger KJ. Chemistry and kinetics of chemical vapor infiltration of pyrocarbon-IV. investigation of methane/hydrogen mixtures. *Carbon* 1999;37(6):931-40.
308. Johansson A, Lu J, Carlsson J. Tem investigation of cvd graphite on nickel. *Thin Solid Films* 1994; 252(1):19-25.
309. Westberg H, Boman M, Norekrans A, Carlsson J. Carbon growth by thermal laser-assisted chemical vapor-deposition. *Thin Solid Films* 1992; 215(2):126-33.
310. Jacobsen R, Tritt T, Guth J, Ehrlich A, Gillespie D. Mechanical-properties of vapor-grown carbon-fiber. *Carbon* 1995;33(9):1217-21.
311. Kohmura N, Sudoh K, Sata K, Hirakuri KK, Miyake K, Friedbacher G. Diamond growth on the high purity iron substrate using hot-filament CVD method. *Proceedings of diamond 2004, the 15th european conference on diamond, diamond-like materials; Nitrides and Silicon; Elsevier Ltd; 2005.*
312. Cheng HF, Chen TT, Tsai C-H, Lin I-N. Nanocarbonaceous materials synthesized by microwave CVD and their characteristics of electron field emission. *IUMRS-ICEM 2002, June 10, 2002 - June 14; 2002; Xi an, China: Elsevier; 2003.*
313. Endo M, Hayashi T, Yoong Ahm Kim, Terrones M, Dresselhaus MS. Applications of carbon nanotubes in the twenty-first century. *Philosophical Transactions of the Royal Society London, Series A (Mathematical, Physical and Engineering Sciences) 2004 10/15;362(1823):2223-38.*
314. Mintmire JW, White CT. Electronic and structural properties of carbon nanotubes. *Carbon* 1995;33(7):893-902.
315. Ebbesen TW, Ajayan PM. Large-scale synthesis of carbon nanotubes. *Nature* 1992;358(6383):220.
316. Guo T, Nikolaev P, Rinzler AG, Tomanek D, Colbert DT, Smalley RE. Self-assembly of tubular fullerenes. *J Phys Chem* 1995;99(27):10694-7.
317. Ren ZF, Huang ZP, Wang DZ, Wen JG, Xu JW, Wang JH, Calvet LE, Chen J, Klemic JF, Reed MA. Growth of a single freestanding multiwall carbon nanotube on each nanonickel dot. *Appl Phys Lett* 1999;75(8):1086-8.

318. Tibbetts GG, Bernardo CA, Gorkiewicz DW, Alig RL. Role of sulfur in the production of carbon fibers in the vapor phase. *Carbon* 1994;32(4):569-76.
319. Andrews R, Jacques D, Qian D, Dickey EC. Purification and structural annealing of multiwalled carbon nanotubes at graphitization temperatures. *Carbon* 2001;39(11):1681-7.
320. Allen MJ, Tung VC, Kaner RB. Honeycomb carbon: A review of graphene. *Chem Rev* 2010 JAN;110(1):132-45.
321. Hernandez Y, Nicolosi V, Lotya M, Blighe FM, Sun Z, De S, McGovern IT, Holland B, Byrne M, Gun'ko YK, et al. High-yield production of graphene by liquid-phase exfoliation of graphite. *Nature Nanotechnology* 2008; 3(9):563-8.
322. Reina A, Jia X, Ho J, Nezich D, Son H, Bulovic V, Dresselhaus MS, Kong J. Large area, few-layer graphene films on arbitrary substrates by chemical vapor deposition. *Nano Lett* 2009; 9(1):30-5.
323. Knight D, White W. Characterization of diamond films by raman-spectroscopy. *J Mater Res* 1989; 4(2):385-93.
324. Kim C, Park S, Cho J, Lee D, Park T, Lee W, Yang K. Raman spectroscopic evaluation of polyacrylonitrile-based carbon nanofibers prepared by electrospinning. *J Raman Spectrosc* 2004;35(11):928-33.
325. Krupke R, Hennrich F, von Lohneysen H, Kappes M. Separation of metallic from semiconducting single-walled carbon nanotubes. *Science* 2003;301(5631):344-7.
326. Merkulov V, Lannin J, Munro C, Asher S, Veerasamy V, Milne W. Uv studies of tetrahedral bonding in diamondlike amorphous carbon. *Phys Rev Lett* 1997; 78(25):4869-72.
327. Ferrari AC, Meyer JC, Scardaci V, Casiraghi C, Lazzeri M, Mauri F, Piscanec S, Jiang D, Novoselov KS, Roth S, et al. Raman spectrum of graphene and graphene layers. *Phys Rev Lett* 2006; 97(18):187401.
328. Ferraro JR, 1918-. *Introductory raman spectroscopy*. Amsterdam: Academic Press; 2003.
329. Ferrari AC. Raman spectroscopy of graphene and graphite: Disorder, electron-phonon coupling, doping and nonadiabatic effects. *Solid State Commun* 2007; 143(1-2):47-57.

330. Dresselhaus MS, Villalpando-Paez F, Samsonidze GG, Chou SG, Dresselhaus G, Jiang J, Saito R, Souza Filho AG, Jorio A, Endo M, et al. Raman scattering from one-dimensional carbon systems. *Physica E-Low-Dimensional Systems & Nanostructures* 2007; 37(1-2):81-7.
331. Gupta A, Chen G, Joshi P, Tadigadapa S, Eklund PC. Raman scattering from high-frequency phonons in supported n-graphene layer films. *Nano Letters* 2006; 6(12):2667-73.
332. WANG Y, ALSMEYER D, MCCREERY R. Raman-spectroscopy of carbon materials - structural basis of observed spectra. *Chemistry of Materials* 1990; 2(5):557-63.
333. Reich S, Thomsen C. Raman spectroscopy of graphite. *Philosophical Transactions of the Royal Society A-Mathematical Physical and Engineering Sciences* 2004; 362(1824):2271-88.
334. Tuinstra F, Koenig J. Raman spectrum of graphite. *J Chem Phys* 1970;53(3):1126.
335. Matthews M, Pimenta M, Dresselhaus G, Dresselhaus M, Endo M. Origin of dispersive effects of the raman D band in carbon materials. *Phys Rev B* 1999; 59(10):R6585-8.
336. Ferrari A, Robertson J. Interpretation of raman spectra of disordered and amorphous carbon. *Phys Rev B* 2000; 61(20):14095-107.
337. Thomsen C, Reich S. Double resonant raman scattering in graphite. *Phys Rev Lett* 2000; 85(24):5214-7.
338. Ferrari A, Robertson J. Resonant raman spectroscopy of disordered, amorphous, and diamondlike carbon. *Physical Review B* 2001; 64(7):075414.
339. Gilkes K, Sands H, Batchelder D, Robertson J, Milne W. Direct observation of sp(3) bonding in tetrahedral amorphous carbon using ultraviolet raman spectroscopy. *Appl Phys Lett* 1997; 70(15):1980-2.
340. Pimenta MA, Dresselhaus G, Dresselhaus MS, Cancado LG, Jorio A, Saito R. Studying disorder in graphite-based systems by raman spectroscopy. *Physical Chemistry Chemical Physics* 2007; 9(11):1276-91.
341. George SM. Atomic layer deposition: An overview. *Chem Rev* 2010;110(1):111-31.
342. Riihela D, Ritala M, Matero R, Leskela M. Introducing atomic layer epitaxy for the deposition of optical thin films. *Thin Solid Films* 1996; 289(1-2):250-5.

343. Cavanagh AS, Lee Y, Yoon B, George SM. Atomic layer deposition of LiOH and Li₂CO₃ using lithium t-butoxide as the lithium source. 6th symposium on atomic layer deposition applications - 218th ECS Meeting, October 10, 2010 - October 15; 2010; Las Vegas, NV, United States: Electrochemical Society Inc; 2010.
344. Kim H. Atomic layer deposition of metal and nitride thin films: Current research efforts and applications for semiconductor device processing. *J Vac Sci Technol B* 2003; 21(6):2231-61.
345. Park K, Doub J, Gougousi T, Parsons G. Microcontact patterning of ruthenium gate electrodes by selective area atomic layer deposition. *Appl Phys Lett* 2005; 86(5):051903.
346. Ritala M, Leskela M, Niinisto L, Prohaska T, Friedbacher G, Grasserbauer M. Development of crystallinity and morphology in hafnium dioxide thin-films grown by atomic layer epitaxy. *Thin Solid Films* 1994 ; 250(1-2):72-80.
347. Tillack B, Yamamoto Y, Knoll D, Heinemann B, Schley P, Senapati B, Kruger D. High performance SiGe : C HBTs using atomic layer base doping. *Appl Surf Sci* 2004; 224(1-4):55-8.
348. Hyde GK, Park KJ, Stewart SM, Hinestroza JP, Parsons GN. Atomic layer deposition of conformal inorganic nanoscale coatings on three-dimensional natural fiber systems: Effect of surface topology on film growth characteristics. *Langmuir* 2007;23(19):9844-9.
349. Hyde GK, Scarel G, Spagnola JC, Peng Q, Lee K, Gong B, Roberts KG, Roth KM, Hanson CA, Devine CK, et al. Atomic layer deposition and abrupt wetting transitions on nonwoven polypropylene and woven cotton fabrics. *Langmuir* 2010; 26(4):2550-8.
350. Putkonen M, Aaltonen T, Alnes M, Sajavaara T, Nilsen O, Fjellvag H. Atomic layer deposition of lithium containing thin films. *Journal of Materials Chemistry* 2009;19(46):8767-71.
351. George SM, Yoon B, Dameron AA. Surface chemistry for molecular layer deposition of organic and hybrid organic-inorganic polymers. *Acc Chem Res* 2009; 42(4):498-508.
352. Yoon B, Seghete D, Cavanagh AS, George SM. Molecular layer deposition of hybrid organic-inorganic alucone polymer films using a three-step ABC reaction sequence. *Chemistry of Materials* 2009; 21(22):5365-74.
353. Kubono A, Okui N, Tanaka K, Umemoto S, Sakai T. Highly oriented polyamide thin-films prepared by vapor-deposition polymerization. *Thin Solid Films* 1991; 199(2):385.

354. Shao H, Umemoto S, Kikutani T, Okui N. Layer-by-layer polycondensation of nylon 66 by alternating vapour deposition polymerization. *Polymer* 1997; 38(2):459-62.
355. Yoshimura T, Tatsuura S, Sotoyama W. Polymer-films formed with monolayer growth steps by molecular layer deposition. *Appl Phys Lett* 1991; 59(4):482-4.
356. Bitzer T, Richardson N. Demonstration of an imide coupling reaction on a si(100)-2x1 surface by molecular layer deposition. *Appl Phys Lett* 1997; 71(5):662-4.
357. McMahon C, Alemany L, Callender R, Bott S, Barron A. Reaction of al(bu-t)(3) with ethylene glycol: Intermediates to aluminum alkoxide (alucone) preceramic polymers. *Chem Mat* 1999; 11(11):3181-8.
358. Gong B, Peng Q, Parsons GN. Conformal organic-inorganic hybrid network polymer thin films by molecular layer deposition using trimethylaluminum and glycidol. *J Phys Chem B* 2011;115(19):5930-8.
359. Miller DC, Foster RR, Jen S, Bertrand JA, Seghete D, Yoon B, Lee Y, George SM, Dunn ML. Thermomechanical properties of aluminum alkoxide (alucone) films created using molecular layer deposition. *Acta Materialia* 2009; 57(17):5083-92.
360. Miller DC, Foster RR, Zhang Y, Jen S, Bertrand JA, Lu Z, Seghete D, O'Patchen JL, Yang R, Lee Y, et al. The mechanical robustness of atomic-layer- and molecular-layer-deposited coatings on polymer substrates. *J Appl Phys* 2009; 105(9):093527.
361. Seghete D, Davidson BD, Hall RA, Chang YJ, Bright VM, George SM. Sacrificial layers for air gaps in NEMS using alucone molecular layer deposition. *Sensors and Actuators A-Physical* 2009; 155(1):8-15.
362. Liang X, Weimer AW. Photoactivity passivation of TiO(2) nanoparticles using molecular layer deposited (MLD) polymer films. *Journal of Nanoparticle Research* 2010; 12(1):135-42.
363. Liang X, King DM, Li P, George SM, Weimer AW. Nanocoating hybrid polymer films on large quantities of cohesive nanoparticles by molecular layer deposition. *AIChE J* 2009; 55(4):1030-9.
364. Qin Y, Yang Y, Scholz R, Pippel E, Lu X, Knez M. Unexpected oxidation behavior of cu nanoparticles embedded in porous alumina films produced by molecular layer deposition. *Nano Lett* 2011; 11(6):2503-9.
365. Armand M, Tarascon J-M. Building better batteries. *Nature* 2008; 451(7179):652-7.

366. Balakrishnan P, Ramesh R, Kumar T. Safety mechanisms in lithium-ion batteries. *J Power Sources* 2006 ; 155(2):401-14.
367. Wagner FT, Lakshmanan B, Mathias MF. Electrochemistry and the future of the automobile. *Journal of Physical Chemistry Letters* 2010; 1(14):2204-19.
368. Xing W, Dahn JR. Study of irreversible capacities for li insertion in hard and graphitic carbons. *J Electrochem Soc* 1997;144(4):1195-201.
369. Thonton J. Carbon nanowalls: Processing, structure and electrochemical properties. Raleigh, NC: North Carolina State University; 2011. Available from: electronic.
370. McClure JP, Thornton JD, Jiang R, Chu D, Cuomo JJ, Fedkiw PS. Oxygen reduction on metal-free nitrogen-doped carbon nanowall electrodes. unpublished.
371. Kim C, Yang KS, Kojima M, Yoshida K, Kim YJ, Kim YA, Endo M. Fabrication of electrospinning-derived carbon nanofiber webs for the anode material of lithium-ion secondary batteries. *Advanced Functional Materials* 2006; 16(18):2393-7.
372. Agend F, Naderi N, Fareghi-Alamdari R. Fabrication and electrical characterization of electrospun polyacrylonitrile-derived carbon nanofibers. *J Appl Polym Sci* 2007; 106(1):255-9.
373. Chung GS, Jo SM, Kim BC. Properties of carbon nanofibers prepared from electrospun polyimide. *J Appl Polym Sci* 2005; 97(1):165-70.
374. Jung YS, Cavanagh AS, Riley LA, Kang S, Dillon AC, Groner MD, George SM, Lee S. Ultrathin direct atomic layer deposition on composite electrodes for highly durable and safe li-ion batteries. *Adv Mater* 2010; 22(19):2172.
375. Oldham CJ, Gong B, Spagnola JC, Jur JS, Senecal KJ, Godfrey TA, Parsons GN. Encapsulation and chemical resistance of electrospun nylon nanofibers coated using integrated atomic and molecular layer deposition. *J Electrochem Soc* 2011;158(9):D549.
376. Zhang SS, Xu K, Jow TR. Charge and discharge characteristics of a commercial LiCoO₂-based 18650 li-ion battery. *J Power Sources* 2006; 160(2):1403-9.
377. Kamali AR, Fray DJ. Tin-based materials as advanced anode materials for lithium ion batteries: A review. *Reviews on Advanced Materials Science* 2011;27(1):14-24.
378. Ferguson J, Smith E, Weimer A, George S. ALD of SiO₂ at room temperature using TEOS and H₂O with NH₃ as the catalyst. *J Electrochem Soc* 2004;151(8):G528-35.

379. Liu H, Wang G, Park J, Wang J, Liu H, Zhang C. Electrochemical performance of alpha- Fe_2O_3 nanorods as anode material for lithium-ion cells. *Electrochim Acta* 2009; 54(6):1733-6.
380. Meduri P, Pendyala C, Kumar V, Sumanasekera GU, Sunkara MK. Hybrid tin oxide nanowires as stable and high capacity anodes for li-ion batteries. *Nano Letters* 2009; 9(2):612-6.
381. Chen JS, Tan YL, Li CM, Cheah YL, Luan D, Madhavi S, Boey FYC, Archer LA, Lou XW. Constructing hierarchical spheres from large ultrathin anatase TiO_2 nanosheets with nearly 100% exposed (001) facets for fast reversible lithium storage. *J Am Chem Soc* 2010; 132(17):6124-30.
382. Ji L, Zhang X. Electrospun carbon nanofibers containing silicon particles as an energy-storage medium. *Carbon* 2009;47(14):3219-26.
383. Ji L, Lin Z, Medford AJ, Zhang X. In-situ encapsulation of nickel particles in electrospun carbon nanofibers and the resultant electrochemical performance. *Chemistry - A European Journal* 2009;15(41):10718-22.
384. Kreuz J, Endrey A, Gay F, Sroog C. Studies of thermal cyclizations of polyamic acids and tertiary amine salts. *Journal of Polymer Science Part A-1-Polymer Chemistry* 1966;4(10PA):2607.
385. Nah C, Han S, Lee M, Kim J, Lee D. Characteristics of polyimide ultrafine fibers prepared through electrospinning. *Polym Int* 2003; 52(3):429-32.
386. Dobrzynski P. Initiation process of L-lactide polymerization carried out with zirconium(IV) acetylacetonate. *J Polym Sci Pol Chem* 2004; 42(8):1886-900.
387. Okada T, Amou S, Haba O, Ueda M. Synthesis of poly(dinaphthylene ether) by oxidative coupling polymerization of di(1-naphthoxy)pentane using cobalt (III) acetylacetonate. *High Perform Polymers* 1998;10(3):241-7.
388. Aaltonen T, Miikkulainen V, Gandrud KB, Pettersen A, Nilsen O, Fjellvag H. ALD of thin films for lithium ion batteries. 7th symposium on atomic layer deposition applications - 220th ECS meeting, October 10, 2011 - October 12; 2011; Boston, MA: Electrochemical Society Inc; 2011.
389. Choi Y, Chung K, Kim W, Sung Y, Park S. Suppressive effect of Li_2CO_3 on initial irreversibility at carbon anode in li-ion batteries. *J Power Sources* 2002; 104(1):132-9.

390. Kim H, Cho J. Superior lithium electroactive mesoporous Si@Carbon core-shell nanowires for lithium battery anode material. *Nano Letters* 2008; 8(11):3688-91.
391. Choy K. Chemical vapour deposition of coatings. *Progress in Materials Science* 2003; 48(2):57-170.
392. Zang JB, Lu J, Qi XH, Wang YH. Characterization of silicon films grown by atomic layer deposition on nanocrystalline diamond. *Diam Relat Mat* 2006; 15(9):1434-7.
393. Hochbaum AI, Yang P. Semiconductor nanowires for energy conversion. *Chem Rev* 2010; 110(1):527-46.
394. Stoller MD, Park S, Zhu Y, An J, Ruoff RS. Graphene-based ultracapacitors. *Nano Lett* 2008; 8(10):3498-502.
395. Burke A. Ultracapacitors: Why, how, and where is the technology. *J Power Sources* 2000; 91(1):37-50.
396. Sun X, Xie M, Wang G, Sun H, Cavanagh AS, Travis JJ, George SM, Lian J. Atomic layer deposition of TiO₂ on graphene for supercapacitors. *J Electrochem Soc* 2012;159(4):A364-9.
397. Lee J, Hon M, Chung Y, Leu I. The effect of TiO₂ coating on the electrochemical performance of ZnO nanorod as the anode material for lithium-ion battery. *Applied Physics A-Materials Science & Processing* 2011; 102(3):545-50.
398. Zhong S, Howes A, Wang G, Bradhurst D, Wang C, Dou S, Liu H. A new process for fabrication of metal-hydride electrodes for nickel-metal hydride batteries. *J Alloys Compounds* 2002; 330:760-5.
399. Expanded Metal - Expanded Metal Foil - Expanded Metal Mesh - Expanded Plastic - Dexmet Corporation [Internet]Wallingford, CT: Dexmet Corporation; c2010 [cited 2012 April 26, 2012]. Available from: <http://www.dexmet.com/Products.html>.